University of Texas at Arlington

Doctoral Thesis

A Multi-Channel Search for Signatures of eV^2-Scale Sterile Neutrinos in IceCube

---

Author:
Benjamin Randolph Smithers

Supervisor:
Dr. Benjamin J.P. Jones

A thesis submitted in fulfillment of the requirements
for the degree of Doctor of Philosophy

in the

University of Texas at Arlington
Department of Physics

December 2023

UNIVERSITY OF TEXAS AT ARLINGTON

Abstract

College of Science

Department of Physics

Doctor of Philosophy

A Multi-Channel Search for Signatures of eV^2-Scale Sterile Neutrinos in IceCube

by Benjamin Randolph Smithers

The IceCube Neutrino Observatory is a cubic-kilometer-scale neutrino observatory built using a gigaton of instrumented ice near the Amundsen-Scott South Pole Station in Antarctica; it measures the Čerenkov light emitted by the daughter particles of deep inelastic scattering interactions occurring inside and around the detector from neutrinos of both astrophysical and atmospheric origin. For eV^2-scale sterile neutrino models, matter-effects can yield resonant $\bar{\nu}_\mu \to \bar{\nu}_s$ oscillations for TeV-scale up-going neutrinos. For certain combinations of mixing angles, this is expected to yield resonant $\bar{\nu}_\mu \to \bar{\nu}_\tau$ oscillations at the same energies and angles as the ν_μ disappearance. This superimposed ν_μ disappearance and ν_τ appearance presents itself as an ideal signature with which we can search for indications of sterile neutrino oscillations.

This dissertation presents the development of novel techniques for quantifying new sources of detector uncertainty, new simulation methods, calculations of the detector's sensitivity to these processes, and applies each of these in a multi-channel analysis searching for signs of both the resonant muon neutrino disappearance alongside the tau neutrino appearance. The analysis finds a best fit at $\Delta m^2_{41} = 7$ eV^2, $|U_{\mu 4}|^2 = 0.03$, and $|U_{\tau 4}|^2 = 0.0$, indicating no significant preference for a sterile neutrino.

Acknowledgements

By some miracle, I turned this dissertation in on time. But rather than by some kind of divine intervention, it was because of the collected efforts and support from dozens of people over the five or so years it took to write and research. Without them either this dissertation wouldn't exist, or you might've instead found yourself reading about something like Dune (not the fun one).

I would like to express my deepest gratitude to my advisor, Benjamin Jones, who was the best advocate and mentor I could have asked for throughout these last five years, and especially so in the race to get this analysis unblinded. I would like need to thank Leslie Rogers and Nick Byrnes for getting me to joint the nuRES group, or at the time REST, to begin with and getting me started on this path. They were the best friends I could've asked for in finding my way through this doctorate. And of course there's Grant Parker for leading the way forward for IceCube at UTA and showing that this all could be done; Austin Schneider and Carlos Argüelles for showing me the ropes in IceCube; Alex, Alfonso, Phillip, Janet, John, Spencer, Marjon, Basia, and all of the other MEOWS folks who have been an invaluable source of feedback, advice, and fun over the years. I also would like to thank my undergraduate advisor Bruce Schumm for giving me my first opportunity to do physics research and for getting me started in high energy physics.

I would also like to thank my parents Mark and Sheila and brother Cree for supporting me always throughout my long, academic, journey over the decades; Amy and Pat for all of snacks, drinks, board games, food again, support, and care throughout my undergrad and onwards. Of course, I would also like to thank my partner Ella for always being there to help me through the hardest parts of my doctorate, especially so during this last year a while everything was coming together. Without her this would've been so much more difficult, and maybe even impossible!

There really are too many people to thank one after the other like above, and so in no particular order I'd also like to thank Jackie, Gunnar, Franz, Karen, Krishan, Akshima, Enakshi, Austin, Sanmitra, Logan, Lesley, Andrew, Juan, Maya, the other Andrew, Andy, Neil, Nick, Tyler, Ross (go blue steel!), Christian, Steven, Ari, Brutus, Michael, Kethry, Alex, and so many others - especially those whose names I accidentally left off of this list.

Contents

Chapter 1

Introduction

1.1 Neutrinos Today

Of the seventeen fundamental particles known to exist, illustrated in Figure 1.1.2, three are neutrinos. This three-neutrino model has been well-established after several decades of study [1, 2, 3, 4, 5, 6]. Despite this success, several anomalies exist in short-baseline neutrino oscillations experiments in $\nu_\mu \to \nu_e$ appearance [7], reactor neutrino experiments [8, 9], and in Gallium [10, 11]. Several of these could be explained by additional oscillations of unknown neutrino mass and flavor eigenstates with eV^2-scale mass squared differences from the known active states [12]. To be consistent with measurements of Z-boson decay [5] any light new flavor state would need to be non weakly-interacting, or "sterile". One of the simplest models satisfying these criteria is the "3+1" light sterile neutrino model in which only a single sterile neutrino is added to the three-neutrino paradigm. This introduces a single mass eigenstate ν_4 that is sufficiently heavy, compared to the other three, such as to be described by a single mass difference $\Delta m_{41} = m_4 - m_1$. Since the states are non-interacting, the most direct way[1] of testing for their existence is through neutrino oscillations.

Several recent developments have further motivated exploration of the 3+1 sterile neutrino landscape. Recent results from MicroBooNE [14, 15] have failed to support the 3+1 explanation of the MiniBoone low-energy excess [7]. While the implications of this new tension were just starting to be understood [16, 17], the Baksan Experiment on Sterile Transitions (BEST) validated existing anomalies in Gallium short-baseline oscillations experiments SAGE [10] and GALLEX [18]:

[1] Indirect probes of sterile neutrinos are possible by measuring the neutrino effective mass in $0\nu\beta\beta$ decays. This will only work if the neutrino is Majorana, however [13]

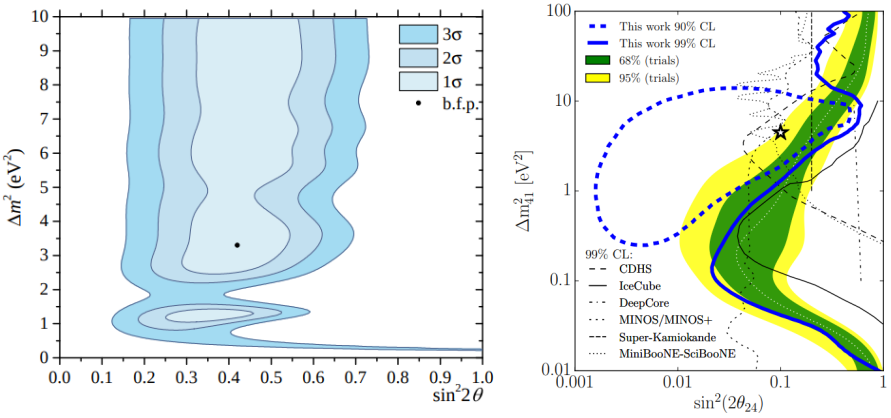

FIGURE 1.1.1: (Left): the exclusion contours for the results of BEST; best fit is at $\Delta m = 3.3$ eV^2 and $\sin^2 2\theta = 0.42$; (right): the exclusion contours from the IceCube matter-enhanced sterile neutrino search. Figures from Ref [20] and Ref [22], respectively.

two experiments designed to detect solar neutrinos through $\nu_e + ^{71}\text{Ga} \rightarrow e^- + ^{71}\text{Ge}$. Known as the gallium anomaly [19], SAGE and GALLEX had observed an event rate 2-3σ below the expected amount, or about 86% what was predicted. This lead to extensive validation studies on cross-sections, germanium extraction efficiency, and counting efficiency; no calibration issues were found, although the lack of observed could be explained by eV^2-scale neutrino oscillations [19]. As a response to this open anomaly, BEST employed a ^{51}Cr source placed at the geometric center of two concentric spherical volumes of Germanium of outer radii 133.5 cm and 234.5 cm. As ^{51}Cr decays via electron capture with ν_e emission at four distinct energies, it is ideal for making precision measurements of very short baseline neutrino oscillations by comparing the ratio of $\nu_e + ^{71}\text{Ga} \rightarrow e^- + ^{71}\text{Ge}$ interaction rates in the inner and outer volumes. In BEST, the gallium anomaly became even more pronounced: the observed rates were 0.77 ± 0.05 and 0.79 ± 0.05 of the predicted rates for the outer and inner rates, respectively. BEST's results prefer 3+1 over the null in excess of 3σ with the best fit at $\Delta m^2 = 3.3$ eV^2 and $\sin^2 2\theta_{14} = 0.42$; its results are shown in Figure 1.1.1 (left) [20, 21].

Meanwhile Neutrino-4 claims signal at a similar significance at 2.9σ in $\bar{\nu}_e$ disappearance, preferring a 3+1 model with $\Delta m^2 = 7.3$ eV^2 and $\sin^2 2\theta_{14} = 0.38$ [9]. By leveraging matter-enhanced oscillations, IceCube has independently observed signal-like evidence at the 90% confidence level in one of the strongest $\bar{\nu}_\mu$ disappearance measurements to date [22, 23]. Its exclusion contours

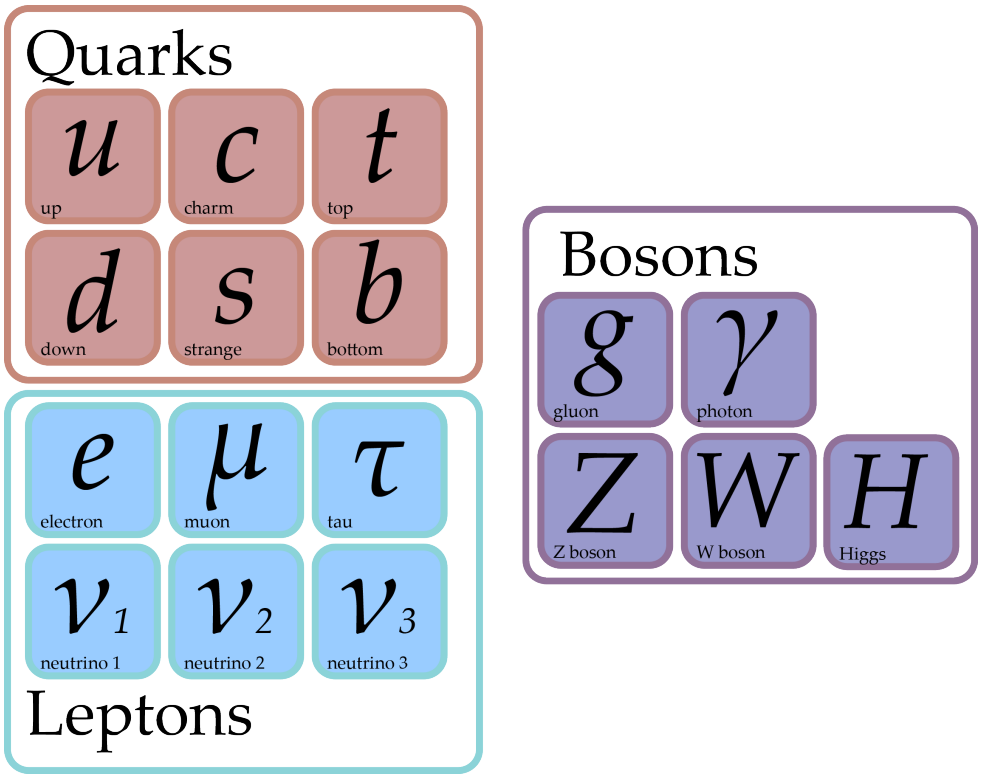

FIGURE 1.1.2: A table of the seventeen fundamental particles. The mass eigenstates for the fermions are shown.

are shown in Figure 1.1.1 (right), and are consistent with constraints from BEST. These results complicate matters as they strongly refute previous solutions to the anomalies in MiniBooNE and LSND [24], and other constraints around 1 eV^2 [25, 26, 12, 27, 28, 29]. These previous IceCube ν_μ disappearance results, however, conservatively assumed $\theta_{14} = \theta_{34} = 0$. And so strong motivations are abundant to expand these previous IceCube analyses in a widened search, taking advantage of newer event morphologies, to study signatures we might expect given the results from BEST and previous IceCube analyses.

First, however, we begin with a review of the physics relevant to neutrinos.

1.2 Neutrino Oscillations

The weak interaction couples left-handed neutrinos and charged leptons in SU(2) doublets,

$$\begin{pmatrix} \nu_e \\ e^- \end{pmatrix} \qquad \begin{pmatrix} \nu_\mu \\ \mu^- \end{pmatrix} \qquad \begin{pmatrix} \nu_\tau \\ \tau^- \end{pmatrix}. \tag{1.2.1}$$

As a consequence, neutrinos can only be produced in one of these three flavor eigenstates. Similar to in the quark sector, the neutrino flavor eigenstates can be expressed as linear superpositions of the mass eigenstates, which are related to one another by the unitary Pontecorvo-Maki-Nakagawa-Sakata (PMNS) matrix in the standard 3ν model

$$U_{\text{PMNS}} = \begin{pmatrix} U_{e1} & U_{e2} & U_{e3} \\ U_{\mu 1} & U_{\mu 2} & U_{\mu 3} \\ U_{\tau 1} & U_{\tau 2} & U_{\tau 3} \end{pmatrix}. \tag{1.2.2}$$

And so the mass-basis is related to the flavor basis as

$$\begin{pmatrix} \nu_e & \nu_\mu & \nu_\tau \end{pmatrix} = \begin{pmatrix} U_{e1} & U_{e2} & U_{e3} \\ U_{\mu 1} & U_{\mu 2} & U_{\mu 3} \\ U_{\tau 1} & U_{\tau 2} & U_{\tau 3} \end{pmatrix} \begin{pmatrix} \nu_1 \\ \nu_2 \\ \nu_3 \end{pmatrix}, \tag{1.2.3}$$

where ν_i, $i \in (1,2,3)$ is in the mass basis and $i \in (e, \mu\tau)$ is in the flavor basis. We can, in general then, express a stationary neutrino state in the flavor basis in terms of the mass basis. First, let us consider two neutrino oscillations, where a generic SU(2) matrix can be written as

$$U_{2d} = \begin{pmatrix} \cos\theta & \sin\theta \\ -\sin\theta & \cos\theta \end{pmatrix} \tag{1.2.4}$$

where θ is some real-valued angle describing a rotation from one basis to the other. So we can write an initial $|\nu_e\rangle$ state as

$$|\nu_e\rangle = \cos\theta\,|\nu_1\rangle + \sin\theta\,|\nu_2\rangle\,. \tag{1.2.5}$$

A time-evolved neutrino state will be one solving the time-dependent Schrödinger Equation,

$$i\frac{\partial}{\partial t}\left|\nu_i(t)\right\rangle = \boldsymbol{H}_\nu \left|\nu_i(t)\right\rangle, \tag{1.2.6}$$

which we can do with a stationary state solution

$$\left|\nu_i(t)\right\rangle = e^{-iEt}\left|\nu_i(0)\right\rangle. \tag{1.2.7}$$

Neutrinos are known to have very small masses [30], and so we expand out an expression of the four-momentum energy and cut off any terms with $\mathcal{O}(> m^2)$.

$$E_i = \sqrt{p^2c^2 + m_i^2c^4} \tag{1.2.8}$$

$$\approxeq pc + \frac{m_i^2c^4}{2E} \tag{1.2.9}$$

The stationary state solution Equation (1.2.7) becomes, using $t = L/c$ and $c = 1$

$$\left|\nu_i(t)\right\rangle = e^{-ipt}e^{-im_i^2L/2E}\left|\nu_i(0)\right\rangle \tag{1.2.10}$$

and for the state described in Equation (1.2.5),

$$\left|\nu_e(t)\right\rangle = e^{-ipt}e^{-im_1^2L/2E}\cos\theta\left|\nu_1\right\rangle + e^{-ipt}e^{-im_2^2L/2E}\sin\theta\left|\nu_2\right\rangle. \tag{1.2.11}$$

Considering the muon flavor state expressed in the mass basis,

$$\left\langle\nu_\mu\right| = -\sin\theta\left\langle\nu_1\right| + \cos\theta\left\langle\nu_2\right|, \tag{1.2.12}$$

the oscillations probabilities can be calculated by projecting the final considered state onto the evolved state.

$$\left\langle\nu_\mu|\nu_e(t)\right\rangle = -e^{-ipt}e^{-im_1^2L/2E}\cos\theta\sin\theta + e^{-ipt}e^{-im_2^2L/2E}\sin\theta\cos\theta \tag{1.2.13}$$

$$\left\langle\nu_\mu|\nu_e(t)\right\rangle = \tfrac{1}{2}e^{-ipt}\left[e^{-im_2^2L/2E} - e^{-im_1^2L/2E}\right]\sin 2\theta \tag{1.2.14}$$

To calculate actual transmission probabilities, we need the conjugate-square of this, $P_{e\mu} \equiv |\langle \nu_\mu | \nu_e(t) \rangle|^2$. While the phase term, e^{-ipt}, cancels we are left with

$$\langle \nu_\mu | \nu_e(t) \rangle = \tfrac{1}{4} \left[e^{-im_2^2 L/2E} - e^{-im_1^2 L/2E} \right] \left[e^{im_2^2 L/2E} - e^{im_1^2 L/2E} \right] \sin^2 2\theta \tag{1.2.15}$$

$$\langle \nu_\mu | \nu_e(t) \rangle = \tfrac{1}{4} \left[1 - e^{-i\Delta m_{21}^2 L/2E} - e^{i\Delta m_{21}^2 L/2E} + 1 \right] \sin^2 2\theta \tag{1.2.16}$$

$$\langle \nu_\mu | \nu_e(t) \rangle = \tfrac{1}{4} \left[2 - 2\cos\left(\Delta m_{21}^2 L/2E\right) \right] \sin^2 2\theta \tag{1.2.17}$$

$$\langle \nu_\mu | \nu_e(t) \rangle = \left[\frac{1 - \cos\left(2\Delta m_{21}^2 L/4E\right)}{2} \right] \sin^2 2\theta \tag{1.2.18}$$

$$\langle \nu_\mu | \nu_e(t) \rangle = \sin^2 \left(\frac{\Delta m_{21}^2 L}{4E} \right) \sin^2 2\theta \tag{1.2.19}$$

Neutrino oscillation probabilities are dependent not on the mass of the neutrino eigenstates, but the differences of square of the masses over which oscillations are considered. Through oscillations, we can only measure the absolute of the difference of the masses, and so the ordering of the masses is invisible to neutrino oscillations. Since oscillations today are well-established, at minimum two of the neutrino masses must be non-zero. Oscillations will also depend on the energy E of the neutrinos involved and the baseline L over which they travel.

For oscillations over a fixed L/E baseline, the mass-squared splitting will affect the frequency of the neutrino oscillations and the elements in the neutrino mixing matrix will affect the amplitudes of the oscillations. A toy-model example is shown in Figure 1.2.1, where an initial ν_μ flux is propagated over a fixed baseline. A varying amount of the initial flux is expected to oscillate to ν_e as a function of energy.

We next consider the general case of a neutrino initially in the electron-flavor neutrino state.

$$|\nu_e\rangle = \sum_j U_{ej} |\nu_j\rangle \tag{1.2.20}$$

Much like before we evolve an arbitrary stationary state

$$|\nu_j(t)\rangle = e^{-ipt} e^{-m_j^2 L/2E} |\nu_j(0)\rangle \tag{1.2.21}$$

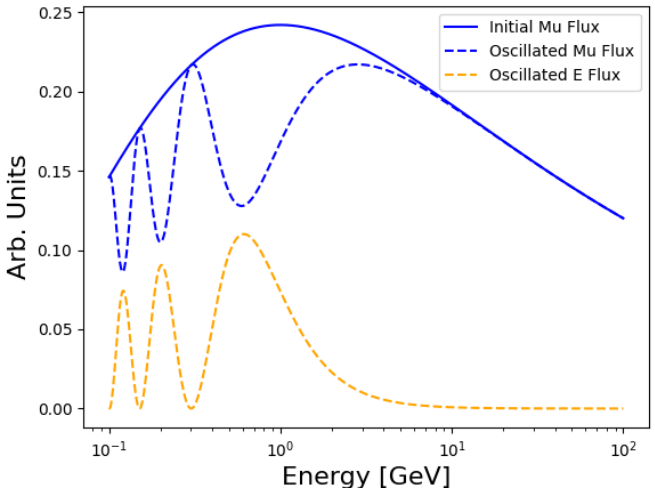

FIGURE 1.2.1: A toy 2-neutrino oscillations example. The initial flux is shown as a solid blue line, and the propagated fluxes are shown as dashed lines in orange and blue.

such that Equation (1.2.20) becomes

$$|\nu_e(t)\rangle = \sum_j U_{ej} e^{-ipt} e^{-m_j^2 L/2E} |\nu_j(0)\rangle \,. \tag{1.2.22}$$

Again, we consider the probability of measuring the neutrino in the muon flavor state some time t after preparing it the electron flavor state.

$$\langle \nu_\mu | \nu_e(t)\rangle = e^{-ipt} \sum_j U_{\mu j}^* U_{ej} e^{-m_j^2 L/2E} \tag{1.2.23}$$

We need the conjugate-square of this, $P_{e\mu} \equiv |\langle \nu_\mu | \nu_e(t)\rangle|^2$.

$$\begin{aligned} P_{\mu e} = \sum_i \Big[&|U_{\mu i}|^2 \, |U_{ei}|^2 \\ &+ 2 \sum_{i>j} U_{\mu i}^* U_{ei} U_{\mu j} U_{ej}^* \; e^{-i\Delta m_{ij}^2 L/2E} \Big] \end{aligned} \tag{1.2.24}$$

Using the sinusoidal form of the exponential, we can write this in other components

$$\begin{aligned} P_{\mu e} = \sum_i \Big[& |U_{\mu i}|^2 \, |U_{ei}|^2 \\ & - 2 \sum_{i>j} \Re(U^*_{\mu i} U_{ei} U_{\mu j} U^*_{ej}) \cos\left(\Delta m^2_{ij} L/2E\right) \\ & - 2 \sum_{i>j} \Im(U^*_{\mu i} U_{ei} U_{\mu j} U^*_{ej}) \sin\left(\Delta m^2_{ij} L/2E\right) \end{aligned} \tag{1.2.25}$$

1.3 Neutrinos and Matter

1.3.1 Matter Effects on Neutrino Oscillations

Although neutrino-anything cross-sections are small compared to all other standard-model interactions, neutrinos at higher energies[2] passing through a large amount of media can result in a measureable effect on the neutrino flux. The neutrinos experience coherent forward elastic scattering with the electrons and nucleons composing the medium through which they propagate. Although all three neutrinos can scatter via Z^0 boson exchange with nucleons; only ν_e can scatter via the exchange of $\mathrm{W}^\pm$ and Z^0 with electrons. The consequence of these interactions is that neutrinos behave as if they had slightly different masses, which are referred to as effective masses, and so their oscillations are impacted. The mass-modification is parametrized through a weak-field effect from the Z^0 and $W^\pm$ on the neutrino flavor state ν_i, which we first write out as

$$V^{Z^0+W^\pm}_{\nu_i,e} = -\frac{\sqrt{2}}{2} G_F N_e + \sqrt{2} G_F N_e \qquad V^{Z^0}_{\nu_i,n} = -\frac{\sqrt{2}}{2} G_F N_n \qquad V^{Z^0}_{\nu_i,p} = \frac{\sqrt{2}}{2} G_F N_p \tag{1.3.1}$$

where G_F is the Fermi constant and N_α is the number density of particle α in the medium. If we assume similar numbers of protons and neutrons in a medium the effects of nucleons cancel for each neutrino flavor. The resulting weak-field effects, per-flavor, are

$$V^{Z^0+W^\pm}_{\nu_e} = \frac{\sqrt{2}}{2} G_F N_e \qquad V^{Z^0}_{\nu_\mu} = -\frac{\sqrt{2}}{2} G_F N_e \qquad V^{Z^0}_{\nu_\tau} = -\frac{\sqrt{2}}{2} G_F N_e \tag{1.3.2}$$

[2] seen to be relevant in IceCube at energies above a few GeV

Differences in the propagation of the different flavors will appear due to a difference in the weak-field potential. Since there are only two unique terms, it follows that

$$V \equiv V_{\nu_e}^{Z^0+W^\pm} - V_{\nu_\mu}^{Z^0} = V_{\nu_e}^{Z^0+W^\pm} - V_{\nu_\tau}^{Z^0} = \sqrt{2} G_F N_e \tag{1.3.3}$$

We now define a function $V(\vec{x}) \equiv \sqrt{2} G_F N_e(\vec{x})$ that depends on the electron number-density at arbitrary position $\vec{x}$. Since the electron flavor is the only one with a unique matter-effect, the potential difference that could modify neutrino oscillations goes like

$$V = V(x) \begin{pmatrix} 1 & 0 & 0 \\ 0 & 0 & 0 \\ 0 & 0 & 0 \end{pmatrix} \tag{1.3.4}$$

From here, we use the small-mass approximation of the neutrino mass

$$\langle \nu_\alpha | H_{vac} | \nu_\beta \rangle = \left\langle \sum_i U_{\alpha i} \nu_i \middle| H_{vac} \middle| \sum_j U_{\beta j}^* \nu_j \right\rangle \tag{1.3.5}$$

$$= \sum_j U_{\alpha j} U_{e\beta}^* \left(p + \frac{m_j^2}{2E} \right) \tag{1.3.6}$$

As in the case of vacuum oscillations, it is the relative phases of the mass eigenstate wave packets that contribute to the interference in the flavor basis. The *difference* in the energies for the different mass states is what gives rise to neutrino oscillations, so we can equivalently express each of the masses as differences from m_1^2

$$H_{\alpha\beta,vac} = \sum_j U_{\alpha j} U_{\alpha j}^* \Delta m_{j1}^2 \tag{1.3.7}$$

$$H_{vac} = \frac{1}{2E} U \begin{pmatrix} 0 & 0 & 0 \\ 0 & \Delta m_{21}^2 & 0 \\ 0 & 0 & \Delta m_{31}^2 \end{pmatrix} U^\dagger. \tag{1.3.8}$$

And so we can construct a modified Hamiltonian with the matter contribution

$$H_{tot} = \frac{1}{2E}\left[U\begin{pmatrix} 0 & 0 & 0 \\ 0 & \Delta m^2_{21} & 0 \\ 0 & 0 & \Delta m^2_{31} \end{pmatrix} U^\dagger + V(x)\begin{pmatrix} 1 & 0 & 0 \\ 0 & 0 & 0 \\ 0 & 0 & 0 \end{pmatrix}\right] \tag{1.3.9}$$

A common tactic for working with this modified Hamiltonian is in the diagonal basis, where the new diagonal elements are treated as *effective* mass eigenstates.

1.3.2 MSW Effect

The Mikheyev-Smirnov-Wolfenstein (MSW) is a neutrino matter effect effecting neutrino oscillations in media of varying density. First, we re-write Equation (1.3.8) in the two neutrino-case.

$$H_{vac} = \frac{1}{2E}\begin{pmatrix} \cos\theta & \sin\theta \\ -\sin\theta & \cos\theta \end{pmatrix}\begin{pmatrix} 0 & 0 \\ 0 & \Delta m^2 \end{pmatrix}\begin{pmatrix} \cos\theta & -\sin\theta \\ \sin\theta & \cos\theta \end{pmatrix} \tag{1.3.10}$$

$$= \frac{\Delta m^2}{2E}\begin{pmatrix} -\sin^2\theta & \cos\theta\sin\theta \\ -\cos\theta\sin\theta & \cos^2\theta \end{pmatrix} \tag{1.3.11}$$

$$= \frac{\Delta m^2}{4E}\begin{pmatrix} -2\sin^2\theta & \sin 2\theta \\ -\sin 2\theta & 2\cos^2\theta \end{pmatrix} \tag{1.3.12}$$

We can subtract an identity from this since its the relative energy of eigenstates that are important for oscillations,

$$H_{vac} = \frac{\Delta m^2}{4E}\begin{pmatrix} -2\sin^2\theta - 1 & \sin 2\theta \\ \sin 2\theta & 2\cos^2\theta - 1 \end{pmatrix}, \tag{1.3.13}$$

$$H_{vac} = \frac{\Delta m^2}{4E}\begin{pmatrix} -\cos 2\theta & \sin 2\theta \\ \sin 2\theta & \cos 2\theta \end{pmatrix}. \tag{1.3.14}$$

When adding in matter-effects, we refer to Equation (1.3.2),

$$H_{matter} = \begin{pmatrix} \frac{\sqrt{2}G_F N_e}{2} & 0 \\ 0 & -\frac{\sqrt{2}G_F N_e}{2} \end{pmatrix} \tag{1.3.15}$$

$$H_{matter} = \frac{\Delta m^2}{4E} \begin{pmatrix} \frac{2\sqrt{2}G_F N_e E}{\Delta m^2} & 0 \\ 0 & -\frac{2\sqrt{2}G_F N_e E}{\Delta m^2} \end{pmatrix} \tag{1.3.16}$$

and we construct the full Hamiltonian by combining Equations (1.3.14) and (1.3.2):

$$H_{tot} = \frac{\Delta m^2}{4E} \begin{pmatrix} -(\cos 2\theta - A) & \sin 2\theta \\ \sin 2\theta & \cos 2\theta - A \end{pmatrix} \qquad A = \frac{2\sqrt{2}G_F N_e E}{\Delta m^2}. \tag{1.3.17}$$

We can then define an effective mass difference as

$$\Delta m^2_M = \Delta m^2 \sqrt{\sin^2 2\theta + (\cos 2\theta - A)^2} \tag{1.3.18}$$

and an effecting mixing amplitude as

$$\sin^2 2\theta_M = \frac{\sin^2 2\theta}{\sin^2 2\theta + (\cos 2\theta + A)^2}. \tag{1.3.19}$$

Using these, the matter-Hamiltonian of Eq (1.3.17) can be written as

$$H_{tot} = \frac{\Delta m^2_M}{4E} \begin{pmatrix} -\cos 2\theta_M & \sin 2\theta_M \\ \sin 2\theta_M & \cos 2\theta_M \end{pmatrix}. \tag{1.3.20}$$

As can be seen, as $A \to 0$ Equations 1.3.18 and 1.3.19 yield the original vacuum forms, and so Equation 1.3.20 would also predict vacuum oscillations in the absence of matter. A itself is also now seen to depend upon the on the sign of the difference of the squares of the mass: in the presence of matter neutrino oscillations can be used to directly probe the neutrino mass ordering.

1.3.3 3+1 Neutrino Oscillations

Including a fourth, sterile, neutrino flavor and mass eigenstate expands the normal PMNS matrix to SU(4). To describe the new SU(4) mixing matrix uniquely, three new mixing angles (θ_{14}, θ_{24}, and θ_{34}) and two new CP-violating phases (δ_{14} and δ_{24}) are required. While this leads to the aforementioned short-baseline neutrino oscillations needed to explain extant oscillation anomalies, it also will yield novel effects in the presence of matter [31, 32, 33, 34, 35].

For eV-scale sterile neutrino models, the mass difference between the new ν_4 and othe mass states are essentially degenerate; we can sufficiently describe the new state using only a single new mass difference $\Delta m_{41} = m_4 - m_1$. MSW matter effects would also yield a near complete disappearance of TeV-energy muon anti-neutrinos passing through the Earth's core [36, 37, 38, 39, 40, 41, 42], as shown in Figure 1.3.1. This is of particular interest to large-volume Čerenkov neutrino observatories, like the IceCube Neutrino Observatory, which have high event rates for up-going muon neutrino events. Recent results from IceCube searching for such a signature have already found signal-like results with closed contours at the 90% confidence level and a best fit point at $\sin^2 2\theta_{24} \sim 0.1$ and $\Delta m^2_{41} = 4.5$ eV^2 [22, 23]. Despite the signal-like results, the measurement is also in tension with the LSND [24], MiniBooNE, and other constraints for values of Δm^2_{41} of around 1eV^2 [25, 26, 12, 27, 28, 29].

1.3.4 Neutrino Propagation with Interactions

In addition to neutrino oscillations and coherent matter effects, several other phenomena effect the full description of neutrino propagation through the Earth. These include, but are not limited to, neutrino flux attenuation as neutrinos interact in the Earth, the process where charged tau leptons produced through neutrino-nucleon interactions decay to produce lower energy tau neutrinos called tau regeneration, and Glashow resonance interactions [43]. These effects become increasingly relevant at the higher energies relevant to the analysis presented in this dissertation. Here we describe the methods used for numerically propagating neutrino fluxes from the Earth's surface to IceCube; these procedures were originally described by Reference [44].

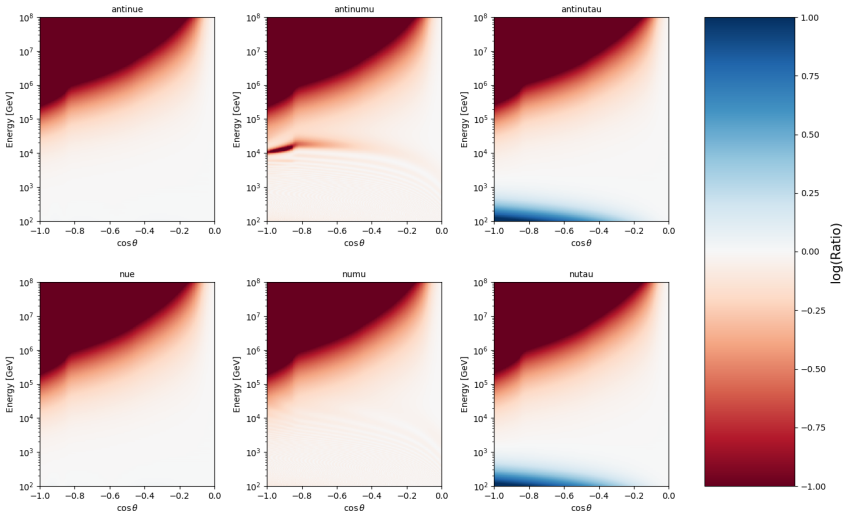

FIGURE 1.3.1: A plot showing the log of the ratio between the neutrino flux at the Earth's surface and at the IceCube detector. The top left corner of each panel shows the disappearance due to the Earth's opacity to high energy neutrinos. The blue region shows tau appearance from 3ν oscillations. The resonance in the $\bar{\nu}_\mu$ channel is an example signature of eV^2-scale sterile neutrinos.

The neutrino flux is described as a function of energy E and location x for neutrino flavor α using the density matrix formalism in the weak-interaction flavor-eigenstate basis as

$$\rho(E,x) = \sum_\alpha \phi_\alpha(E,x) \left|\nu_\alpha\right\rangle \left\langle\nu_\alpha\right| , \tag{1.3.21}$$

where ϕ_α specifies the neutrino flux of the flavor α. The evolution of the system can be described by the von Neumann equation,

$$\frac{\partial\rho(E,x)}{\partial x} = -i\left[H(E,x), \rho(E,x)\right] , \tag{1.3.22}$$

where H is the Hamiltonian for the whole system. H can be approximated, in the case of small perturbations, as

$$H(E,x) = H_0(E) + H_1(E,x) \tag{1.3.23}$$

where H_0 is the term giving vacuum neutrino oscillations, which can be solved exactly, and H_1 is an additional term incorporating matter-effects. These are, for neutrinos,

$$H_0(E) = \frac{1}{2E}\begin{pmatrix} 0 & 0 & 0 \\ 0 & \Delta m^2_{21} & 0 \\ 0 & 0 & \Delta m^2_{31} \end{pmatrix} \tag{1.3.24}$$

$$H_1(E,x) = \sqrt{2} G_F N_e(x) U^{\dagger}_{PMNS} \begin{pmatrix} 1 & 0 & 0 \\ 0 & 0 & 0 \\ 0 & 0 & 0 \end{pmatrix} U_{PMNS}, \tag{1.3.25}$$

where G_F is the Fermi constant, U_{PMNS} is the PMNS neutrino mixing matrix, N_e is the electron number density at position x, and the Δm^2 terms are the mass-squared splittings. Since the evolution of the vacuum component can be soled analytically, it is more convenient to evolve of the system in the interaction basis. So, we transform the density matrix and the mass-effect terms as

$$\rho_1(E,x) = e^{-iH_0 x}\rho(E,x)e^{-iH_0 x}. \tag{1.3.26}$$

$$H_{I,1}(E,x) = e^{-iH_0 x}H_1(E,x)e^{-iH_0 x}. \tag{1.3.27}$$

Similarly to Equation (1.3.22), the evolution in the interaction basis is dependent on the matter-effect term,

$$\frac{\partial_1 \rho(E,x)}{\partial x} = -i\left[H_{I,1}(E,x), \rho(E,x)\right]. \tag{1.3.28}$$

We require a series of additional terms that modify Eq (1.3.28) to account for the effects which do not preserve neutrino number and energy. The first of which is the attenuation of the fluxes from neutrino-Earth interactions, which follow

$$\Gamma(E,x) = \frac{1}{2}\sum_{\alpha\in(e,\mu,\tau)} \frac{\Pi_\alpha(E,x)}{\lambda^\alpha_{NC}(E,x) + \lambda^\alpha_{CC}(E,x)} \tag{1.3.29}$$

$$\bar{\Gamma}(E,x) = \frac{1}{2}\sum_{\alpha\in(e,\mu,\tau)} \frac{\bar{\Pi}_{\alpha(E,x)}}{\bar{\lambda}^\alpha_{NC}(E,x) + \bar{\lambda}^\alpha_{CC}(E,x) + \bar{\lambda}^\alpha_{GR}(E,x)} \tag{1.3.30}$$

where Π_α is a neutrino projector onto the flavor $\alpha \in \{e, \mu\tau\}$, ν^α_{CC} (ν^α_{NC}) is the charged (neutral) current neutrino interaction length given by $1/\left[N_{nuc}(x)\sigma^\alpha_{CC(NC)}(E)\right]$ [45, 46, 47, 48, 49], and $\bar{\lambda}^e_{GR}$ is the mean free path due to the Glashow Resonance $1/\left[N_e(x)\sigma^e_{GR}(E)\right]$ [43].

We also account for tau regeneration, neutrino-antineutrino coupling, and low-energy neutrino re-injection from neutral current interactions following the functional forms for neutrinos F and antineutrinos $\bar{F}$ given by

$$
\begin{aligned}
F\left[\rho, \bar{\rho}, E, x\right] = & \sum_\alpha \Pi_\alpha(E, x) \int_E^\infty \frac{\mathrm{Tr}\left[\Pi(E_{\nu_\alpha}, x)\rho(E_{\nu_\alpha}, x)\right]}{\lambda^\alpha_{NC}(E_{\nu_\alpha}, x)} \frac{\partial N^\alpha_{NC}(E_{\nu_\alpha}, E)}{\partial E} dE_{\nu_\alpha} \\
& + \Pi_\tau(E, x) \int_E^\infty \int E_\tau{}^\infty \frac{\mathrm{Tr}\left[\Pi(E_{\nu_\tau}, x)\rho(E_{\nu_\tau}, x)\right]}{\lambda^\tau_{NC}(E_{\nu_\tau}, E)} \frac{\partial N^\tau_{NC}(E_{\nu_\tau}, x)}{\partial E} \\
& \times \frac{\partial N^{all}_{dec}(E_\tau, E)}{\partial E} dE_{\nu_\tau} dE_\tau \\
& + \Bigg[\mathrm{Br}\left(\tau^- \to \bar{\nu}_e\right) \Pi_e(E, x) \int_E^\infty \int_{E_\tau}^\infty \frac{\mathrm{Tr}\left[\bar{\Pi}(E_{\nu_\tau}, x)\bar{\rho}(E_{\nu_\tau}, x)\right]}{\bar{\lambda}^\tau_{NC}(E_{\bar{\nu}_\tau}, x)} \\
& + \mathrm{Br}\left(\tau^- \to \bar{\nu}_\mu\right) \Pi_\mu(E, x) \int_E^\infty \int_{E_\tau}^\infty \frac{\mathrm{Tr}\left[\bar{\Pi}(E_{\nu_\tau}, x)\bar{\rho}(E_{\nu_\tau}, x)\right]}{\bar{\lambda}^\tau_{NC}(E_{\bar{\nu}_\tau}, x)} \Bigg] \\
& \times \frac{\partial \bar{N}^\tau_{CC}(E_{\bar{\nu}_\tau}, E)}{\partial E} \frac{\partial \bar{N}^{lep}_{dec}(E_\tau, E)}{\partial E} dE_{\bar{\nu}_\tau} dE_\tau
\end{aligned}
\tag{1.3.31}
$$

and

$$
\begin{aligned}
\bar{F}\left[\rho,\bar{\rho},E,x\right] = & \sum_{\alpha}\bar{\Pi}_{\alpha}(E,x)\int_{E}^{\infty}\frac{\mathrm{Tr}\left[\bar{\Pi}(E_{\bar{\nu}_{\alpha}},x)\bar{\rho}(E_{\bar{\nu}_{\alpha}},x)\right]}{\bar{\lambda}^{\alpha}_{NC}(E_{\bar{\nu}_{\alpha}},x)}\frac{\partial\bar{N}^{\alpha}_{NC}(E_{\bar{\nu}_{\alpha}},E)}{\partial E}dE_{\bar{\nu}_{\alpha}} \\
& + \bar{\Pi}_{\tau}(E,x)\int_{E}^{\infty}\int_{E_{\tau}}^{\infty}\frac{\mathrm{Tr}\left[\bar{\Pi}(E_{\bar{\nu}_{\tau}},x)\bar{\rho}(E_{\bar{\nu}_{\tau}},x)\right]}{\bar{\lambda}^{\tau}_{NC}(E_{\bar{\nu}_{\tau}},x)}\frac{\partial\bar{N}^{\tau}_{NC}(E_{\bar{\nu}_{\tau}},E)}{\partial E} \\
& \times\frac{\partial\bar{N}^{all}_{dec}(E_{\tau},E)}{\partial E}dE_{\bar{\nu}_{\tau}}dE_{\tau} \\
& + \left[\mathrm{Br}\left(\tau^{+}\rightarrow\nu_{e}\right)\bar{\Pi}_{e}(E,x)\int_{E}^{\infty}\int_{E_{\tau}}^{\infty}\frac{\mathrm{Tr}\left[\Pi(E_{\nu_{\tau}},x)\rho(E_{\nu_{\tau}},x)\right]}{\lambda^{\tau}_{NC}(E_{\nu_{\tau}},x)}\right. \\
& \left. + \mathrm{Br}\left(\tau^{+}\rightarrow\nu_{\mu}\right)\bar{\Pi}_{\mu}(E,x)\int_{E}^{\infty}\int_{E_{\tau}}^{\infty}\frac{\mathrm{Tr}\left[\Pi(E_{\nu_{\tau}},x)\rho(E_{\nu_{\tau}},x)\right]}{\lambda^{\tau}_{NC}(E_{\nu_{\tau}},x)}\right] \\
& \times\frac{\partial N^{\tau}_{CC}(E_{\nu_{\tau}},E)}{\partial E}\frac{\partial N^{lep}_{dec}(E_{\tau},E)}{\partial E}dE_{\nu_{\tau}}dE_{\tau} \\
& + \left(\sum_{\alpha}\bar{\Pi}_{\alpha}(E,x)\right)\int_{E}^{\infty}\frac{\mathrm{Tr}\left[\bar{\Pi}_{e}(E_{\bar{\nu}_{e}},x)\bar{\rho}(E_{\bar{\nu}_{e}},x)\right]}{\bar{\lambda}^{e}_{GR}(E_{\bar{\nu}_{e}},x)} \\
& \times\frac{\partial\bar{N}^{e}_{GR}(E_{\bar{\nu}_{e}},E)}{\partial E}dE_{\bar{\nu}_{e}}
\end{aligned}
\tag{1.3.32}
$$

Interaction rates in these functionals for neutral current, charged current, and Glashow resonance interactions are given by

$$
\frac{\partial N^{\tau}_{NC(CC)}(E_{\nu_{\tau}},E)}{\partial E} = \frac{1}{\sigma^{\alpha}_{NC(CC)}(E_{\nu_{\alpha}})}\frac{\partial\sigma^{\alpha}_{NC(CC)}(E_{\nu_{\alpha}},E_{\alpha})}{\partial E_{\alpha}} \qquad \text{and,} \tag{1.3.33}
$$

$$
\frac{\bar{N}^{e}_{GR}(E_{\bar{\nu}_{e}},E)}{\partial E} = \frac{1}{\sigma^{e}_{GR}(E_{\bar{\nu}_{e}})}\frac{\partial\sigma^{e}_{GR}(E_{\bar{\nu}_{e}},E_{e})}{\partial E}. \tag{1.3.34}
$$

The tau decay distributions for the leptonic-only modes (N^{lep}_{dec}) and for all-modes (N^{all}_{dec}) are given by

$$
\frac{\partial N^{lep}_{dec}(E_{\tau},E)}{\partial E} = \frac{1}{\bar{\Gamma}^{\tau}_{lep}(E_{\tau})}\frac{\partial\bar{\Gamma}^{\tau}_{lep}(E_{\tau},E)}{\partial E} \tag{1.3.35}
$$

$$
\frac{\partial N^{all}_{dec}(E_{\tau},E)}{\partial E} = \frac{1}{\bar{\Gamma}^{\tau}_{all}(E_{\tau})}\frac{\partial\bar{\Gamma}^{\tau}_{all}(E_{\tau},E)}{\partial E} \tag{1.3.36}
$$

These systems are implemented within the `nuSQuIDS` framework [50, 44], which implements Equations (1.3.29)-(1.3.30) to numerically propagate the state-density matrix along a neutrino fluxes' baseline. Different neutrino oscillation parameters can be specified, along with various other new physics scenarios, if desired.

1.4 Structure

In this dissertation I present the work for and the results from a multichannel search of signatures of matter-enhanced neutrino oscillations with eV^2-scale sterile neutrinos. It is organized as follows:

Chapter 1 has introduced the background physics relevant for this work and the sterile neutrino model we are testing.

Chapter 2 will describe the IceCube Neutrino Observatory and the details of its operation.

Chapter 3 will describe the upcoming IceCube Upgrade and ongoing work being done to test the new optical modules.

Chapter 4 will provide the calculations for the predicted sensitivities for this analysis [51].

Chapter 5 will discuss the event generation schema and Monte Carlo simulation procedure used in IceCube [52].

Chapter 6 will summarize the sources of systematic uncertainty relevant for this analysis.

Chapter 7 will provide the results of this analysis.

Chapter 8 will discuss the implications of the results presented here.

Chapter entries with citations refer to the papers in which the work discussed was published.

Chapter 2

The IceCube Neutrino Observatory

The IceCube Neutrino Observatory is a gigaton-scale Cherenkov observatory instrumented across a cubic kilometer at the South Pole, two kilometers deep, in the Antarctic glacial ice [53]. As shown in Figure 2.0.1 (left) IceCube is composed of 5160 photo-multiplier tubes encased within glass pressure vessels, called "Digital Optical Modules" (DOMs) [54], which are used to detect the Cherenkov light emission from the charged daughter-particles resulting from neutrino interactions in and around the detector. These DOMs are arranged vertically with a seventeen-meter spacing into seventy-nine strings, which themselves are aligned into a hexagonal lattice with a 125-meter spacing. A more densely instrumented sub-detector called DeepCore was also installed towards the bottom-center of the main detector [55]; the additional strings of this dense in-fill brings the total string count to eighty-six. Working primarily as a cosmic-ray air shower detector, an array of surface detectors named IceTop is installed on surface of the IceCube glacier. A schematic illustration of the IceCube string and IceTop tank locations is shown in Figure 2.0.1[1].

2.1 Event topologies

Large-volume neutrino telescopes, like IceCube, typically are sensitive in the TeV to PeV energies; here, Deep-Inelastic Scattering (DIS) [56] interactions dominate, and Glashow Resonance [43] interactions have only just been observed [57]. The detected neutrino interaction events fall into two morphological categories: tracks and cascades.

[1] String 37 is off-grid as a result of a sub-surface crate of pork chops obstructing the original drill-site, see Appendix A.1.

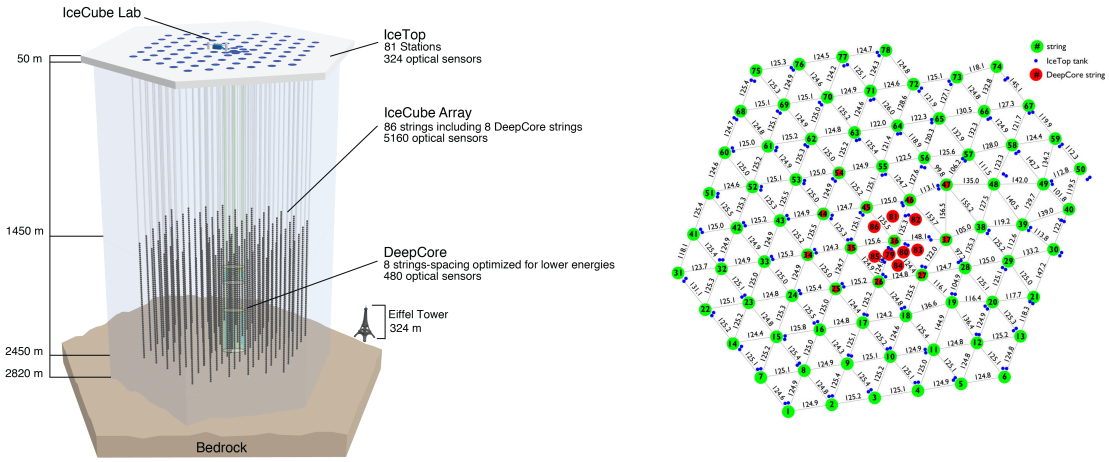

FIGURE 2.0.1: Left: a side-view of the IceCube Neutrino Observatory detector array, showing the span of the instrumented volume and DeepCore, plus the IceCube Lab and IceTop on the surface. The IceCube Lab is not to scale. Right: a top-down schematic showing the distribution of IceCube and DeepCore strings and the distances between them.

Charged-current (CC) ν_μ DIS events result in muons at energies where radiative processes dominate energy loss rates. As a result, energy losses are stochastically driven and the produced muons travel for kilometers. The consequences are threefold: muons are difficult to fully contain in neutrino telescopes, muon energies are poorly correlated with progenitor muon-neutrino energies, and muons' long travel-distance can allow for reconstructing their direction to within 1° [58]. These events are called *tracks* [59].

All neutral-current (NC) DIS events result in a hadronic shower spreading around the interaction point and a secondary neutrino invisibly carrying away a proportion of the parent neutrino's energy. These events are often contained with a roughly spherical topology. ν_e-CC interactions develop similarly to neutral-current interactions, but repeated inverse Compton scattering of the produced electron initiates an electromagnetic shower superimposed over the hadronic shower. Thus, nearly all of the interacting neutrino's energy is observable as detectable light. These events are called *cascades*. Such events tend to be well-contained permitting an efficient energy reconstruction, although they suffer from poor angular reconstruction [59].

The evolution of a ν_τ-CC interaction is highly dependent on the energies involved. A tau is produced simultaneously as a hadronic cascade propagates around the interaction point, and then the tau decays. Due to their large mass, taus have a short lifetime and a decay length of

$\sim$ 50 m per PeV of tau energy [60]. From the tau branching ratios [1], 17.37% of the charged tau decays evolve as muon tracks, while the remainder of the decays evolve as electromagnetic or hadronic cascades. Only at neutrino energies above 60 TeV do ν_τ-CC interactions yield events with potentially distinguishable primary and secondary cascades [60]; at lower energies the secondary cascade is indistinguishable from the hadronic one. Tau events which decay into muons will appear as starting track events while the remainder appear as cascades.

2.2 The Ice

As discussed in Ref [61], the Antarctic ice containing IceCube is a rapidly-moving[2] glacier formed over hundreds of thousands of years of compacted snowfall. The first few hundred meters, known as the *firn* layer, is an opaque layer of geologically new snow. At greater depths the integrated weight of the snow overburden compresses the firn layer snow into an ice characterized by short scattering lengths ($\mathcal{O}$(meters)) dominated by trapped bubbles of air. At even greater depths, the pressures reach an extreme enough level such that the ice enters a new crystalline phase along with the air molecules. The resulting, *clathrate* ice boasts good optical properties, where the optical defects are characterized instead by microscopic grains of dust and pollutants. Scattering lengths at these depths are on the order of 10s of meters while the absorption lengths rise to 100s of meters. Layers formed at the same point in time, or isochrons, tend to have similar ice optical properties as a result.

The properties were studied during the deployment of IceCube using a *dust logger*, a long, ruggedized, device with a fan-shaped 404 nanometer diode laser that could probe a 60 degree wide field of view. It used a downward-looking PMT at the bottom of the device to measure the intensity of back-scattered light. This device was lowered down six of the eighty-six boreholes dug during the IceCube deployment, which are shown on the right of Figure 2.2.2. A diagram of the dust logger is shown in Figure 2.2.1.

Data from the dust logger, shown in Figure 2.2.2, demonstrate that the absorption length and scattering length vary greatly as a function of depth. The depth-profiles also varied slightly

[2] several meters per year

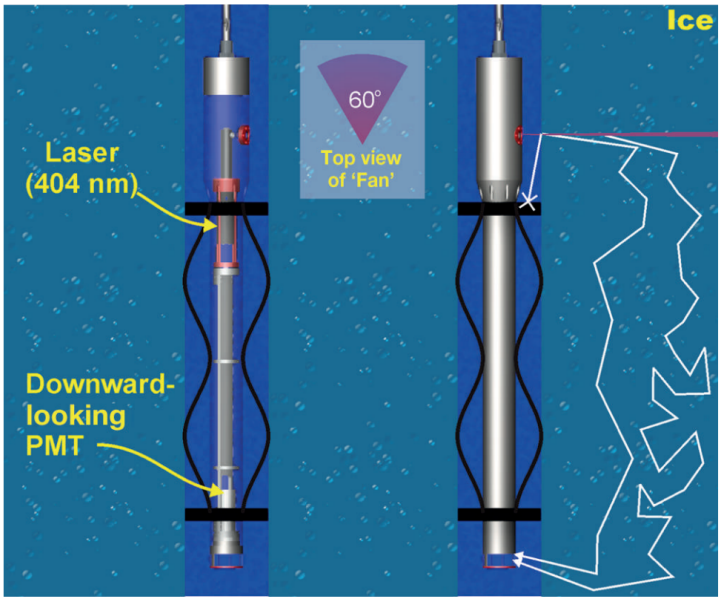

FIGURE 2.2.1: A diagram of the IceCube dust logger.

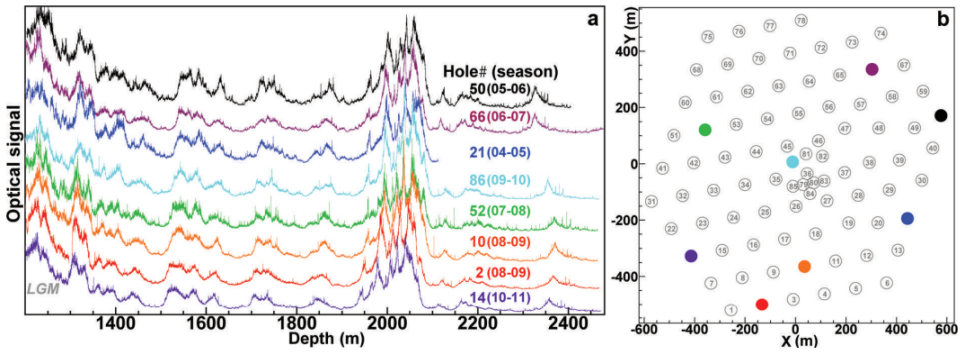

FIGURE 2.2.2: On the right we show which of the eighty-six boreholes dust-logger data was taken, and on the left we show the intensity of the back-scattered light as measured at each of the sampled holes as a function of depth.

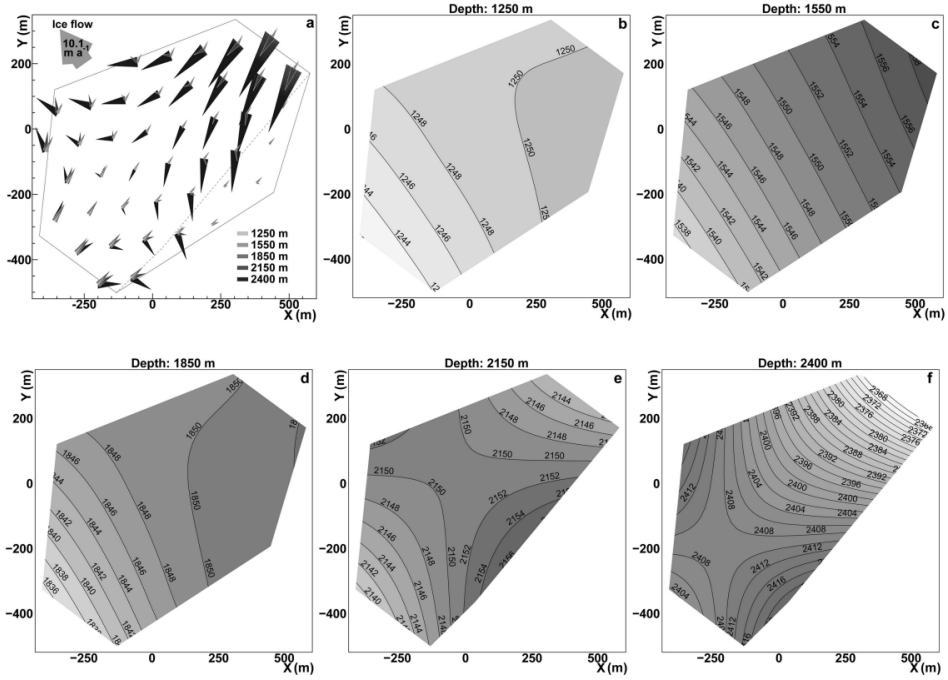

FIGURE 2.2.3: (a) shows the flow direction of the South Pole glacier (b-f) Cross-sections of the ice at various depths showing contours for different isochrons: demonstrating the tilt of the ice.

from hole-to-hole: suggesting ice at similar depths, but separated laterally, did not have the same optical properties.

As the glacier around the present day location of IceCube moved and formed over hundreds of thousands of years, the pressures of the ice over the hard bedrock beneath it warped and bent the glacier. The result of this is that the layers of ice with similar optical properties are not flat layers, but tilted and warped. Uncertainty in the bulk ice properties and their impacts on analysis-level quantities are discussed in Section 6.2.2.

As the borehole water refroze around the IceCube strings, it froze inwards from the glacial wall. This drew in trapped air from the clathrate air, resulting in a column of bubbles which formed in the central 5-10 cm of each borehole. This bubbly "hole ice" results in a much shorter scattering length when compared to the bulk ice in the region around the DOMs. The models which describe it, and its impact on analysis quantities, are described in Section 6.2.3.

During one of the dust-logger ascents, it was observed to smoothly rotate at a rate of one revolution per 25 meters depth. Below 1100 meters, a consistent intensity in the back-scattered

light was observed when the fan-laser was aligned with the direction of the glacial flow. Later in-ice studies attributed the optical anisotropy to a process where the flow of the glacial ice induced a shear between ice crystal grains and reorienting them to be orthogonal to the flow axis. The ice crystals became birefringent, such that light diffusion is greatest along the flow axis, and light would deflect towards the flow axis [62, 63]. Only some newer, internal, IceCube ice models account for the birefringence. Legacy models, like **S**outh **P**ole **ICE** 3.2.1 (Spice 3.2.1), are still widely used for analyses. Newer models, like **B**ire**FR**ingence v2 (BFR v2), are slowly being adopted by other analyses where it is shown that birefringence is found to be a relevant effect. This adoption is slowed, however, by the expensive cost of re-generating Monte Carlo samples with the updated ice models and by the need to then validate changes to the simulation.

2.3 Čerenkov Radiation

As charged particles move through ice (or any transparent media), due to dielectric effects the particles themselves can move faster than the phase velocity of the light within it. The particle will collectively polarize molecules in the surrounding bulk as it passes, and as these molecules relax to their original orientations. This manifests as the emission of light in the shape of a cone opening outwards into the direction of the particle's propagation: Čerenkov Radiation.

The threshold above which this happens can be found from energy-momentum relationships with a velocity substitution of the 3-momentum, or

$$E^2 = m^2 + \frac{m^2 v^2}{1 - v^2}. \tag{2.3.1}$$

We then consider a transparent material with an index of refraction $n = 1./v_{critical}$, where v is the phase velocity light in the medium. Particles travelling at a velocity at or above this threshold

will emit Čerenkov radiation. The associated energy $E_{critical}$ can be solved for algebraically,

$$E_{critical}^2 = m^2 + \frac{m^2 v_{critical}^2}{1 - v_{critical}^2} \tag{2.3.2}$$

$$E_{critical}^2 - m^2 - E_{critical}^2 v_{critical}^2 + m^2 v_{critical}^2 = m^2 v_{critical}^2 \tag{2.3.3}$$

$$E_{critical}^2 \left(1 - v_{critical}^2\right) = m^2 \tag{2.3.4}$$

$$\sqrt{\frac{m^2}{(1 - n^{-2})}} = E_{critical} \tag{2.3.5}$$

Like a sonic boom of light, the light is emitted in a cone which opens at an angle θ_c relative to the direction at which the particle travels. This angle is given by

$$\tan \theta_c = \sqrt{v^2 n^2 - 1}. \tag{2.3.6}$$

Although the light is emitted in the forward direction, the Čerenkov light wave-front counter-intuitively trails in a cone opening behind the radiating particle.

For highly relativistic particles travelling through ice, this angle is 41°, and the emitted light ranges from 300 to 600 nm.

2.4 The Digital Optical Modules

IceCube's Digital Optical Modules, or DOMs, are composed of a 0.5" thick borosilicate glass pressure vessel with a downwards-facing 10" Hamamatsu R7081-02 PMT and an onboard computer mounted internally on the DOM mainboard. The PMT has single-photon sensitivity in the 300-650 nm range with a 25% peak quantum efficiency at 390 nm [64]. The PMT is optically connected with the glass pressure vessel using gel to maximize transmittance of light through the vessel and into the PMT; it is protected from the Earth's magnetic field via a mu-metal wire mesh. The DOM's onboard computer houses the electronics and software necessary to trigger the DOM on any signal incident upon the PMT. A schematic design of a DOM is shown in Figure 2.4.1.

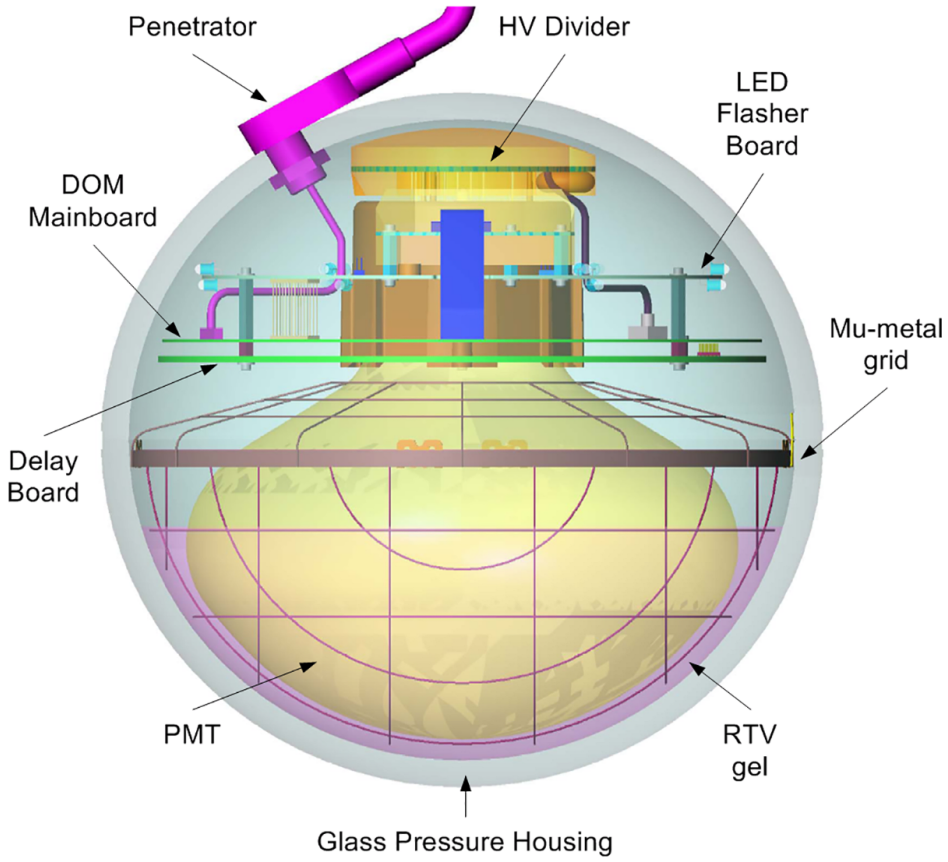

FIGURE 2.4.1: A schematic of a Digital Optical Module (DOM).

2.5 Data Acquisition

When a DOM's PMT reads sufficient charge to cross the single-photon threshold, the DOM is triggered and signal collection starts.

To minimize spurious detector triggers a coincidence threshold trigger is used. Upon DOM triggering, DOMs communicate directly with their neighbors, and if any neighboring DOMs are triggered within a 1μs window, a "hard local coincidence" (HLC) occurs. After an HLC, the surface-based IceCube Lab (ICL) registers a 'hit' and the DOMs transmit their trigger timing information and full PMT waveforms. At the ICL a Simple Multiplicity Trigger (SMT) is applied: if eight[3] HLC hits or more are detected in a 5μs window, a global detector trigger occurs and the trigger window is extended until another 5μs window passes with no further HLC hits neighboring the DOM hits. At this point, the global detector trigger rate is approximately 2kHz and the raw data output is around 1 TB/day. This data rate is too large, and so, all hits within the time window are collected into an Event and passed to the ICL "Processing aNd Filtering" (PnF) system in order to reduce the data volume below the amount allocated for IceCube's satellite collection (100 GB/day). A rudimentary reconstruction is run to calculate an approximate event interaction vertex, direction, and energy. About 25 separate filters are then applied on these reconstructed event values to select only those Events of interest for ongoing IceCube analyses: if any trigger passes then the event is kept, processed further, and transmitted to the North[4]. Each filter is carefully studied before implementation, analyzers must provide predictions for the expected data bandwidth, CPU core-hours of processing required, data storage requirements, and extensive testing of the software responsible for running the trigger. Approximately 15% of all events are selected by one or more filter [53].

[3] Starting in 2024 runs, this threshold is changing to twelve

[4] Anywhere that isn't Antarctica: the *North* usually refers to Madison, Wisconsin, however.

Chapter 3

IceCube Upgrade

The IceCube Upgrade [65] is a planned expansion of the IceCube array designed to improve its sensitivity to low-energy neutrino events, which at the moment has a planned deployment for the 2025/6 south-pole season. It will consist of seven additional strings of 700 optical sensors, which will be embedded near the bottom-center of the existing IceCube array where the ice is optically cleanest. An illustration of the Upgrade is shown in Figure 3.0.1 Two new optical sensors will be installed in Upgrade: the Multi-PMT Digital Optical Module (mDOM) [66], and the Ellipsoid Glass for Gen2 (D-Egg) module [67].

These modules are designed to improve the photon detector efficiency and overall calibration of the detector within a small two megaton volume within the greater array. This will allow for the use of the main IceCube array to act as a veto layer for high-precision measurements of neutrino interactions in the $\mathcal{O}(1 \sim 10\text{GeV})$ energy range. This will allow for the measurement of tau neutrino appearances with high precision, allow for cutting-edge measurements of neutrino oscillations, and to probe the unitarity of the Pontecorvo-Maki-Nakagawa-Sakata neutrino mixing matrix. Figure3.0.2, from Reference [65], shows how well IceCube Upgrade will be able to constraint three-neutrino oscillations using only three years of data.

3.1 IceCube D-Eggs

The "**D**ual optical sensors in an **E**llipsoid **G**lass for **G**en2," or D-Egg, is a new module designed for future extensions of IceCube. A schematic of a D-Egg is shown in Figure 3.1.1 In particular, it is one of the planned optical modules to be deployed at the IceCube Neutrino Observatory

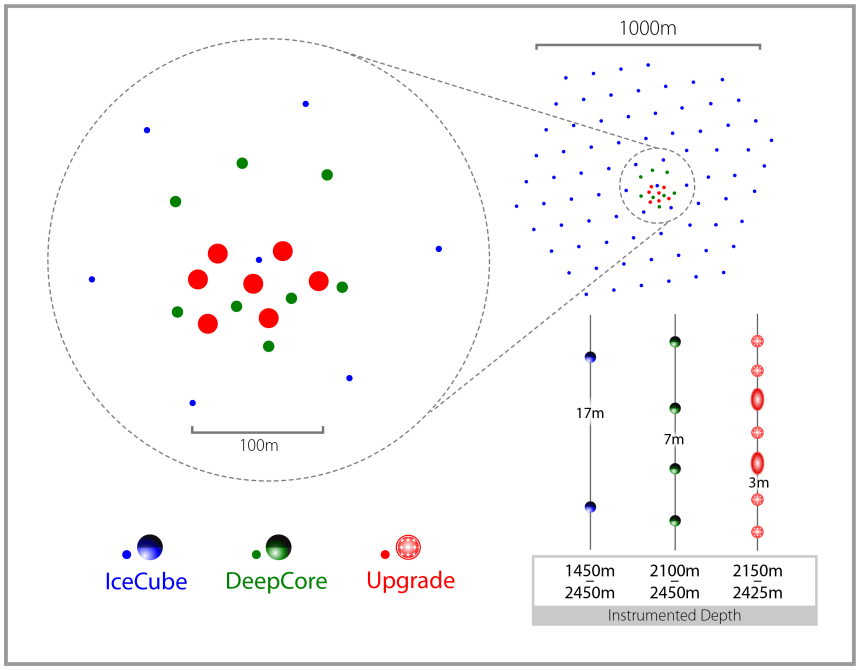

FIGURE 3.0.1: A top-down view of the planned installation locations of IceCube Upgrade strings relative to existing IceCube and DeepCore strings.

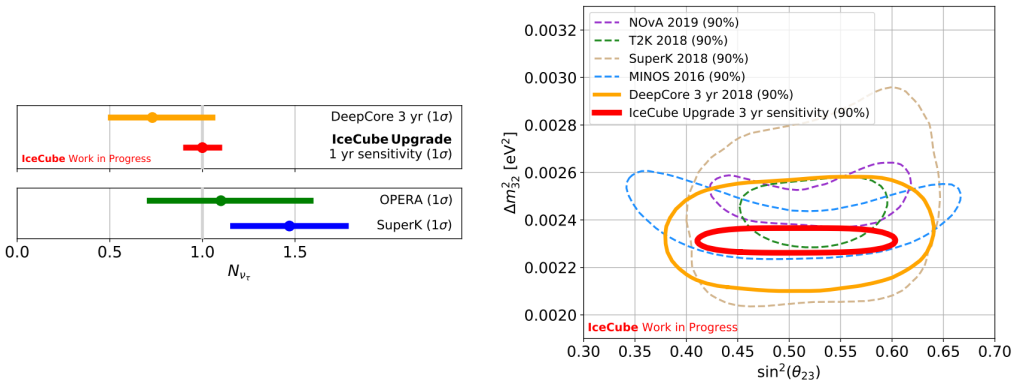

FIGURE 3.0.2: On the left, the 1σ sensitivity of the IceCube Upgrade (and other experiments) to constrain the normalization of the tau normalization, where we assume a normalization of one with one year of data. On the right, the predicted sensitivity of IceCube Upgrade to the 3ν oscillations parameters $\sin^2(\theta_{24})$ and Δm^2_{32} with comparisons to References [68, 69, 70, 71, 72]

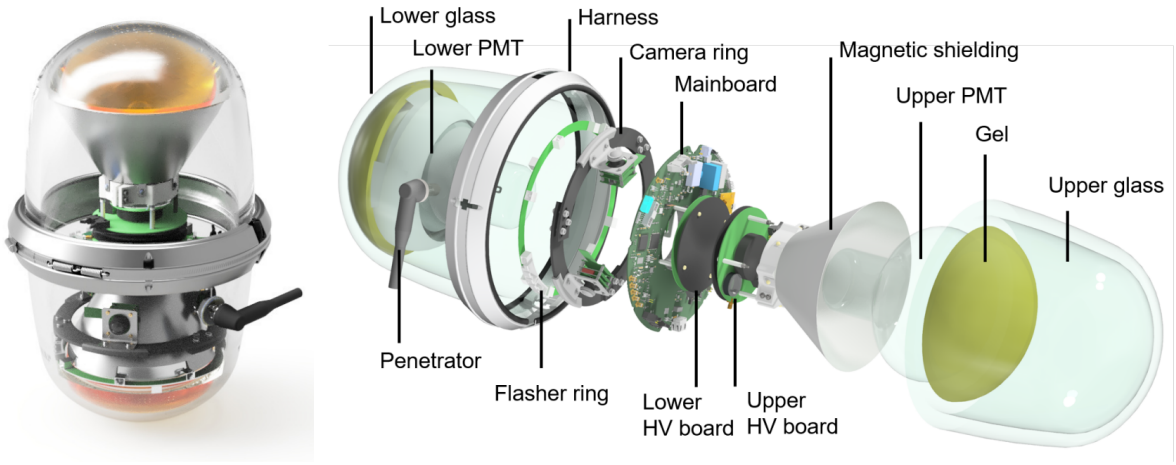

FIGURE 3.1.1: (left) A D-Egg with the harness around its equator, which is used to hold the device during deployment, and its sealed UV-transparent glass housing. (right) An exploded figuring showing the D-Egg internal structure, including: the mainboard, three cameras, twelve LED flashers, two PMTs, optical coupling silicone gel, and the magnetic shielding.

as part of IceCube Upgrade, with a planned deployment in the 2025-2026 South Pole season. The D-Eggs have been designed with an elongated egg-like shape and narrow cross-section to maximize its photon-sensitive area while maintaining a slim shape to reduce the time needed for deployment-hole drilling in the Antarctic ice to depths of up to 2,700 meters. Two 8-inch R5912-100-70 high-efficiency PMTs from Hamamatsu are used per D-Egg: one each facing upwards and downwards. Rather than the mu-metal cage, D-Eggs have a newer magnetic shielding made of FINEMET foil wrapped into a conical shape around the neck of each PMT.

In order to minimize damage to the sensitive PMTs, whenever a D-Egg is not actively being tested it is either kept in its shipping boxes or covered under a protective UV-opaque black plastic bag, as shown in Figure 3.1.3.

3.2 Final Acceptance Testing of D-Eggs

Before being packed and shipped to the pole, the IceCube D-Eggs undergo a rigorous testing procedure to ensure they meet the standards and performance requirements for necessary for IceCube Upgrade. In this Final Acceptance Testing (FAT), the D-Eggs are tested in batches of fifteen along with one reference D-Egg. They are loaded into a large freezer, which is capable of

FIGURE 3.1.2: A D-Egg PMT

FIGURE 3.1.3: Several D-Eggs are placed on carts and covered with opaque, protective, black plastic bags at an undisclosed location.

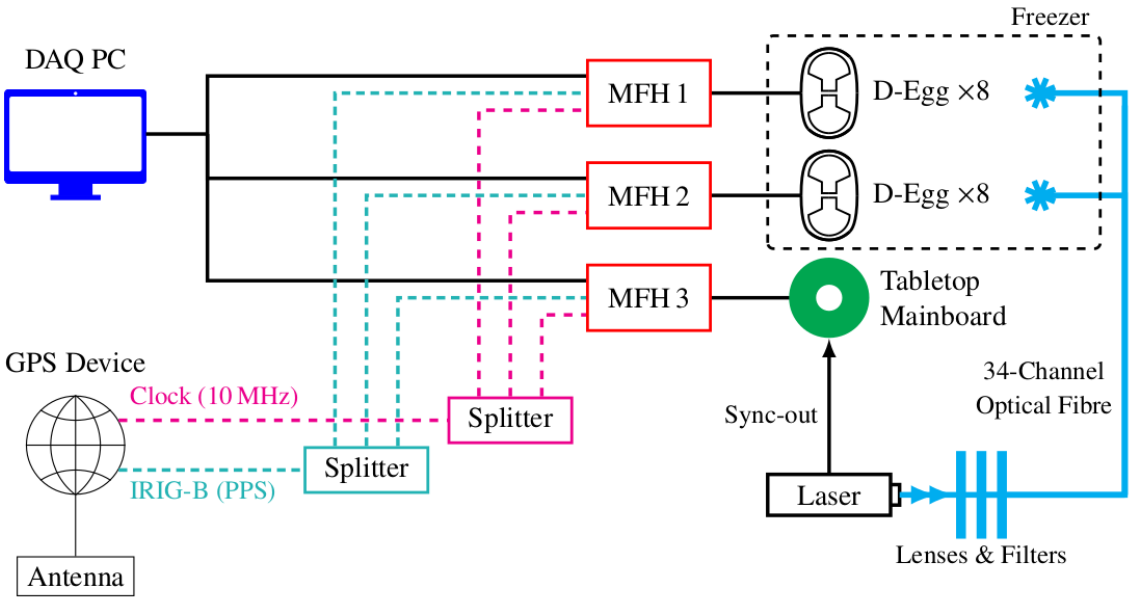

FIGURE 3.2.1: A schematic layout of the FAT apparatus.

reaching temperatures as low as negative sixty degrees Celsius, and placed into light-sealed boxes in order to isolate individual D-Eggs from one another and from any external sources of light that may interfere with measurements. Optical fibers and insulated cables are routed into the freezer to provide communications, power, and light sources to each D-Egg.

IceBoot sessions are established with each of the sixteen D-Eggs allowing for communication between the D-Eggs and a PC which runs a series of tests on the D-Eggs at various freezer temperatures and PMT high-voltages; this PC is called the "DAQ PC," or Data AcQuisition PC. Measurements are taken on a consistent basis as the freezer is brought to negative forty degrees Celsius, then up to negative twenty Celsius, back down to negative forty Celsius, and then returned to room temperature (approximately positive twenty degrees Celsius).

The block-diagram FAT facility and network architecture is shown in Figure 3.2.1. The DAQ PC is used to communicate with the D-Eggs via two Mini FieldHubs (MFHs); these are simplified versions of the hardware used on-site at the South Pole to communicate with in-ice DOMs. A third MFH is used to synchronize timing between a pulsed laser source and the other two MFHs: the Mini FieldHubs and DAQ PC are shown in Figure 3.2.2. The light source used to test the PMT response is a Hamamatsu PLP-10 C10196 with a 400 nm picosecond laser diode head M10306. Two programmable filter wheels with six distinct neutral density filters are used to attenuate the

FIGURE 3.2.2: Working on one of the Mini FieldHubs at the International Center for Hadron Astrophysics in Chiba, Japan; the DAQ PC can be seen running in the background.

laser light by discrete amounts. The laser light is carried through optical fiber and a series of splitters to expose both the top and bottom PMTs of each D-Egg; sixteen total PMTs. This allows for the characterization of the gain of each D-Egg PMT at light levels ranging from low-occupancy SPE signals to levels greater than 200 SPE.

A 10 MHz clock and the IRIB-B GPS time signals are split and fed into each of the MFHs to synchronize their internal clocks to UTC. This allows for conversion of the internal D-Egg timestamps to UTC using the standard IceCube Reciprocal Active Pulsing (RAPCal) method [54].

Data readouts for the PMTs are triggered in two ways: an Analog-to-Digital Converter (ADC) counts trigger, and a Finite Impulse Response (FIR) trigger. In the former, the analog current from the waveform is discretized into a time-dependent number of counts. Generally single-electron events are then used to calibrate the number of ADC counts to a physical quantity. Then, a threshold number of ADC counts measured is used as a trigger to indicate when an event occurs in the PMT. FIR triggering, on the other hand, uses a rolling-average of the raw waveform before the ADC conversion happens. This smooths out the waveform and typically yields a lower dark rate.

Quantity	Temperature	Criteria
HV at 1e7 Gain	Various	$1000 \leq x \leq 2000$
darknoise max	Various	$x \leq 4000$
darknoise δt	Various	$x \leq 3.5$
timing resolution	Various	$x \leq 3.5$
Q_{obs}/Q_{ideal} at 200pe	-20, -5	$0.6 \leq x$
I_{obs}/I_{ideal} at 200pe	-20, -5	$0.6 \leq x$
double pulse separation	-20	$x \leq 4000$
double pulse peak-to-valley	-20, -5	$1.5 \leq x \leq 2.0$
double pulse peak-to-valley 2	-20, -5	$1.75 \leq x \leq 2.8$

TABLE 3.2.1: The tests ran for each D-Egg. Tests with temperature "various" were run with the freezer set at room temperature, -40C, -20C, -40C, and room temperature again.

3.2.1 Detailed Monitoring

As the temperature in the freezer is moving to its new target temperature, gain scans are regularly performed on the D-Eggs. The D-Egg PMTs have been independently measured to have an SPE pulse full-width half-maximum of approximately 14 nanoseconds and an amplitude of approximately 12 mV. Mainboard electronics on the D-Eggs broaden these pulses to an approximate amplitude of 6mV and FWHM of 20ns. As such, a trigger threshold of 2.0mV is typically used.

To calculate the gain, a charge distribution is first constructed from the read-out SPE waveforms by integrating from ten bins before the peak to fifteen bins after it. A Gaussian is then fitted to the charge histogram, whose peak corresponds to the PMT voltage at a given set high-voltage. An example SPE waveform and charge distribution is shown in Figure FIG. This procedure is repeated at varying high voltages until the calculated gain is within $\pm 2\%$ of 10^7. A typical high voltage found is around 1500V.

3.2.2 Analyses

Once the measurements are taken, data are transferred from the local DAQ PC to the grappa server system in Chiba. Several analyses are then performed, as described in Ref. [67]. Tests are then ran on the results of these analyses, which are enumerated in Table 3.2.1.

The most important of these is the gain analysis. We verify that each PMT is capable of reaching a gain of 1e7 at a high voltage between 1-2 kV. In addition to that, we verify a linear

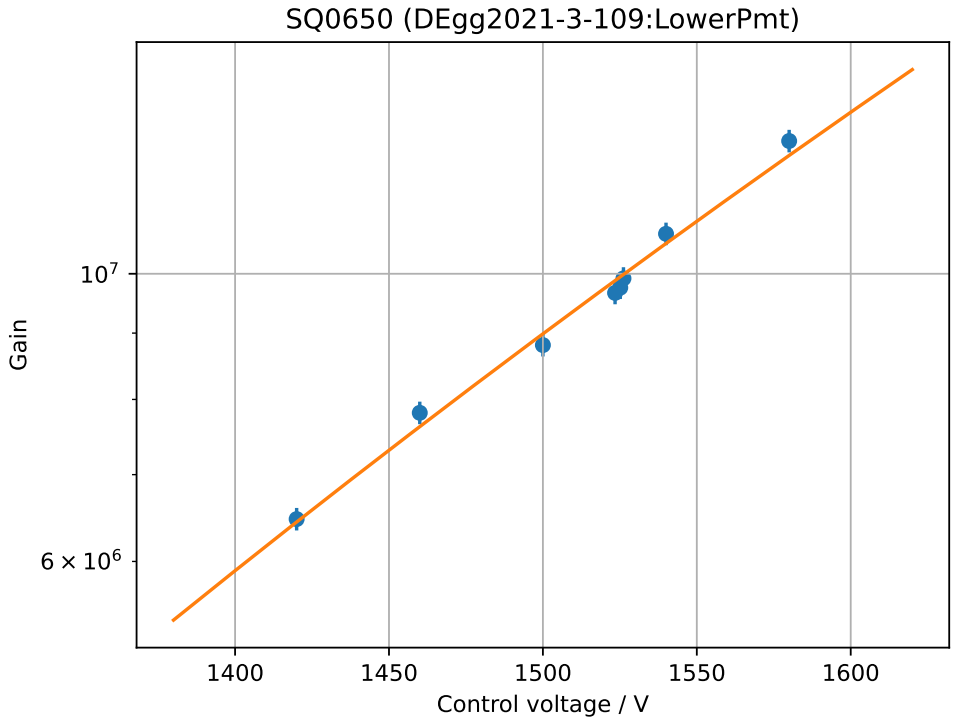

FIGURE 3.2.3: The gain fit for DEgg `DEgg2021-3-109`'s lower PMT, `SQ0650`. Data are shown in blue diamonds and the fit is shown in orange.

relationship exists between the high voltage and the log of the gain. An example of a good high-voltage versus gain relationship is shown in Figure 3.2.3.

Dark noise rates are also verified to be within acceptable bounds. Dark noise describes any events that trigger the detector and which do not originate from an external photon hitting the detector. The sources of these photons are thermionic cathode emissions, PMT afterpulses, and any radioactive processes within the glass pressure vessel. These have been observed to be highly dependent on temperature.

Two triggering methods are used; one uses a simple ADC triggering and the other uses the FIR-filtered triggering. Test are done for each D-Egg to verify that the dark noise rates do not ever exceed 10 MHz, and it should not consistently exceed 10kHz. For the FIR-smoothed rates, we verify that the trigger rate does not exceed 5kHz. Figure 3.2.4 shows examples of good and bad dark rates.

We also measure the linearity of the D-Egg response when compared to a known amount of injected light. By using the D-Egg filter wheels, the amount of light incident on the PMTs can

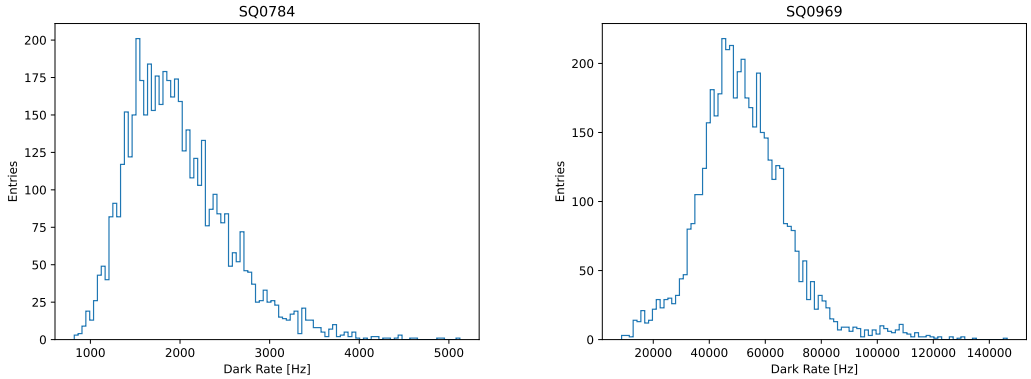

FIGURE 3.2.4: Histograms showing the dark rates for PMTs `SQ0784` (left) and `SQ0969` (right). Dark rates are abnormally high for PMT `SQ0969`.

be set to nine different settings ranging from 2.5% to 100%. The test laser intensity was also calibrated such that a 5% filter corresponds to an observed signal of few 10s of PMTs.

One additional analysis is performed to test the ability of the D-Eggs to distinguish between the light from a charged tau lepton and its decay product. This requires being able to separately identifying two PMT pulses separated by only a few nanoseconds. To emulate a tau-like signal, a function generator creates two picosecond bursts separated by 20 nanoseconds. The generator creates then waits one microsecond before creating another burst of pulses. A peak-finding algorithm is then run 5000 digitized waveforms and the separation of the fit peaks are verified to be consistent with 20 nanoseconds and any error within half of the width mainboard timing bins. An example good PMT response to this double-pulse test is shown in Figure 3.2.6.

The results of all analyses and tests are automatically compiled into a pdf by software I developed and wrote. A PDF for each D-Egg is generated including a table of the test results and relevant plots for failed tests are fetched and included. A second PDF is generated which summarizes the results of each D-Egg's tests and lists it as either Passing, Failing, or concerning. In the latter, it raises warning, and individual intervention is required to decide if the D-Egg will go to the pole or be left behind.

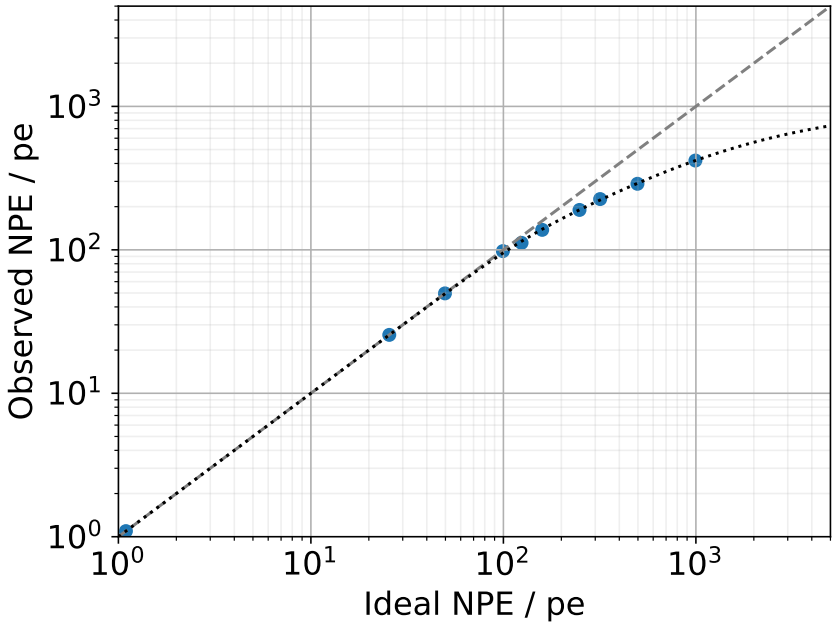

FIGURE 3.2.5: Linearity of the charge-response for PMT SQ0514. Measurements are shown as blue dots and a linear fit is shown as a dotted line. This is an example of a good linearity relationship.

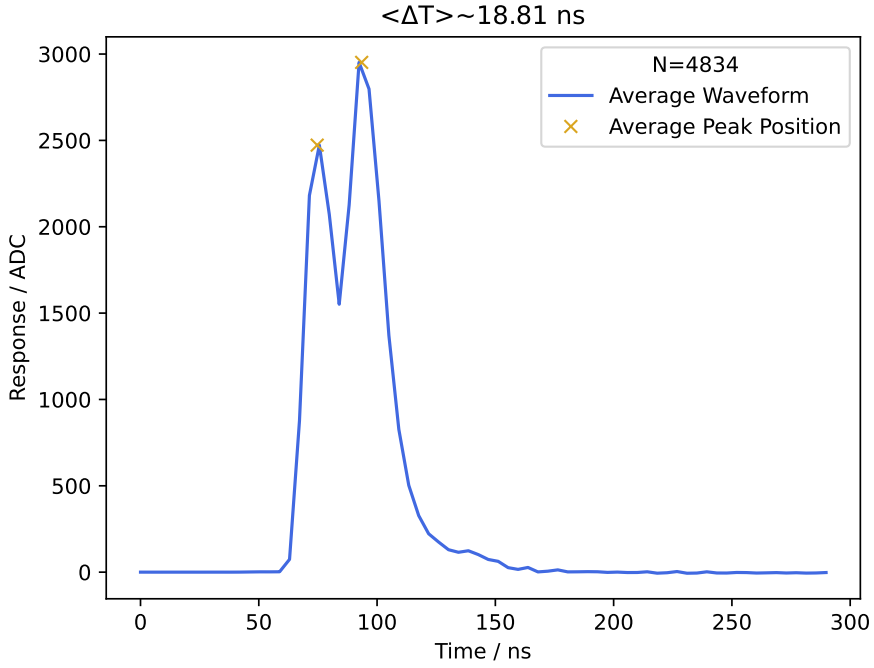

FIGURE 3.2.6: Averaged waveform of 5000 double-pulse signal tests for PMT SQ1016. A fit peak-separation of 18 nanoseconds; this is consistent with the injected 20 nanosecond signal separation to within half the width of the mainboard timing bins.

Chapter 4

Sterile Neutrino Oscillation Sensitivities

Following the signal-like results from the 8-year analysis searching for matter enhanced oscillations with steriles, there was motivation to further explore the 3+1 phase space using multiple event morphologies. We first found that in the case of non-zero $|U_{\mu 4}|^2$ and $|U_{\tau 4}|^2$, a strong ν_τ appearance signature could be expected; this is shown in Figure 4.0.1. Work was then carried out to predict IceCube's sensitivity to these $\nu_\mu \to \nu_s \to \nu_\tau$ oscillations using a joint track+cascade analysis and IceCube's latest public effective areas. This work, published in Reference [51], is included below.

Cascade appearance signatures of sterile neutrinos at 1–100 TeV

B. R. Smithers,[1,*] B. J. P. Jones,[1] C. A. Argüelles,[2] J. M. Conrad,[3] and A. Diaz[3]

[1]Department of Physics, University of Texas at Arlington, Arlington, Texas 76019, USA
[2]Department of Physics, Harvard University, Cambridge, Massachusetts 02138, USA
[3]Department of Physics, Massachusetts Institute of Technology, Cambridge, Massachusetts 02139, USA

(Received 2 December 2021; accepted 31 January 2022; published 1 March 2022)

Neutrino telescopes provide strong sensitivity to sterile-neutrino oscillations through matter effects occurring in the few TeV energy range for eV^2-scale neutrino mass-squared splittings. Prior searches have focused on ν_μ disappearance, which has a particularly strong sensitivity to the mixing angle θ_{24} via $\nu_\mu \to \nu_s$ transitions. Nowadays, the $\nu_\mu \to \nu_e$ and $\nu_\mu \to \nu_\tau$ appearance channels have been considered less promising at neutrino telescopes, due in part to the much smaller target volume for cascades relative to tracks. This work explores the detectability of these signatures at neutrino telescopes given present constraints on sterile-neutrino mixing, and as an example, forecasts the sensitivity of the IceCube Neutrino Observatory to the mixing angles θ_{14}, θ_{24}, and θ_{34} in the $3+1$ sterile-neutrino model using the cascade channel with 10 yr of data. We find that ν_τ appearance signatures consistent with the existing IceCube ν_μ disappearance best-fit point are discoverable for values of θ_{34} consistent with world constraints, and that the sterile-neutrino parameters favored by the BEST and gallium anomalies are expected to be testable at the 95% confidence level.

DOI: 10.1103/PhysRevD.105.052001

I. INTRODUCTION

The three-mass and three active-flavor neutrino paradigm has been well studied [1–6]. However, several anomalies persist at short baselines, including in $\nu_\mu \to \nu_e$ appearance in decay-in-flight [7] and decay-at-rest [8] beams and $\nu_e \to \nu_e$ disappearance at reactors [9,10] and with ^{71}Ga electron capture sources [11,12]. These anomalies have been attributed to possible oscillations of unknown neutrinos with mass-squared differences in the range of $\Delta m^2 \sim 0.1$–10 eV^2 [13]. Such an additional neutrino flavor state must be nonweakly interacting, or "sterile," to be consistent with observed decay widths of the Z boson [5]; the simplest such model is known as the "$3+1$" light sterile-neutrino model in which a single sterile neutrino is added.

There have been interesting recent developments for the $3+1$ model. The BEST experiment appears to validate the anomalous electron neutrino disappearance signature of the previous gallium anomalies with a new level of statistical significance and experimental precision [14]. The Neutrino-4 experiment claims evidence of short-baseline oscillations in the $\bar{\nu}_e$ disappearance channel with $\Delta m^2 \sim 7.3$ eV^2 at the 2.9σ level. Meanwhile results from the MicroBooNE [15–17] experiment challenge the interpretation that the MiniBooNE low-energy excess [7] is due entirely to the electron neutrino by placing a constraint on the sterile-neutrino interpretation of the excess, though the impact of this observation on the $3+1$ model is just beginning to be assessed [18,19]. Continued exploration of sterile-neutrino mixing in all channels and all energy ranges thus remains strongly motivated [20].

The addition of a fourth neutrino mass and flavor eigenstate expands the unitary mixing matrix to four dimensions. The four-neutrino oscillation model becomes an extension of the three-neutrino model with three additional mixing angles θ_{14}, θ_{24}, and θ_{34}, and two new CP-violating phases δ_{14} and δ_{24}. These three new mixing angles parametrize the amplitude of oscillations between the three active states and the one sterile state, and lead to additional short-baseline vacuumlike oscillations as well as novel effects in the presence of matter [21–25]. In this work we consider CP-conserving models with all CP-violating phases set to zero.

Of particular interest to neutrino telescopes, matter effects can result in the near complete disappearance of TeV-scale muon antineutrinos passing through Earth's core for a sterile neutrino with eV-scale mass-squared differences [26–32]. This signature of matter-enhanced resonant disappearance has been targeted by the IceCube

*Corresponding author.
benjamin.smithers@mavs.uta.edu

Neutrino Observatory [33,34], leading to one of the most sensitive ν_μ disappearance analyses to date. The result of the analysis was a closed 90% contour with a best-fit point at $\sin^2 2\theta_{24} \sim 0.1$ and $\Delta m^2_{41} = 4.5$ eV^2, under the conservative assumption (for the ν_μ disappearance channel) that $\theta_{34} = \theta_{14} = 0$. In addition to being a strong refutation, lower mass solutions consistent with the LSND [8] and MiniBooNE anomalies and constraints around 1 eV^2 [13,35–39], a possible interpretation of this result is as a statistically weak hint of a disappearance signature around $\Delta m^2_{41} \sim 4.5$ eV^2. Further exploration of this region of parameter space in other channels at neutrino telescopes is therefore strongly motivated.

In this work, we explore the potential of sterile-neutrino searches at gigaton-scale neutrino telescopes using matter-enhanced ν_τ and ν_e appearance signatures that occur when either θ_{34} or θ_{14} are nonzero [40]. We will show that ν_τ appearance of considerable strength may accompany ν_μ disappearance within the IceCube allowed region for Δm^2_{41} and θ_{24}, for values of θ_{34} that remain consistent with world datasets. We will also demonstrate that these signatures can be probed using IceCube's public data samples. Finally, we will also explore possible sensitivity to ν_e appearance at levels consistent with the gallium and BEST anomalies.

The IceCube Neutrino Observatory is described at length in Ref. [41]. Briefly, the detector is a cubic-kilometer Cherenkov neutrino observatory 1.5 km deep in the Antarctic ice [41]. There, 5160 photomultiplier tubes encased within glass pressure vessels, or "digital optical modules" (DOMs) [42] detect Cherenkov emission from charged particles traversing the ice. The DOMs are arranged vertically with a 17 m spacing into 79 strings, which themselves are aligned into a hexagonal lattice with a 125 m spacing. An additional, more densely instrumented subdetector called DeepCore exists toward the bottom center of the main detector [43]. The observatory has been running for over a decade and has accumulated large numbers of ν_μ charged-current (CC) interactions which make depositions of light that make long signatures in the detector called tracks, and neutral current, electron neutrino, and tau neutrino events which deposit light in bloblike shapes called cascades. These event topologies are elaborated upon in Sec. II.

IceCube analyses targeting ν_μ disappearance are considered tracklike only, since the only available signature under the previous mixing assumptions $\theta_{14} = \theta_{34} = 0$ is $\nu_\mu \to \nu_s$ disappearance. In similar models with both nonzero θ_{24} and θ_{34}, however, resonant $\nu_\mu \to \nu_\tau$ oscillations lead to a strong appearance signature of ν_τ as shown in Fig. 1. While some of the ν_τ will produce $\tau^\pm$ that decay leptonically to produce additional tracks, dampening the ν_μ disappearance signature, most charged-current ν_τ and $\bar{\nu}_\tau$ interactions will produce localized energy deposits that will be reconstructed as single cascades at these energies [44]. As in the $\nu_\mu \to \nu_s$ channel, the most striking feature of the signature is a resonant flavor oscillation for Earth-core-crossing antineutrinos at a specific energy, proportional to the sterile neutrino Δm^2_{41} value. Since this matter effect occurs because of an interference between the vacuum oscillation phase and the matter-driven phase, the latter changing sign between neutrinos and antineutrinos, for small mixing angles the resonance is only present in antineutrinos, given a heavier sterile neutrino. The

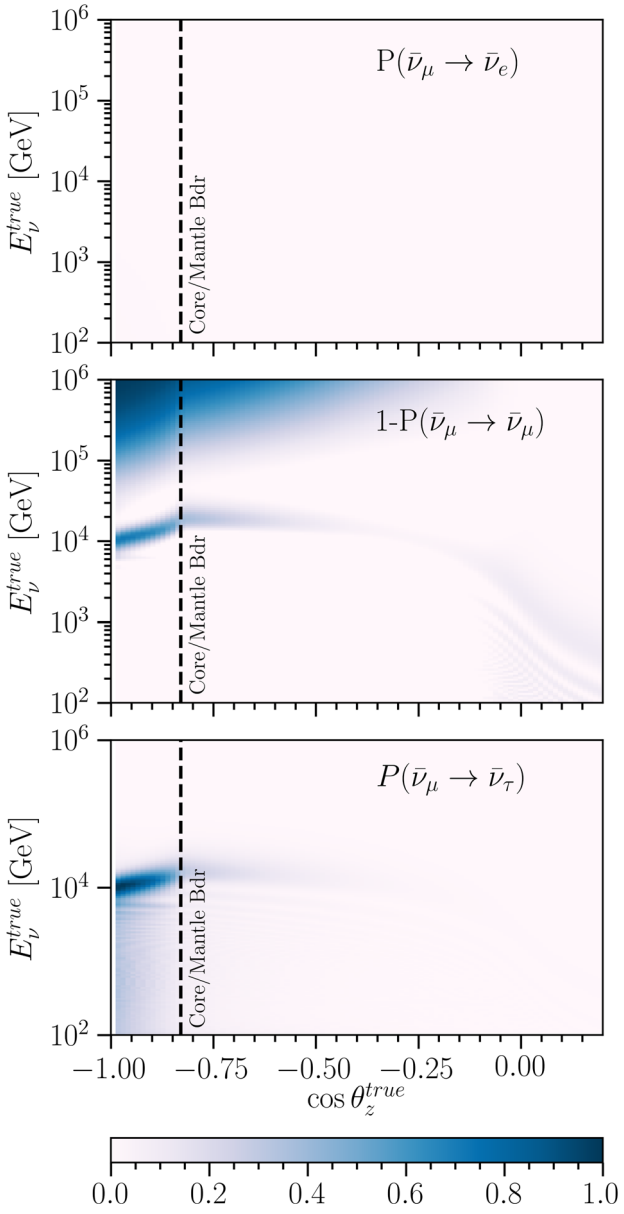

FIG. 1. Transition probabilities $P(\bar{\nu}_\mu \to \bar{\nu}_\alpha)$ for $\bar{\nu}_e$ (top panel), $\bar{\nu}_\mu$ (middle panel), and $\bar{\nu}_\tau$ (bottom panel) for a sterile-neutrino flux with $\sin^2(2\theta_{24}) = 0.1$, $\sin^2(2\theta_{34}) = 0.2$, and $\Delta m^2_{41} = 4.5$ eV^2. A dashed black line is used to denote the outer core-mantle boundary, and a solid black line denotes the inner-outer core boundary. These probabilities are shown as a function of the neutrino's energy (E_ν^{true}) and the cosine of the angle measured from an upward direction, toward the neutrino's origin.

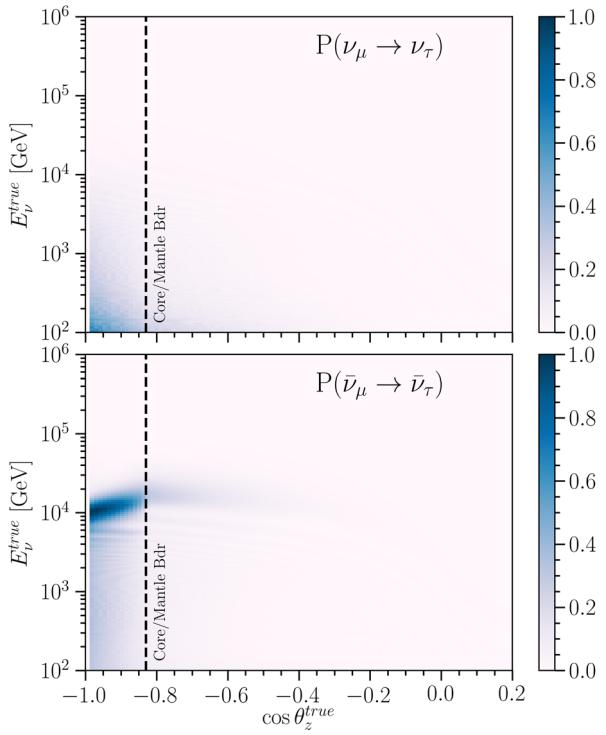

FIG. 2. Appearance probabilities for $P(\nu_\mu \to \nu_\tau)$ (top panel) and $P(\bar{\nu}_\mu \to \bar{\nu}_\tau)$ (bottom panel) for a sterile-neutrino flux with $\sin^2(2\theta_{24}) = 0.1$, $\sin^2(2\theta_{34}) = 0.19$, and $\Delta m^2_{41} = 4.5$ eV^2.

appearance probabilities for $\nu_\mu \to \nu_\tau$ and $\bar{\nu}_\mu \to \bar{\nu}_\tau$ are shown separately in Fig. 2.

For zero θ_{24} very little signal is expected since the muon neutrinos, which dominate the flux at IceCube, cease to mix with the heavier mass state. As a consequence there will be a negligible ν_τ appearance, regardless of the value of θ_{34}. However, recent IceCube results favor a nonzero value for $\sin^2(2\theta_{24})$ of around 0.1, and assuming ν_μ/ν_4 mixing at this level, the observable ν_τ appearance will depend strongly on the value of θ_{34}. At the smallest values of θ_{34} ($\theta_{34} \lesssim 0.1$), $\nu_\mu \to \nu_s$ oscillations dominate over the $\nu_\mu \to \nu_\tau$ appearance from standard oscillations, and ν_μ disappearance is the only visible signature. For values of θ_{34} larger than this threshold, the $\nu_\mu \to \nu_\tau$ oscillations begin to dominate and ν_τ appearance manifests, leading to the appearance signature shown in Fig. 1 (bottom panel). Increasing Δm^2_{41} has the effect of broadening the appearance signature until $\sim$10 eV^2, after which raising the mass-squared splitting has only a marginal effect. Increasing θ_{24} while reducing θ_{34} proportionately leaves the appearance signatures mostly unchanged while diminishing the disappearance amplitude.

In addition, the effects of nonzero mixing angle θ_{14} can also be considered, having the consequence of introducing similar appearance signatures into the ν_e appearance channel [45]. For practical purposes ν_e and ν_τ charged-current events are indistinguishable at these energies in IceCube. Notably, neutrino telescopes are the only experiments in the world with substantial sensitivity to a sterile neutrino–induced ν_τ appearance, so such direct constraints on the θ_{34} parameter are specific to these programs. Constraints on θ_{14}, on the other hand, may directly relate to anomalies in $\nu_\mu \to \nu_e$ and ν_e disappearance. As we will show, constraining the ν_e appearance signature at IceCube under the nonzero presently favored value of θ_{24} from ν_μ disappearance have direct implications for the BEST anomaly and the associated reactor-$\bar{\nu}$ anomaly.

This rich phenomenology motivates multi-mixing-angle and multichannel searches to fully explore sterile-neutrino mixing around the matter resonance at neutrino telescopes. In this work, we explore this space of mixing parameters by using publicly available tools, effective areas, and Monte Carlo simulation to estimate IceCube's sensitivity to θ_{24}, θ_{34}, and Δm^2_{41} through cascades.

II. NEUTRINO ENERGY DEPOSITION

Large-volume neutrino telescopes typically are sensitive in the TeV to PeV energies; here, deep-inelastic scattering (DIS) [46] and the recently observed [47] Glashow-resonance [48] interactions dominate. The detected neutrino interaction events fall into two morphological categories: tracks and cascades.

CC ν_μ DIS events result in muons at energies where radiative processes dominate energy loss rates. As a result, energy losses are stochastically driven and the produced muons travel for kilometers. The results are threefold: muons are difficult to fully contain in neutrino telescopes, muon energies are poorly correlated with progenitor muon-neutrino energies, and muons' long travel distance can allow for reconstructing their direction to within 1° [49]. These events are called *tracks* [50].

All neutral-current DIS events result in a hadronic shower spreading around the interaction point and a secondary neutrino invisibly carrying away a proportion of the parent neutrino's energy. These events are often contained with a spherical topology. ν_e-CC interactions develop similarly to neutral-current interactions, but repeated inverse Compton scattering of the produced electron initiates an electromagnetic shower superimposed over the hadronic shower. Thus, nearly all of the interacting neutrino's energy is observable as detectable light. These events are called *cascades.* Such events tend to be well contained, permitting an efficient energy reconstruction, although they suffer from poor angular reconstruction [50].

The evolution of a ν_τ-CC interaction is highly dependent on the energies involved. A tau is produced simultaneously with a hadronic cascade propagating around the interaction point, and then the tau decays. Due to their large mass, taus have a short lifetime and a decay length of $\sim$50 m per PeV of tau energy [44]. From the tau branching ratios [6], 17.37% of the charged tau decays evolve as muon tracks, while the remainder of the decays evolve as

electromagnetic or hadronic cascades. Only at neutrino energies above 60 TeV do ν_τ-CC interactions yield events with distinguishable primary and secondary cascades [44].

Several distinct event samples have been developed to study these different types of events in IceCube. The high-energy starting event sample [51], for example, was developed to study both taus and high-energy neutrinos that are likely astrophysical in origin. There exist other event samples optimized for higher event rates at lower energies, such as the medium-energy starting events [52], and the 5-yr inelasticity sample [53]. There are also samples optimized for muon purity, such as the 8-yr atmospheric muon sample [34] and others optimized for accurate energy resolution such as the 6-yr cascade sample [54]. This work will consider the cascade event selection described in [55] and the track event selection previously used in IceCube sterile-neutrino searches [56].

III. NEUTRINO FLUXES

We calculate the expected event rates in IceCube exclusively using publicly available data on effective areas and publicly available Monte Carlo simulation samples. By studying the expected event rates in both track and cascade channels, we are able to estimate IceCube's sensitivities to sterile-neutrino parameters given the existing 10-yr dataset. At sensitive energies there are two relevant neutrino populations whose flux must be modeled: atmospheric and astrophysical neutrinos.

Predicting atmospheric neutrino event rates requires a progenitor cosmic-ray flux, simulation of the resulting air showers, propagation of the shower-born neutrinos through Earth, and convolution of these fluxes with effective areas for a given sample selection to yield a final predicted event rate. For this work, we use the MCEq cascade equation solver [57] with the three-population Hillas-Gaisser 2012 H3a cosmic-ray-flux model [58] and using the SYBILL 2.3c hadronic interaction model [59] to simulate air showers. The polygonato model for the cosmic-ray flux [60] and the QGSJET-II-04 model for hadronic interactions [61] were also found to produce similar results for this analysis.

These fluxes are then propagated through Earth using the Simple Quantum Integro-Differential Solver for neutrino oscillations (nuSQuIDS) [62–64]. We have configured nuSQuIDS to propagate the fluxes according to a spherically symmetric preliminary reference Earth model [65] where it accounts for both coherent and noncoherent interactions relevant at these energies [48,66] as well as tau-neutrino regeneration [67]. For this work, we use the cross sections calculated in Ref. [68]. We fix the three-neutrino oscillation parameters to their global best-fit values [69].

Astrophysical neutrino event rates are calculated similarly, although the neutrino flux prior to propagation through Earth instead is expected to follow a power-law spectrum as a function of neutrino energy E_ν,

$$\Phi_{\mathrm{astr},\alpha}(E_\nu) = r_\alpha \Phi_0 \left(\frac{E_\nu}{E_0}\right)^{-\gamma}, \tag{1}$$

normalized at $E_0 = 100$ TeV and with $\Phi_0 = 2.85 \times 10^{-18}$ $[\mathrm{GeV}\cdot\mathrm{cm}^2\cdot\mathrm{sr}\cdot\mathrm{s}]^{-1}$, a spectral index of $\gamma = 2.39$ [34], and a flavor ratio r_α for $\alpha \in (e,\mu,\tau)$. The flux is assumed isotropic and to have a $\nu{:}\bar{\nu}$ ratio of 1:1. Astrophysical neutrinos are assumed to be created with regard to the pion decay–induced flavor ratio of 1:2:0 [70,71]; these are then propagated through vacuum over large energy-baseline ratios, recovering the expected $\frac{1}{3}:\frac{1}{3}:\frac{1}{3}$ flavor ratio at Earth for the three-neutrino model [72]. The same is done for sterile-neutrino hypotheses to predict expected four-flavor flavor ratios [73].

A. Cascade rates

Total cascade event rates in IceCube are calculated binwise, linearly in $\log(E^{\mathrm{true}})$ and $\cos\theta_z^{\mathrm{true}}$, by integrating over a product of flux and effective area A_{eff} in each bin (i,j), summing for each neutrino species (α), and multiplying by lifetime τ. This is shown below in Eq. (2):

$$N_{i,j}^{\mathrm{evt}} = 2\pi\tau \sum_\alpha \int_{E_i}^{E_{i+1}} dE_\nu^{\mathrm{true}} \int_{\cos\theta_j}^{\cos\theta_{j+1}} d(\cos\theta_z^{\mathrm{true}}) \times \Phi_\alpha(E_\nu^{\mathrm{true}}, \cos\theta_z) A_{\mathrm{eff},\alpha}(E_\nu^{\mathrm{true}}, \cos\theta_z^{\mathrm{true}}). \tag{2}$$

The effective areas used are publicly available and are determined from the gradient boosted decision tree method event selection developed and available in Ref. [55]. The expected binwise event counts N^{mn} at reconstructed energy $(E_\nu^{\mathrm{reco}})_m$ and zenith $(\cos\theta_z^{\mathrm{reco}})_n$ follow from smearing from these expected true values by a bin-to-bin reconstruction probability P_{mn}^{ij},

$$N_{mn}^{\mathrm{reco}} = N_{ij}^{\mathrm{true}} P_{ijmn}, \tag{3}$$

calculated according to published reconstruction resolutions [50,74]. Angular error in reconstruction is nominalized with a Kent distribution [75] over azimuths to extract the zenith error. The width of the Kent distribution, θ_z^{err}, is energy dependent according to the 50% angular error presented in Ref. [74], so we solve for the parameter (κ) using

$$-\int_1^{\cos\theta_z^{\mathrm{err}}(E_\nu^{\mathrm{true}})} \frac{\kappa}{2\sinh\kappa} e^{\kappa\cos\theta} d\cos\theta = 0.50 \tag{4}$$

at each analysis bin.

The expected number of events for 10 yr of lifetime is shown at the bottom of Fig. 3, and one-dimensional histograms of the number of events are shown in Fig. 4.

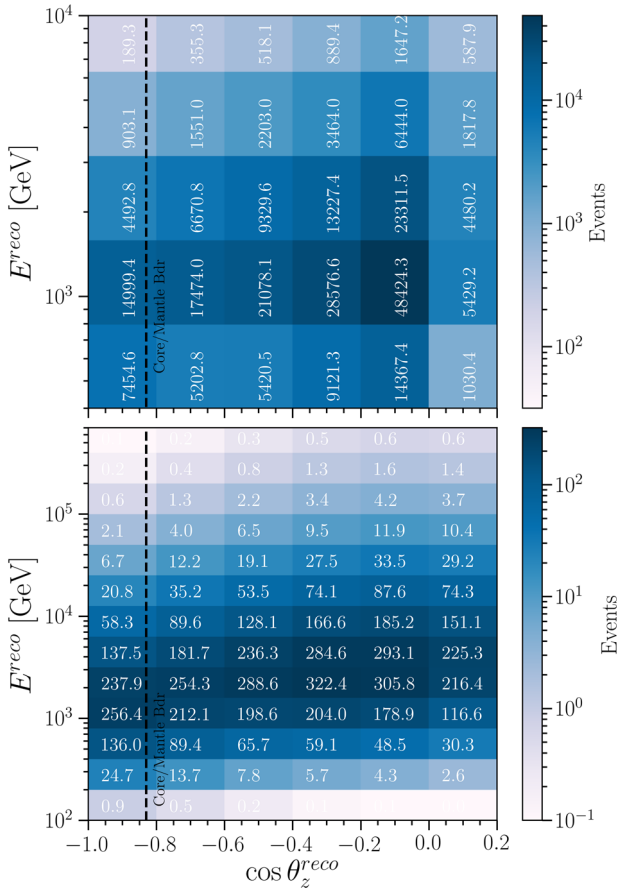

FIG. 3. Expected number of through-going tracks (top panel) and cascades (bottom panel) for 10 yr of lifetime using the Hillas Gaisser H3a cosmic-ray-flux model, the SYBILL 2.3c interaction model, and the event selection described in Ref. [55].

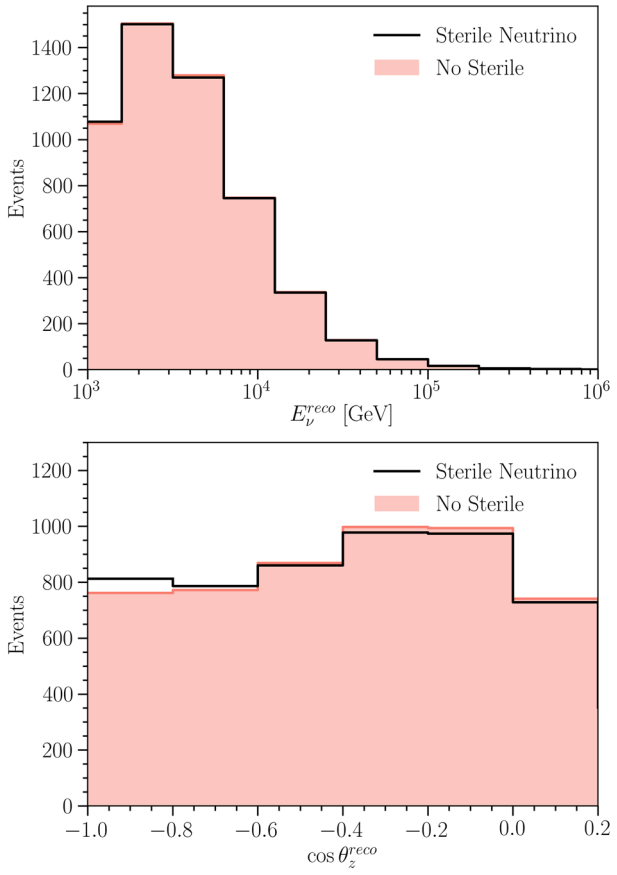

FIG. 4. Expected number of cascades for 10 yr of lifetime using the Hillas Gaisser H3a cosmic-ray-flux model, the SYBILL 2.3c interaction model, and the event selection described in Ref. [55] for a three-neutrino model (salmon) and a $3+1$ sterile neutrino model (black line) with $\sin^2(2\theta_{24}) = 0.1$, $\sin^2(2\theta_{34}) = 0.2$, and $\Delta m^2_{41} = 4.5$ eV^2. The number of events is summed over zenith angles (top panel) and energy (bottom panel) bins. Note that the oscillation signature is a correlated function of both variables, so it appears very indistinctly in these projections.

B. Track rates

In order to calculate the expected track event rate in IceCube, we use a Monte Carlo set published as part of a previous 1-yr search for sterile neutrinos [56]. We use the same energy and cosine-zenith binning used in Sec. III A, and similarly scale the data to 10 yr of lifetime. The expected number of tracks for 10 yr of lifetime is shown in Fig. 3 (top panel).

IV. SYSTEMATIC UNCERTAINTIES

A detailed treatment of IceCube's sources of systematic uncertainties would be prohibitively complex and would require proprietary IceCube tools, so a truly rigorous sensitivity calculation for each channel can only be provided by the IceCube Collaboration. Nevertheless, to estimate the expected impact of such effects we use publicly available data from Ref. [34] to apply a simplified treatment of the expected scale of systematic uncertainties. Dominant sources of systematic uncertainty are expected to derive from the shape and normalization of the atmospheric and astrophysical neutrino fluxes and the properties of the South Pole ice as in Ref. [34]. Other sources of uncertainty, such as the efficiencies of IceCube's DOMs, neutrino, and antineutrino interaction cross sections, were not used in this preliminary analysis since they are subleading effects.

Absorption and scattering of light in the ice are treated using the effective gradient approach developed in Ref. [76] and used by Ref. [33]. Uncertainties in the depth dependence of the absorption and scattering of South Pole ice leads to uncertainties in energy reconstruction, and therefore an uncertainty in the energy spectrum of expected event rates.

The 1σ deviations to the cosmic-ray flux are considered as in Ref. [34]. These deviations calculate the expected 1σ shifts in the expected atmospheric neutrino rates. Similarly, we perturb the slope of the astrophysical neutrino flux to determine variances in expected astrophysical neutrino rates. Per-bin uncertainties are then summed in quadrature to calculate a net systematic uncertainty.

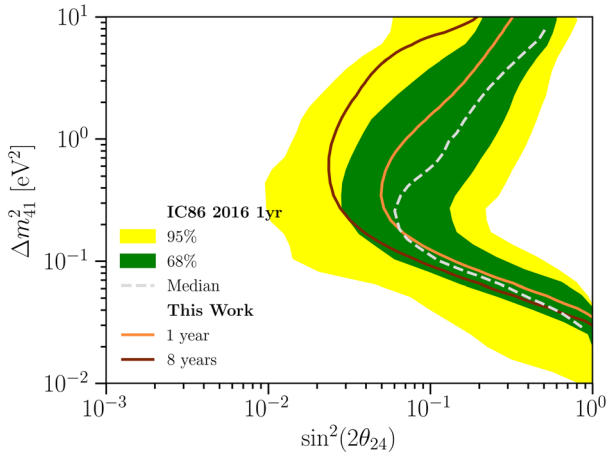

FIG. 5. 2 d.o.f., 90% C.L. sensitivity to $|U_{24}|^2$ and Δm^2_{41} with $\theta_{34} = 0.0$. These results closely reproduce those of Ref. [34].

Overall normalization of fluxes is treated as a nuisance parameter and allowed to float freely, such that we are studying energy and zenith shape and flavor ratio effects only, and not the absolute neutrino rate. We fit to the normalization before calculating the log-likelihood at each physics point. As will be described below, this simplified prescription has been tested by regenerating IceCube's sensitivity to θ_{24} via ν_μ disappearance, and a similar median sensitivity to the published IceCube analysis is obtained (shown in Fig. 5). Although both imperfect and incomplete, we believe that this prescription captures the majority of the important effects of the relevant systematic uncertainties for present purposes.

V. PREDICTED SENSITIVITIES

A binned-likelihood approach is used in calculating the log-likelihood for the expected numbers of events for each set of physical parameters. The test statistic at each point in parameter space is calculated according to

$$\mathrm{TS} = -2\Delta LLH = -2(\ln L - \ln L_{\max}) \tag{5}$$

after removing the overall normalization effect by fitting the no-sterile-neutrino flux to the parameter point of interest and adjusting the hypothesis normalization accordingly. We have performed likelihood based analyses in three samples: tracks only, cascades only, and tracks and cascades combined.

A. Tracks-only sensitivity to ν_μ disappearance

We first perform likelihood analysis for IceCube's track sample: calculating the sensitivity to θ_{24} and Δm^2_{41}, using the procedure described in Sec. III to predict the expected number of tracks in only 8 yr of lifetime. These results are shown in Fig. 5, which accurately reproduce the sensitivities presented in Ref. [56]. We have chosen this point of comparison rather than the more recent results of Ref. [33] as the updated event selection there improves efficiencies at low energy, while the data release required to make these studies is only available at present for the earlier, 1-yr analysis. Approximate agreement of the median sensitivity, well within the bounds of expected fluctuations, validates our simplified analysis methodology as capturing the essential elements needed for a robust sensitivity estimate. For completeness we also present an 8-yr projection.

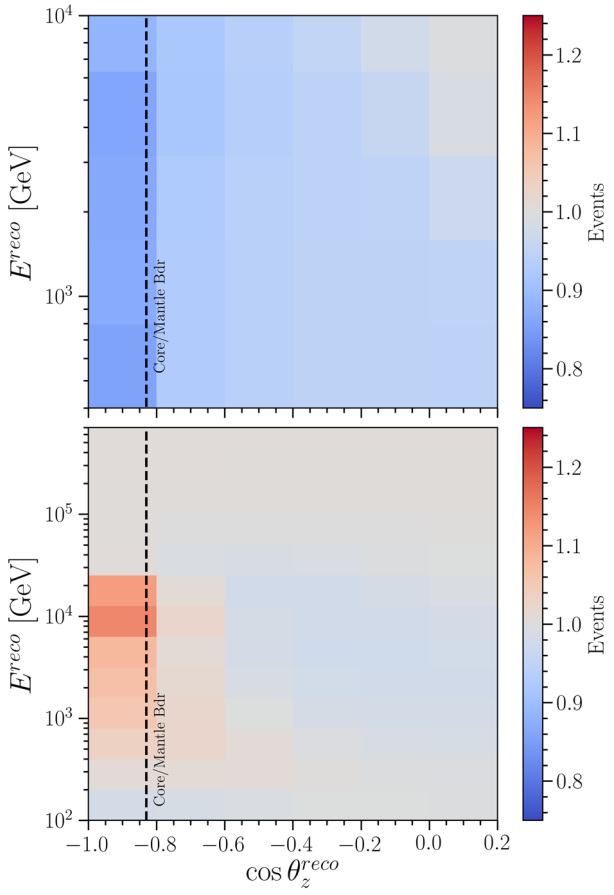

FIG. 6. Ratio of expected tracks (top panel) and cascades (bottom panel) for a sterile-neutrino model with $\sin^2(2\theta_{24}) = 0.1$, $\sin^2(2\theta_{34}) = 0.2$, and $\Delta m^2_{41} = 4.5$ eV^2 and the standard three-neutrino model. Fluxes are calculated using the Hillas-Gaisser H3a cosmic-ray-flux model and the SYBILL 2.3c interaction model. A broad disappearance is expected in upgoing tracks coincident with an appearance of upgoing cascades.

B. Cascades-only sensitivity to ν_τ appearance

Signatures of ν_τ appearance require nonzero values for all of Δm^2_{41}, θ_{24}, and θ_{34}. An example of a point with a nontrivial appearance signature that is consistent with existing experimental limits is shown in Fig. 6. This signature in reconstructed space is calculated by fixing θ_{24} and Δm^2_{41} at their best-fit points from IceCube's ν_μ

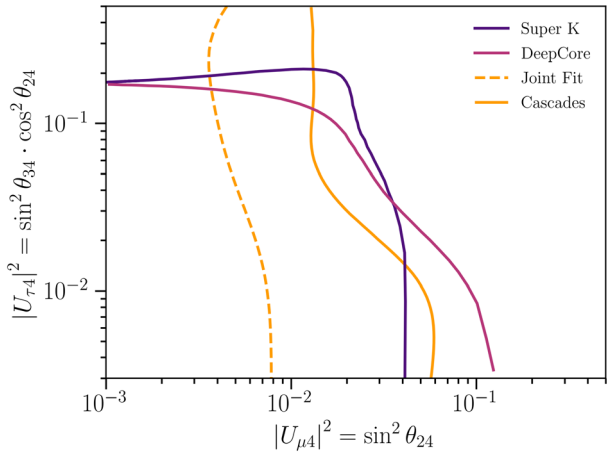

FIG. 7. 2 d.o.f., 90% C.L. sensitivity to the θ_{24} and θ_{34} neutrino mixing parameters from this work with $\Delta m^2_{41} = 1$ eV^2 for this work, IceCube's DeepCore [77], and Super-Kamiokande [79]. The sensitivity through cascades is shown in the solid contour, and the joint track-cascade contour is dashed.

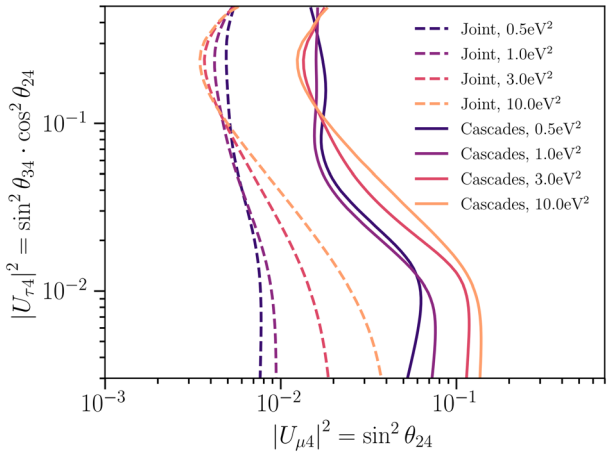

FIG. 8. Cross sections of the 3 d.o.f., 90% C.L. sensitivity surface to θ_{24}, θ_{34}, and Δm^2_{41}. The sensitivity through cascades is shown in the solid contour, and the joint track-cascade contour is dashed.

disappearance searches, and fixing $\sin^2(2\theta_{34}) = 0.2$, comfortably consistent with current bounds, which are around $\sin^2(2\theta_{34}) \lesssim 0.6$ [77,78].

Since all three of the above parameters must be nonzero to observe ν_τ appearance, sensitivities should be expressed in three-dimensional spaces (or four dimensional, if θ_{14} is also included). However, to facilitate presentation of results on 2D plots in this work we have primarily opted to present two-dimensional sensitivities under specific and experimentally motivated assumptions on the third parameter.

Using the methods described in Sec. III, we calculate expected cascade rates in IceCube at combinations of θ_{24}, θ_{34}, and Δm^2_{41}. The effects of θ_{14} are marginal unless large mixing angles are reached, and so for this part of the analysis it was kept to zero. The matter effects on these oscillations are similarly only marginally affected by the *CP*-violating phases [34], and so they are fixed to zero. The results of the sensitivity scan over cascade events only are shown as the solid line of Fig. 7, with sensitivities from other experiments overlaid, at the conventional benchmark point of $\Delta m^2_{41} = 1$ eV^2; sensitivities at other values of Δm^2_{41} are shown as the solid lines of Fig. 8. We see that with cascades alone we expect a sensitivity competitive with other leading sensitivities from Super-Kamiokande [79] and IceCube's DeepCore [77]. Sensitivities are the most competitive for points in phase space where both θ_{24} and θ_{34} are large; here, the transition probability $P(\nu_\mu \to \nu_\tau)$ is maximized.

Meanwhile, in regions where $|U_{\tau 4}|^2$ is small, ν_μ disappearance is most significant in a signal similar to those in Refs. [33,34], but as ν_μ cascades. A small increase to $|U_{\tau 4}|^2$ can then lead to competing ν_τ appearance and ν_μ disappearance, and so for small values of Δm^2_{41}, this leads to a reduction of sensitivity. Since ν_μ events overwhelmingly lead to cascades while ν_τ often cause tracks, at higher $|U_{\mu 4}|^2$ the ν_τ appearance begins to dominate and sensitivity improves. Finally, since a tau appearance follows a $\nu_\mu \to \nu_s \to \nu_\tau$ appearance channel, a nonzero $|U_{\mu 4}|^2$ is needed to for any sensitivity; this causes a lower bound on the $|U_{\mu 4}|^2$ sensitivity.

C. Joint sensitivity for ν_μ disappearance and ν_τ appearance

By performing a joint sensitivity using both cascadelike and tracklike events, we are able to significantly improve the sensitivity, by exploring a flavor ratio rather than a pure shape effect. Tracklike events will provide a method to fit to the overall flux normalization and further constrain sensitivities. Specifically, the process described in Sec. V B is performed for track events, and the fit event-number normalization is then used in calculating the log-likelihood in the cascade channel. The combined likelihood for both is then used in determining sensitivity contours. These results are shown in Fig. 7. A significant sensitivity enhancement relative to either tracks or cascades alone is obtained.

In addition to calculating sensitivity, we examine the results that may be expected in the presence of a sterile neutrino with nonzero θ_{24} and θ_{34}. In Fig. 9 we show the result obtained by injecting a signal with $\sin^2(2\theta_{24}) = 0.1$, $\sin^2(2\theta_{34}) = 0.2$, and $\Delta m^2_{41} = 4.64$ eV^2 and fitting over values of the mixing parameters; this mass-squared splitting was chosen out of computational convenience as it lines up with a point at which fluxes were calculated. We include four slices through the space in Δm^2_{41} at several benchmark points, and provide contours at 90% C.L. calculated using χ^2 assuming that the test statistic, TS, satisfies Wilk's theorem and is distributed with a χ^2 distribution with thresholds consistent with 3 degrees of

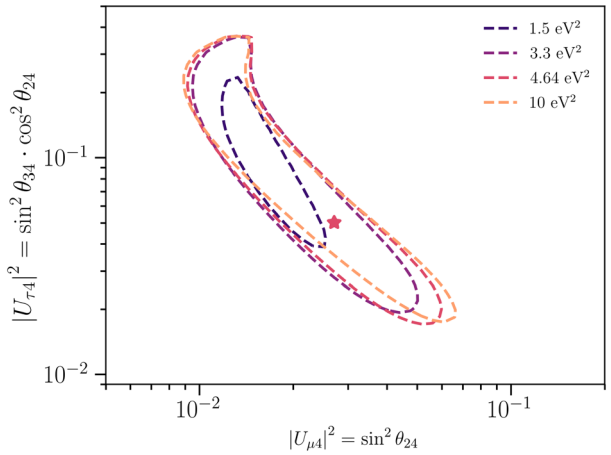

FIG. 9. 3 d.o.f., 90% C.L. sensitivity to the $|U_{\mu 4}|^2$ and $|U_{\tau 4}|^2$ Pontecorvo-Maki-Nakagawa-Sakata matrix elements, at various values of Δm^2_{41}, for this work using a joint track-cascade likelihood assuming a sterile neutrino with $\sin^2(2\theta_{24}) = 0.1$, $\sin^2(2\theta_{34}) = 0.2$, and $\Delta m^2_{41} = 4.64$ eV^2.

freedom. A signature of this form which is consistent with present constraints would be potentially discoverable in a joint track and cascade analysis at IceCube.

D. Joint sensitivity for ν_μ and disappearance generic cascade appearance

Cascade appearance may be introduced not only from ν_τ appearance, but also from ν_e appearance. A nonzero value for θ_{14} is motivated in particular by recent results from the BEST experiment, which motivates us to consider whether IceCube fitting both cascade and track channels has sensitivity to values of θ_{14} consistent with such a ν_e disappearance effect. IceCube can of course not rule out the BEST anomaly alone, since a scenario with $\theta_{24} = 0$ will generate no substantial appearance signatures in IceCube for any value of θ_{14}. But in principle it may be able confirm the BEST anomaly, given sizable enough values for both θ_{24} and θ_{14}. In such a model with nonzero θ_{14}, θ_{24}, and θ_{34}, resonant oscillations lead to appearances in both the ν_τ and ν_e channels shown in Fig. 10, wherein the BEST best-fit values were used for θ_{14} and Δm^2_{41}.

To assess sensitivity to this effect in IceCube, scans over θ_{14} and θ_{34} were performed at multiple values of Δm^2_{41} and θ_{24}. In Fig. 11 we show IceCube's sensitivity to a $3+1$ sterile-neutrino model with $\theta_{14} = 0.0$. These contours represent the median expected 90% confidence level that could be drawn if no sterile neutrino were present, given assumptions on the nonplotted parameters shown in the caption. The two choices of assumptions made on the nonfitted parameters correspond to $\theta_{24} = 0.1609$ (the ν_μ disappearance best-fit point from Ref. [33]) or $\theta_{24} = 0.3826$ (a value within the 90% results contour of Ref. [33]), and $\Delta m^2_{41} = 1$ eV^2 (a standard benchmark point in the field), $\Delta m^2_{41} = 3.3$ eV^2 (the BEST best-fit point), and $\Delta m^2_{41} = 4.64$ eV^2 (close to the IceCube ν_μ disappearance best-fit point at 4.5 eV^2). It is observed that IceCube has significant sensitivity in this high-dimensional parameter space for many values of the mixing parameters consistent with the present BEST and IceCube results, assuming a nonzero value of θ_{24} consistent with IceCube's existing preferred regions from ν_μ disappearance measurements.

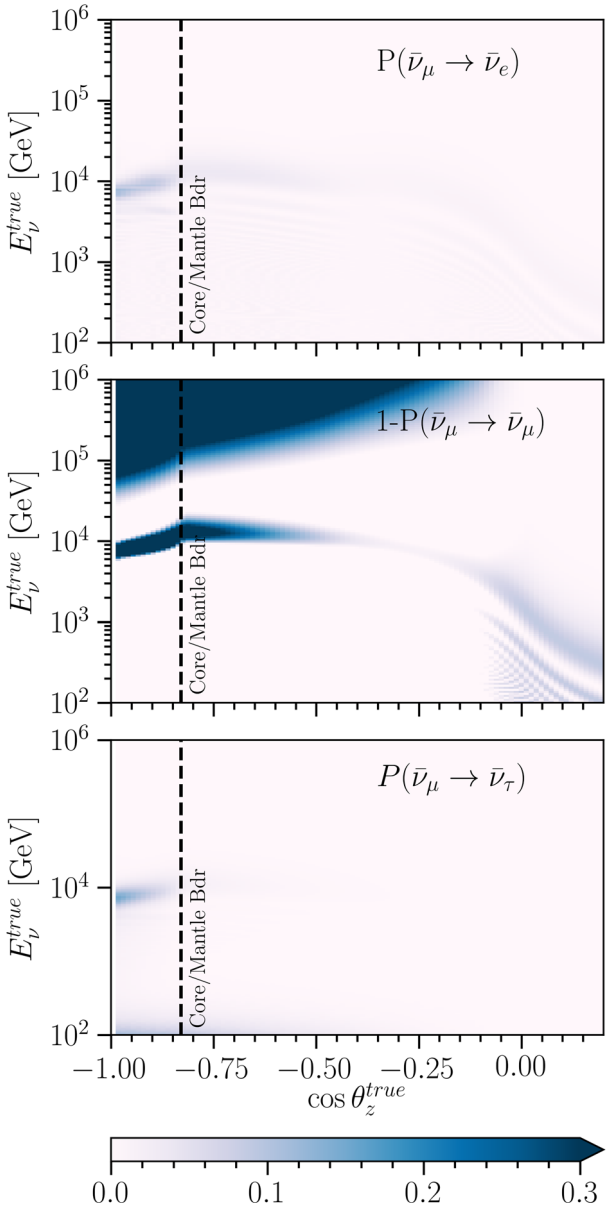

FIG. 10. Transition probabilities $P(\bar{\nu}_\mu \to \bar{\nu}_\alpha)$ for $\bar{\nu}_e$ (top panel), $\bar{\nu}_\mu$ (middle panel), and $\bar{\nu}_\tau$ (bottom panel) for a sterile-neutrino flux with $\sin^2(2\theta_{14}) = 0.43$, $\sin^2(2\theta_{24}) = 0.1$, $\sin^2(2\theta_{34}) = 0.01$, and $\Delta m^2_{41} = 3.3$ eV^2. A dashed black line is used to denote the outer core-mantle boundary.

A more intuitive picture of IceCube's capability to confirm the BEST anomaly as being sterile neutrino related, given values of other mixing parameters consistent with

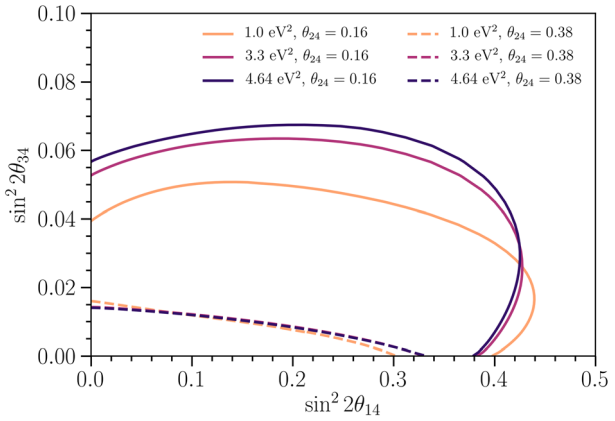

FIG. 11. 2 d.o.f., 90% C.L. sensitivity contours for $\sin^2\theta_{14}$ and $\sin^2\theta_{34}$, using a joint track-cascade likelihood, for a $3+1$ sterile-neutrino model with various values of Δm^2_{41} and θ_{24}, and $\theta_{14} = 0.0$.

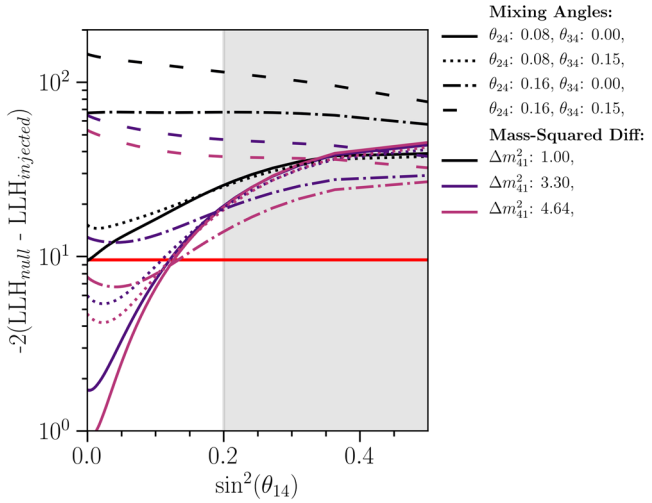

FIG. 12. Test statistics values for various different injected $3+1$ sterile-neutrino models, using a joint track-cascade likelihood, compared to a three-neutrino hypothesis. The red line represents a 4 d.o.f. 95% C.L. sensitivity threshold; the shaded region represents the 95% confidence level bounds from the BEST best fit.

IceCube and world data, is shown in Fig. 12. Here, likelihoods are calculated according to injected sterile-neutrino parameters and assuming a three-neutrino model; the resulting test statistics are shown. For all considered combinations, IceCube is seen to be capable of discriminating a BEST-like sterile-neutrino flux from a three-neutrino model at the 95% confidence level. Thus, IceCube appears to have the capability to confirm the best anomaly at least 95% confidence, given suitable values of the other mixing parameters, within existing constraints and uncertainties.

VI. CONCLUSIONS

We have considered IceCube's sensitivity to sterile neutrinos through the cascade appearance channel. Both ν_τ and ν_e appearance signatures are in principle observable by IceCube for θ_{14} and θ_{34} values within existing constraints, θ_{24} around IceCube's present preferred values from ν_μ disappearance, and many possible values Δm^2_{41}.

We have found that IceCube's sensitivity in the joint $U_{\tau 4}$, $U_{\mu 4}$ space that has been explored by previous analyses at Super-Kamiokande and IceCube will be enhanced significantly at the benchmark point of $\Delta m^2 = 1\ \mathrm{eV}^2$ by a joint fit to both track and cascade samples. Strong sensitivity is also obtained for other mass points, under the standard mixing assumption of $\theta_{14} = 0$. Cascade signatures that may accompany tentative but weak hints of ν_μ disappearance for $\Delta m^2_{41} \sim 4.5\ \mathrm{eV}^2$ and $\sin^2(\theta_{24}) \sim 0.1$ are discoverable at IceCube with values θ_{34} that remain consistent with world data, strongly motivating investigation of ν_τ appearance via cascades in parallel with the established IceCube searches for ν_μ disappearance using tracks.

We have also explored the effect of introducing non-trivial ν_e appearance, consistent with the BEST and gallium anomalies, via nonzero θ_{14}. IceCube cannot rule out the BEST or gallium preferred regions in θ_{14} alone, since sensitivity of IceCube to this parameter requires nonzero θ_{24}. For modest values of θ_{24} at either the IceCube best-fit point in ν_μ disappearance or at a point near the 90% C.L. upper limit in this channel, however, values of θ_{14} and Δm^2_{41} around the best-fit point can be probed at a better than 90% confidence level.

We conclude that our joint analysis of track and cascade topologies at IceCube can contribute to the ongoing worldwide project of understanding short-baseline anomalies in both ν_e appearance and disappearance channels. The IceCube dataset, probing both ν_μ disappearance and ν_e and ν_τ appearance near the matter resonance for core crossing neutrinos, provides unique and powerful insights into possible mixing of heavier neutrino mass states with the ν_τ flavor, as well as offering sensitivity to ν_e appearance in experimentally relevant parts of parameter space associated with the BEST and gallium anomalies.

ACKNOWLEDGMENTS

B. R. S. and B. J. P. J. are supported by the National Science Foundation under Grant No. 1913607. C. A. A. is supported by the Faculty of Arts and Sciences of Harvard University, and the Alfred P. Sloan Foundation. J. M. C. and A. D. are supported by the National Science Foundation under Grant No. 1912764.

[1] L. Berns (T2K Collaboration), in *Proceedings of the 55th Rencontres de Moriond on Electroweak Interactions and Unified Theories, 2021*, https://inspirehep.net/literature/1863309 (unpublished).
[2] F. Capozzi, E. Lisi, A. Marrone, D. Montanino, and A. Palazzo, Nucl. Phys. **B908**, 218 (2016).
[3] I. Esteban, M. C. Gonzalez-Garcia, A. Hernandez-Cabezudo, M. Maltoni, and T. Schwetz, J. High Energy Phys. 01 (2019) 106.
[4] P. de Salas, D. Forero, C. Ternes, M. Tórtola, and J. Valle, Phys. Lett. B **782**, 633 (2018).
[5] S. Schael *et al.* (ALEPH, DELPHI, L3, OPAL, SLD, LEP Electroweak Working Group, SLD Electroweak Group, and SLD Heavy Flavour Group Collaborations), Phys. Rep. **427**, 257 (2006).
[6] M. Tanabashi *et al.* (Particle Data Group), Phys. Rev. D **98**, 030001 (2018).
[7] A. Aguilar-Arevalo *et al.*, Phys. Rev. Lett. **121**, 221801 (2018).
[8] C. Athanassopoulos *et al.* (LSND Collaboration), Phys. Rev. Lett. **81**, 1774 (1998).
[9] G. Mention, M. Fechner, T. Lasserre, T. A. Mueller, D. Lhuillier, M. Cribier, and A. Letourneau, Phys. Rev. D **83**, 073006 (2011).
[10] A. P. Serebrov *et al.*, JETP Lett. **109**, 213 (2019).
[11] J. N. Abdurashitov *et al.*, Phys. Rev. C **73**, 045805 (2006).
[12] C. Giunti and M. Laveder, Phys. Rev. C **83**, 065504 (2011).
[13] K. N. Abazajian *et al.*, arXiv:1204.5379.
[14] V. V. Barinov *et al.* (BEST Collaboration), arXiv:2109.11482.
[15] P. Abratenko *et al.* (MicroBooNE Collaboration), arXiv:2110.14065.
[16] P. Abratenko *et al.*, arXiv:2110.14080.
[17] P. Abratenko *et al.*, arXiv:2110.14054.
[18] C. A. Argüelles *et al.*, arXiv:2111.10359.
[19] P. B. Denton, arXiv:2111.05793.
[20] P. A. N. Machado, O. Palamara, and D. W. Schmitz, Annu. Rev. Nucl. Part. Sci. **69**, 363 (2019).
[21] E. K. Akhmedov, Sov. J. Nucl. Phys. **47**, 301 (1988).
[22] E. K. Akhmedov and A. Y. Smirnov, Phys. Rev. Lett. **85**, 3978 (2000).
[23] M. Chizhov, M. Maris, and S. T. Petcov, arXiv:hep-ph/9810501.
[24] M. V. Chizhov and S. T. Petcov, Phys. Rev. Lett. **83**, 1096 (1999).
[25] P. Krastev and A. Smirnov, Phys. Lett. B **226**, 341 (1989).
[26] V. Barger, Y. Gao, and D. Marfatia, Phys. Rev. D **85**, 011302 (2012).
[27] S. Choubey, J. High Energy Phys. 12 (2007) 014.
[28] A. Esmaili, F. Halzen, and O. Peres, J. Cosmol. Astropart. Phys. 11 (2012) 041.
[29] A. Esmaili and A. Smirnov, J. High Energy Phys. 12 (2013) 014.
[30] M. Lindner, W. Rodejohann, and X.-J. Xu, J. High Energy Phys. 01 (2016) 124.
[31] H. Nunokawa, O. L. G. Peres, and R. Z. Funchal, Phys. Lett. B **562**, 279 (2003).
[32] S. T. Petcov, Int. J. Mod. Phys. A **32**, 1750018 (2017).
[33] M. G. Aartsen *et al.* (IceCube Collaboration), Phys. Rev. Lett. **125**, 141801 (2020).
[34] M. G. Aartsen *et al.* (IceCube Collaboration), Phys. Rev. D **102**, 052009 (2020).
[35] M. Cirelli, G. Marandella, A. Strumia, and F. Vissani, Nucl. Phys. **B708**, 215 (2005).
[36] M. Dentler, Á. Hernández-Cabezudo, J. Kopp, M. Maltoni, and T. Schwetz, J. High Energy Phys. 11 (2017) 099.
[37] A. Diaz, C. Argüelles, G. Collin, J. Conrad, and M. Shaevitz, Phys. Rep. **884**, 1 (2020).
[38] S. Gariazzo, C. Giunti, M. Laveder, and Y. F. Li, J. High Energy Phys. 06 (2017) 135.
[39] J. Kopp, P. A. N. Machado, M. Maltoni, and T. Schwetz, J. High Energy Phys. 05 (2013) 050.
[40] A. Esmaili, F. Halzen, and O. Peres, J. Cosmol. Astropart. Phys. 07 (2013) 048.
[41] M. Aartsen *et al.* (IceCube Collaboration), J. Instrum. **12**, P03012 (2017).
[42] R. Abbasi *et al.* (IceCube Collaboration), Nucl. Instrum. Methods Phys. Res., Sect. A **601**, 294 (2009).
[43] R. Abbasi *et al.* (IceCube Collaboration), Astropart. Phys. **35**, 615 (2012).
[44] R. Abbasi *et al.* (IceCube Collaboration), arXiv:2011.03561.
[45] Y. Wang and O. Yasuda, arXiv:2110.12655.
[46] R. Gandhi, C. Quigg, M. Hall Reno, and I. Sarcevic, Astropart. Phys. **5**, 81 (1996).
[47] M. G. Aartsen *et al.* (IceCube Collaboration), Nature (London) **591**, 220 (2021); **592**, E11 (2021).
[48] S. L. Glashow, Phys. Rev. **118**, 316 (1960).
[49] M. G. Aartsen *et al.* (IceCube Collaboration), Astrophys. J. **835**, 151 (2017).
[50] M. G. Aartsen *et al.* (IceCube Collaboration), J. Instrum. **9**, P03009 (2014).
[51] R. Abbasi *et al.* (IceCube Collaboration), Phys. Rev. D **104**, 022002 (2021).
[52] M. G. Aartsen *et al.* (IceCube Collaboration), Phys. Rev. D **91**, 022001 (2015).
[53] M. G. Aartsen *et al.* (IceCube Collaboration), Phys. Rev. D **99**, 032004 (2019).
[54] M. G. Aartsen *et al.* (IceCube Collaboration), Phys. Rev. Lett. **125**, 121104 (2020).
[55] H. Niederhausen, Ph.D. thesis, State University of New York at Stony Brook, 2018.
[56] M. G. Aartsen *et al.* (IceCube Collaboration), Phys. Rev. Lett. **117**, 071801 (2016).
[57] A. Fedynitch, R. Engel, T. K. Gaisser, F. Riehn, and T. Stanev, EPJ Web Conf. **99**, 08001 (2015).
[58] T. K. Gaisser, Astropart. Phys. **35**, 801 (2012).
[59] F. Riehn *et al.*, *Proc. Sci.*, ICRC2017 (2018) 301 [arXiv:1709.07227].
[60] J. R. Hörandel, Astropart. Phys. **19**, 193 (2003).
[61] S. Ostapchenko, Phys. Rev. D **83**, 014018 (2011).
[62] C. A. Argüelles, J. Salvado, and C. N. Weaver, Comput. Phys. Commun. **196**, 569 (2015).
[63] C. A. Argüelles, J. Salvado, and C. N. Weaver, computer code nuSQuIDS, https://github.com/Arguelles/nuSQuIDS (2015).
[64] C. A. Argüelles, J. Salvado, and C. N. Weaver, arXiv:2112.13804.
[65] A. M. Dziewonski and D. L. Anderson, Phys. Earth Planet. Inter. **25**, 297 (1981).

[66] M. C. Gonzalez-Garcia, F. Halzen, and M. Maltoni, Phys. Rev. D **71**, 093010 (2005).
[67] F. Halzen and D. Saltzberg, Phys. Rev. Lett. **81**, 4305 (1998).
[68] A. Cooper-Sarkar, P. Mertsch, and S. Sarkar, J. High Energy Phys. 08 (2011) 042.
[69] I. Esteban, M. Gonzalez-Garcia, M. Maltoni, T. Schwetz, and A. Zhou, J. High Energy Phys. 09 (2020) 178.
[70] H. Athar, C. S. Kim, and J. Lee, Mod. Phys. Lett. A **21**, 1049 (2006).
[71] J. F. Beacom, N. F. Bell, D. Hooper, S. Pakvasa, and T. J. Weiler, Phys. Rev. D **68**, 093005 (2003).
[72] M. G. Aartsen *et al.* (IceCube Collaboration), Phys. Rev. Lett. **114**, 171102 (2015).
[73] C. A. Argüelles, K. Farrag, T. Katori, R. Khandelwal, S. Mandalia, and J. Salvado, J. Cosmol. Astropart. Phys. 02 (2020) 015.
[74] M. G. Aartsen *et al.* (IceCube Collaboration), Astrophys. J. **846**, 136 (2017).
[75] J. T. Kent, J. R. Stat. Soc. Ser. B Methodol. **44**, 71 (1982).
[76] M. Aartsen *et al.* (IceCube Collaboration), J. Cosmol. Astropart. Phys. 10 (2019) 048.
[77] M. G. Aartsen *et al.* (IceCube Collaboration), Phys. Rev. D **95**, 112002 (2017).
[78] P. Adamson *et al.*, Phys. Rev. Lett. **107**, 011802 (2011).
[79] K. Abe *et al.* (Super-Kamiokande Collaboration), Phys. Rev. D **91**, 052019 (2015).

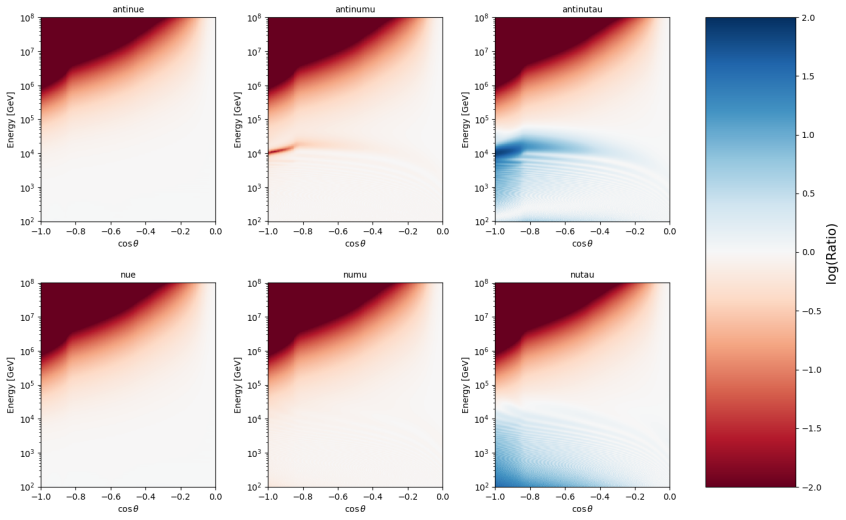

FIGURE 4.0.1: A plot showing the log of the ratio of the neutrino fluxes at the Earth's surface and the flux at IceCube. Like in Figure 1.3.1, the top let corner shows disappearance due to Earth's opacity to neutrinos at high energies and the narrow red band shows the MSW resonance with sterile neutrinos. Here, however, the blue region is showing an MSW-enhanced tau appearance signature for 3+1 sterile neutrino models with non-zero $|U_{\tau 4}|^2$.

Chapter 5

Event Generation and Filters

5.1 Event Generation

Like in the analysis presented in this dissertation, neutrino telescopes are often used to search for the signatures of new physics. Traditional neutrino generation schema, however, coupled the neutrino event generation with the neutrino Earth-propagation and interaction cross-sections. As a consequence of this, probing nonstandard neutrino cross-sections, or new physics effecting the neutrino survival probability would be cumbersome. The response to this was the *NuFSGen* approach, later be renamed to the LeptonInjector/Weighter approach; in which the detector neutrino flux prediction and interaction were fully decoupled to allow for easy testing of various physics hypotheses. This system was published in Reference [52], and is included in full here.

5.2 Continued Simulation

After event generation in `LeptonInjector`, particles are propagated and their energy losses simulated in-ice using PROPOSAL [73]. Low energy cascades are represented as stationary light sources, while those above 1TeV are elongated along the cascade trajectory. Photon propagation, the most expensive simulation step, is done using CLSim [74]. The detector and electronics response to light is then simulated using proprietary software. This accounts for DOM noise, wavelength and angular acceptance of the PMTs, and the signal digitization process. From here, MC and data are treated identically: the detector trigger is ran, a simple filter is applied, and a basic reconstruction is carried out on the passing events.

5.3 Cascades Pre-filter

The cascade pre-filter is used to reduce the large number of triggered background events before more complicated event reconstructions must be run. The first step is to identify single events and coincident events; only single events are kept. Large numbers of cosmic ray air showers yield large quantities of down-going muons; by removing any events with topologically separated features, we cut down on background cosmic ray muons tremendously.

Background muon events also enter into the detector from above, while the signal cascades start from within. The next step for the cascades filter is to then identify which events are fully contained within the detector and which are not; uncontained (through-going) events are discarded. This also tremendously reduces the background in the sample. The cascades' reconstruction algorithm, Monopod, is then run on the events that survive for use in analysis-specific cuts.

Computer Physics Communications 266 (2021) 108018

Contents lists available at ScienceDirect

Computer Physics Communications

www.elsevier.com/locate/cpc

LeptonInjector and LeptonWeighter: A neutrino event generator and weighter for neutrino observatories ☆,☆☆

R. Abbasi [q], M. Ackermann [be], J. Adams [r], J.A. Aguilar [l], M. Ahlers [v], M. Ahrens [av], C. Alispach [ab], A.A. Alves Jr. [ae], N.M. Amin [ao], R. An [n], K. Andeen [am], T. Anderson [bb], I. Ansseau [l], G. Anton [z], C. Argüelles [n], S. Axani [o], X. Bai [as], A. Balagopal V. [ak], A. Barbano [ab], S.W. Barwick [ad], B. Bastian [be], V. Basu [ak], V. Baum [al], S. Baur [l], R. Bay [h], J.J. Beatty [t,u], K.-H. Becker [bd], J. Becker Tjus [k], C. Bellenghi [aa], S. BenZvi [au], D. Berley [s], E. Bernardini [be,1], D.Z. Besson [af,2], G. Binder [h,i], D. Bindig [bd], E. Blaufuss [s], S. Blot [be], S. Böser [al], O. Botner [bc], J. Böttcher [a], E. Bourbeau [v], J. Bourbeau [ak], F. Bradascio [be], J. Braun [ak], S. Bron [ab], J. Brostean-Kaiser [be], A. Burgman [bc], R.S. Busse [an], M.A. Campana [ar], C. Chen [f], D. Chirkin [ak], S. Choi [ax], B.A. Clark [x], K. Clark [ag], L. Classen [an], A. Coleman [ao], G.H. Collin [o], J.M. Conrad [o], P. Coppin [m], P. Correa [m], D.F. Cowen [ba,bb], R. Cross [au], P. Dave [f], C. De Clercq [m], J.J. DeLaunay [bb], H. Dembinski [ao], K. Deoskar [av], S. De Ridder [ac], A. Desai [ak], P. Desiati [ak], K.D. de Vries [m], G. de Wasseige [m], M. de With [j], T. DeYoung [x], S. Dharani [a], A. Diaz [o], J.C. Díaz-Vélez [ak], H. Dujmovic [ae], M. Dunkman [bb], M.A. DuVernois [ak], E. Dvorak [as], T. Ehrhardt [al], P. Eller [aa], R. Engel [ae], J. Evans [s], P.A. Evenson [ao], S. Fahey [ak], A.R. Fazely [g], S. Fiedlschuster [z], A.T. Fienberg [bb], K. Filimonov [h], C. Finley [av], L. Fischer [be], D. Fox [ba], A. Franckowiak [k,be], E. Friedman [s], A. Fritz [al], P. Fürst [a], T.K. Gaisser [ao], J. Gallagher [aj], E. Ganster [a], S. Garrappa [be], L. Gerhardt [i], A. Ghadimi [az], C. Glaser [bc], T. Glauch [aa], T. Glüsenkamp [z], A. Goldschmidt [i], J.G. Gonzalez [ao], S. Goswami [az], D. Grant [x], T. Grégoire [bb], Z. Griffith [ak], S. Griswold [au], M. Gündüz [k], C. Haack [aa], A. Hallgren [bc], R. Halliday [x], L. Halve [a], F. Halzen [ak], M. Ha Minh [aa], K. Hanson [ak], J. Hardin [ak], A.A. Harnisch [x], A. Haungs [ae], S. Hauser [a], D. Hebecker [j], K. Helbing [bd], F. Henningsen [aa], E.C. Hettinger [x], S. Hickford [bd], J. Hignight [y], C. Hill [p], G.C. Hill [b], K.D. Hoffman [s], R. Hoffmann [bd], T. Hoinka [w], B. Hokanson-Fasig [ak], K. Hoshina [ak,3], F. Huang [bb], M. Huber [aa], T. Huber [ae], K. Hultqvist [av], M. Hünnefeld [w], R. Hussain [ak], S. In [ax], N. Iovine [l], A. Ishihara [p], M. Jansson [av], G.S. Japaridze [e], M. Jeong [ax], B.J.P. Jones [d], R. Joppe [a], D. Kang [ae], W. Kang [ax], X. Kang [ar], A. Kappes [an], D. Kappesser [al], T. Karg [be], M. Karl [aa], A. Karle [ak], U. Katz [z], M. Kauer [ak], M. Kellermann [a], J.L. Kelley [ak], A. Kheirandish [bb], J. Kim [ax], K. Kin [p], T. Kintscher [be], J. Kiryluk [aw], S.R. Klein [h,i], R. Koirala [ao], H. Kolanoski [j], L. Köpke [al], C. Kopper [x], S. Kopper [az], D.J. Koskinen [v], P. Koundal [ae], M. Kovacevich [ar], M. Kowalski [j,be], K. Krings [aa], G. Krückl [al], N. Kurahashi [ar], A. Kyriacou [b], C. Lagunas Gualda [be], J.L. Lanfranchi [bb], M.J. Larson [s], F. Lauber [bd], J.P. Lazar [n,ak], K. Leonard [ak], A. Leszczyńska [ae], Y. Li [bb], Q.R. Liu [ak], E. Lohfink [al], C.J. Lozano Mariscal [an], L. Lu [p], F. Lucarelli [ab], A. Ludwig [x,ah], W. Luszczak [ak], Y. Lyu [h,i],

☆ The review of this paper was arranged by Prof. Z. Was.

☆☆ This paper and its associated computer program are available via the Computer Physics Communications homepage on ScienceDirect (http://www.sciencedirect.com/science/journal/00104655).

E-mail addresses: aschn@mit.edu (A. Schneider), analysis@icecube.wisc.edu (The IceCube Collaboration).

[1] Also at Università di Padova, I-35131 Padova, Italy.

[2] Also at National Research Nuclear University, Moscow Engineering Physics Institute (MEPhI), Moscow 115409, Russia.

[3] Also at Earthquake Research Institute, University of Tokyo, Bunkyo, Tokyo 113-0032, Japan.

https://doi.org/10.1016/j.cpc.2021.108018

W.Y. Ma [be], J. Madsen [ak], K.B.M. Mahn [x], Y. Makino [ak], P. Mallik [a], S. Mancina [ak], I.C. Mariş [l], R. Maruyama [ap], K. Mase [p], F. McNally [ai], K. Meagher [ak], A. Medina [u], M. Meier [p], S. Meighen-Berger [aa], J. Merz [a], J. Micallef [x], D. Mockler [l], G. Momenté [al], T. Montaruli [ab], R.W. Moore [y], R. Morse [ak], M. Moulai [o], R. Naab [be], R. Nagai [p], U. Naumann [bd], J. Necker [be], L.V. Nguyễn [x], H. Niederhausen [aa], M.U. Nisa [x], S.C. Nowicki [x], D.R. Nygren [i], A. Obertacke Pollmann [bd], M. Oehler [ae], A. Olivas [s], E. O'Sullivan [bc], H. Pandya [ao], D.V. Pankova [bb], N. Park [ak], G.K. Parker [d], E.N. Paudel [ao], P. Peiffer [al], C. Pérez de los Heros [bc], S. Philippen [a], D. Pieloth [w], S. Pieper [bd], A. Pizzuto [ak], M. Plum [am], Y. Popovych [a], A. Porcelli [ac], M. Prado Rodriguez [ak], P.B. Price [h], B. Pries [x], G.T. Przybylski [i], C. Raab [l], A. Raissi [r], M. Rameez [v], K. Rawlins [c], I.C. Rea [aa], A. Rehman [ao], R. Reimann [a], M. Renschler [ae], G. Renzi [l], E. Resconi [aa], S. Reusch [be], W. Rhode [w], M. Richman [ar], B. Riedel [ak], S. Robertson [h,i], G. Roellinghoff [ax], M. Rongen [a], C. Rott [ax], T. Ruhe [w], D. Ryckbosch [ac], D. Rysewyk Cantu [x], I. Safa [n,ak], S.E. Sanchez Herrera [x], A. Sandrock [w], J. Sandroos [al], M. Santander [az], S. Sarkar [aq], S. Sarkar [y], K. Satalecka [be], M. Scharf [a], M. Schaufel [a], H. Schieler [ae], P. Schlunder [w], T. Schmidt [s], A. Schneider [ak], J. Schneider [z], F.G. Schröder [ae,ao], L. Schumacher [a], S. Sclafani [ar], D. Seckel [ao], S. Seunarine [at], A. Sharma [bc], S. Shefali [a], M. Silva [ak], B. Skrzypek [n], B. Smithers [d], R. Snihur [ak], J. Soedingrekso [w], D. Soldin [ao], G.M. Spiczak [at], C. Spiering [be,2], J. Stachurska [be], M. Stamatikos [u], T. Stanev [ao], R. Stein [be], J. Stettner [a], A. Steuer [al], T. Stezelberger [i], R.G. Stokstad [i], T. Stuttard [v], G.W. Sullivan [s], I. Taboada [f], F. Tenholt [k], S. Ter-Antonyan [g], S. Tilav [ao], F. Tischbein [a], K. Tollefson [x], L. Tomankova [k], C. Tönnis [ay], S. Toscano [l], D. Tosi [ak], A. Trettin [be], M. Tselengidou [z], C.F. Tung [f], A. Turcati [aa], R. Turcotte [ae], C.F. Turley [bb], J.P. Twagirayezu [x], B. Ty [ak], M.A. Unland Elorrieta [an], N. Valtonen-Mattila [bc], J. Vandenbroucke [ak], D. van Eijk [ak], N. van Eijndhoven [m], D. Vannerom [o], J. van Santen [be], S. Verpoest [ac], M. Vraeghe [ac], C. Walck [av], A. Wallace [b], T.B. Watson [d], C. Weaver [x], A. Weindl [ae], M.J. Weiss [bb], J. Weldert [al], C. Wendt [ak], J. Werthebach [w], M. Weyrauch [ae], B.J. Whelan [b], N. Whitehorn [x,ah], K. Wiebe [al], C.H. Wiebusch [a], D.R. Williams [az], M. Wolf [aa], K. Woschnagg [h], G. Wrede [z], J. Wulff [k], X.W. Xu [g], Y. Xu [aw], J.P. Yanez [y], S. Yoshida [p], T. Yuan [ak], Z. Zhang [aw]

[a] *III. Physikalisches Institut, RWTH Aachen University, D-52056 Aachen, Germany*
[b] *Department of Physics, University of Adelaide, Adelaide, 5005, Australia*
[c] *Dept. of Physics and Astronomy, University of Alaska Anchorage, 3211 Providence Dr., Anchorage, AK 99508, USA*
[d] *Dept. of Physics, University of Texas at Arlington, 502 Yates St., Science Hall Rm 108, Box 19059, Arlington, TX 76019, USA*
[e] *CTSPS, Clark-Atlanta University, Atlanta, GA 30314, USA*
[f] *School of Physics, Center for Relativistic Astrophysics, Georgia Institute of Technology, Atlanta, GA 30332, USA*
[g] *Dept. of Physics, Southern University, Baton Rouge, LA 70813, USA*
[h] *Dept. of Physics, University of California, Berkeley, CA 94720, USA*
[i] *Lawrence Berkeley National Laboratory, Berkeley, CA 94720, USA*
[j] *Institut für Physik, Humboldt-Universität zu Berlin, D-12489 Berlin, Germany*
[k] *Fakultät für Physik & Astronomie, Ruhr-Universität Bochum, D-44780 Bochum, Germany*
[l] *Université Libre de Bruxelles, Science Faculty CP230, B-1050 Brussels, Belgium*
[m] *Vrije Universiteit Brussel (VUB), Dienst ELEM, B-1050 Brussels, Belgium*
[n] *Department of Physics, Laboratory for Particle Physics and Cosmology, Harvard University, Cambridge, MA 02138, USA*
[o] *Dept. of Physics, Massachusetts Institute of Technology, Cambridge, MA 02139, USA*
[p] *Dept. of Physics, Institute for Global Prominent Research, Chiba University, Chiba 263-8522, Japan*
[q] *Department of Physics, Loyola University Chicago, Chicago, IL 60660, USA*
[r] *Dept. of Physics and Astronomy, University of Canterbury, Private Bag 4800, Christchurch, New Zealand*
[s] *Dept. of Physics, University of Maryland, College Park, MD 20742, USA*
[t] *Dept. of Astronomy, Ohio State University, Columbus, OH 43210, USA*
[u] *Dept. of Physics, Center for Cosmology and Astro-Particle Physics, Ohio State University, Columbus, OH 43210, USA*
[v] *Niels Bohr Institute, University of Copenhagen, DK-2100 Copenhagen, Denmark*
[w] *Dept. of Physics, TU Dortmund University, D-44221 Dortmund, Germany*
[x] *Dept. of Physics and Astronomy, Michigan State University, East Lansing, MI 48824, USA*
[y] *Dept. of Physics, University of Alberta, Edmonton, Alberta, T6G 2E1, Canada*
[z] *Erlangen Centre for Astroparticle Physics, Friedrich-Alexander-Universität Erlangen-Nürnberg, D-91058 Erlangen, Germany*
[aa] *Physik-department, Technische Universität München, D-85748 Garching, Germany*
[ab] *Département de Physique Nucléaire et Corpusculaire, Université de Genève, CH-1211 Genève, Switzerland*
[ac] *Dept. of Physics and Astronomy, University of Gent, B-9000 Gent, Belgium*
[ad] *Dept. of Physics and Astronomy, University of California, Irvine, CA 92697, USA*
[ae] *Karlsruhe Institute of Technology, Institute for Astroparticle Physics, D-76021 Karlsruhe, Germany*
[af] *Dept. of Physics and Astronomy, University of Kansas, Lawrence, KS 66045, USA*
[ag] *SNOLAB, 1039 Regional Road 24, Creighton Mine 9, Lively, ON, P3Y 1N2, Canada*
[ah] *Department of Physics and Astronomy, UCLA, Los Angeles, CA 90095, USA*
[ai] *Department of Physics, Mercer University, Macon, GA 31207-0001, USA*
[aj] *Dept. of Astronomy, University of Wisconsin–Madison, Madison, WI 53706, USA*
[ak] *Dept. of Physics, Wisconsin IceCube Particle Astrophysics Center, University of Wisconsin–Madison, Madison, WI 53706, USA*

[al] Institute of Physics, University of Mainz, Staudinger Weg 7, D-55099 Mainz, Germany
[am] Department of Physics, Marquette University, Milwaukee, WI, 53201, USA
[an] Institut für Kernphysik, Westfälische Wilhelms-Universität Münster, D-48149 Münster, Germany
[ao] Bartol Research Institute, Dept. of Physics and Astronomy, University of Delaware, Newark, DE 19716, USA
[ap] Dept. of Physics, Yale University, New Haven, CT 06520, USA
[aq] Dept. of Physics, University of Oxford, Parks Road, Oxford OX1 3PU, UK
[ar] Dept. of Physics, Drexel University, 3141 Chestnut Street, Philadelphia, PA 19104, USA
[as] Physics Department, South Dakota School of Mines and Technology, Rapid City, SD 57701, USA
[at] Dept. of Physics, University of Wisconsin, River Falls, WI 54022, USA
[au] Dept. of Physics and Astronomy, University of Rochester, Rochester, NY 14627, USA
[av] Oskar Klein Centre, Dept. of Physics, Stockholm University, SE-10691 Stockholm, Sweden
[aw] Dept. of Physics and Astronomy, Stony Brook University, Stony Brook, NY 11794-3800, USA
[ax] Dept. of Physics, Sungkyunkwan University, Suwon 16419, Republic of Korea
[ay] Institute of Basic Science, Sungkyunkwan University, Suwon 16419, Republic of Korea
[az] Dept. of Physics and Astronomy, University of Alabama, Tuscaloosa, AL 35487, USA
[ba] Dept. of Astronomy and Astrophysics, Pennsylvania State University, University Park, PA 16802, USA
[bb] Dept. of Physics, Pennsylvania State University, University Park, PA 16802, USA
[bc] Dept. of Physics and Astronomy, Uppsala University, Box 516, S-75120 Uppsala, Sweden
[bd] Dept. of Physics, University of Wuppertal, D-42119 Wuppertal, Germany
[be] DESY, D-15738 Zeuthen, Germany

ARTICLE INFO

Article history:
Received 12 January 2021
Received in revised form 15 April 2021
Accepted 23 April 2021
Available online 27 May 2021

Keywords:
Neutrino generator
Event generator
Neutrino interaction
Neutrino simulation
Weighting

ABSTRACT

We present a high-energy neutrino event generator, called `LeptonInjector`, alongside an event weighter, called `LeptonWeighter`. Both are designed for large-volume Cherenkov neutrino telescopes such as IceCube. The neutrino event generator allows for quick and flexible simulation of neutrino events within and around the detector volume, and implements the leading Standard Model neutrino interaction processes relevant for neutrino observatories: neutrino-nucleon deep-inelastic scattering and neutrino-electron annihilation. In this paper, we discuss the event generation algorithm, the weighting algorithm, and the main functions of the publicly available code, with examples.

Program summary

Program Titles: `LeptonInjector` and `LeptonWeighter`
CPC Library link to program files: https://doi.org/10.17632/662gkpjfd9.1
Developer's repository links: https://github.com/icecube/LeptonInjector and https://github.com/icecube/LeptonWeighter
Licensing provisions: GNU Lesser General Public License, version 3.
Programming Language: C++11
External Routines:

- Boost
- HDF5
- nuflux (https://github.com/icecube/nuflux)
- nuSQuIDS (https://github.com/arguelles/nuSQuIDS)
- Photospline (https://github.com/icecube/photospline)
- SuiteSparse (https://github.com/DrTimothyAldenDavis/SuiteSparse)

Nature of problem: `LeptonInjector`: Generate neutrino interaction events of all possible topologies and energies throughout and around a detector volume.
`LeptonWeighter`: Reweight Monte Carlo events, generated by a set of `LeptonInjector` Generators, to any desired physical neutrino flux or cross section.
Solution method: `LeptonInjector`: Projected ranges of generated leptons and the extent of the detector, in terms of column depth, are used to inject events in and around the detector volume. Event kinematics follow distributions provided in cross section files.
`LeptonWeighter`: Event generation probabilities are calculated for each Generator, which are then combined into a generation weight and used to calculate an overall event weight.

1. Introduction

Neutrinos have been measured in a wide energy range from MeV energies in solar and reactor experiments to PeV energies in neutrino telescopes [1]. Different neutrino interaction processes [2] are relevant in this wide energy range, from *e.g.* coherent-neutrino scattering [3] at very small momentum (Q^2) transfer, to very large Q^2 processes which create W bosons [4–8] and heavy quark flavors [9]. However, deep-inelastic scattering [10] is always the dominant process above ∼10 GeV. This broad energy range has led to the development of various neutrino event generators used by experiments to simulate neutrino interactions [11–14], most of which have been optimized for GeV neutrino energy ranges and sub-megaton target mass detectors [12]. Such generators are not optimal for gigaton-scale neutrino detectors, often known as neutrino telescopes, such as the currently operating IceCube Neutrino Observatory at the Amundsen-Scott South Pole Station [15] and next-generation observatories such as KM3NeT [16] in the Mediterranean Sea and GVD in Lake Baikal [17].

The first neutrino telescope event generators started their simulation at the Earth's surface [18–21], which required solving two

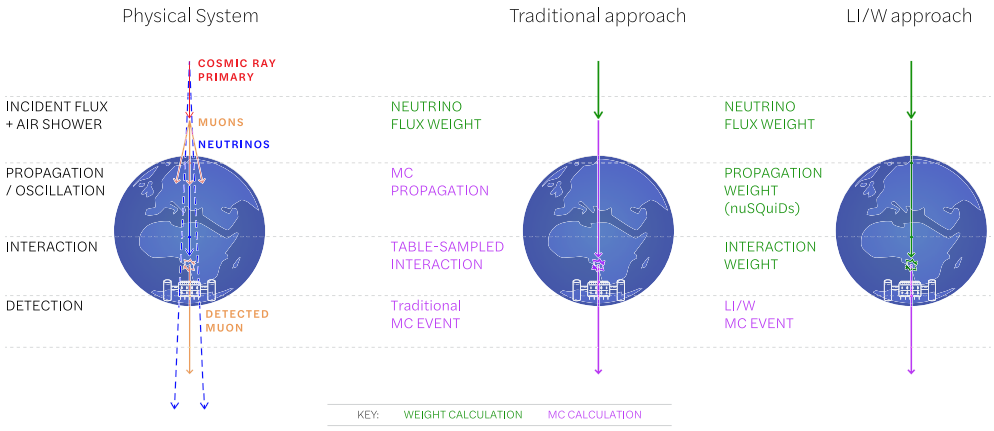

Fig. 1.1. A diagram illustrating the different event generation and weighting steps for traditional methods compared with the `LeptonInjector` and `LeptonWeighter` philosophy.

distinct problems: neutrino transport through the planet and the generation of neutrino events near the sensitive volume. The first such event generator was `NUSIM` [19], developed in the 1990s for the Antarctic Muon and Neutrino Detector Array (AMANDA); see also [22] for a similar effort for ANTARES. `NUSIM` established the fundamental concepts of what would later evolve into this project by breaking the problem of event generation into a three-step procedure. First a neutrino energy was randomly drawn from a prior distribution, then forced to interact somewhere near the detector, and finally an event weight would be calculated and applied [19]. This process relied on costly calculations of survival probability of the neutrino through the entirety of the Earth, and tightly coupled the generation and interaction of each neutrino to the calculation of its event weight.

In 2005, `NUSIM` was ported to `C++` and released as the All Neutrino Interaction Simulation (`ANIS`) [20], and then modified and adopted into the IceCube internal framework [23] as neutrino-generator, or `NuGen`. The basic simulation scheme remained unchanged, although with each update of the software the scope of features grew and the fundamental features and techniques of the algorithm were further refined and optimized. In the past five years, efficient algorithms to solve the neutrino transport problem have become publicly available [21,24–29], allowing the possibility of simplifying event generation to only consider the problem of event generation in and around a volume near the detector. This allowed the event generation scheme to be separated into two standalone and publicly-available software projects: `LeptonInjector` [30] and `LeptonWeighter` [31]. This separation is not only convenient from software maintenance point of view, but also facilitates optimizations in different energy ranges. For example, IceCube's analyses focusing in EeV energies [32], where the Earth is opaque to neutrinos, have used the JAVA-based JULIeT [21,33] software package for neutrino transport. JULIeT, much like the `C++`-based nuSQuIDS [24,25] package, has the computational advantage of solving Earth propagation using a set of differential equations instead of a Monte Carlo approach. The combination of software presented in this work allows for the user to choose the neutrino transport solution that best suits their needs. This simulation technique, the `LeptonInjector`/`LeptonWeighter` (LI/W), and traditional techniques are illustrated in Fig. 1.1

In this paper, we will describe the structure and function of the LeptonInjector software package, as well as a companion package called LeptonWeighter. In Section 2 we describe the basic functionality of LeptonInjector, focusing on the structure of the software (Section 2.1), the injection of particles into the detector (Section 2.2), and a comparison between the output of LeptonInjector and `NuGen`. Section 3 contains a description of LeptonWeighter and provides examples of reweighted neutrino samples from various physical sources of neutrinos. We conclude in Section 4. Details of the event and file structures provided by the software packages, as well as example driver scripts, are provided in Supplemental Material.

2. `LeptonInjector`

`LeptonInjector` is written in `C++` with `boost-python` bindings, and uses `Photospline` [34] for the cross sections needed for kinematic variable sampling. A standalone version of the code is publicly available from the IceCube GitHub repository [30]. In the description of the software that follows, we use `monospace` font to refer to libraries and packages, **bold** font to refer to classes, and *italic* font to refer to members of a class.

`LeptonInjector` is capable of simulating neutrino events of all flavors over a wide range of energies from 10 GeV to 100 PeV and beyond, undergoing neutrino-nucleon interaction in the Deep Inelastic Scattering (DIS) regime and antineutrino-electron scattering producing W in a Glashow Resonance (GR) interaction, ($\bar{\nu}_e + e^- \rightarrow W^-$). The initial event energy is sampled according to a single power-law spectrum at any desired spectral index, and final state kinematics are sampled from spline interpolations of the differential cross sections for the relevant interaction. These splines are saved in `FITS` files generated by `Photospline` [34]. For optimum efficiency, the spectrum of generated events would match the physical one. Atmospheric and astrophysical neutrino fluxes, for example, follow a power-law flux. As it is often desirable to maintain large sample size at high energies, events can be generated at one flux and subsequently reweighted to any physical flux using `LeptonInjector`'s sister software package `LeptonWeighter`, available at [31]. Because the event generation starts from near the detector, the primary neutrino energy will be guaranteed to follow the spectral index of event generation; this is not the case for event generators beginning at the Earth's surface.

To facilitate the reweighting, `LeptonInjector` creates configuration objects complete with a full description of all relevant event generation parameters. `LeptonWeighter` uses these configuration files to reweight events to any desired physical distribution.

Following the event generation, described in this work, the IceCube Monte Carlo proceeds using the following publicly available packages. First, leptons are propagated using `PROPOSAL` [35], a software package based on `MMC` [36], while hadronic or electromagnetic showers are propagated by the `Cascade Monte Carlo` (CMC) package, which implements the physics described in [37] and [38–40]. Next, Cherenkov photons arising from the

Table 2.1
Final state particles. Final state particle types are given, in the right two columns, for various possible desired interactions.

Event type	Interaction	*finalType1*	*finalType2*
Nu{E,Mu,Tau}	CC	{E,Mu,Tau}Minus	Hadrons
Nu{E,Mu,Tau}	NC	Nu{E,Mu,Tau}	Hadrons
Nu{E,Mu,Tau}Bar	CC	{E,Mu,Tau}Plus	Hadrons
Nu{E,Mu,Tau}Bar	NC	Nu{E,Mu,Tau}Bar	Hadrons
NuEBar	GR	Hadrons	Hadrons
NuEBar	GR	{E,Mu,Tau}Minus	Nu{E,Mu,Tau}Bar

Table 2.2
Flux properties. Parameter names are given in the left column, their description in the center column, and values on the right column. These parameters are chosen with respect to the desired flux. The allowed energy range is driven by the extent of the provided cross section tables.

Parameter	Description	Allowed ranges
$E_\nu^{\min}$, $E_\nu^{\max}$	Neutrino injected energy	[100 GeV, 1 EeV]
γ	Spectral index power law	$(-\infty, \infty)$
$\theta_\nu^{\min}$, $\theta_\nu^{\max}$	Injected primary zenith angle	$[0, \pi]$
$\phi_\nu^{\min}$, $\phi_\nu^{\max}$	Injected primary azimuth angle	$[0, 2\pi]$

charged particles are simulated by direct photon propagation using `CLSim` [41,42] or `PPC` [43,44]. Finally, a detector response is produced using a proprietary detector simulation.

`LeptonInjector` requires two kinds of objects: one or more **Injectors** and a **Controller**. An **Injector** object represents one primary neutrino type and one interaction channel, one cross section model to guide interactions, a number of neutrinos to be injected, and one parameter to control the sampling of the interaction vertex: ranged or volume mode, which are described in Section 2.1. In practice, the type of primary neutrino and interaction channel are specified in the **Injector** as a pair of particles that would be generated in such an interaction. These final state particles are called *finalType1* and *finalType2*, and the order of these particles is strictly defined in Table 2.1. A 'Hadrons' particle is used to represent the hadronic shower produced by the recoiling nucleus from the DIS interaction and the hadronic decay channel from a W produced in a GR interaction. Ideally the propagation of the hadronic showers would be simulated directly using GEANT4 or a similar particle interaction framework, although this process is far too computationally expensive to be practical. Instead, a parametrization is used for the propagation of the hadronic shower, developed through GEANT4 simulations, as described in [38].

The **Controller** defines energy ranges, azimuth and zenith ranges, and a spectral index of the primary neutrino as shown in Table 2.2. One or more **Injector** objects must be assigned to a Controller as well as the destinations for the output files. Once the **Controller** is configured, the simulation is initialized by calling the *Execute* member function. The Controller iterates over its member **Injectors**, with each combining the **Controller**'s flux properties with its own injection parameters into a **Generator**, and generating events until reaching their target number as set by the user. This process is illustrated in Fig. 2.1. In both ranged and volume injection modes, **Injectors** generate a 'primary' neutrino according to a power-law spectrum with the configured spectral index. This 'primary' neutrino is the neutrino as it was in the instant before interaction. The direction of the primary neutrino is sampled uniformly from the allowed ranges in azimuth and cosine of zenith. The event location is selected according to the injection mode, which is described in detail later in Section 2.1.

The event kinematics are defined in terms of the Bjorken x and Bjorken y kinematic variables. As shown in Eq. (2.1), Bjorken y is the fractional energy carried away by the out-going lepton in a DIS interaction and Bjorken x is the fraction of primary-particle momentum transferred by the weak interaction. These two variables are given by

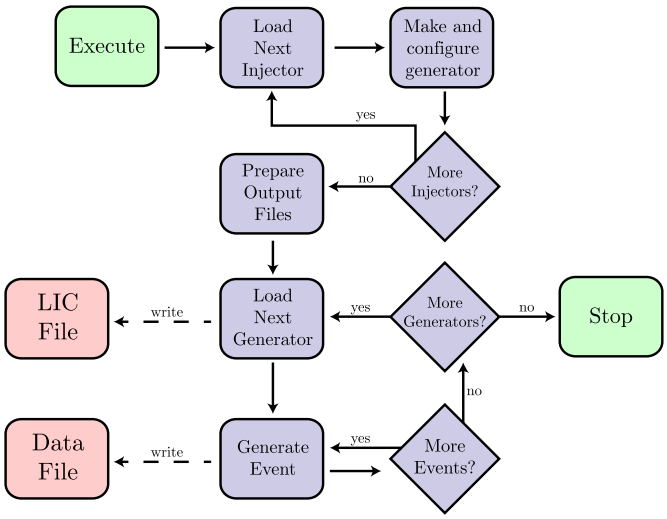

Fig. 2.1. Flowchart displaying the iterative process by a **Controller** prepares to generate, and then generates events. The **Generator** object is used by `LeptonInjector` to store all necessary information to simulate events.

$$y = 1 - \frac{E_f}{E_i} \qquad x = \frac{4E_i E_f \sin^2\theta}{2m_p(E_i - E_f)}, \tag{2.1}$$

where θ is the angle between the trajectories of the initial- and final-state leptons, m_p the proton mass, and E_i and E_f are the energies of the initial and final state lepton, respectively.

The Bjorken quantities are sampled, using b-splines from a joint 3D probability density function in the logarithm of each of E_i, x, and y space, using the Metropolis-Hastings algorithm [45]. Final state particle energies and deviations from the injected primary direction are then calculated analytically according to these kinematic variables. Events are written to an `HDF5` file as they are generated, and a `LeptonInjector` Configuration (LIC) file is written in parallel storing the exact configuration settings used for generation including both differential and total cross sections used. These LIC files are structured binary data files containing a header for meta-data, including a version number, and may evolve over time. The backwards-compatibility of LIC files is of importance, and will be maintained in future versions of `LeptonInjector` and `LeptonWeighter`. The structure of the `HDF5` files and exact specifications of the LIC files are described in Appendices A and B, respectively.

2.1. Injection

The two modes for injecting events are ranged mode and volume mode; each accepts and requires the parameters described in Table 2.3. An overview of the injection process is shown in Fig. 2.2.

In volume mode, a cylinder, oriented vertically, is constructed around the origin according to specified parameters and an interaction point is selected uniformly within that cylinder's volume. This injection mode is suitable for simulating events which are approximately point-like for the purposes of detection, such as neutral-current interactions and charged-current ν_e interactions which produce particle showers which are fairly short in dense media compared to the size of the detector.

The ranged mode process is illustrated in Fig. 2.3. This mode is intended as a counterpart of the volume injection mode. Ranged mode is suitable for simulating events where the detection is due to visible daughter particles ($\mu^\pm$, $\tau^\pm$) which travel through

Table 2.3
Detector properties. Parameter names are given in the left column, their description in the middle-left column, and Defaults on the middle-right column. These parameters are chosen in order to cover the detector. Example parameters for the IceCube Neutrino Observatory are provided on the far-right column.

Parameter	Description	Defaults	IceCube example
InjectionRadius	Max distance of closest approach from origin for injection	1200 m	900 m
EndcapLength	Possible longitudinal extent of injection from point of closest approach	1200 m	900 m
CylinderRadius	Radius of injection cylinder	1200 m	700 m
CylinderHeight	Height of injection cylinder	1200 m	1000 m

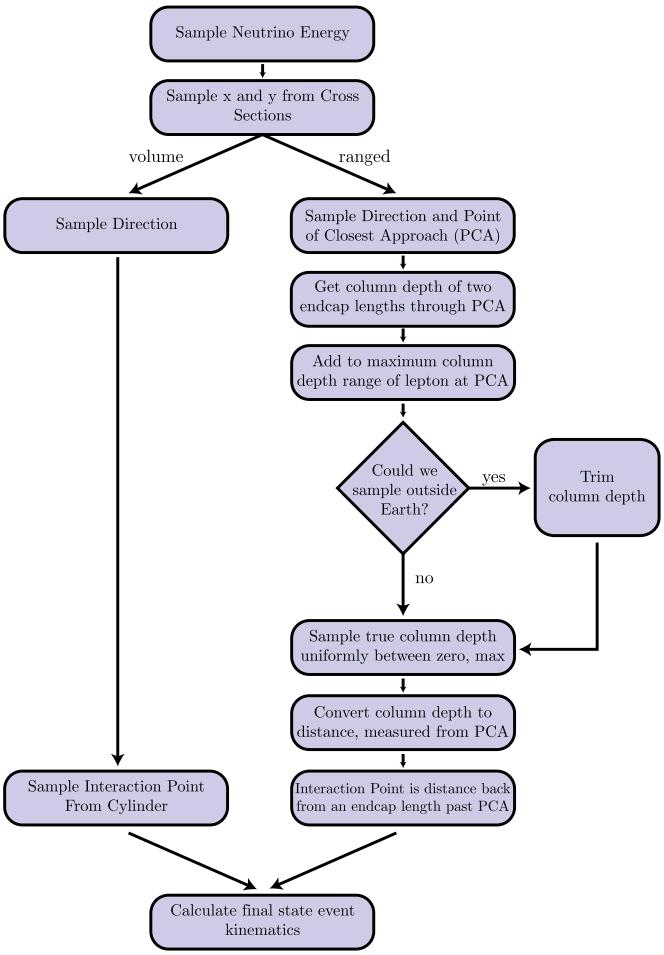

Fig. 2.2. A flowchart demonstrating the process of generating an event.

dense media for distances comparable to or larger than the size of the detector. It ensures sampling of interaction positions, over the whole volume of a target detector, both as far away as possibly visible to the detector due to daughter particles leaving the interaction, and proportional to local material density. A typical example of an interaction type in this category is the charged-current ν_μ interaction.

During generation in ranged mode, a direction for the primary neutrino is first chosen within the allowed range of azimuth and zenith angles; this is shown in Fig. 2.3a. Then, as in Fig. 2.3b, a point is randomly chosen from a disk of radius *InjectionRadius* centered at the origin and perpendicular to the sampled direction; this point will be the point of closest approach (PCA) of the injected neutrino's projected path. The distance from the sampled PCA to the origin is called the impact parameter. Next, a range of possible positions along this path is determined in which the interaction position may be sampled. This includes two 'endcaps,' specified as lengths (*EndcapLength*) on either side of the disk containing the PCA, and a maximum lepton 'range.' The endcaps are added to ensure that events are sampled over the entire volume of the detector, and the range is computed to account for the maximum distance that the charged lepton daughter of the interaction may travel. This maximum distance is calculated according to

$$R_\mu(E) = \frac{1}{d_b}\log\left(1 + E\frac{d_a}{d_b}\right), \text{ and} \tag{2.2}$$

$$R_\tau(E) = R_\mu(E) + \left(3.8\times10^4\right)\log\left(1 + \tfrac{1}{5.6\times10^7}\right), \tag{2.3}$$

with $d_a = 0.212/1.2$ [GeV mwe^{-1}] and $d_b = (0.251\times10^{-3})/1.2$ [mwe^{-1}] [46]. R_μ and R_τ represent the maximum ranges, in meters water equivalent, for 99.9% of muons and taus of energy E in GeV respectively. The factor of 1.2 is to account for the observed deviations from the fits producing these max range functions. The maximum deviation was less than 20%, and as such d_b is appropriately scaled.

The range of possible positions is converted to common units of column depth by taking into account the density of the material along the line formed by the two endcap lengths, including both local material around the detector and the Earth more generally, using a variation of the Preliminary Reference Earth Model (PREM) [47], which we have extended with three uniform-density layers: a 2.6 km thick clear-ice layer, a 200 m thick firn layer, and a 103 km atmosphere layer; these are demonstrated in Appendix C. These extra layers cover the entire Earth, and are required to accurately distribute the events, with respect to depth, in ranged mode. This gives the preliminary maximum column depth within which the generator should ideally sample the interaction point. The geometry of this calculation is shown in Fig. 2.3c. The model of the surrounding material is then integrated again, to determine whether the amount of column depth desired from the preliminary calculation actually exists along the path; at high energies it may not if the lepton range is sufficient to extend outside the outermost layer of the Earth model. In this case, the maximum column depth is reduced to the physically available value, as in Fig. 2.3d. The resulting column depth is called the total column depth. The amount of column depth the neutrino should traverse before interacting is then sampled uniformly between zero and this total column depth, and then converted to a physical position along the chosen path by a final integration of the material model as shown in Fig. 2.3e.

2.2. Comparisons

Prior to this generator, in IceCube, the primary neutrino event generator has been `NuGen`. Similar to `LeptonInjector`, `NuGen` has been used to generate both up- and down-going neutrino events of all flavors and neutrino type; it has been used for the Monte Carlo event generation of numerous studies in IceCube and is thoroughly vetted. As part of the development of `LeptonInjector`, comparisons were made between identical MC samples generated by `LeptonInjector` and `NuGen`'s 'Detector Mode,' which uses an injection scheme roughly analogous to `LeptonInjector`'s ranged mode. Events of all flavor, for both neutrino and anti-neutrino primaries, were generated for each neutrino type at a spectrum of E^{-1} over all azimuth angles and up-going zenith angles. A comparison of the spectra of injected lepton energies is shown in Fig. 2.5, and a comparison of the average inelasticity parameter as a function of primary neutrino energy is shown

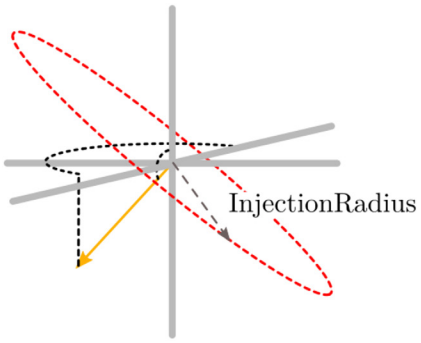

(a) A direction (orange) is chosen and a perpendicular disc of radius `InjectionRadius` (red) is constructed.

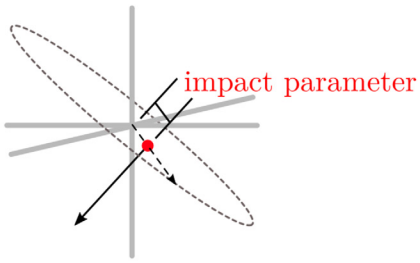

(b) A point of closest approach is randomly sampled on that `InjectionRadius` disk.

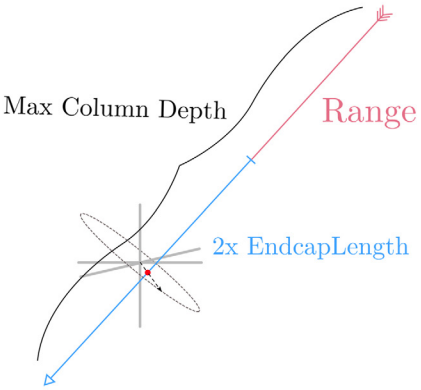

(c) Preliminary column depth calculation of the lepton range (red) plus two `EndcapLengths` (blue)

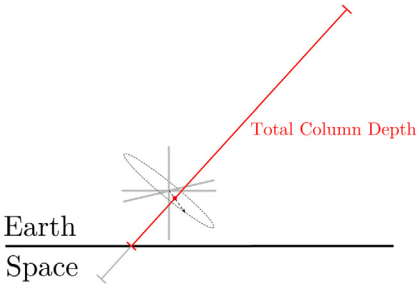

(d) If the actual column depth available is less than the column depth computed in part (c), reduce it appropriately.

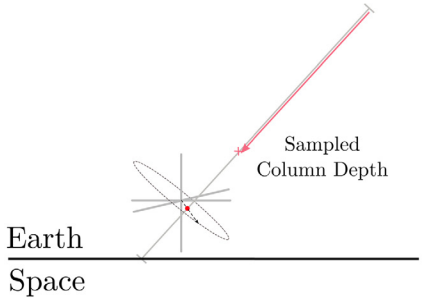

(e) Sample uniformly from the total column depth available for insertion depth.

Fig. 2.3. Visualization of the ranged injection process and geometry.

in Fig. 2.4b. Additional comparisons were carried out for distributions of Bjorken x and y, and the opening angle between injected particles, and were all found to be in agreement.

`LeptonInjector` was also verified to produce events with a realistic distribution of final state kinematics. Among other tests, to this end, we compared a large sample of generated events with the theoretical predictions of the final states resulting from CC, NC, and GR interactions, for which we use [48] to model the DIS interactions and the analytical expressions given in [4,10] for the GR. Fig. 2.4a compares the average inelasticity for an interaction of a given energy for neutral- and charged-current interactions with both neutrinos and anti-neutrinos; results from a five-year IceCube study on inelasticity distributions are overlaid [49] along with a flux-averaged `LeptonInjector` sample. This trend closely follows the predictions of [48]; see [50] for an extended discussion.

3. LeptonWeighter

The events produced by the `LeptonInjector` algorithm described in Section 2 are generated at an arbitrary rate chosen by the user; `LeptonWeighter` allows these events to then be re-weighted to any physical neutrino flux and interaction cross section. Here, we briefly explain the reweighting procedure.

Suppose a sample of events was generated according to some ansatz distribution $\Phi(E)$, *e.g.* according to

$$\frac{dN}{dE} = \Phi(E), \tag{3.1}$$

where E is the neutrino energy and dN/dE is the expected flux density. To re-weight the sample to a uniform distribution in energy, a weight w_{event} is applied to each event, inversely proportional to the generating probability density:

$$w_{\text{event}}(E_0) = 1/\Phi(E_0), \tag{3.2}$$

where E_0 is the energy of the event. Suppose instead two subsamples were generated from distributions Φ_a and Φ_b, with the same domain in energy, and were then combined into one. To re-weight events in the combined sample to a uniform distribution, a weight of

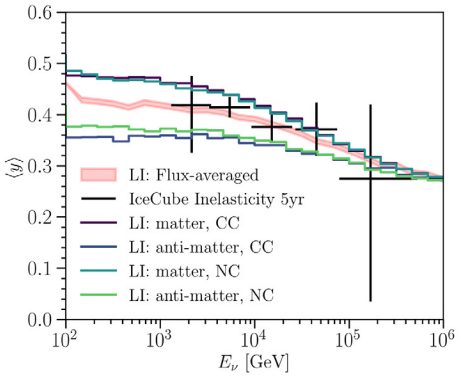

(a) `LeptonInjector` simulation with five years of IceCube inelasticity measurements overlaid.

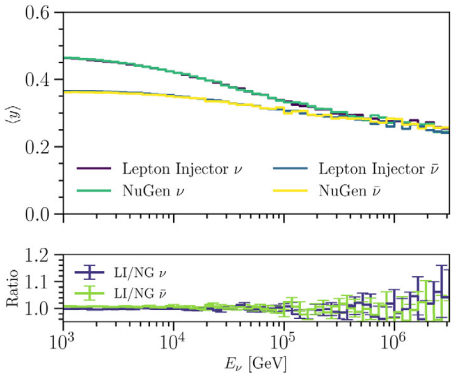

(b) Top: $\langle y \rangle$ as a function of E_ν, generated by `LeptonInjector`and `NuGen`. Note that trend lines are directly superimposed. Bottom: the ratio of $\langle y \rangle$ from `LeptonInjector` and `NuGen`.

Fig. 2.4. Average event inelasticity, with respect to neutrino energy in GeV, for NC and CC events resulting from neutrinos and anti-neutrinos.

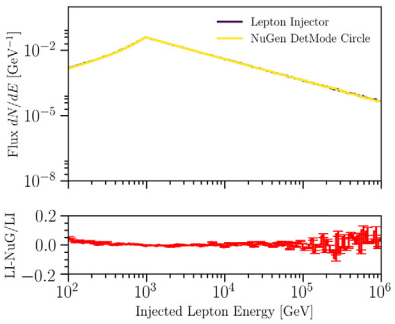

(a) Top: injected lepton energy for an anti-neutrino events. Bottom: relative difference between `LeptonInjector` and `NuGen`.

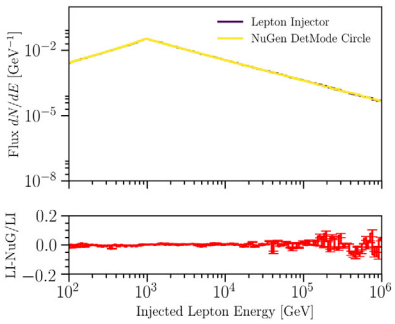

(b) Top: injected lepton energy for neutrino events. Bottom: relative difference between `LeptonInjector` and `NuGen`.

Fig. 2.5. Comparison between `LeptonInjector` and `NuGen`'s Detector Mode for the spectrum of the energies of leptons produced in the interactions. Total event energies were sampled with a 1 TeV minimum. Note that the `LeptonInjector` and `NuGen` lines are directly superimposed.

$$w_{\text{event}}(E_0) = \frac{1}{\Phi_a(E_0) + \Phi_b(E_0)} \tag{3.3}$$

would be applied. This is the generation weight, and accounts for the probability that either distribution could produce any given event. Events can then be re-weighted to a new distribution by evaluating their probability density in the new distribution and dividing by the generation weight.

Extending this to `LeptonInjector`, the probability density that a given **Generator** could have produced an event for each event is

$$p_{\text{MC}} = N_{\text{gen}} \frac{1}{\Omega_{\text{gen}} A_{\text{gen}}} \times \frac{\rho_{\text{gen}}(\ell)}{X^{\text{col}}_{\text{gen}}} \times \frac{1}{\sigma_{\text{tot}}} \frac{\partial^2 \sigma}{\partial x \partial y} \times \frac{\Phi(E)}{\int_{E_{\text{min}}}^{E_{\text{max}}} \Phi(E) dE} \tag{3.4}$$

where Ω_{gen} is the solid angle over which events were generated, $\Phi(E)$ is the power-law flux spectrum of the **Generator**, A_{gen} is the integrated area of the sampling surface, $\rho_{\text{gen}}(\ell)$ is the local mass density of targets, $X^{\text{col}}_{\text{gen}}$ is total column depth of targets in the sampling region, N_{gen} is the total number of generated events, and $\partial_{xy}\sigma$ and σ_{total} are the differential and total cross sections evaluated for the event, respectively. As a result, p_{MC} has units of sr^{-1} cm^{-3} GeV^{-1}. For a single MC generator, whose exact definitions are discussed in [51], the generation weight is the inverse of the generation probability density:

$$w_{\text{gen}} = \frac{1}{p_{\text{MC}}}. \tag{3.5}$$

In the regime of small neutrino interaction probability, an event's final weight, in units of s^{-1}, is approximately given by

$$w_{\text{event}} = \sum_{\{\text{gen}\}} \underbrace{\left(\frac{X^{\text{col}}_{\text{physical}} N_A}{M_{\text{target}}} \times \frac{\rho_{\text{physical}}(\ell)}{X^{\text{col}}_{\text{physical}}} \times \frac{\partial^2 \sigma}{\partial x \partial y} \times \Phi_{\text{physical}} \right)}_{\text{physical distribution}} \times \underbrace{w_{\text{gen}}}_{\text{gen weight}}, \tag{3.6}$$

where {gen} indicates the set of generators, M_{target} is the molar mass of the target, Φ_{physical} is the desired physical flux of neutrinos at the detector, N_A is Avogadro's constant, $X^{\text{col}}_{\text{physical}}$ is calculated as

$$X^{\text{col}}_{\text{physical}} = \int_{\ell_i}^{\ell_f} \rho_{\text{physical}}(\ell) d\ell \tag{3.7}$$

along the path ℓ the particle would take to interact, and $\partial_{xy}\sigma$ is the differential cross section evaluated for the event. Note that $X^{\text{col}}_{\text{physical}}$ is the physical column density between the generation boundaries ℓ_f and ℓ_i, which are not necessarily the same across different generators. If the physical and generation density models are the same, then the $\rho_{\text{physical}}(\ell)/X^{\text{col}}_{\text{physical}}$ and $\rho_{\text{gen}}(\ell)/X^{\text{col}}_{\text{gen}}$ terms cancel. For a more complete description of the weighting that covers non-negligible interaction probabilities, see Appendix D.

This weighting calculation procedure is implemented in the `LeptonWeighter` `C++` library and Python module; it is available

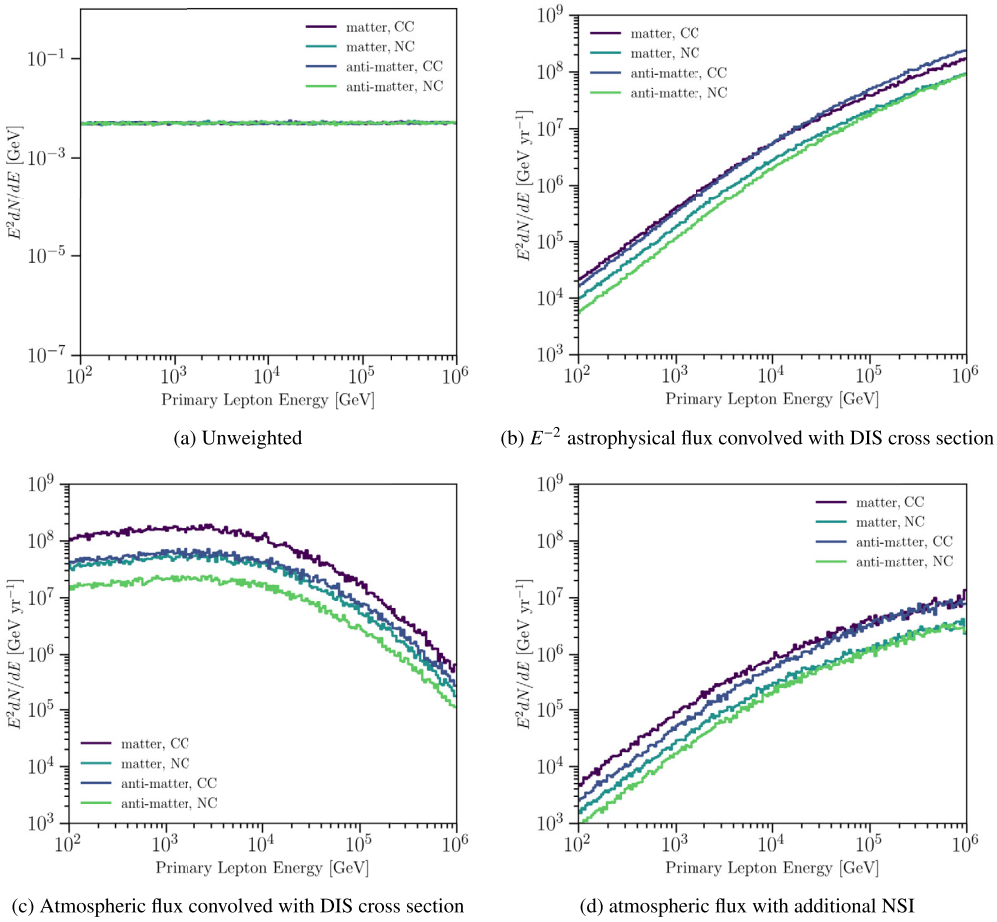

(a) Unweighted

(b) E^{-2} astrophysical flux convolved with DIS cross section

(c) Atmospheric flux convolved with DIS cross section

(d) atmospheric flux with additional NSI

Fig. 3.1. Several re-weightings of the same sample with one year of live-time. Top-left: unweighted, top-right: re-weighted to an E^{-2} astrophysical flux, bottom-left: re-weighted to an atmospheric flux, bottom-right: re-weighted to a sample with non-standard interactions used propagation of atmospheric neutrinos. Here an extra, lepton-number violating, non-diagonal, term has been added to the neutrino propagation Hamiltonian.

in [31]. `LeptonWeighter` uses the LIC files generated by `LeptonInjector` to calculate the above generation weights, then a user-specified cross section and flux to calculate event weights.

3.1. Code structure

`LeptonWeighter` divides its functionality into distinct components: fluxes, cross sections, **Generators**, and **Weighters**. **Flux** objects are constructed to define a flux to which a sample should be weighted. **CrossSection** objects are similarly constructed with paths to locally saved FITS files of the same format as those used by `LeptonInjector`, and are used to define the cross sections used to weight the sample's events. `LeptonWeighter` constructs **Generators** by reading LIC files from disk and deserializing them. These **Generators** contain the exact simulation parameters used by `LeptonInjector` to generate events, and are able to calculate the generation weight for any event following a process illustrated in Fig. 3.2.

`LeptonWeighter` creates a **Weighter** object by using a list of **Generators**, a **Flux** object, and a **CrossSection** object. The **Weighter** object uses an event's properties, see Fig. A.1 in the Appendix, to calculate a weight as defined by Eq. (3.6). Fig. 3.1 demonstrates an all-flavor Monte Carlo sample composed of equal parts neutral- and charged-current DIS events, generated using an E^{-2} spectrum, and re-weighted to multiple different fluxes. The top-left plot shows the unweighted sample; the top-right left plot shows the sample reweighed to an astrophysical flux and weighted to the CSMS calculation of the DIS cross section [48]; the bottom-

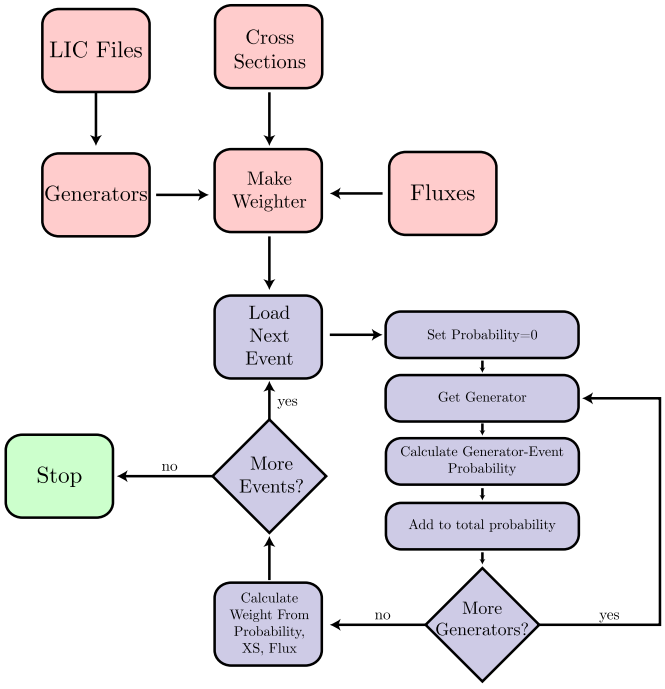

Fig. 3.2. A flowchart illustrating the process for calculating the individual weights of a collection of events.

left is re-weighted to an atmospheric neutrino flux and convolved with the same DIS cross sections [48]; the bottom-right plot shows the sample re-weighted to an atmospheric neutrino flux, with non-standard neutrino interaction (NSI) parameter strength of $\varepsilon_{\mu\tau} = 2 \times 10^{-1}$. See [52] for a precise definition of this parameter and nuSQuIDS [24,25] for the NSI implementation used.

In general, the weighting scheme allows to modify an already generated Monte Carlo set to any cross section that maps onto the same final states. For example, the DIS cross section could be a perturbative QCD calculation such as the CSMS@NLO [48] or the BGR@NNLO calculation given in [53] or a phenomenological estimate using the color-dipole model [25]. Similarly for the Glashow process one could use the original tree-level calculation in [4] or the updated calculation including radiative corrections given in [54].

4. Broader applications

Although `LeptonInjector` and `LeptonWeighter` have principally been developed for use by IceCube, the injection and weighting techniques are broadly applicable for experiments that need to simulate natural sources of neutrinos above 10 GeV. To adapt the software to other experiments we must account for differences in detector geometry and material composition within and around the detector.

The size of the injection region can be easily adjusted by changing the *InjectionRadius*, *EndcapLength*, *CylinderRadius*, and *CylinderHeight* parameters to encompass the extent of the detector. As long as the detector occupies a significant fraction of this cylindrical volume, the event injection remains efficient.

The material model used by `LeptonInjector` and `LeptonWeighter` has a simple implementation that models the Earth as a series of spherical shells with a radially varying polynomial density distribution. The polar ice cap is modeled as an offset spherical shell, also with a radially varying polynomial density. This implementation works well for detectors embedded in media that conform to spherical symmetry such as KM3NeT [16] in the Mediterranean Sea. However, this approach to the material model breaks down when the symmetry is broken, as is the case for GVD in Lake Baikal [17] and the 17 kt liquid Argon modules planned for DUNE [55]. To accommodate these experiments a more detailed software model of the surrounding material would need to be implemented. As long as the injection and weighting procedures query the updated material mode, no other modifications should be necessary.

5. Conclusions

Here we have presented the first publicly available neutrino telescope event generator for GeV-PeV+ energy ranges that factorizes the problem of Earth and atmospheric propagation from the event generation. The valid energy range of the generator is not limited by the software, but by the input cross sections provided by the user. The default CSMS cross section [48] provided with the code has less than 5% uncertainty in the 100 GeV to 100 EeV energy range. The factorization allows for streamlined and efficient production of neutrino events. `LeptonInjector`, along with its sister software `LeptonWeighter`, satisfy the needs of generating events for gigaton-scale neutrino observatories. The current implementation contains the most significant processes relevant to current analyses performed by these observatories, however we expect that this work will be extended as new calculations are made available and newer experimental needs arise. To this end, the code discussed in this paper follows an open-source model. Improvements recently proposed in the literature include: adding sub-leading neutrino interactions such as interactions with the nuclear coulomb field [5–8], which is expected to be a 10% contribution at 1 PeV; use of updated DIS models such as those given in [29]; inclusion of trident neutrino events [56–59,8]; inclusion of nuclear effects on interactions [53]; inclusion of new physics processes such as production of heavy-neutral leptons [60–62] or dark neutrinos [63–67]; inclusion of new neutrino interactions mediated by light Z-prime [68–70]; among others.

Declaration of competing interest

The authors declare that they have no known competing financial interests or personal relationships that could have appeared to influence the work reported in this paper.

Acknowledgements

The IceCube collaboration acknowledges the significant contributions to this manuscript from Carlos Argüelles, Austin Schneider, and Benjamin Smithers. We acknowledge the support from the following agencies: USA – U.S. National Science Foundation-Office of Polar Programs, U.S. National Science Foundation-Physics Division, Wisconsin Alumni Research Foundation, Center for High Throughput Computing (CHTC) at the University of Wisconsin-Madison, Open Science Grid (OSG), Extreme Science and Engineering Discovery Environment (XSEDE), Frontera computing project at the Texas Advanced Computing Center, U.S. Department of Energy-National Energy Research Scientific Computing Center, Particle astrophysics research computing center at the University of Maryland, Institute for Cyber-Enabled Research at Michigan State University, and Astroparticle physics computational facility at Marquette University; Belgium – Funds for Scientific Research (FRS-FNRS and FWO), FWO Odysseus and Big Science programmes, and Belgian Federal Science Policy Office (Belspo); Germany – Bundesministerium für Bildung und Forschung (BMBF), Deutsche Forschungsgemeinschaft (DFG), Helmholtz Alliance for Astroparticle Physics (HAP), Initiative and Networking Fund of the Helmholtz Association, Deutsches Elektronen Synchrotron (DESY), and High Performance Computing cluster of the RWTH Aachen; Sweden – Swedish Research Council, Swedish Polar Research Secretariat, Swedish National Infrastructure for Computing (SNIC), and Knut and Alice Wallenberg Foundation; Australia – Australian Research Council; Canada – Natural Sciences and Engineering Research Council of Canada, Calcul Québec, Compute Ontario, Canada Foundation for Innovation, WestGrid, and Compute Canada; Denmark – Villum Fonden, Danish National Research Foundation (DNRF), Carlsberg Foundation; New Zealand – Marsden Fund; Japan – Japan Society for Promotion of Science (JSPS) and Institute for Global Prominent Research (IGPR) of Chiba University; Korea – National Research Foundation of Korea (NRF); Switzerland – Swiss National Science Foundation (SNSF); United Kingdom – Department of Physics, University of Oxford. United Kingdom – Science and Technology Facilities Council (STFC), part of UK Research and Innovation.

Appendix A. `LeptonInjector` event structure

All `LeptonInjector` events from a single process are saved to a single `HDF5` file. Each **Injector** used in the generation process is given its own dataset inside the `HDF5` file with four lists containing an entry for each event generated. Two lists are stored for the two final state particles' parameters, a third list contains the initial state particles' parameters, and a fourth list contains overall parameters for the events. Each of the event-entries in each of the three lists of particles contain, in order: a number differentiating whether it is initial or final state, the particles' PDG ID [71], the particles' positions, the particles' directions in radians,

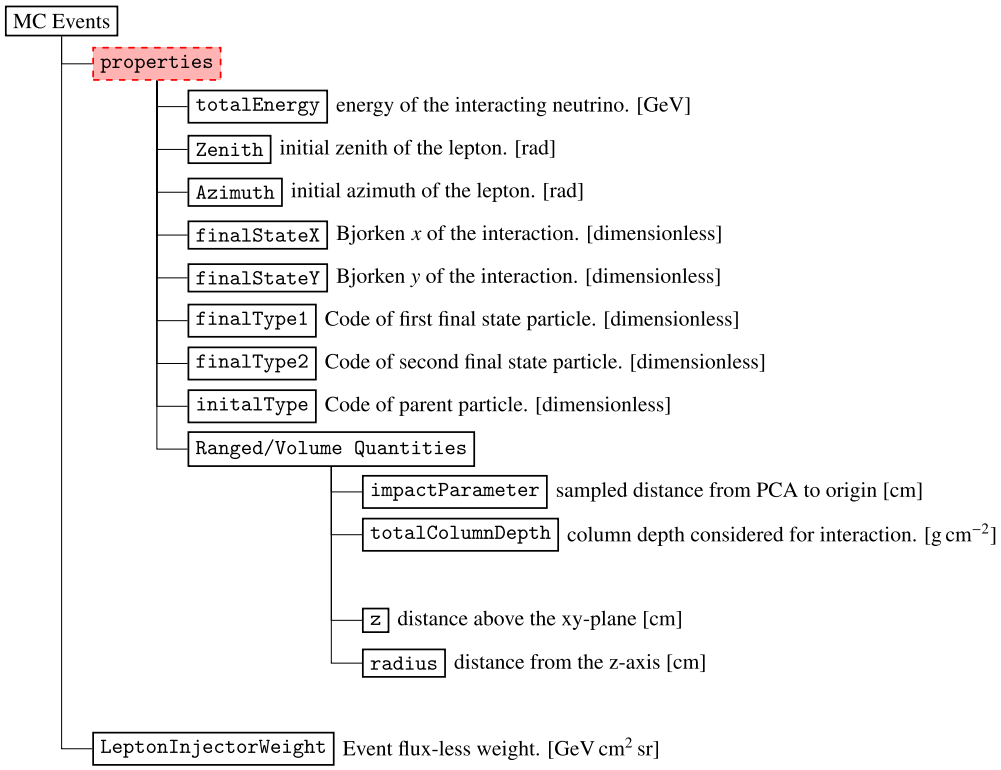

Suppl. Figure A.1. Lepton Injector Monte Carlo event structure.

and the particles' energies. The overall properties stored for each event are shown in Fig. A.1. The impact parameter and total column depth are defined in Section 2.1 and shown graphically in Figs. 2.3b and 2.3d.

Appendix B. LIC file structure

Data serialized in the LIC file is written little-endian, regardless of machine architecture. When a LIC file is first opened, the **Controller** either overwrites any existing file with the same destination name or begins appending to the end of such an existing file. This behavior follows according to user-specification. If a new file is being written or an existing one overwritten, a block is first written to the file enumerating all `LeptonInjector` particle types. A header is first written specifying the size of the block, the name of the enumeration, and the length of the enumeration. Then the name and number of each entry in the particle enumeration is written.

Afterwards, each time a new **Generator** is prepared, the **Controller** writes a new block to the LIC file. Each of these blocks is prefaced with a header specifying the size of the block, the name of the block, and the version of the `LeptonInjector` serialization code used to write the block. Then, all relevant generation parameters are written to the block.

Appendix C. Earth model density

`LeptonInjector` uses a modified Preliminary Reference Earth Model (PREM) for column depth calculations around the injection region. The density profile of which is shown in Fig. C.1.

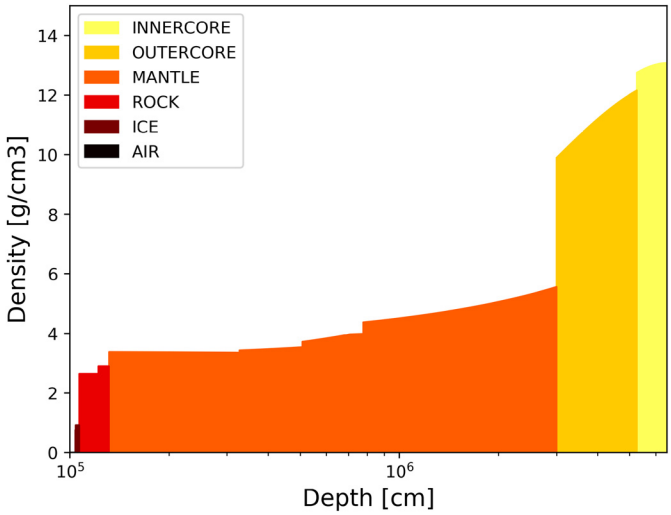

Suppl. Figure C.1. The density of the `LeptonInjector` Earth model as a function of depth from the edge of Earth's atmosphere.

Appendix D. Weighting

The generation procedure produces a set of neutrino properties that include the position, direction, energy, neutrino type, interaction type, and final state kinematic properties. The distribution of these properties at generation may differ from those we would expect in a physical scenario, so the weighting procedure is designed to correct for these differences. Beyond the distribution differences, weighting also corrects for differences in dimensionality and raw numbers of events. In our prototypical scenario, the weight of an event is dimensionless so only a correction factor to the total number of events is needed ($N_{\text{physical}}/N_{\text{gen}}$).

In the case of ranged injection we can separate the generation probability density of an event into several independent components

$$p_{\text{gen}} = p_{\text{gen}}^{\text{neutrino type}} \times p_{\text{gen}}^{\text{interaction type}} \times p_{\text{gen}}^{\text{energy}} \times p_{\text{gen}}^{\text{direction}}$$

$$\times\, p_{\text{gen}}^{\text{impact}} \times p_{\text{gen}}^{\text{depth}} \times p_{\text{gen}}^{\text{kinematics}}. \tag{D.1}$$

The generators in `LeptonInjector` only deal with one neutrino and interaction type each, so $p_{\text{gen}}^{\text{neutrino type}}$ and $p_{\text{gen}}^{\text{interaction type}}$ will either be one or zero depending on if the event matches what can be produced by the generator. Similarly, $p_{\text{gen}}^{\text{energy}}$ is the probability distribution of injected neutrino energies which is zero for events with neutrino energies outside the bounds of the generator. Directions are distributed uniformly in ranged injection and so $p_{\text{gen}}^{\text{direction}} = 1/\Omega_{\text{gen}}$ where Ω_{gen} is the total solid angle available to the generator. The $p_{\text{gen}}^{\text{impact}}$ term is the probability distribution related to the impact parameter and angle; since events are sampled uniformly on a disk, this term is the inverse of the disk area, $p_{\text{gen}}^{\text{impact}} = 1/A_{\text{gen}}$, for events intersecting the disk and zero otherwise. Events are sampled uniformly with respect to column depth along the considered line segment, so the positional distribution of events can be described as $p_{\text{gen}}^{\text{depth}} = \rho_{\text{gen}}(\ell)/X_{\text{gen}}^{\text{col}}$, where $\rho_{\text{gen}}(\ell)$ is the local target mass density where the event is injected and $X_{\text{gen}}^{\text{col}}$ is the total column depth of targets along the considered line segment. Finally, $p_{\text{gen}}^{\text{kinematics}}$ is the probability distribution of the events kinematic variables; for charged current and neutral current events this is $p_{\text{gen}}^{\text{kinematics}} = (\partial_{xy}\sigma_{\text{gen}}^{\text{tot},i})/(\sigma_{\text{gen}}^{\text{tot},i})$.

These terms in the generation probability must then be paired with their physical counterparts. Since our hypothesis can specify the number of neutrinos per type, the neutrino type can be neglected beyond this number correction and the $p_{\text{gen}}^{\text{neutrino type}}$ term from the generator. The energy, direction, and impact terms all have their counterpart in the neutrino flux Φ_{physical}, which specifies the physical neutrino distribution in energy, direction, area, and time. The flux, when paired with a detector livetime L_{physical} also specifies the total number of neutrinos N_{physical} by the relation

$$L_{\text{physical}} \times \Phi_{\text{physical}} = N_{\text{physical}} \times p_{\text{physical}}^{\text{neutrino type}} \times p_{\text{physical}}^{\text{energy}} \times p_{\text{physical}}^{\text{direction}} \times p_{\text{physical}}^{\text{impact}}. \tag{D.2}$$

The remaining terms, $p_{\text{gen}}^{\text{interaction type}}$, $p_{\text{gen}}^{\text{depth}}$, and $p_{\text{gen}}^{\text{kinematics}}$, deal with the neutrino interaction itself, which requires special care. The generation process assumes that the neutrino interacts within a certain region and with a specific interaction type. In reality, neutrinos on a path to the detector are potentially subject to any of several different interactions, and may pass through the Earth entirely unimpeded. Thus, we need to account for the probability that the neutrino in the physical scenario would interact within the region considered by the generator $p_{\text{physical}}^{\text{interaction}}$, the depth distribution of all neutrino interactions within that region $p_{\text{physical}}^{\text{depth}}$, the probability that a specific interaction occurs once the interaction point has been chosen $p_{\text{physical}}^{\text{interaction type}}$, and finally the kinematic distribution $p_{\text{physical}}^{\text{kinematics}}$. The former two terms, $p_{\text{physical}}^{\text{interaction}}$ and $p_{\text{physical}}^{\text{depth}}$ depend explicitly on the line segment considered by the generator when choosing the neutrino interaction vertex. The interaction probability can be cast in terms of the "survival" probability, $p_{\text{physical}}^{\text{interaction}} = 1 - p_{\text{physical}}^{\text{survival}}$, the probability that the neutrino will pass through the region without interacting. The survival probability is given by

$$p_{\text{physical}}^{\text{survival}} = \exp\left(-\int_{\ell_i}^{\ell_f} d\ell \sum_{p,i} n_{\text{physical}}^{p}(\ell)\sigma_{\text{physical}}^{\text{tot},p,i}\right), \tag{D.3}$$

where p iterates over the possible targets (usually nucleons and electrons), i iterates over interaction types, and $n_{\text{physical}}^{p}(\ell)$ is the density of target p at a point ℓ along the considered line segment Thus,

$$p_{\text{physical}}^{\text{interaction}} = 1 - \exp\left(-\int_{\ell_i}^{\ell_f} d\ell \sum_{p,i} n_{\text{physical}}^{p}(\ell)\sigma_{\text{physical}}^{\text{tot},p,i}\right). \tag{D.4}$$

Another way of writing this is in terms of the total column depth for each target $X_{\text{physical}}^{\text{col},p}$, target molar mass M_p, and Avagadro's number N_A, such that

$$p_{\text{physical}}^{\text{interaction}} = 1 - \exp\left(-N_A \sum_{p,i} (X_{\text{physical}}^{\text{col},p}/M_p)\sigma_{\text{physical}}^{\text{tot},p,i}\right). \tag{D.5}$$

The implementation in `LeptonWeighter` groups protons and neutrons together and assumes that the molar mass of nucleons is 1 g mol^{-1}. The depth distribution $p_{\text{physical}}^{\text{depth}}$ follows a similar form as the survival probability, but is normalized within the generation bounds such that

$$p_{\text{physical}}^{\text{depth}} = \exp\left(-\int_{\ell_i}^{\ell} d\ell \sum_{p,i} n_{\text{physical}}^{p}(\ell)\sigma_{\text{physical}}^{\text{tot},p,i}\right) \Big/ \int_{\ell_i}^{\ell_f} d\ell \exp\left(-\int_{\ell_i}^{\ell} d\ell \sum_{p,i} n_{\text{physical}}^{p}(\ell)\sigma_{\text{physical}}^{\text{tot},p,i}\right), \tag{D.6}$$

which can similarly be recast in terms of the density or column depth. The last two terms, $p_{\text{physical}}^{\text{interaction type}}$ and $p_{\text{physical}}^{\text{kinematics}}$, depend only on the position and type of the interaction, and so are independent of the generator. Once we assume that an interaction occurs at a known location, the probability of a specific interaction $p_{\text{physical}}^{\text{interaction type}}$ is the ratio of total cross sections at that location $p_{\text{physical}}^{\text{interaction type}} = (\sigma_{\text{physical}}^{\text{tot},i})/(\sum_j \sigma_{\text{physical}}^{\text{tot},j})$ where the subscript j iterates over all possible interactions. For the chosen interaction type, the kinematic distribution is simply $p_{\text{physical}}^{\text{kinematics}} = (\partial_{xy}\sigma_{\text{physical}}^{\text{tot},i})/(\sigma_{\text{physical}}^{\text{tot},i})$ in the case of charged or neutral current interactions.

By pairing up the terms we can see all the effects that are accounted for in the event weight

$$w_{\text{MC}} = \frac{N_{\text{physical}}}{N_{\text{gen}}} p_{\text{physical}}^{\text{interaction}} \frac{p_{\text{physical}}^{\text{neutrino type}}}{p_{\text{gen}}^{\text{neutrino type}}} \frac{p_{\text{physical}}^{\text{interaction type}}}{p_{\text{gen}}^{\text{interaction type}}} \frac{p_{\text{physical}}^{\text{energy}}}{p_{\text{gen}}^{\text{energy}}} \times \frac{p_{\text{physical}}^{\text{direction}}}{p_{\text{gen}}^{\text{direction}}} \frac{p_{\text{physical}}^{\text{impact}}}{p_{\text{gen}}^{\text{impact}}} \frac{p_{\text{physical}}^{\text{depth}}}{p_{\text{gen}}^{\text{depth}}} \frac{p_{\text{physical}}^{\text{kinematics}}}{p_{\text{gen}}^{\text{kinematics}}}. \tag{D.7}$$

Practical implementations of this replace some of the physical terms with the flux and livetime to obtain the event weight

$$w_{\text{MC}} = \frac{L_{\text{physical}}\Phi_{\text{physical}}}{N_{\text{gen}} p_{\text{gen}}^{\text{neutrino type}} p_{\text{gen}}^{\text{energy}} p_{\text{gen}}^{\text{direction}} p_{\text{gen}}^{\text{impact}}} \times p_{\text{physical}}^{\text{interaction}} \times \frac{p_{\text{physical}}^{\text{interaction type}}}{p_{\text{gen}}^{\text{interaction type}}} \times \frac{p_{\text{physical}}^{\text{depth}}}{p_{\text{gen}}^{\text{depth}}} \times \frac{p_{\text{physical}}^{\text{kinematics}}}{p_{\text{gen}}^{\text{kinematics}}}. \tag{D.8}$$

When simulation is created using multiple generators we must consider the probability that a particular event may be generated in either generator, regardless of which generator it originated from. The behavior we desire is such that events from non-overlapping regions of the parameter space retain their original single-generator weights, but events that reside in the overlap

regions are down-weighted to account for the overlap. The event weight then takes the form

$$w_{\mathrm{MC}} = \left[\sum_i \left(p^i_{\mathrm{physical}} \right)^{-1} \times p^i_{\mathrm{gen}} \right]^{-1}, \tag{D.9}$$

where the superscript i denotes the different generators, p^i_{physical} is the physical contribution to the weighting, and p^i_{gen} is the generation contribution to the weighting. Note the superscript i on the physical contribution is there because the terms $p^{\mathrm{interaction}}_{\mathrm{physical}}$ and $p^{\mathrm{depth}}_{\mathrm{physical}}$ depend on the particular generator. If the generation settings governing the line segment along which the event is injected are common to all generators then this dependence can be dropped and p_{physical} can be factored out.

The above description in the weighting starts from the ranged injection procedure, but only minor modifications are needed for this to be applicable to volume injection. The difference arises from the $p^{\mathrm{depth}}_{\mathrm{gen}}$ and $p^{\mathrm{impact}}_{\mathrm{gen}}$ terms on the generation side and $p^{\mathrm{depth}}_{\mathrm{physical}}$ and $p^{\mathrm{interaction}}_{\mathrm{physical}}$ on the physical side. These generation terms are directly analogous to steps in the ranged injection procedure where the position of closest approach and interaction vertex position are chosen. In the volume injection, the interaction vertex is chosen in a single step, so we can replace these two generation terms with the single $p^{\mathrm{position}}_{\mathrm{gen}}$ term which is a uniform probability density along the line segment within the injection cylinder and zero outside. The physical terms only differ in that the line segment considered for the calculation now must come from the volume injection procedure. Specifically, the line segment considered passes through the interaction vertex following the injected neutrino direction, beginning and ending at the boundaries of the injection cylinder.

These differences between the ranged and volume injection mean that the physical contributions to the weighting will differ between the two, and must be calculated separately for each event if both methods are used in the event generation.

Finally, the approximation used in Eq. (3.6) can be obtained by expanding the depth and interaction terms for a vanishing product of the interaction cross section and column depth. For the column depths and cross sections used in `LeptonInjector`, this approximation remains valid for sub ZeV neutrino energies.

Appendix E. Generation example

This `Python` example is included in the `LeptonInjector` source code. It creates an Injector in Ranged mode for producing CC muon-neutrino events of initial energy between 1000 GeV to 100 000 GeV, and outputs the data to an `HDF5` file.

```
import LeptonInjector as LI
from math import pi
import os

xs_folder = os.path.join( os.path.dirname(__file__), '..' )

n_events    = 1000
diff_xs     = xs_folder + "/test_xs.fits"
total_xs    = xs_folder + "/test_xs_total.fits"
# Ranged Mode, described in  Section II.A
is_ranged   = True
# Particles chosen for NuMu-CC using Table II.1
final_1     = LI.Particle.MuMinus
final_2     = LI.Particle.Hadrons
# Build the Injector object described in Section 2
the_injector = LI.injector( n_events , final_1, final_2, diff_xs,
      total_xs, is_ranged)

deg = pi/180.
minE        = 1000.     # [GeV]
maxE        = 100000.   # [GeV]
gamma       = 2.
minZenith   = 80.*deg
maxZenith   = 180.*deg
minAzimuth  = 0.*deg
maxAzimuth  = 180.*deg

# constructing the Controller object described in Section II
controller  = LI.Controller( the_injector, minE, maxE, gamma,
     minAzimuth, maxAzimuth, minZenith, maxZenith)

# specify the output
controller.Output("./data_output.h5")
controller.LICFile("./config.lic")

# Starts the Process, as illustrated in Figure II.1
controller.Execute()
```

Appendix F. Weighting example

The following `Python` example is included in `LeptonWeighter`. It reads a set of generated events and computes the weights of for a given neutrino cross sections and fluxes. The result is stored in an HDF5 file for later usage.

```
import LeptonWeighter as LW
import h5py as h5
import numpy as np

"""
This calculates the weight of each event in the LeptonInjector
     example script.
"""

# These objects are all defined in Section III.A

# Create generator
#    if there were multiple LIC files, you would instead make a
     list of Generators
net_generation = [LW.MakeGeneratorsFromLICFile("config.lic")]

# This cross section object takes four differential cross
     sections (dS/dEdxdy)
#           Neutrino CC-DIS xs
#       Anti-Neutrino CC-DIS xs
#           Neutrino NC-DIS xs
#       Anti-Neutrino NC-DIS xs
cross_section_location = "/path/to/cross_sections/"
xs = LW.CrossSectionFromSpline(
                    cross_section_location+"/dsdxdy_nu_CC_iso.
     fits",
                    cross_section_location+"/dsdxdy_nubar_CC_iso.
     fits",
                    cross_section_location+"/dsdxdy_nu_NC_iso.
     fits",
                    cross_section_location+"/dsdxdy_nubar_NC_iso.
     fits")

#                       GeV      unitless       GeV
flux_params={ 'constant': 10**-18, 'index':-2, 'scale':10**5 }
liveTime    = 3.1536e7 # [s]


flux = LW.PowerLawFlux( flux_params['constant'] , flux_params['
     index'] , flux_params['scale'] )

# build weighter
weight_event = LW.Weighter( flux, xs, net_generation )

def get_weight( props ):
    """
    This function takes the "properties" object from a LI-Event.
     It then calculates and returns the weight
    """
    LWevent = LW.Event()
    LWevent.energy = props[0]
    LWevent.zenith = props[1]
    LWevent.azimuth = props[2]
```

```
    LWevent.interaction_x = props[3]
    LWevent.interaction_y = props[4]
    LWevent.final_state_particle_0 = LW.ParticleType( props[5] )
    LWevent.final_state_particle_1 = LW.ParticleType( props[6] )
    LWevent.primary_type = LW.ParticleType( props[7] )
    LWevent.radius = props[8]
    LWevent.total_column_depth = props[9]
    LWevent.x = 0
    LWevent.y = 0
    LWevent.z = 0

    weight = weight_event(LWevent)

    # this would alert us that something bad is happening
    if weight==np.nan:
        raise ValueError("Bad Weight!")

    return( weight*liveTime )


data_file = h5.File("data_output.h5")
injector_list = data_file.keys() # Each injector is treated as an
      entry in a dictionary
print("Loaded {} Injectors: {}".format(len(injector_list),
     injector_list))

for injector in data_file.keys():
    print("Evaluating {}".format(injector))
    for event in range(len( data_file[injector]['properties'] )):
        print("     Event {0:06d} Weight: {}".format(event,
     get_weight( data_file[injector]['properties'][event]) ))

data_file.close()
```

References

[1] E. Vitagliano, I. Tamborra, G. Raffelt, Grand unified neutrino spectrum at Earth, arXiv:1910.11878, 2019.
[2] J.A. Formaggio, G.P. Zeller, Rev. Mod. Phys. 84 (2012) 1307–1341, https://doi.org/10.1103/RevModPhys.84.1307, arXiv:1305.7513.
[3] D. Akimov, et al., Science 357 (6356) (2017) 1123–1126, https://doi.org/10.1126/science.aao0990, https://science.sciencemag.org/content/357/6356/1123.full.pdf, https://science.sciencemag.org/content/357/6356/1123.
[4] S.L. Glashow, Phys. Rev. 118 (1960) 316–317, https://doi.org/10.1103/PhysRev.118.316.
[5] D. Seckel, Phys. Rev. Lett. 80 (1998) 900–903, https://doi.org/10.1103/PhysRevLett.80.900, arXiv:hep-ph/9709290.
[6] I. Alikhanov, Phys. Lett. B 741 (2015) 295–300, https://doi.org/10.1016/j.physletb.2014.12.056, arXiv:1402.6678.
[7] B. Zhou, J. Beacom, Phys. Rev. D 101 (02) (2020), https://doi.org/10.1103/PhysRevD.101.036011.
[8] B. Zhou, J.F. Beacom, Phys. Rev. D 101 (3) (2020) 036010, https://doi.org/10.1103/PhysRevD.101.036010, arXiv:1910.10720.
[9] V. Barger, E. Basso, Y. Gao, W.-Y. Keung, Phys. Rev. D 95 (9) (2017) 093002, https://doi.org/10.1103/PhysRevD.95.093002, arXiv:1611.00773.
[10] R. Gandhi, C. Quigg, M.H. Reno, I. Sarcevic, Astropart. Phys. 5 (1996) 81–110, https://doi.org/10.1016/0927-6505(96)00008-4, arXiv:hep-ph/9512364.
[11] Y. Hayato, Nucl. Phys. Proc. Suppl. 112 (2002) 171–176, https://doi.org/10.1016/S0920-5632(02)01759-0.
[12] C. Andreopoulos, et al., Nucl. Instrum. Methods A 614 (2010) 87–104, https://doi.org/10.1016/j.nima.2009.12.009, arXiv:0905.2517.
[13] T. Golan, J.T. Sobczyk, J. Zmuda, Nucl. Phys. Proc. Suppl. 229–232 (2012) 499, https://doi.org/10.1016/j.nuclphysbps.2012.09.136.
[14] O. Lalakulich, K. Gallmeister, U. Mosel, J. Phys. Conf. Ser. 408 (012053) (2013), https://doi.org/10.1088/1742-6596/408/1/012053, arXiv:1110.0674, 2011.
[15] M.G. Aartsen, et al., J. Instrum. 12 (03) (2017) P03012, https://doi.org/10.1088/1748-0221/12/03/P03012, arXiv:1612.05093.
[16] S. Adrian-Martinez, et al., J. Phys. G 43 (8) (2016) 084001, https://doi.org/10.1088/0954-3899/43/8/084001, arXiv:1601.07459.
[17] A.D. Avrorin, et al., EPJ Web Conf. 191 (2018) 01006, https://doi.org/10.1051/epjconf/201819101006, arXiv:1808.10353.
[18] A. Roberts, in: DUMAND - Deep Underwater Muon and Neutrino Detection 1978 Summer Workshop, Session 2: Ultra High Energy Interactions and Astrophysical Neutrino Sources, 1978.
[19] G.C. Hill, Experimental and theoretical aspects of high energy neutrino astrophysics, Ph.D. thesis, Adelaide U., 9, 1996.
[20] A. Gazizov, M.P. Kowalski, Comput. Phys. Commun. 172 (2005) 203–213, https://doi.org/10.1016/j.cpc.2005.03.113, arXiv:astro-ph/0406439.
[21] S. Yoshida, R. Ishibashi, H. Miyamoto, Phys. Rev. D 69 (2004) 103004, https://doi.org/10.1103/PhysRevD.69.103004, arXiv:astro-ph/0312078.
[22] D.J. Bailey, Monte Carlo tools and analysis methods for understanding the ANTARES experiment and predicting its sensitivity to Dark Matter, Ph.D. thesis, Wolfson College, 2002.
[23] T.R. De Young, IceTray: a software framework for IceCube, https://doi.org/10.5170/CERN-2005-002.463, http://cds.cern.ch/record/865626, 2005.
[24] C.A. Argüelles, J. Salvado, C.N. Weaver, Comput. Phys. Commun. 255 (2020) 107405, https://doi.org/10.1016/j.cpc.2020.107405.
[25] C.A. Argüelles, J. Salvado, C.N. Weaver nuSQuIDS, https://github.com/Arguelles/nuSQuIDS, 2015.
[26] E. Zas, in: PoS ICRC2017, 2018, p. 972.
[27] A.C. Vincent, C.A. Argüelles, A. Kheirandish, J. Cosmol. Astropart. Phys. 1711 (11) (2017) 012, https://doi.org/10.1088/1475-7516/2017/11/012, arXiv:1706.09895.
[28] I. Safa, A. Pizzuto, C.A. Argüelles, F. Halzen, R. Hussain, A. Kheirandish, J. Vandenbroucke, J. Cosmol. Astropart. Phys. 2001 (01) (2020) 012, https://doi.org/10.1088/1475-7516/2020/01/012, arXiv:1909.10487.
[29] A. Garcia, R. Gauld, A. Heijboer, J. Rojo, J. Cosmol. Astropart. Phys. 2020 (09) (2020) 025, https://doi.org/10.1088/1475-7516/2020/09/025.
[30] IceCube, LeptonInjector code, https://github.com/icecube/LeptonInjector, 2020.
[31] IceCube, LeptonWeighter code, https://github.com/icecube/LeptonWeighter, 2020.
[32] M.G. Aartsen, et al., Phys. Rev. D 98 (6) (2018) 062003, https://doi.org/10.1103/PhysRevD.98.062003, arXiv:1807.01820.
[33] S. Yoshida, M. Meier, ShigeruYoshida/JULIeT: first official release with a DOI, https://doi.org/10.5281/zenodo.4018117, Sep. 2020.
[34] N. Whitehorn, J. van Santen, S. Lafebre, Comput. Phys. Commun. 184 (9) (2013) 2214–2220, https://doi.org/10.1016/j.cpc.2013.04.008, http://www.sciencedirect.com/science/article/pii/S0010465513001434.
[35] J. Koehne, K. Frantzen, M. Schmitz, T. Fuchs, W. Rhode, D. Chirkin, J. Becker, Comput. Phys. Commun. 184 (2013) 2070–2090, https://doi.org/10.1016/j.cpc.2013.04.001.
[36] D. Chirkin, W. Rhode, Muon Monte Carlo: a high-precision tool for muon propagation through matter, arXiv:hep-ph/0407075, 7, 2004.
[37] V. Niess, V. Bertin, Astropart. Phys. 26 (4–5) (2006) 243–256, https://doi.org/10.1016/j.astropartphys.2006.06.005.
[38] C.H.V. Wiebusch, The Detection of Faint Light in Deep Underwater Neutrino Telescopes, Chapter 7, Ph.D. thesis, Physikalishe Institute RWTH Aachen, 12, 1995.
[39] L. Rädel, C. Wiebusch, Astropart. Phys. 38 (2012) 53–67, https://doi.org/10.1016/j.astropartphys.2012.09.008, arXiv:1206.5530.
[40] L. Rädel, C. Wiebusch, Astropart. Phys. 44 (2013) 102–113, https://doi.org/10.1016/j.astropartphys.2013.01.015, arXiv:1210.5140.
[41] D. Chirkin, J.C. Díaz-Vélez, C. Kopper, A. Olivas, B. Riedel, M. Rongen, D. Schultz, J. van Santen, in: 2019 15th International Conference on eScience, eScience, 2019, pp. 388–393.
[42] C. Kopper, CLSim, https://github.com/claudiok/clsim, 2019.
[43] D. Chirkin, in: GPU Computing in High-Energy Physics, 2015, pp. 217–220.
[44] D. Chirkin, PPC standalone code, https://icecube.wisc.edu/~dima/work/WISC/ppc/, 2020.
[45] W. Hastings, Biometrika 57 (1970) 97–109, https://doi.org/10.1093/biomet/57.1.97, https://inspirehep.net/literature/1114360.
[46] D. Chirkin, W. Rhode, Propagating leptons through matter with muon Monte Carlo (mmc), arXiv:hep-ph/0407075, 2004.
[47] A.M. Dziewonski, D.L. Anderson, Phys. Earth Planet. Inter. 25 (4) (1981) 297–356, https://doi.org/10.1016/0031-9201(81)90046-7, http://www.sciencedirect.com/science/article/pii/0031920181900467.
[48] A. Cooper-Sarkar, P. Mertsch, S. Sarkar, J. High Energy Phys. 08 (2011) 042, https://doi.org/10.1007/JHEP08(2011)042, arXiv:1106.3723.
[49] M.G. Aartsen, et al., Phys. Rev. D 99 (2019) 032004, https://doi.org/10.1103/PhysRevD.99.032004, https://link.aps.org/doi/10.1103/PhysRevD.99.032004.
[50] G.A. Binder, Measurements of the Flavor Composition and Inelasticity Distribution of High-Energy Neutrino Interactions in IceCube, Ph.D. thesis, UC, Berkeley, 2017.
[51] J.S. Gainer, J. Lykken, K.T. Matchev, S. Mrenna, M. Park, J. High Energy Phys. 10 (2014) 078, https://doi.org/10.1007/JHEP10(2014)078, arXiv:1404.7129.
[52] P.S. Bhupal Dev, et al., SciPost Phys. Proc. 2 (2019) 001, https://doi.org/10.21468/SciPostPhysProc.2.001, arXiv:1907.00991.
[53] V. Bertone, R. Gauld, J. Rojo, J. High Energy Phys. 01 (2019) 217, https://doi.org/10.1007/JHEP01(2019)217, arXiv:1808.02034.
[54] R. Gauld, Phys. Rev. D 100 (9) (2019) 091301, https://doi.org/10.1103/PhysRevD.100.091301, arXiv:1905.03792.
[55] B. Abi, et al., J. Instrum. 15 (08) (2020) T08010, https://doi.org/10.1088/1748-0221/15/08/T08010, arXiv:2002.03010.
[56] W. Altmannshofer, S. Gori, M. Pospelov, I. Yavin, Phys. Rev. Lett. 113 (2014) 091801, https://doi.org/10.1103/PhysRevLett.113.091801, arXiv:1406.2332.
[57] S.-F. Ge, M. Lindner, W. Rodejohann, Phys. Lett. B 772 (2017) 164–168, https://doi.org/10.1016/j.physletb.2017.06.020, arXiv:1702.02617.

[58] P. Ballett, M. Hostert, S. Pascoli, Y.F. Perez-Gonzalez, Z. Tabrizi, R. Zukanovich Funchal, J. High Energy Phys. 01 (2019) 119, https://doi.org/10.1007/JHEP01(2019)119, arXiv:1807.10973.
[59] W. Altmannshofer, S. Gori, J. Martín-Albo, A. Sousa, M. Wallbank, Phys. Rev. D 100 (11) (2019) 115029, https://doi.org/10.1103/PhysRevD.100.115029, arXiv:1902.06765.
[60] P. Coloma, P.A.N. Machado, I. Martinez-Soler, I.M. Shoemaker, Phys. Rev. Lett. 119 (2017) 201804, https://doi.org/10.1103/PhysRevLett.119.201804, https://link.aps.org/doi/10.1103/PhysRevLett.119.201804.
[61] G. Magill, R. Plestid, M. Pospelov, Y.-D. Tsai, Phys. Rev. D 98 (11) (2018) 115015, https://doi.org/10.1103/PhysRevD.98.115015, arXiv:1803.03262.
[62] J.M. Cline, M. Puel, T. Toma, J. High Energy Phys. 05 (2020) 039, https://doi.org/10.1007/JHEP05(2020)039, arXiv:2001.11505.
[63] E. Bertuzzo, S. Jana, P.A.N. Machado, R. Zukanovich Funchal, Phys. Rev. Lett. 121 (24) (2018) 241801, https://doi.org/10.1103/PhysRevLett.121.241801, arXiv:1807.09877.
[64] M. Blennow, E. Fernandez-Martinez, A. Olivares-Del Campo, S. Pascoli, S. Rosauro-Alcaraz, A. Titov, Eur. Phys. J. C 79 (7) (2019) 555, https://doi.org/10.1140/epjc/s10052-019-7060-5, arXiv:1903.00006.
[65] P. Ballett, M. Hostert, S. Pascoli, Phys. Rev. D 99 (9) (2019) 091701, https://doi.org/10.1103/PhysRevD.99.091701, arXiv:1903.07590.
[66] P. Coloma, Eur. Phys. J. C 79 (9) (2019) 748, https://doi.org/10.1140/epjc/s10052-019-7256-8, arXiv:1906.02106.
[67] A. Abdullahi, M. Hostert, S. Pascoli, A dark seesaw solution to low energy anomalies: MiniBooNE, the muon $(g-2)$, and BaBar, arXiv:2007.11813, 7, 2020.
[68] John F. Cherry, Alexander Friedland, Ian M. Shoemaker, Short-baseline neutrino oscillations, Planck, and IceCube, arXiv:1605.06506, 5, 2016.
[69] P. Bakhti, Y. Farzan, M. Rajaee, Phys. Rev. D 99 (5) (2019) 055019, https://doi.org/10.1103/PhysRevD.99.055019, arXiv:1810.04441.
[70] P. Ballett, M. Hostert, S. Pascoli, Y.F. Perez-Gonzalez, Z. Tabrizi, R. Zukanovich Funchal, Phys. Rev. D 100 (5) (2019) 055012, https://doi.org/10.1103/PhysRevD.100.055012, arXiv:1902.08579.
[71] M. Tanabashi, et al., Phys. Rev. D 98 (2018) 030001, https://doi.org/10.1103/PhysRevD.98.030001, https://link.aps.org/doi/10.1103/PhysRevD.98.030001.

Chapter 6

Sources of Systematic Uncertainties

In this Chapter the sources of systematic uncertainty and strategies for marginalizing their effects in this analysis are discussed. In Section 6.1, we discuss two methods used to this end: SnowStorm and systematic downsizing. SnowStorm is used for extracting the analysis-level effects of highly correlated sources of systematic uncertainty, and systematic downsizing is used for marginalizing these correlated parameters in an uncorrelated basis as well as only manipulating the strongest of those uncorrelated nuisance parameters. Then, in Section 6.2, the implementation schema are discussed alongside the expected shape-effects of these nuisance parameters in analysis space. Two different models were implemented and investigated to describe uncertainties on the conventional neutrino flux; they are described in Subsections 6.2.4 and 6.2.5.

6.1 Methods

6.1.1 Snowstorm

While some sources of systematic uncertainty can be easily addressed through re-weighting, such as uncertainties on cosmic ray fluxes, others can have non-trivial effects on the reconstruction of events. These 'low-level' sources of systematic uncertainty typically, and historically, required a dedicated MC sample where the parameter was perturbed by some fixed, discrete, amount. This method becomes intractable when multiple, highly correlated, sources of systematic uncertainty are present, such as in the case of the dust concentration as a function of depth in IceCube, which is discussed in Reference [75]. The dust, or any optical impurities, influence the scattering and absorption length of light in ice and can therefore have complicated effects on reconstructed energy

and direction of events. To address these particularly complex source of systematic uncertainty, a new method for efficiently determining the effects of these parameters was developed for IceCube analyses: SnowStorm[1]. Several Snowstorm implementations are used in this analysis, and although it is discussed at length elsewhere [76], it is briefly introduced and discussed in the section that follows.

Snowstorm relies on two underlying assumptions, both of which are generally necessary for most of the commonly used methods of systematic uncertainty estimation.

1. the effects of systematic uncertainty are sufficiently small such as to be treated perturbatively.

2. the Monte Carlo statistical uncertainty is small compared to the data.

Consider some set of parameters $\vec{\eta}$, called "nuisance parameters," which are imperfectly known and yet contribute to the predicted final event rates. We wish to, given some choice of $\vec{\eta}$, calculate a predicted event rate $\psi_{\vec{\rho},\vec{\eta}}(E_\alpha)$, where the nominal prediction is denoted $\psi_{\vec{\rho},\vec{0}}(E_\alpha)$.

Traditional approaches would require generating several, discrete, Monte Carlo sets: each of which being generated for some perturbed value of each of the nuisance parameters. For correlated sets of nuisance parameters, additional Monte Carlo sets would be required for each of the possible pairings of nuisance parameters: this quickly becomes cumbersome. A SnowStorm Monte Carlo ensemble instead consists of a single sample where each constituent event (or grouping of events) draw(s) a unique set of nuisance parameters $\vec{\eta}$ from prior constraints. A graphical representation of a SnowStorm ensemble's distinction from classical MC methods is shown in Figure 6.1.1, left. By careful manipulation of this SnowStorm ensemble it can then be possible to extract the effects of these variations on analysis-space.

We first require that the prior function describing the nuisance parameters $\vec{\eta}$ is normalized and symmetric for each η_i, such that

$$P(\eta_i, \vec{\eta}_{j\neq i}) = P(-\eta_i, \vec{\eta}_{j\neq i}) \qquad \forall i \tag{6.1.1}$$

$$\int d^N \eta P(\vec{\eta}) = 1 \tag{6.1.2}$$

[1]The name SnowStorm reflects the idea that each event in the sample is distinct, like each snowflake in a snowstorm.

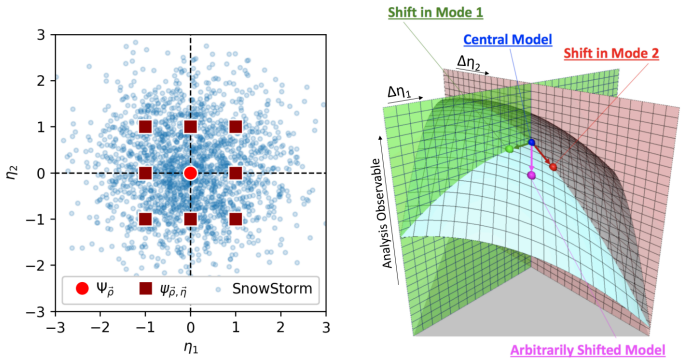

FIGURE 6.1.1: On the left: an illustration of the difference between the classical systematic uncertainty implementation of discrete Monte Carlo samples (red squares) and the single SnowStorm ensemble (blue dots). On the right: an illustration of the cutting (vertical planes) methods used for gradient extraction (green and red arrows), and the combination of those gradients to create an arbitrarily shifted model (purple arrow).

We explicitly choose a prior function for the nuisance parameters that is a product of equal-width Gaussian functions:

$$P(\vec{\eta}) = \prod_i \frac{1}{\sigma\sqrt{2\pi}} e^{-\eta_i^2/2\sigma^2}. \tag{6.1.3}$$

The effects of these nuisance parameters on analysis space can be calculated, in principle, if we know the gradients about the central distribution:

$$\psi_{\vec{\rho},\vec{\eta}} = \psi_{\vec{\rho},\vec{0}}(E_\alpha) + \vec{\eta}\cdot\vec{\nabla}_\eta \left[\psi_{\vec{\rho},\vec{\eta}}(E_\alpha)\right]_{\vec{\eta}=0} + \mathcal{O}(\eta^2). \tag{6.1.4}$$

Since we have assumed that the effects are sufficiently small, we can neglect the higher-order terms. This can be verified by considering the integrated prediction of the SnowStorm sample:

$$\psi_{\vec{\rho}}^{SnowStorm} = \int d\vec{\eta} P(\vec{\eta}) \left[\psi_{\vec{\rho},\vec{0}} + \vec{\eta}\cdot\vec{\nabla}_\eta \left[\psi_{\vec{\rho},\vec{\eta}}\right]_{\vec{\eta}=0} + \mathcal{O}(\eta^2)\right] \tag{6.1.5}$$

$$= \psi_{\vec{\rho},\vec{0}} + \int d\vec{\eta} P(\eta)\mathcal{O}(\eta^2) \tag{6.1.6}$$

If the non-linear term here is smaller than the available statistical uncertainty, then this test passes, and so Equation (6.1.4) reduces to

$$\psi_{\vec{\rho},\vec{\eta}} = \psi_{\vec{\rho},\vec{0}} + \vec{\eta}\cdot\vec{G}_{\vec{\rho}} \qquad \vec{G}_{\vec{\rho}} \equiv \vec{\nabla}_\eta \left[\psi_{\vec{\rho},\vec{\eta}}\right]_{\vec{\eta}=\vec{0}} \tag{6.1.7}$$

From the single SnowStorm ensemble, the method used for gradient extraction involves the subdivision of the full ensemble by cutting it along different directions. For example, to extract the η_i gradient, we divide it along the $\eta_i = 0$ plane into sub-samples $\psi^{i+}_{\vec{\rho}}$ and $\psi^{i-}_{\vec{\rho}}$, which each encode the predictions:

$$\psi^{i+}_{\vec{\rho}} = \int_0^\infty d\eta_i \int_{-\infty}^\infty d^{N-1}\eta P(\vec{\eta}) \left[\psi_{\vec{\rho},\vec{0}} + \vec{\eta}\cdot\vec{G}_{\vec{\rho}}\right] \tag{6.1.8}$$

$$\psi^{i-}_{\vec{\rho}} = \int_{-\infty}^0 d\eta_i \int_{-\infty}^\infty d^{N-1}\eta P(\vec{\eta}) \left[\psi_{\vec{\rho},\vec{0}} + \vec{\eta}\cdot\vec{G}_{\vec{\rho}}\right] \tag{6.1.9}$$

By symmetry, the integrals along directions other than i give no contribution. The integration then yields

$$\psi^{i\pm}_{\vec{\rho}} = \frac{1}{2}\psi_{\vec{\rho},\vec{0}} \pm \frac{\sigma}{\sqrt{2\pi}} G_{\vec{\rho},i}, \tag{6.1.10}$$

from which we can extract the gradient in that direction

$$G_{\vec{\rho},i} = \frac{1}{\sigma}\sqrt{\frac{\pi}{2}}\left(\psi^{i+}_{\vec{\rho}} - \psi^{i-}_{\vec{\rho}}\right). \tag{6.1.11}$$

By then cutting the ensemble along each direction sequentially, the full gradient vector can be extracted completely.

Two Monte Carlo samples were generated to evaluate the effects of various sources of systematic uncertainty on analysis space. In one, a sample was generated while allowing the amplitudes and phases, for a Fourier series describing the depth-dependence of the absorption length and scattering length, to vary according to the priors shown in Figure 6.1.2. A full description of this and the process of extracting these widths from calibration is described in detail in Subsection 6.2.2.

In the other sample the DOM efficiency (Section 6.2.1), both unified hole ice parameters (Section 6.2.3), a parameter effecting ice anisotropy, and two parameters effecting bulk absorption and scattering lengths were allowed to vary. The anisotropy, bulk absorption, and bulk scattering gradients were not used in this analysis. The priors used for this SnowStorm set are shown in Table 6.1.1.

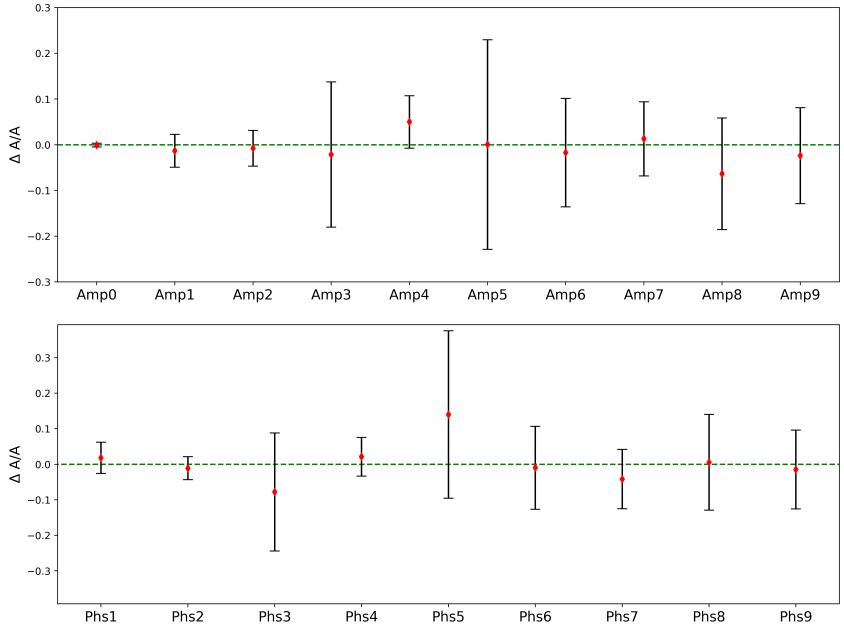

FIGURE 6.1.2: The widths of the phases and amplitudes, as determined from calibration data, for a Fourier series describing the depth-dependence of absorption length and scattering length in ice at IceCube.

Systematic	Sampling Distribution	Range	Comments
Scattering	uniform	[0.9,1.1]	bulk effect, not used
Absorption	uniform	[0.9,1.1]	bulk effect, not used
Anisotropy Scale	uniform	[0,2]	equal to 0-15%, not used
DOM Efficiency	uniform	[0.9, 1.1]	
Unified HoleIce	uniform	p0 ∈ [-0.84, 0.3] p1 ∈ [-0.134, 0.05]	

TABLE 6.1.1: A table listing all SnowStorm systematic perturbations and their ranges used in the nuisance parameter MC set.

6.1.2 Systematic Downsizing

In this analysis, several sets of nuisance parameters are correlated to various degrees: the astrophysical flux, the cosmic ray flux and hadronic model[2], and the absorption and scattering lengths as functions of depth in IceCube. PISA [77], the fitting framework used for this analysis, is incompatible with correlated priors due to details of its construction. To account for this, a new method for (1) fitting these correlated priors in an uncorrelated way and (2) representing the effects with fewer parameters was developed and adopted.

Consider a set of n nuisance parameters $\vec{x}$ with means $\vec{\mu}$. A positive-definite, $n \times n$, matrix Σ defines the covariance between the nuisance parameters. If we assume the distribution is jointly normally distributed, then the probability density function defining the probability of a set of nuisance parameters $\vec{y}$ being the "true" values is given by

$$P(\vec{y}) = \frac{1}{(2\pi)^{n/2}\,|\Sigma|^{1/2}} \exp\left[-\tfrac{1}{2}(\vec{y}-\vec{\mu})^T \Sigma^{-1}\,(\vec{y}-\vec{\mu})\right] \tag{6.1.12}$$

where $|\Sigma|$ is the determinant of the covariance matrix Σ. We then consider the simple coordinate transformation $\vec{p} \equiv \vec{y} - \vec{\mu}$. For consistency with goodness of fits tests and usefulness in minimization applications, we also focus on the log of this likelihood distribution.

$$\mathcal{L} \equiv \log P = -\tfrac{1}{2}\vec{p}^T \Sigma^{-1} \vec{p} + C \tag{6.1.13}$$

We diagonalize this matrix by considering a transformation $U \in SO(N)$ satisfying $A = U\Sigma^{-1}U^T$, where A is a diagonal matrix with $1/\lambda_i$'s on the diagonal.

$$\mathcal{L} \equiv \log P = -\tfrac{1}{2}\vec{p}^T U^T U \Sigma^{-1} U^T U \vec{p} \tag{6.1.14}$$

or where the primed coordinates are the transformed coordinates,

$$\mathcal{L} \equiv \log P = -\tfrac{1}{2}(\vec{p}')^T A \vec{p}'. \tag{6.1.15}$$

Thus, we can always rotate a correlated nuisance parameter basis to one where the priors on the

[2] This depends on whether or not I got to use DaemonFlux...

parameters are uncorrelated. To solve for the transformation, all we have to do is move some terms around starting from the construction of A and U,

$$A = U\Sigma^{-1}U^T \tag{6.1.16}$$

$$A^{-1} = U^T\Sigma U \tag{6.1.17}$$

$$\Sigma U = U \begin{bmatrix} \lambda_1 & 0 & \dots & 0 \\ 0 & \lambda_2 & \dots & 0 \\ \vdots & \vdots & \ddots & \vdots \\ 0 & 0 & \dots & \lambda_n \end{bmatrix}. \tag{6.1.18}$$

By re-writing the transformation matrix U as a vector of its column vectors η_i, $U = \begin{bmatrix} \eta_1 & \dots & \eta_n \end{bmatrix}$, then the equation can be expressed simply as

$$\Sigma\eta_i = \lambda_i\eta_i. \tag{6.1.19}$$

The column vectors of the transformation matrix are the right eigenvectors of the covariance matrix, and each of the corresponding eigenvalues of the covariance matrix are the diagonals of the new matrix A, and are the squares of the widths of the distribution along the axes in the uncorrelated basis. We lay out a procedure then for any given covariance matrix:

1. Solve for its eigenvalues and eigenvectors; the values each represent a normal prior width for new, uncorrelated, parameters in the new basis

2. The block-matrix of the eigenvectors is the transformation matrix allowing for transforming from the correlated basis to the uncorrelated basis.

3. Fits are performed in the uncorrelated basis - to evaluate effects of systematic uncertainty we transform whatever point is in question back to the correlated basis and evaluate the effects using the original parametrization.

The parameters, in the uncorrelated basis, with the strongest effects can then be identified. Parameters whose effects are sufficiently small[3] can then be fixed in fits.

[3] how small is sufficiently small is analysis-dependent

6.2 Analysis Applications

Two tables listing all fit systematic uncertainties, their central values, their prior widths, the event morphologies they apply to, and other notes about their implementation are included. Table 6.2.1 shows nuisance parameters when the Hillas-Gaisser H3a model is used as the central model and CR uncertainty model; Table 6.2.2 shows the same but when using the DaemonFlux nominal flux and CR systematic uncertainty model. The former uses a normalization uncertainty that applies only to the conventional flux while the latter uses a normalization uncertainty applying to the entire predicted neutrino flux.

6.2.1 DOM Efficiency

Cascades To evaluate the effects of varying the DOM efficiency on reconstructed event rates, a Monte Carlo sample was generated following the Snowstorm method for low-level systematic uncertainties.

For each batch of ten simulated MC events the DOM efficiency is sampled from its prior. The wavelength acceptance of the DOMS in CLSim is then adjusted according to the new DOM model, and the photon propagation is carried out. The remainder of the MC simulation chain is then performed. The final-level MC is then weighted, one at a time, to the conventional, prompt, and astrophysical neutrino fluxes.

In order to calculate the effects of perturbing the DOM efficiency on the reconstrucion level quantities, we bin events in terms of $\log_{E_\nu^{reco}}$, $\cos\theta_\nu^{reco}$, and the events' sampled DOM efficiencies. We then account for the sampling bias in each DOM efficiency bin by integrating the prior PDF over each DOM efficiency bin and scaling up the weights of events in those bins by one over the cumulative probability of sampling that given bin. The sum of the weights in each bin therefore would be a function only of (1) the central expectation in that bin and (2) the bias generated by using a perturbed DOM efficiency. For each ($\log E_\nu^{reco}$, $\cos\theta_\nu^{reco}$) slice, each DOM efficiency bin is then rescaled around the central bin's value; this yields a quantity in each bin that represents the proportional effect of perturbing the DOM efficiency.

Then, a spline fit is carried out over the full 3D binned space using Photospline [78]. Events can then be reweighted to a new DOM efficiency by evaluating the spline $\mathcal{S}$ at the event's reconstructed

Parameter	Center	Prior	Boundary	Morphology
Conventional Flux				
Atm. Density	0.0	0.0±1.0	[-4, 4]	Both
Barr WM	0.0	0.0 ± 1.0	[-4, 4]	Both
Barr WP	0.0	0.0 ± 1.0	[-4, 4]	Both
Barr YM	0.0	0.0 ± 1.0	[-4, 4]	Both
Barr YP	0.0	0.0 ± 1.0	[-4, 4]	Both
Barr ZM	0.0	0.0 ± 1.0	[-4, 4]	Both
Barr ZP	0.0	0.0 ± 1.0	[-4, 4]	Both
Spectral Shift $\Delta\gamma$	0.0	0.0 ± 0.25	[-4, 4]	Both
Normalization Φ_{conv}	1.0	1.0 ± 0.4	[0, 4]	Both
Astrophysical Flux				
astro_rotated_0†	0.0	0.0 ± 0.42	[-2.1, 2.1]	Both
astro_rotated_1†	0.0	0.0 ± 0.20	[-0.95, 0.95]	Both
Cross Sections				
Cross section σ_{ν}	1.0	1.0 ± 0.03	[0.5, 1.5]	Both
Cross section $\sigma_{\bar{\nu}}$	1.0	1.0 ± 0.075	[0.5, 1.5]	Both
Kaon energy loss σ_{KA}	0.0	0.0 ± 1.0	[-4.0, 4.0]	Both
Detector				
hole_ice_scale	-1.0	-1 ± 10	[-4, 1]	Tracks
holeice p_0	0.0	0 ± 1.0	[-4, 4]	Cascades
holeice p_1	0.0	0 ± 1.0	[-4, 4]	Cascades
ice_0‡	0.0	0 ± 1.0	[-4, 4]	Cascades
ice_1‡	0.0	0 ± 1.0	[-4, 4]	Cascades
ice_3‡	0.0	0 ± 1.0	[-4, 4]	Cascades
ice_5‡	0.0	0 ± 1.0	[-4, 4]	Cascades
ice_6‡	0.0	0 ± 1.0	[-4, 4]	Cascades
ice_grad_0_rotated*	0.0	0 ± 1.0	[-4, 4]	Tracks
ice_grad_1_rotated*	0.0	0 ± 1.0	[-4, 4]	Tracks
DOM Efficiency	1.0	1.00 ± 0.123	[0.972, 1.058]	Both
Muons				
Normalization Φ_{muon}	1.0	1.0 ± 0.2	[0, 2]	Cascades

TABLE 6.2.1: The central values, priors, and boundaries for all nuisance parameters. The ice gradients and astrophysical parameters are all listed here in the uncorrelated basis and in terms of the 1σ priors calculated from a PCA of their covariance matrices; these parameters are linear combinations of correlated parameters and are marked with $*$, †, or ‡.

Parameter	Center	Prior	Boundary	Morphology
Conventional Flux				
Atm. Density	0.0	0.0±1.0	[-4, 4]	Both
Daemon 0**	0.0	0.0 ± 1.0	[-4, 4]	Both
Daemon 1**	0.0	0.0 ± 1.0	[-4, 4]	Both
Daemon 9**	0.0	0.0 ± 1.0	[-4, 4]	Both
Daemon 12**	0.0	0.0 ± 1.0	[-4, 4]	Both
Daemon 18**	0.0	0.0 ± 1.0	[-4, 4]	Both
Daemon 19**	0.0	0.0 ± 1.0	[-4, 4]	Both
Daemon 20**	0.0	0.0 ± 1.0	[-4, 4]	Both
Daemon 23**	0.0	0.0 ± 1.0	[-4, 4]	Both
Astrophysical Flux				
astro_rotated_0†	0.0	0.0 ± 0.42	[-2.1, 2.1]	Both
astro_rotated_1†	0.0	0.0 ± 0.20	[-0.95, 0.95]	Both
astro_flavor	0.0	0.0 ± 1.0	[-1.3, 1.25]	Both
Cross Sections				
Cross section σ_ν	1.0	1.0 ± 0.03	[0.5, 1.5]	Both
Cross section $\sigma_{\bar{\nu}}$	1.0	1.0 ± 0.075	[0.5, 1.5]	Both
Kaon energy loss σ_{KA}	0.0	0.0 ± 1.0	[-4.0, 4.0]	Both
Detector				
hole_ice_scale	-1.0	-1 ± 10	[-4, 1]	Tracks
holeice p_0	0.0	0 ± 1.0	[-4, 4]	Cascades
holeice p_1	0.0	0 ± 1.0	[-4, 4]	Cascades
ice_0‡	0.0	0 ± 1.0	[-4, 4]	Cascades
ice_1‡	0.0	0 ± 1.0	[-4, 4]	Cascades
ice_3‡	0.0	0 ± 1.0	[-4, 4]	Cascades
ice_5‡	0.0	0 ± 1.0	[-4, 4]	Cascades
ice_6‡	0.0	0 ± 1.0	[-4, 4]	Cascades
ice_grad_0_rotated*	0.0	0 ± 1.0	[-4, 4]	Tracks
ice_grad_1_rotated*	0.0	0 ± 1.0	[-4, 4]	Tracks
DOM Efficiency	1.0	1.00 ± 0.123	[0.972, 1.058]	Both
Muons				
Normalization Φ_{muon}	1.0	1.0 ± 0.2	[0, 2]	Cascades
Normalization				
Normalization Φ_ν	1.0	1.0 ± 0.2	[0, 2]	Both

TABLE 6.2.2: The central values, priors, and boundaries for all nuisance parameters. The ice gradients and astrophysical parameters are all listed here in the uncorrelated basis and in terms of the 1σ priors calculated from a PCA of their covariance matrices; these parameters are linear combinations of correlated parameters and are marked with $*$,**, †, or ‡.

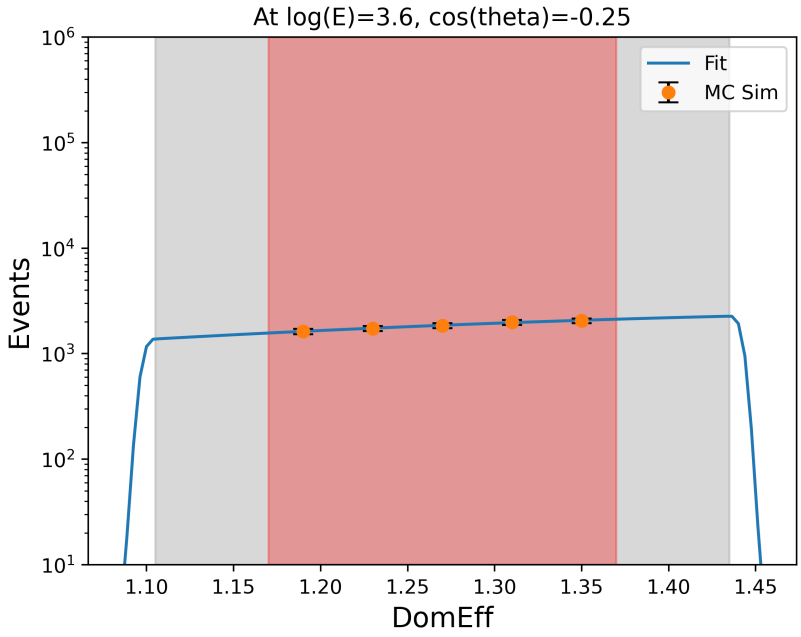

FIGURE 6.2.1: The predicted number of events in reconstructed space for a bin centered at $\log E_\nu^{reco} = 3.6$ and $\cos\theta_\nu^{reco} = 0.25$ as a function of the DOM efficiency. The MC data are represented by orange dots, and the spline fit is the trend in blue. The gray shaded region represent the extents of the spline, and the red bands represents prior-allowed region.

energy and zenith, and the new DOM efficiency $\mathcal{D}_{OM}$; this is shown in Equation EQ.

$$w' = w + w \times \mathcal{S}(\log E_\nu^{reco}, \cos\theta_\nu^{reco}, \mathcal{D}_{OM}) \tag{6.2.1}$$

A slice of the full 3D fit for the conventional neutrino fluxes is shown in Figure 6.2.1, and the effects on overall reconstructed even rates are shown for cascades on the right of Figure 6.2.2.

Tracks For the track sample, discrete Monte Carlo samples were generated for DOM efficiencies of 1.23, 1.25, 1.27, 1.30, and 1.33. For each DOM Efficiency, a 2D spline was done to the expected number of events in the sample at the central expectation. Each of these splines was then stacked into a 3D spline, which allows for the continuous sampling of the event rate as a function of zenith, energy, and DOM efficiency. The effects on overall reconstructed even rates are shown for tracks on the left of Figure 6.2.2.

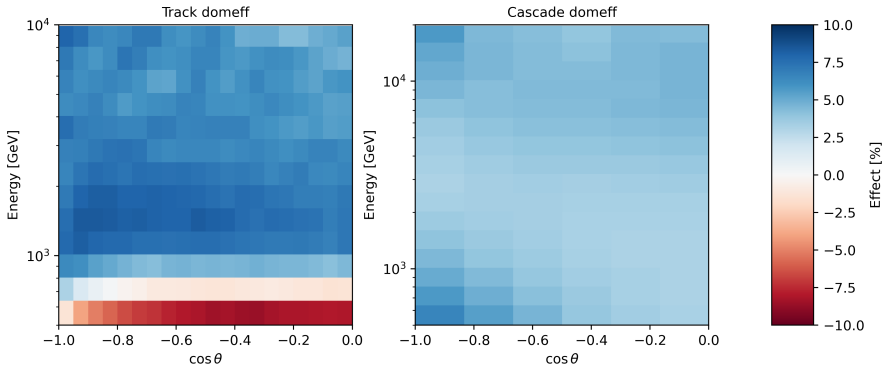

FIGURE 6.2.2: The effects of perturbing the DOM efficiency on expected numbers of tracks (left) and cascades (right). The shape effect is not shown here to demonstrate how the DOM efficiency in cascades is mostly a normalization effect

6.2.2 Bulk Ice

The bulk ice in the ice is characterised by uncertainties in the absorption and scattering length. Initially, every ten meter section of the ice was assigned an absorption length and a scattering length with some uncertainty. Over the 1500 meter span of IceCube, this would require 300 separate nuisance parameters to account for these parameters fully.

This is an overwhelming and intractable quantity. For this and similar analyses, a Fourier decomposition of the depth (x) dependence of the absorption and scattering is used instead, as described in Ref [76]:

$$\frac{1}{2}\log\left(\text{Abs}\times\text{Sca}\right) = \frac{A_0}{2} + \sum_{n=1}^{N} A_n \sin\left(\frac{2\pi n x}{L} + \phi_n\right) \tag{6.2.2}$$

where A_n and ϕ_n are amplitudes and phases for the n'th term in the series expansion, L is the vertical extent of IceCube, and Abs and Sca are the in-ice absorption and scattering lengths.

To calibrate these amplitudes and phases and to determine the covariance between them, we use the IceCube in-situ flasher data [75]. These use the 12 on-board LEDs mounted in the housings of each DOM. The LEDs on all DOMs of string 63 are flashed, and then the measured light throughout IceCube, minus string 63, is logged. Then, PPC simulations were carried out for various, perturbed, ice models were performed. PPC simulations were performed by perturbing the amplitudes and phases for the first five modes in the Fourier series expansion of the depth dependence of absorption and scattering in the bulk ice. PPC simulations were also performed by

perturbing various combinations of these modes. These PPC simulations were used, in conjunction with the measured flasher data, to quantify the likelihood of the observed data assuming different ice models,

For each amplitude and phase, these likelihoods were calculated for icemodels where the first five Fourier amplitudes and the first five Fourier phases were shifted. These values were shifted large amounts first, from which an approximate minimum and width was determined. Then, more granular PPC simulations were carried out by varying these amplitudes and phases about the approximate centers. Off-axis simulations were also carried out by shifting every possible combination of nuisance parameters, either both positively or both negatively, by varying amounts.

For each amplitude and phase a quadratic fit was then done to the log likelihood distributions,

$$\mathcal{L}(\eta_i) = A_i\eta_i^2 + B_i\eta_i + C_i \tag{6.2.3}$$

where η_i is for any one amplitude or phase. These fits are shown in Figure 6.2.3 after being normalized by the minimum likelihood found in each fit, and were carried out to verify that these nuisance parameters are normally distributed about the minima. The widths of each of these distributions are shown in Figure 6.1.2. A similar scan was then done for combinations of nuisance parameters by shifting each possible pairing of them by amounts proportional to the widths of the nuisance parameters.

For a normally-distributed, correlated, set of nuisance parameters $\vec{\eta}$, the prior penalty of the likelihood function is equal to

$$\mathcal{L} = \vec{\eta}^T\Sigma^{-1}\vec{\eta} + C \tag{6.2.4}$$

where C is a constant prefactor to normalize the distribution and Σ is the covariance matrix. The inverse of the covariance matrix, Σ^{-1} is also known as the Hessian matrix; in determining the covariance it is easiest to first directly fit to the Hessian, and then to invert the Hessian to get the covariance matrix. In order for the prior penalty function to normalizable, both the covariance matrix and the hessian must be real-valued and positive semi-definite: all eigenvalues and its determinant must be greater than or equal to zero. A consequence of this, and the use of a Cholesky decomposition, is that the Hessian can be written as the matrix product of a

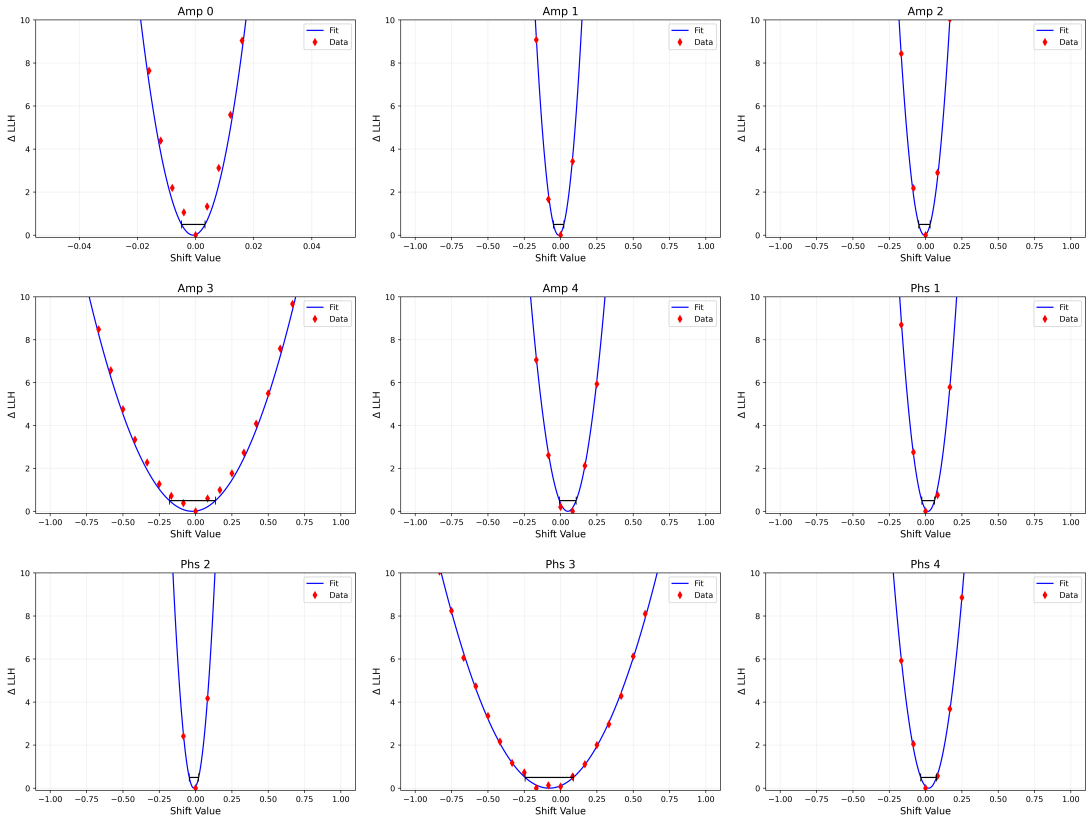

FIGURE 6.2.3: The first five amplitude fits and the first four phase fits for the plus-mode Fourier series decomposition. 'Shift Value' corresponds to the difference of the best fit value from the PPC simulations to the previous best-fit value for the parameter. The black line at 0.5 ΔLLH represents the 1σ uncertainty band.

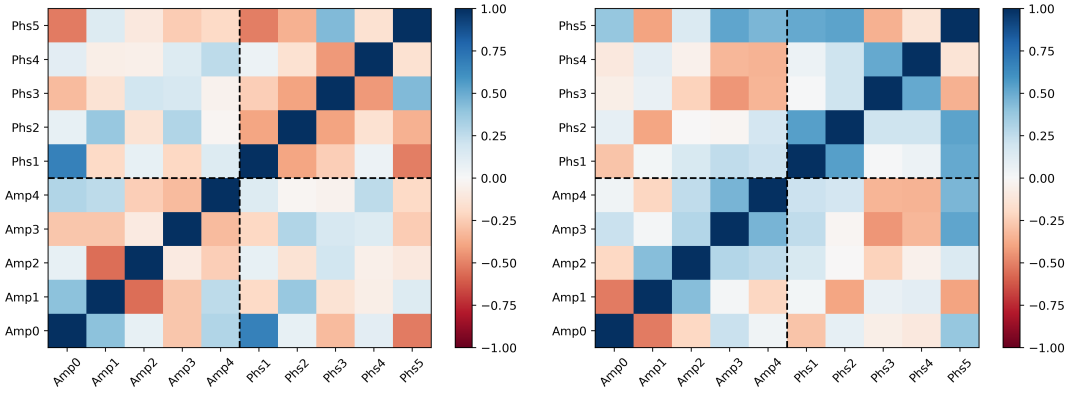

FIGURE 6.2.4: The fit hessian matrix (left) in nuisance parameter space for the first five amplitudes and first four phases, and the correlation matrix (right) determined by inverting the hessian.

lower-diagonal matrix and its transpose:

$$\Sigma^{-1} = H = LL^T, \tag{6.2.5}$$

where L is some lower-diagonal matrix. We can therefore parametrize any Hessian matrix H using values occupying the lower-diagonal of such a matrix L. This takes $n(n-1)/2$ values, where n is the rank of the covariance.

We use the Cauchy robust loss function as a metric for the fits, in which we minimize the lower-diagonal matrix $\boldsymbol{L}$,

$$M(\boldsymbol{L}) = \sum_{i}^{m} \log\left[1 + \left(\mathcal{L}_i - \tfrac{1}{2}(\vec{\eta}_i)^T \boldsymbol{L}\boldsymbol{L}^T \vec{\eta}_i\right)^2\right] \tag{6.2.6}$$

for the m sampled ice models where $\vec{\eta}_i$ is the i'th sampled set of nuisance parameters at which a log likelihood of $\mathcal{L}_i$ was recovered through PPC simulation. This likelihood function, which has been used in previous IceCube analyses [79], was chosen such that bad fits far off the true likelihood contours do not negatively affect the fit. The fit, despite running over forty-five parameters, was found to be extremely stable and fast. The fit Hessian $H = \boldsymbol{L}\boldsymbol{L}^T$ is show in Figure 6.2.4 (left) and the correlation matrix (right).

Using these the expected variation of ice models can be calculated. Five thousand random ice models were drawn, using the correlation matrix and the fit widths of the amplitudes and phases,

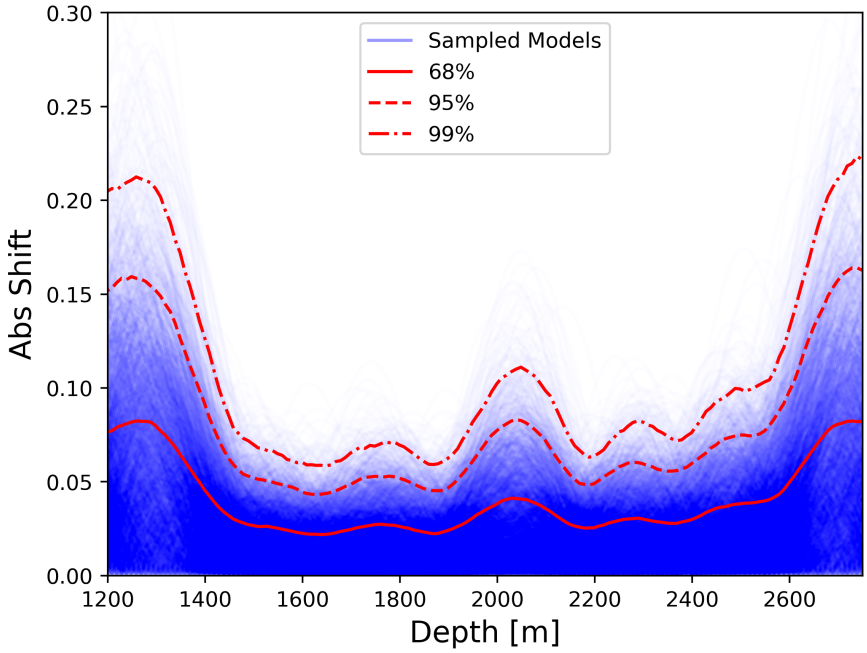

FIGURE 6.2.5: The results of sampling five thousand ice models using the fit correlation matrix and widths for the amplitudes and phases. A solid red line is drawn, below which the fractional shift of the absorption length of 68% of sampled models lie. Similar lines for 95% and 99%. IceCube lies between 1500 and 2500 meters of depth. The bump in the middle lines up with the dust layer in IceCube, and rises at the end are caused by poor constraint due to the physical extent of the detector.

and are shown in Figure 6.2.5.

The widths on the ice models were then used in an application of the SnowStorm technique. A purpose-build Monte Carlo sample was prepared generating only events that would yield cascades; since we were not interested in developing a sample to test event selection efficiency, background events were not included. This sample was generated using the same procedure as described in Chapter 5, starting with LeptonInjector for event generation and LeptonWeight for event weighting [52]. Energies were all sampled at according to a power law with a spectral index $\gamma = -2$. Sub-samples were prepared spanning different energy regimes and using different numbers of events per file, injection cylinder sizes, and events per model. The full ensemble of event generation parameters are shown in Table 6.2.3.

From these, splits were applied to the full sample and 2D linear gradients were calculated. Photospline [78] was then used to perform spline fits of the 2D gradients to smooth out MC

	1001	1002	1003	1004	1005	1006	1007	1008	1009	1010
Flavor	ν_e	ν_μ	ν_τ	ν_e	ν_τ	ν_e	ν_μ	ν_τ	ν_e	ν_τ
Current	NC	NC	NC	CC	CC	NC	NC	NC	CC	CC
Events Per File			50,000					10,000		
E_{min} [GeV]			100					$5e3$		
E_{max} [GeV]			$5e3$					$10e6$		
Zenith Range					Full Sky					
Cylinder Height					1400 m					
Cylinder Radius			700 m					750 m		
Sampled γ					-2					
Events Per Model			5					10		

TABLE 6.2.3: MC generation specifications for the snowstorm cascades sample. Cylinder height and radius are defined in Ref [52]. The number of events per model refers to the number of MC events simulated before shuffling the amplitudes and phases for the ice model.

statistical variance. A table of spline fits is shown below in Figure 6.2.6.

Each of these were then implemented in our fitting framework, and the effects in analysis space were calculated. Using the previously calculated covariance matrix and the methods for de-correlating the nuisance parameters from Section 6.1.2, uncorrelated nuisance parameters were constructed as a simple basis change from the original amplitude/phase basis. Of the ten new parameters, only five were found to have a significant impact on analysis rates. The other five are kept at their central values in fits. The strongest five are shown in Figure 6.2.7.

6.2.3 Hole Ice

The hole ice represents a bubbly, refrozen region of ice around the DOMs. The bubbles, which formed during the refreezing, greatly decrease the scattering length of light. This has the effect of changing the light-acceptance of the DOMs as a function of photon incident angle. A plethora of different angular acceptance curves existed from various different calibration studies done to understand this region of the ice; and work was carried out to approximate these different curves and the space they spanned. Two separate hole ice models were used for the tracks and cascades; although it is expected that there are correlations between the priors, we expect that an uncorrelated fit to be a conservative approach in this context.

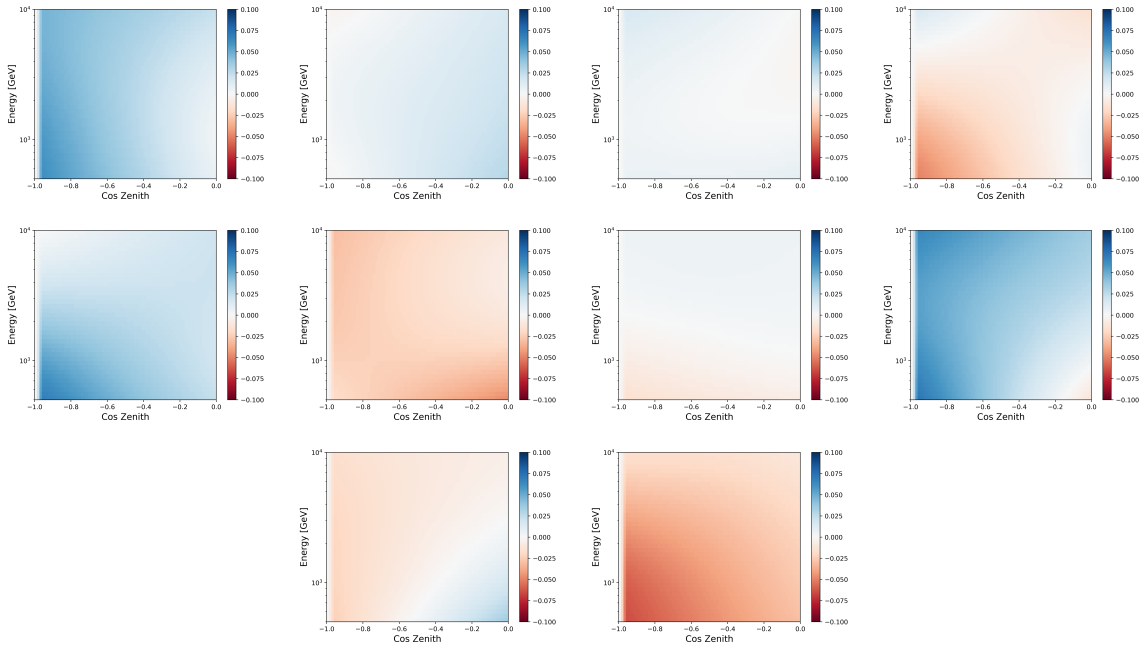

FIGURE 6.2.6: Evaluations of the Photospline [78] spline-fits to the 2D gradients as functions of energy and zenith. Left to right from top to bottom: Amplitude 0, Amplitude 1, Amplitude, 2, Amplitude 3, Amplitude 4, Phase 1, Phase 2, Phase 3, Phase 4, and Phase 5.

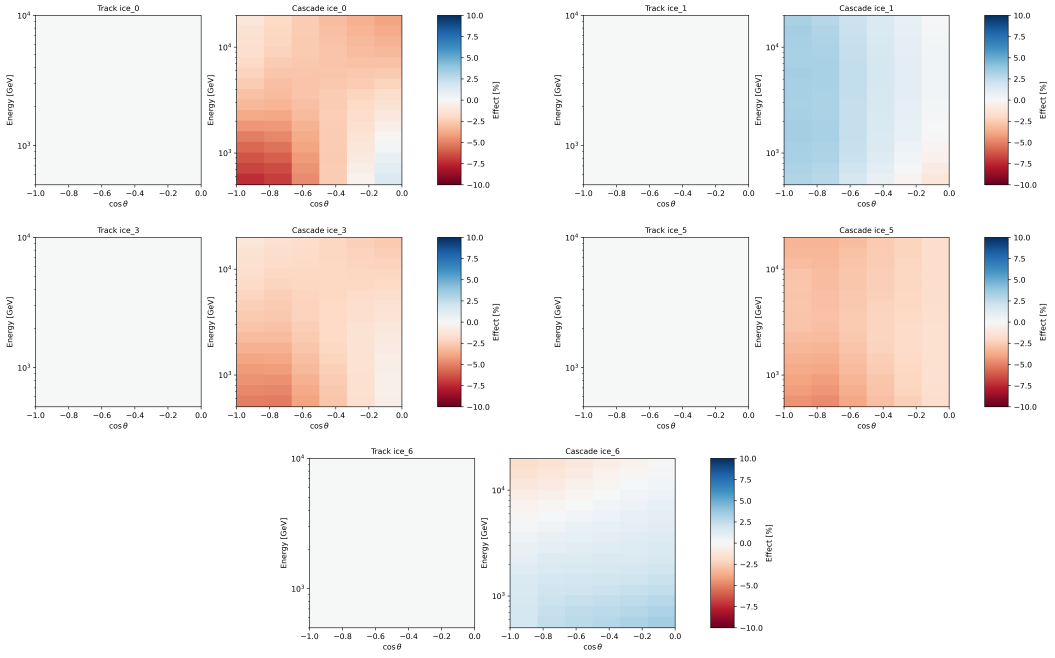

FIGURE 6.2.7: Shape effects from perturbing each of the uncorrelated nuisance parameters by one sigma. Note that although named after phases and amplitudes, perturbing each of these is identical to perturbing a linear combination of all amplitudes and phases simultaneously.

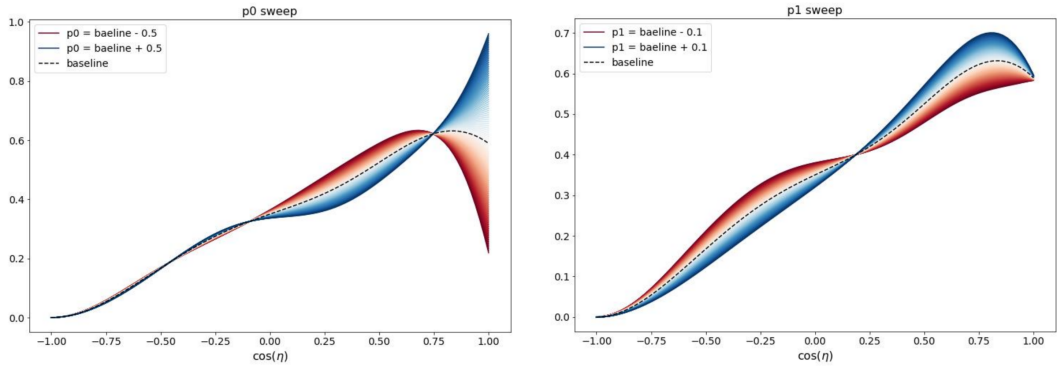

(A) A sweep of the unified hole ice model p_0 parameter.

(B) A sweep of the unified hole ice model p_1 parameter.

FIGURE 6.2.8: Effects of varying unified hole ice model parameters. η represents angle of photon incidence on the DOM; -1 is the DOM backside, and +1 is the DOM PMT face.

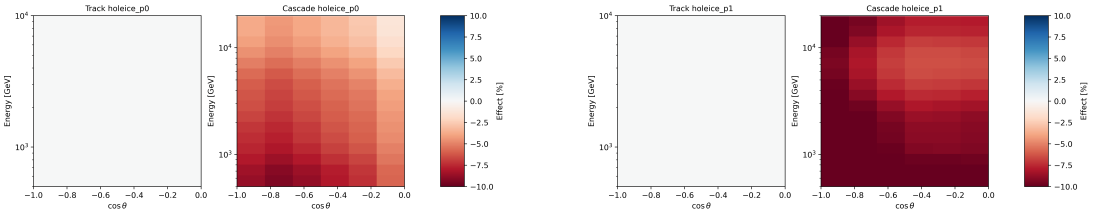

(A) A sweep of the unified hole ice model p_0 parameter.

(B) A sweep of the unified hole ice model p_1 parameter.

FIGURE 6.2.9: Effects of varying unified hole ice model parameters. η represents angle of photon incidence on the DOM; -1 is the DOM backside, and +1 is the DOM PMT face.

Cascades For the cascades, spline-fits were carried out using seven support points and by forcing the acceptance to zero at the DOM backside (opposite the PMT). This resulted in six free, correlated, parameters needed to describe the acceptance curve. A principal component analysis was carried out, and it was found that all acceptance curves span a phase space of lower dimensionality. Only two components were needed to describe the space of angular acceptance curves, and those were named p_0 and p_1. This is called the Unified Hole Ice Model. The impacts of perturbing each one, individually, are demonstrated in Figure 6.2.8. In doing so, a small amount of error is introduced, though the overall uncertainty on the hole ice that remains is far greater than the introduced error.

Like the DOM Efficiency, a SnowStorm MC ensemble was prepared for the cascades sample in which the hole ice parameters p_0 and p_1 were allowed to vary. For each batch of ten simulated MC

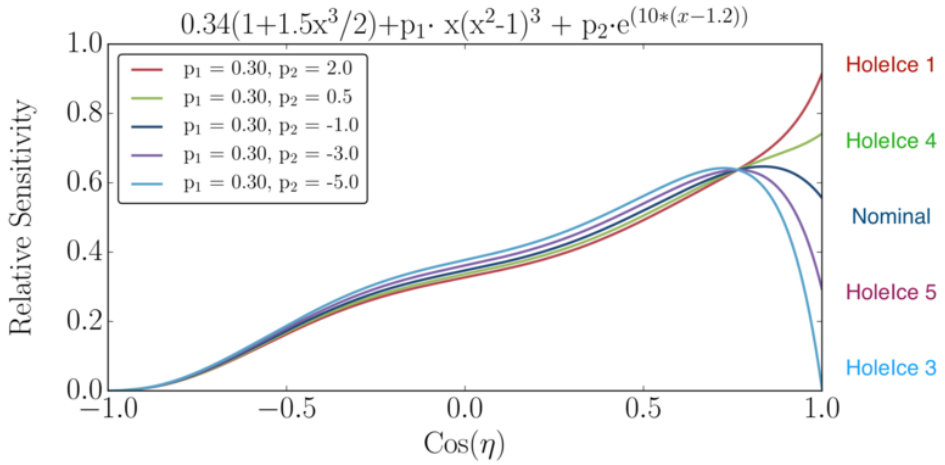

FIGURE 6.2.10: The hole ice parametrization of the MSU hole ice model. The H2 model is an earlier model used and developed internally.

events these parameters p_0 and p_1 are randomly sampled uniformly from the ranges $p_0 \in [-0.84, 0.3]$ and $p_1 \in [-0.134, 0.05]$. The angular acceptance of the DOMs in CLSim is then manually adjusted according to the new angular acceptance and the photon propagation is then carried out. The remainder of the MC simulation chain is then performed as usual.

The SnowStorm technique is applied to this MC sample using the cutting technique described in Ref [76], and the 2D analysis gradients are constructed. These are shown in Figure 6.2.9.

Tracks The track sample uses a previous implementation originally developed for Ref [23]. Several MC samples were generated according to an angular acceptance model parametrized by

$$\mathcal{A}(\eta) = 0.34\left(1 + 1.5\cos\eta - \cos^3\eta/2\right) + p_1\cos\eta\left(\cos^2\eta - 1\right)^3 + p_2\exp\left(10(\cos\eta - 1.0)\right) \quad (6.2.7)$$

where $\mathcal{A}$ is the relative acceptance of the DOMs as a function of *eta*, the angle of photon incidence on the DOM. This is plotted for various values of p_1 and p_2 in Figure 6.2.10.

A nominal sample was generated using $p_1 = 0.3$ and $p_2 = -1.0$, and then support points were generated at p_2 values of -5, -3, -1, 0.5, and 2. A 3D spline-fit was carried out over p_2, $\log E$, and $\cos\theta$; the p_1 parameter was observed to have a negligible effect on reconstructed rates. The effects of perturbing this parameter on the reconstructed rates are shown in Figure 6.2.11.

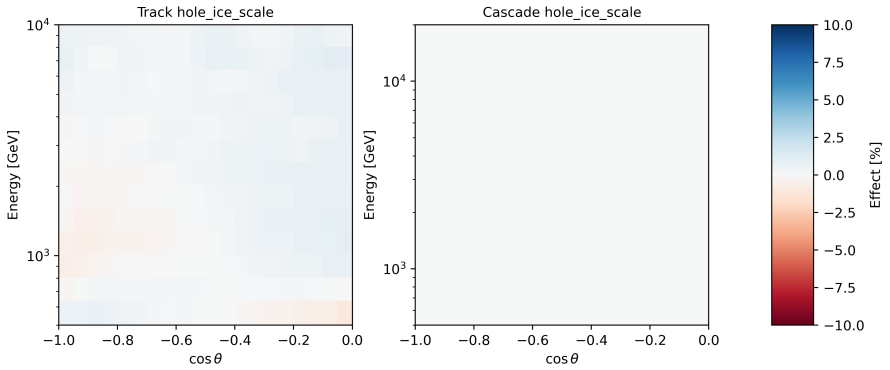

FIGURE 6.2.11: The effects of perturbing the track sample's hole ice parameter on the track sample (left) and cascades sample (right).

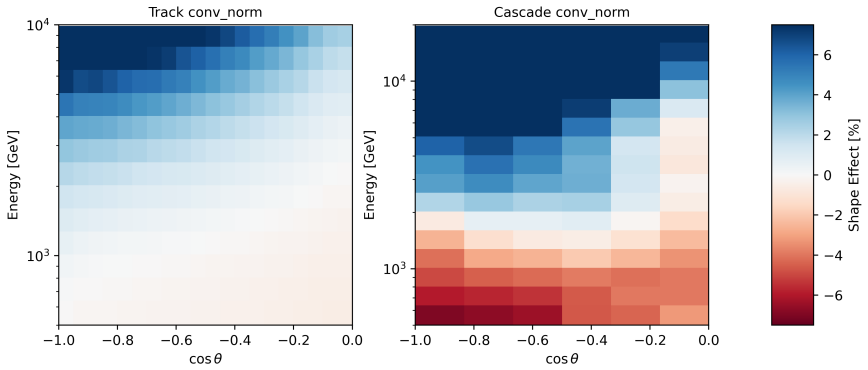

FIGURE 6.2.12: The shape-effect of perturbing the normalization of the conventional neutrino flux.

6.2.4 Conventional Flux Uncertainties

Sterile neutrino models with large values of Δm^2_{41} feature oscillations signatures with a peak-to-peak separation too narrow for our detector resolution, and a large shift in the normalization. As a consequence, we allow the normalization of the conventional neutrino flux to float in fits to prevent spurious preferences for high Δm^2_{41} in global fit scans. At 1 TeV, the uncertainties on pion and kaon production, hadronic interaction cross section, and atmospheric density yield an expected error of 25% on the normalization [23]. So, we allow for a conservative 40% uncertainty on the conventional flux normalization.

We also parametrize an uncertainty on the shape of the conventional neutrino flux, which has been measured to approximately follow a power-law with an energy dependence of $E^{-2.65}$, with a

Experiment	Energy Range	Slope
CREAM-III [80]	1-200 TeV	-2.64 ± 0.03
HAWC [81]	10-500 TeV	-2.64 ± 0.03
Argo-YBJ [82]	3-300 TeV	-2.64 ± 0.03
PAMELA [83]	50GeV-15 TeV	-2.64 ± 0.03

TABLE 6.2.4: Measurements of the slope of the cosmic ray flux from several experiments.

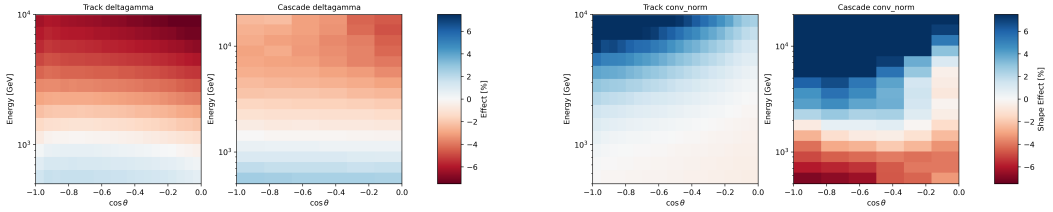

FIGURE 6.2.13: (Left) the shape-effect of perturbing the spectral index of the conventional neutrino flux; (right) the shape-effect of perturbing the normalization of the conventional neutrino flux.

spectral shift $\Delta\gamma$,

$$\Phi(E, \Delta\gamma) = \Phi(E) \left(\frac{E}{E_0} \right)^{-\Delta\gamma} \tag{6.2.8}$$

where the pivot $E_0 = 2.2$TeV has been chosen to approximately preserve the normalization. Existing measurements of the cosmic ray flux are shown in Table 6.2.4.

More recently, calculations have shown a softening in the cosmic ray spectrum at energies above 10TeV [84]. To account for this and previous measurements, we use a prior width on $\Delta\gamma$ of 0.25. The effect of a 0.03 perturbation on the spectral index is shown inFigure 6.2.13 (left)

Like in the 8-year track-only analysis [22, 23], we parametrize the uncertainty in the production of pions and kaons in air showers using the model developed by Barr et. al. [85] (refered to as the Barr Parametrization from here on).

This nominal cosmic ray flux prediction uses the Hillas-Gaisser H3a [86] cosmic ray flux model. This model is broken into five distinct mass-range populations: p, He, CNO, Fe, and MgSi; each of which correlate to a range of cosmic ray masses. These are then grouped into three populations combining p and He, and CNO and Fe. This is demonstrated in Figure 6.2.14 (left), which shows the full cosmic ray flux prediction (black line) overlain with results from eleven measurements of the cosmic ray spectrum. The $\nu_\mu/\bar{\nu}_\mu$, or charge ratio, is highly relevant for the signal strength of this analysis. A figure showing it is shown in Figure 6.2.14 (right).

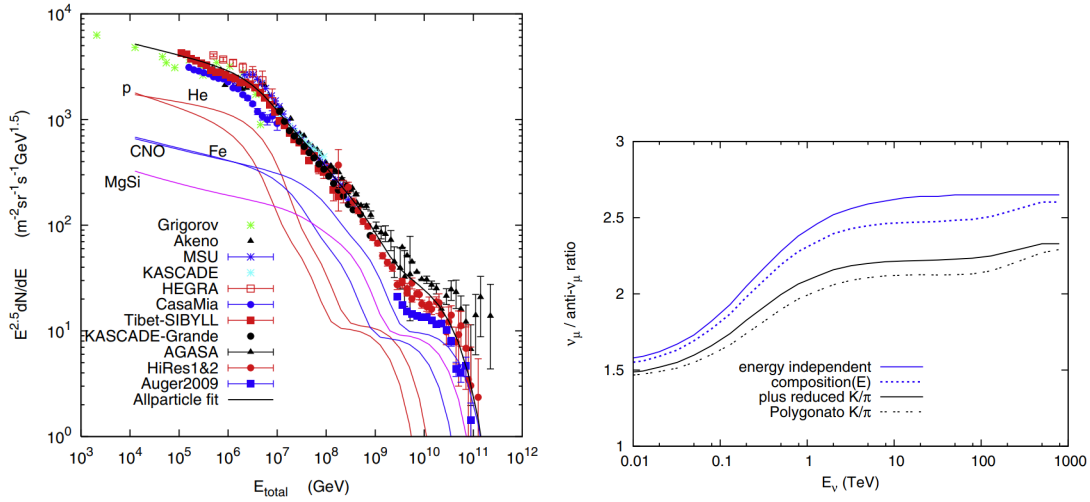

FIGURE 6.2.14: (Left) the Hillas-Haisser H3a flux prediction (all particle fit) compared to data; (right) the $\nu_\mu/\bar{\nu}_\mu$ ratio. Both figures are from Ref [86]

The neutrino flux predictions are determined by propagating these air showers using Matrix Cascade Equations (MCEq) [87], the `SIBYLL` 2.3c interaction model [88], and an atmospheric density model using the Atmospheric InfraRed Sounder satellite [89]. MCEq establishes a series of particle production and decay rates for air-shower evolution according to a given atmospheric model and interaction model. It then numerically integrates the initial states to yield the expected final state rates of any chosen particle at the Earth's surface for a given zenith angle.

The Barr Parametrization uses existing accelerator data to constrain production rates of pions and kaons in cosmic ray air showers as a function of the incident projectile particle energy and the Bjorken x scaling variable, which is itself defined as the fractional momentum transfer from the incident projectile to the hadronic component of the interaction as observed in the lab frame. In the lab frame with the target at rest,

$$x = \frac{2M_p^2 - p_4^2}{2M_p^2} \tag{6.2.9}$$

where p_4 is the vector four-momentum of the hadronic component. Regions in this phase-space with similar constraints are established, and indexed, shown in Figure 6.2.15 from Ref [85]. The uncertainties with in each region are fully correlated, and are fully uncorrelated for points in different regions. Due to the strong effect of the charge ratio on this signal's analysis, we double the number of parameters in order to independently perturb the production rates of mesons and

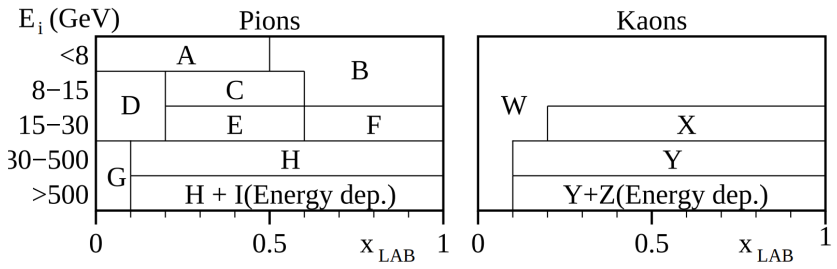

FIGURE 6.2.15: Uncertainty regions for the Barr parametrization.

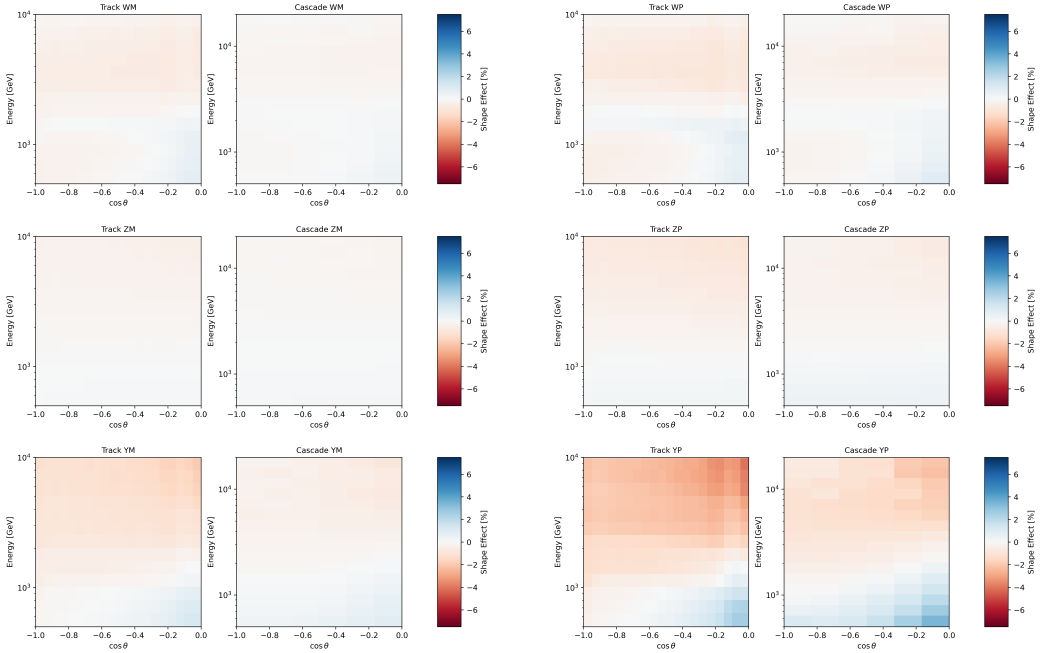

FIGURE 6.2.16: The effects of perturbing each Barr systematic uncertainty parameter.

anti-mesons. As shown in References [22, 23, 90], since the neutrino flux is kaon-dominated at these energies only the W, Y, and Z regions are relevant for this analysis.

We evalutate the effect of perturbing each of these parameters, both postively and negatively, on the expected neutrino flux at the Earth's surface over a $1^\circ \times 1^\circ$ solid-angle grid. At each point and for each different perturbation, we marginalize over months in a year and hours in a day. Since the analysis is zenith-only, we also marginalize over azimuths. Then gradients are calculated for each of the Barr Parameters for ν's and $\bar{\nu}$'s for each active neutrino flavor. These gradients are then evolved through nuSQuIDS for each tested 3+1 sterile physics point. The effect of a 1σ perturbation for each Barr Parameter in reconstructed space is shown in Figure 6.2.16.

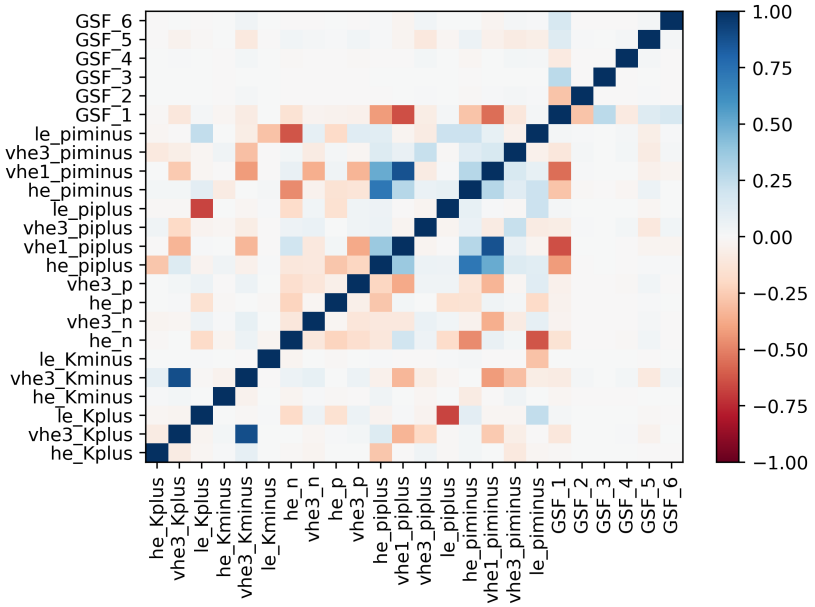

FIGURE 6.2.17: The correlation between the parameters used in the DaemonFlux model.

6.2.5 Alternative Conventional Flux Model: daemonflux

An alternative model for conventional flux uncertainties, the DAta-rivEn MuOn-calibrated Neutrino Flux [91] (daemonflux) model was also investigated. Daemonflux uses two approaches. First, a principal component analysis was done to a glboal spline fit [92] of the cosmic ray flux. Six components were found to be sufficient to span the given uncertainties on the cosmic ray flux, and a new correlation matrix was calculated to describe the full uncertainty on the flux they predict. Then, additional constraints from fixed-target experiments are used to describe uncertainties on particle production rates of protons, neutrons, $\pi^{\pm}$, and $K^{\pm}$ at four different energy scales. Cosmic Ray muon data are used to further constrain and describe the uncertainties in the global spline fit and the hadronic production rates. A correlated prior was evaluated for the full ensemble of 24 parameters, as shown in Figure 6.2.17.

The fractional difference in the fluxes from the old fluxmodel, which used a Hillas-Gaisser H3a model [86] with the `Sibyll` 2.3c interaction model [88], to daemonflux, is shown in Figure 6.2.18. From this figure we can see that daemonFlux predicts a smaller $\bar{\nu}$ flux. Since the signature of the sterile neutrino oscillations is a disappearance of $\bar{\nu}_{\mu}$, we expect a suppression our predicted sensitivity when daemonflux is used as the nominal flux model.

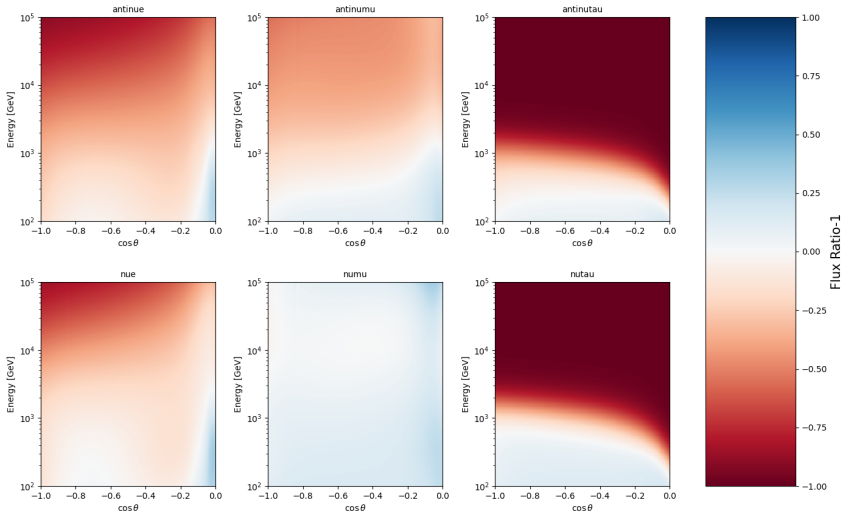

FIGURE 6.2.18: The fractional difference between daemonflux and a Hillas-Gaisser H3a cosmic ray flux with the Sibyll2.3c interaction model. Red represents a smaller predicted flux. It is apparent that the new model predicts a smaller $\bar{\nu}$ flux.

For this analysis, the effects of perturbing each of these 24 parameters are evaluated after a one-sigma from their central values. From these perturbed fluxes and the central expectations, we extract the flux-gradients for each of these parameters. These neutrino flux gradients are then evolved using nuSQuIDS to get the full-flavor gradient flux at IceCube. The effects of perturbing each parameter, independently, is shown for the cascades sample assuming no sterile neutrino in Figure 6.2.19. It is observed that only a small subset of all 24 parameters were relevant for this analysis. The procedures described in Section 6.1.2 were first carried out to identify the strongest parameters in the uncorrelated basis. Random expectations were then sampled from the full DaemonFlux ensemble, and fits were carried out while allowing the n, strongest, uncorrelated parameters to float. The distributions of the resulting ΔLLH values of these fits were logged after running over a thousand fits for both cascades and tracks, separately, and are shown in Figure 6.2.20 for tracks (left) and cascades (right). It was also observed that the same parameters had the strongest effects on both the track and cascade expectations, and that only 7 parameters are necessary to sufficiently span the expectation-space; eight were used to be conservative.

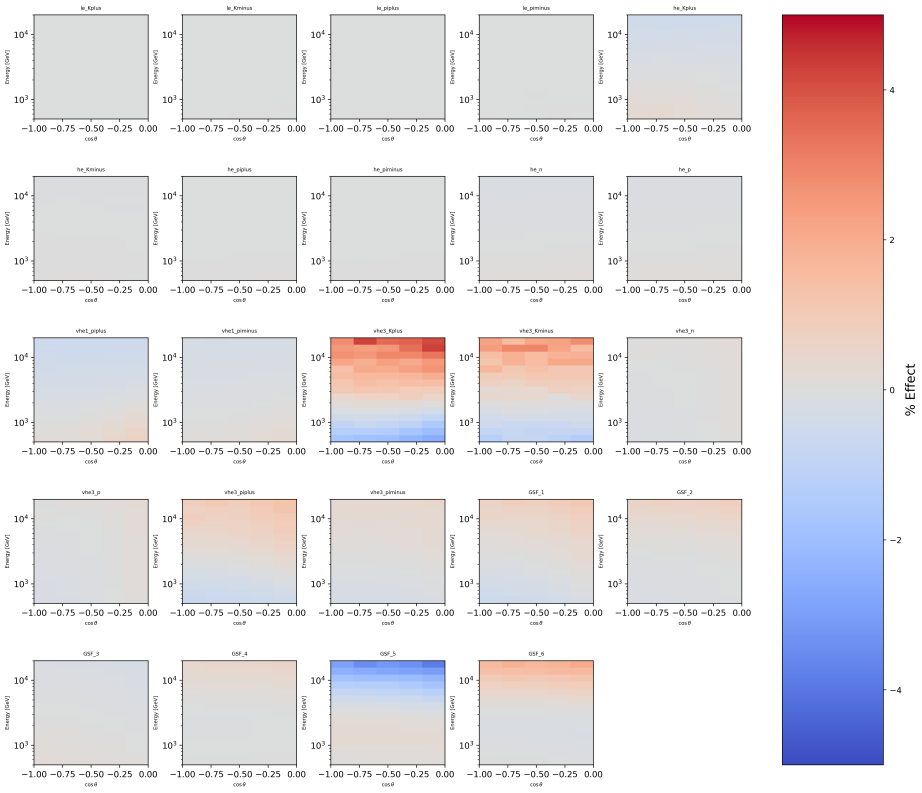

FIGURE 6.2.19: Shape-effect of perturbing each of the 24 DaemonFlux nuisance parameters by one-sigma in analysis space. Plots here are showing the effects on the cascades sample; the effects on the track sample have been observed to be extremely similar.

The effects of perturbing the eight strongest parameters by one sigma are shown for both tracks and cascades in Figures 6.2.21 and 6.2.22.

6.2.6 Atmospheric Density

During air shower evolution, the delicate balance between kaon production, re-interaction, and decay heavily influence the energy spectrum of the resulting neutrinos. The local atmospheric conditions of the temperature, density, and pressure all influence this balance; an effect that has previously been studied in the neutrino spectrum by IceCube [93, 94]. We incorporate an uncertainty on the atmospheric density by perturbing the Earth's atmospheric temperature within

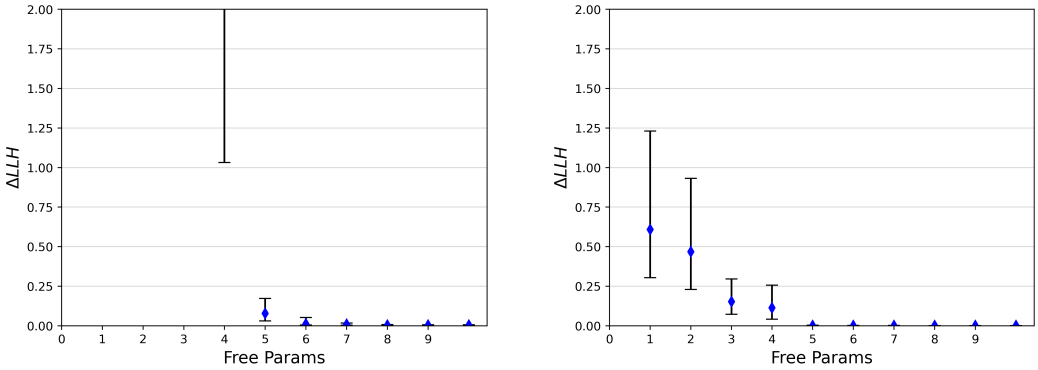

FIGURE 6.2.20: Fit accuracy as a function of free parameters used to a randomly sampled DaemonFlux expectation; tracks are shown on the left and cascades on the right

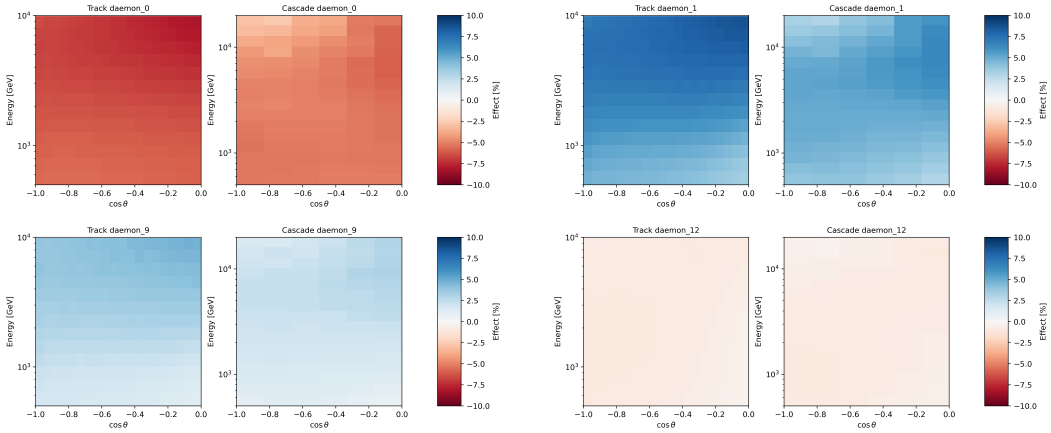

FIGURE 6.2.21: The shape-effect of perturbing four of the strongest uncorrelated DaemonFlux parameters for tracks and cascades.

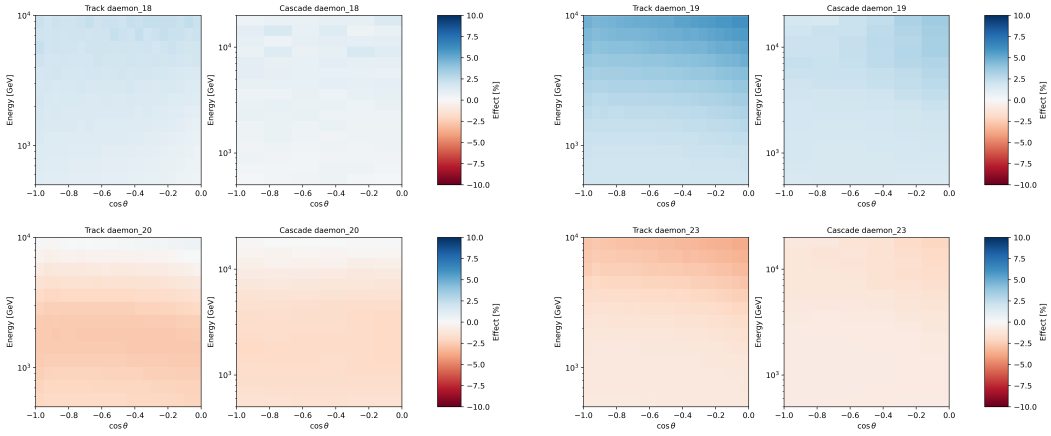

FIGURE 6.2.22: The shape-effect of perturbing four more of the strongest uncorrelated DaemonFlux parameters for tracks and cascades.

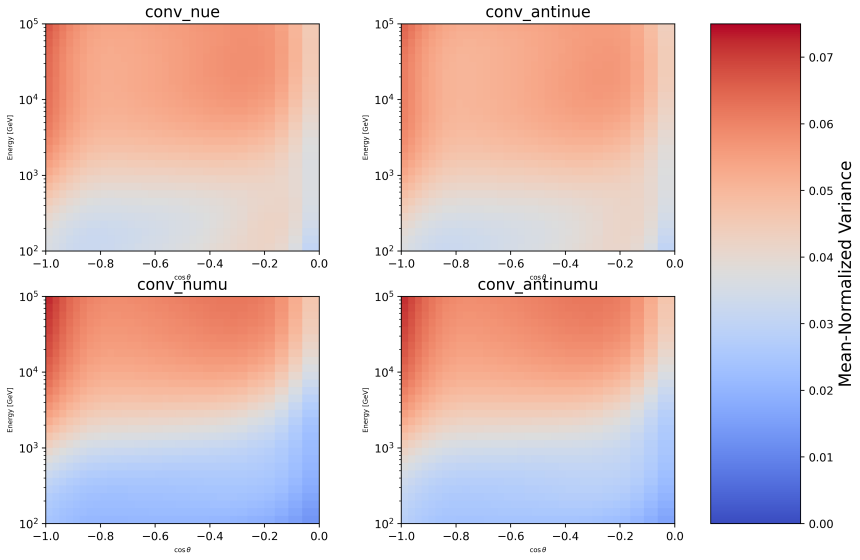

FIGURE 6.2.23: The variance in predicted atmospheric models for various neutrino fluxes before nuSQuIDS propagation. From the top left, going clockwise, ν_e, $\bar{\nu}_e$, ν_μ, and $\bar{\nu}_\mu$.

the ranges specified by NASA's Atmospheric InfraRed Sounder (AIRS) [89] satellite data. This satellite provides an open-source dataset for the temperature profile of the atmospheric as a function of atmospheric depth and location. We evaluate the variation in the temperature of the atmosphere over a whole year in a $1^\circ \times 1^\circ$ grid across the Earth's surface. The standard deviation of the predictions from all models are then calculated as functions of zenith and energy. This standard deviation is shown for muon and electron neutrinos in Figure 6.2.23.

This is then used as the atmospheric density uncertainty after being forced through zero near $\cos\theta_z = -0.7$ to account for the temperature offset between the Northern and Southern hemispheres. Figure 6.2.24 shows the effect on neutrino fluxes after forcing it through zero at the equator. The effects of this nuisance parameter, and this source of systematic uncertainty, is shown in Figure 6.2.25.

The 1976 United States Standard atmosphere [95] was also used as a baseline for cross-checks, and it was found to lie within the allowed envelope.

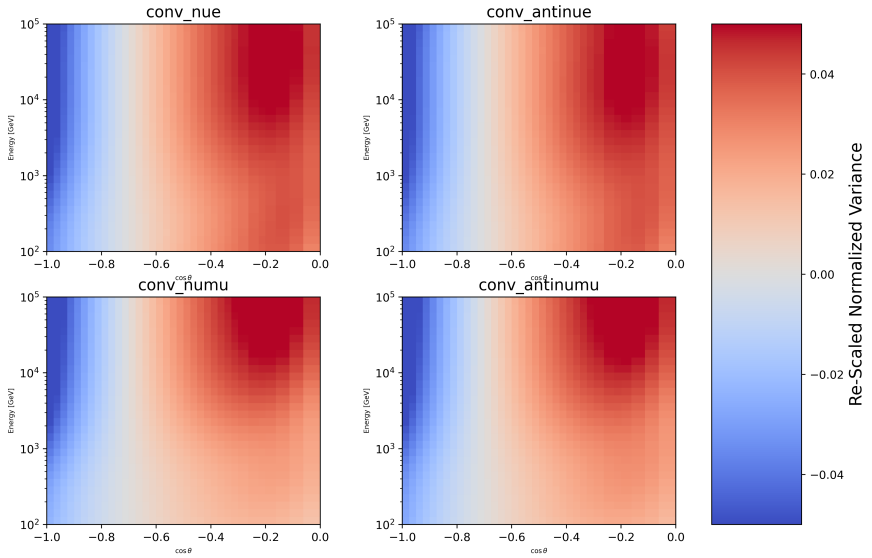

FIGURE 6.2.24: The effect of the atmospheric uncertainty parameter on predicted neutrino fluxes before nuSQuIDS propagation. This is after forcing the effect through zero at the equator, and implementing opposite effects in the opposite hemispheres. From the top left, going clockwise, ν_e, $\bar{\nu}_e$, ν_μ, and $\bar{\nu}_\mu$.

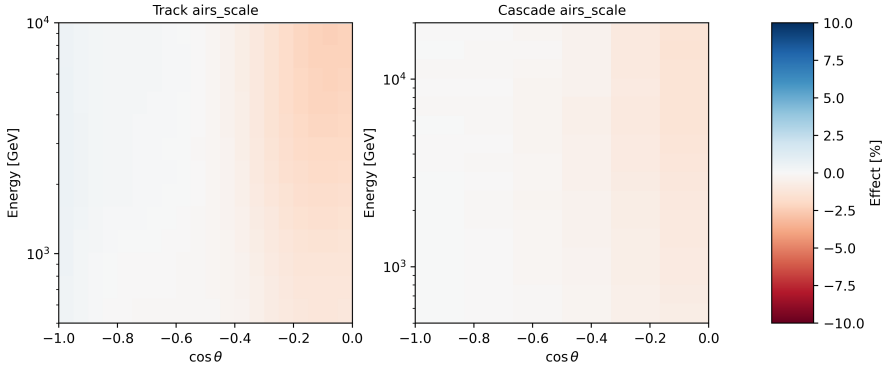

FIGURE 6.2.25: Effects of the atmospheric uncertainty on reconstructed event rates for tracks (left) and cascades (right).

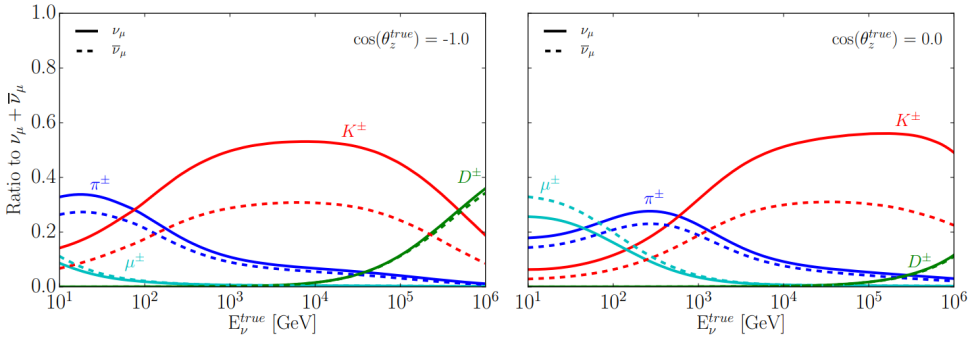

FIGURE 6.2.26: Contribution of different parent particles to the total atmospheric neutrino fluxes as functions of energy. The contributions to up-going neutrinos are shown on the left, and horizontal neutrinos are on the right. Figure from Ref [23]

6.2.7 Kaon-nucleon Total Cross-Section

The majority of the neutrino flux at the energies relevant to this analysis come from the decays of Kaons, as shown in Figure 6.2.26.

After the creation of a kaon it can either decay or inelastically scatter with the nucleons in the air. Such interactions would down-scatter the kaon to a lower energy in addition to creating other mesons. The relative probabilities of these can and do have a direct impact on the expected shape of the neutrino flux coming out of these cosmic ray air showers.

Unfortunately, though, the total cross-section for $K^\pm$-nucleons has not been measured above the lower end of our energy spectrum, 310GeV [1]. Cross-section measurements have been done at higher energies using proton-proton collisions however, and one can extrapolate a kaon-nucleon cross-section through a Glauber [96, 97] and Gribov-Regge [98] multiple scattering formalism.

A direct extrapolation of the uncertainty on the total kaon-nuclei cross-section of 4%, which we conservatively extrapolate out to a value of ±7.5%. Future proton-Oxygen collisions in Run 3 at the LHC could constrain the uncertainty in this cross-section, however [99].

6.2.8 Astrophysical Neutrino Flux

Astrophysical neutrinos are a background to this analysis; it is modeled here as an isotropic, unbroken power law spectrum with equal contributions from each neutrino variety. The priors are the same as for the previous track analyses [22, 23], which use the IceCube High-Energy Starting Events sample [100] to construct a correlated prior for the normalization and spectral

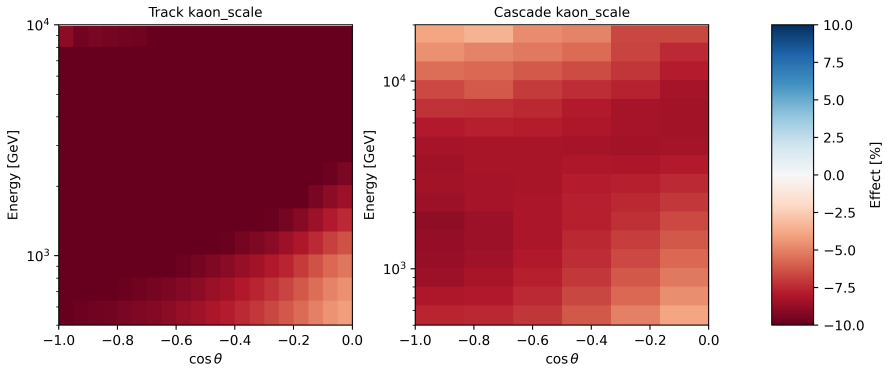

FIGURE 6.2.27: The effects in analysis space on tracks (left) and cascades (right) after perturbing the kaon-nucleon cross-section by 7.5%.

index. Constraints are shown in Figure 6.2.28, where the spectral index and normalization are defined according to

$$\frac{dN_\nu}{dE} = \Phi_{astro} \left(\frac{E_\nu}{100 \text{ TeV}} \right)^{-2.5+\Delta_{\gamma_{\text{astro}}}} \tag{6.2.10}$$

were $\Delta_{\gamma_{\text{astro}}}$ represents a shift in the spectral index, and the flux has a normalization Φ_{astro} at 100TeV of

$$\Phi_{astro} = 0.787 \times 10^{-18} \left[\text{GeV} \cdot \text{sr} \cdot \text{s} \cdot \text{cm}^2. \right]^{-1} \tag{6.2.11}$$

Two new uncorrelated nuisance parameters are constructed following the same procedures of Section 6.1.2. The effects of perturbing each of these new, uncorrelated, parameters are shown in Figure 6.2.29 with tracks on the left and cascades on the right.

From Figure 6.2.29 it is evident that the astrophysical neutrinos contribute far more strongly to the cascade sample than to the tracks sample. To demonstrate why this is the case, consider the fluxes and cross-sections contributing to each event morphology.

$$\text{Tracks} \propto \Phi_{\nu_\mu} \times \sigma^{CC}_{\nu_\mu} \tag{6.2.12}$$

$$\text{Cascades} \propto \Phi_{\nu_\mu} \times \sigma^{NC}_{\nu_\mu} + \sum_{\alpha \in (e,\tau)} \Phi_{\nu_\alpha} \times \left(\sigma^{CC}_{\nu_\alpha} + \sigma^{NC}_{\nu_\alpha} \right) \tag{6.2.13}$$

For conventional fluxes, the electron and tau components are almost negligible. Whereas we can reasonably expect a 1-1-1 flavor ratio for the astrophysical neutrino flux. Since efficiencies

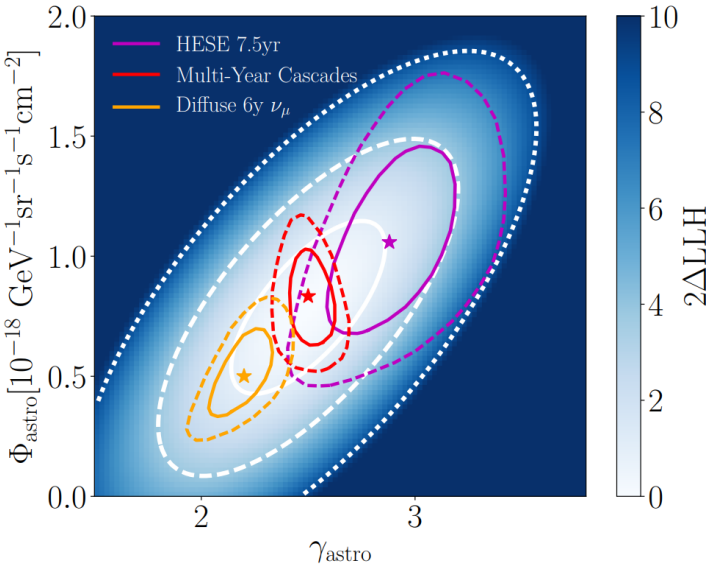

FIGURE 6.2.28: Constraints on the normalization and spectral index of the astrophysical neutrino flux. Contributions to the overall prior are shown from the IceCube Northern tracks sample [101], the multi-year cascades sample [102], and from the IceCube high-energy starting events sample [100]. Figure from Ref [23].

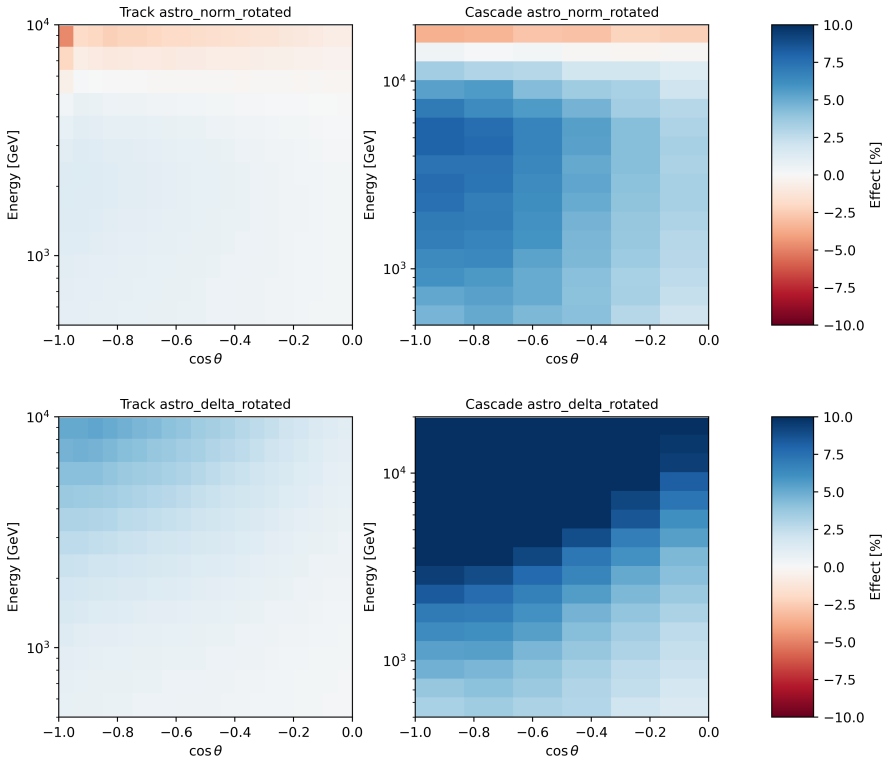

FIGURE 6.2.29: Effects in analysis space for tracks (left) and cascades (right) from perturbing the uncorrelated astrophysical nuisance parameters (top and bottom) individually by one sigma.

are equivalent regardless of neutrino origin, these expressions are also consistent with total event rates. In the case of cascades, it is evident that the astrophysical neutrinos will contribute a proportionally greater amount to the total event rate.

The astrophysical flavor ratio describes the relative fluxes of ν_e, ν_μ, and ν_τ expected at the Earth and of astrophysical origin. Three different sources are generally considered: pion decay with a 1:2:0 ($f_e : f_\mu : f_\tau$) initial state, muon damping with a 0:1:0 initial state, and neutron decay with a 1:0:0 initial state. These initial states have been evolved over astrophysical distances to predict what ratio of flavors is expected at the Earth [103]. The final states, corresponding to each of these initial states, are shown in Figure 6.2.30 (left). The localization of these at-Earth flavor ratios are dependent on how well constrained neutrino oscillation parameters are. The 'astrophysical bowtie,' shown in Figure 6.2.30 (right) and from Reference [104] shows the final-state flavor ratios allowed at 3σ for a unitary PMNS matrix in blue, and a non-unitary PMNS matrix in pink. Matrix elements were sampled from a global best-fit with [2] and without [105] unitarity. Constraints from Reference [106] are overlain.

The nominal astrophysical model assumes a 1-1-1 $\nu_e - \nu_\mu - \nu_\tau$ flavor ratio. Deviation from this prediction could lead to an imbalance between the ralative rates in the cascades and the tracks sample, and so an additional nuisance parameter is included derived which allows some flexibility in the flavor ratio.

The expected effect on reconstructed event rates from perturbing the flavor ratio by 1σ is shown in Figure 6.2.31.

6.2.9 Neutrino-Nucleon Interaction Uncertainty

Neutrino-nucleon cross-sections, in the context of this high-energy work, are well beyond the 'even remotely' regime of MeV, or even few-GeV, analyses. We are well and truly under the rule of the DIS kingdom. The cross-section at these energies runs in energy as a power law with a knee near 10^4 GeV as valence quark interaction parton density begins to weaken compared to the sea [107].

While the uncertainty was previously found to be inconsequential to the event rate at the detector [108, 109], it also manifests as the degree to which high-energy neutrino fluxes are attenuated as they propagate through the Earth [110, 111, 49]. Although previous analyses for

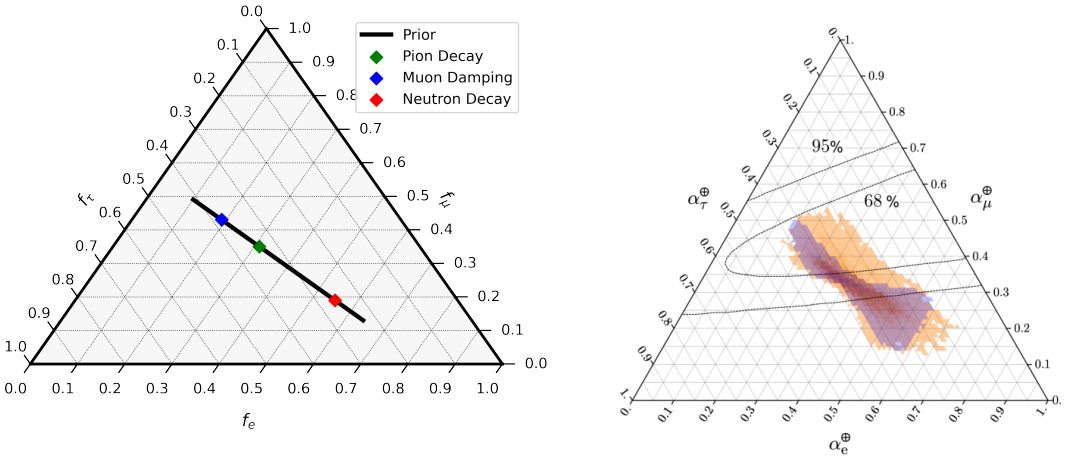

FIGURE 6.2.30: (left) The predicted astrophysical flavor ratios at the Earth given different neutrino production mechanisms and the chosen prior that spans all three. (Right) the flavor bowties for 3-neutrino oscillations (purple), and 3+ neutrino oscillations (orange), from Ref [104].

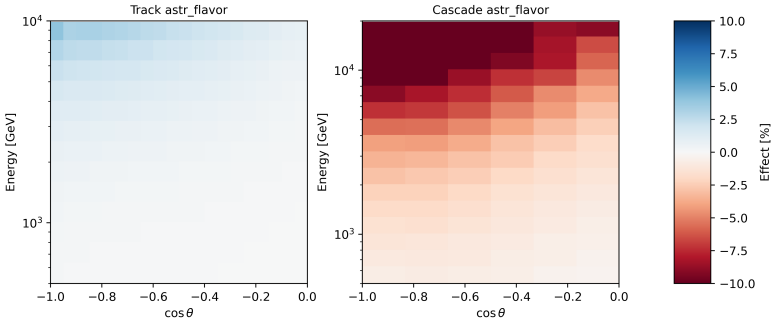

FIGURE 6.2.31: The shape-effect of perturbing the astrophysical flavor ratio by 1σ.

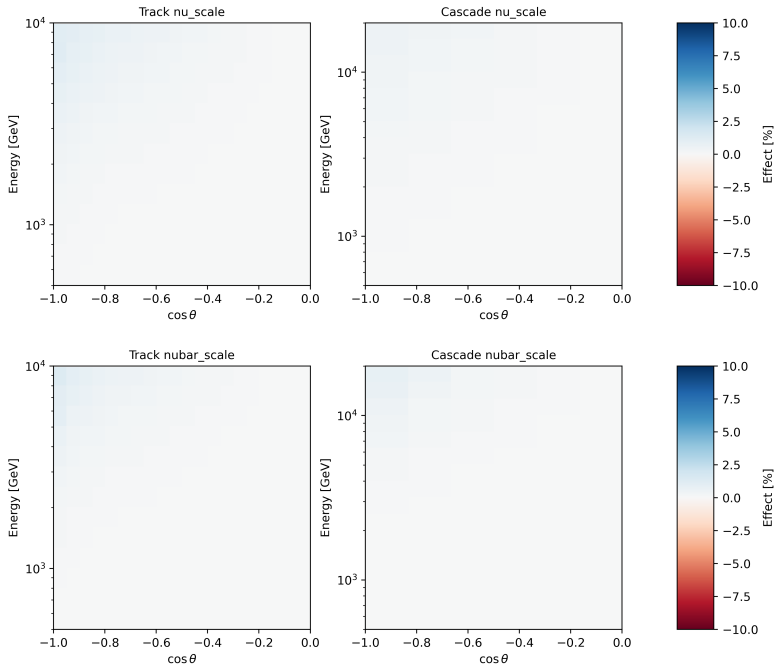

FIGURE 6.2.32: The effects of neutrino (antineutrino) cross-section uncertainty are shown on the top (bottom) for tracks (left) and cascades (right). Effect manifests as a sub-percent level disappearance of Earth-crossing events at energies over 10TeV.

tracks had found this to be a not-negligible source of uncertainty [22, 23], this was not the case for the cascades sample where the reconstructed cascade energy is closer to the true energy of the parent neutrino. The effects of the uncertainties on the neutrino and antineutrino cross-section on reconstructed cascade event rate are shown in Figure 6.2.32. Because the effects are so small, we elected to fix the uncertainty of the neutrino-nucleon cross-section to its central value in fits.

6.2.10 Cosmic Ray Muon Background

One of the most difficult sources of background in IceCube comes from the muons forged in the cosmic ray air showers above IceCube. These muons enter IceCube at a rate of about 2 kilohertz, and so over the ten years of livetime for the cascades sample, an estimated 3.15×10^{11} muons would have entered the volume over a wide range of energies. Although the series of filters are highly effective at cutting these sneaking muons, several still manage to enter in and deposit light near the center of IceCube, and pass the event selection criteria. The numbers of cosmogenic

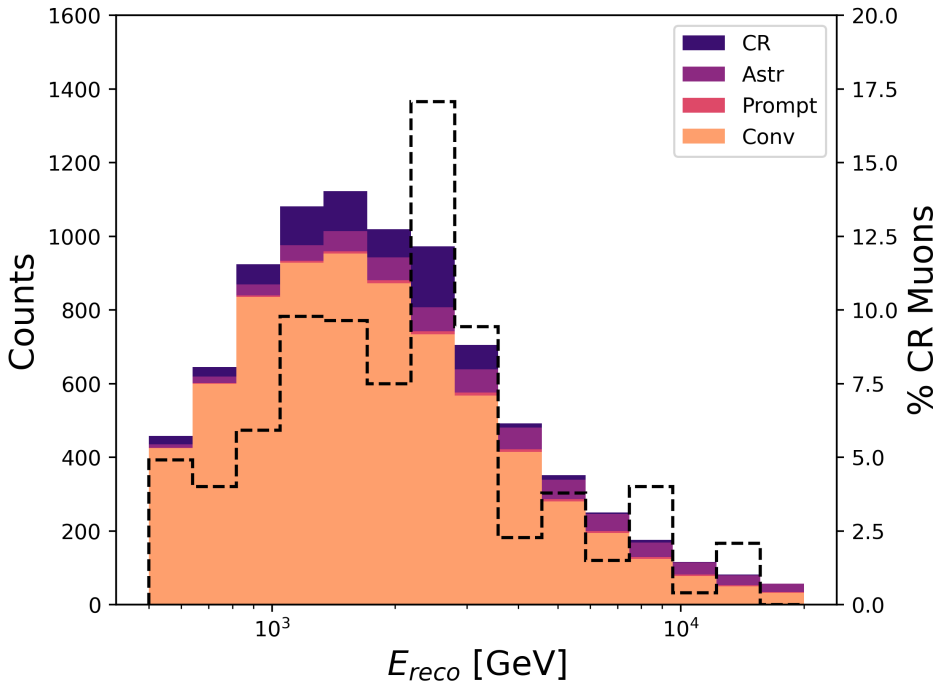

FIGURE 6.2.33: A stacked histogram showing the contributions, to the total event counts as a function of reconstructed energy, from conventional neutrinos (orange), prompt neutrinos (salmon), astrophysical neutrinos (purple), and cosmic ray muons misidentified as cascades (deeper purple). The percent of each bin which is made of CR muons is show as a black dashed line.

muons which pass these cuts, and are misidentified as neutrino cascades, and the percent of each bin they encompass, is shown in Figure 6.2.33.

The distribution of these muon events in reconstructed energy and zenith is shown in Figure 6.2.34, left. Due to the large number of events necessary to simulate to recover MC-statistically significant muon rates, a Gaussian kernel density estimate (KDE) is used to approximate the expected distribution that would likely lead to the simulated MC sample. The expected distribution of events is shown after the KDE smoothing is applied in Figure 6.2.34, right.

Uncertainty on these muons is extrapolated from the original MC statistical error. The same KDE smoothing procedure is carried out on the sum of the squares of the weights in each bin; the resulting error and the ratio between the error and means are shown in Figure 6.2.35

The overall normalization of the muon rate is allowed to float freely in fits with a 20% prior width chosen to match that of the neutrino fluxes, and the per-bin error on the muons is considered large enough to account for the variance possible from MC statistical error. The shape effect from

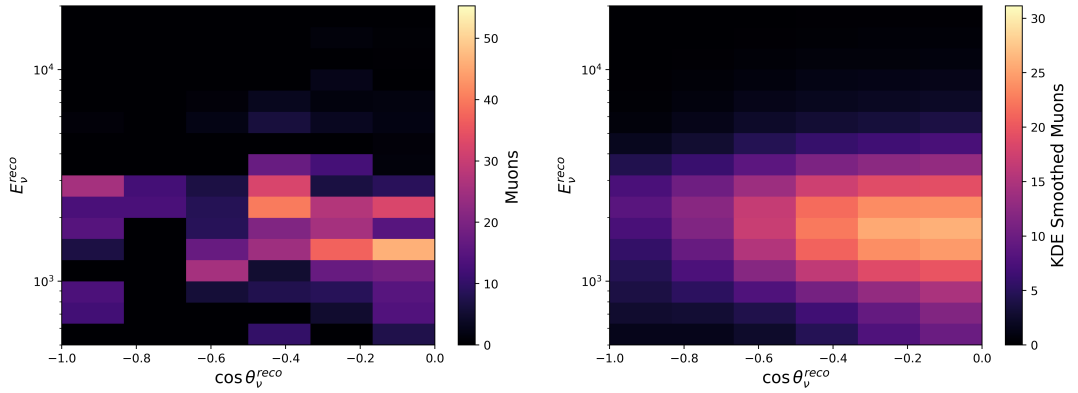

FIGURE 6.2.34: 2D heatmaps showing the expected number of muons after ten years of livetime in the analysis binning. Rates are shown before (left) and after (right) the kernel density smoothing is applied.

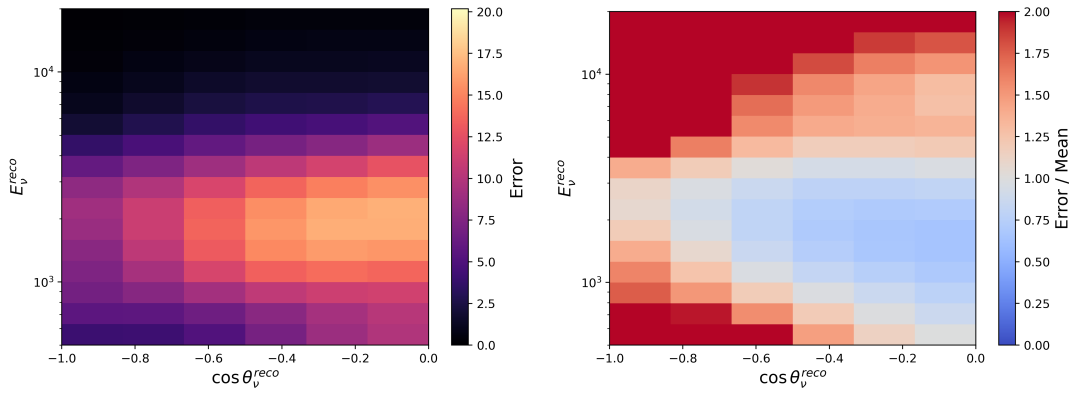

FIGURE 6.2.35: 2D heatmaps showing the KDE-smoothed MC statistical error for the muons (left) and the ratio of this value to the mean calculated from the KDE-smoothed muon rates (right).

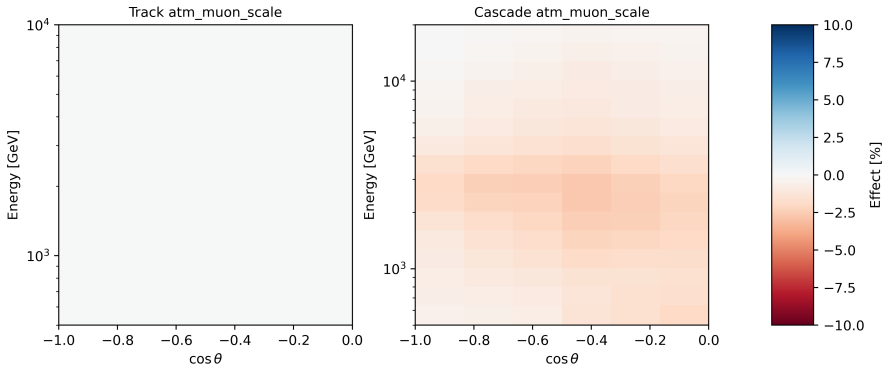

FIGURE 6.2.36: The shape-only effect of increasing the CR muon normalization by 20%. This manifests as an increase in event rates at 1-3 TeV across all zeniths; apparent suppression at high energies is an artifact of this being a shape-only plot.

allowing the atmospheric muon scale to float is shown in Figure 6.2.36.

The impacts of the other cosmic ray parameters on the expected muon background were also investigated. Using MCEq [87], we calculated the linear gradients for the effects of perturbing Barr parameters W, Y, Z, I, H, and I on expected muon rates at the surface of the Earth. Each of these gradients are shown below in Figures 6.2.37 and 6.2.38 separately for mesons and anti-mesons.

These gradients are then propagated using the MUon inTensity codE (MUTE) [112] to factor in muon survival probabilities as a function of energy and column-depth of ice traversed. The gradients, after smearing these with the survival tensors, are shown in Figures 6.2.39 and 6.2.40

These effects, taken together, represent an approximate 15% impact on muon rates. This is subdominant to the already-existing 50%+ error from the added MC statistical error, and so the existing treatment was considered sufficent.

The possibility of using a set of cuts was investigated as well. Multiple additional reconstructed quantities are provided during reconstruction and event selection, beyond just energy and zenith, with which cuts can be applied. The track and cascade boosted decision-tree scores, reconstructed depth, and the reconstructed 'contained-ness' of the events all provide extra leverage with which cosmic ray muons and true neutrino events can be discriminated. A series of cuts, listed in Table 6.2.5, were found capable of cutting all simulated CR muons out of the cascades sample. However, the required cuts were found to be aggressive enough that the remaining signal neutrinos would be insufficient to have the needed statistics to make a strong measurement. The number of

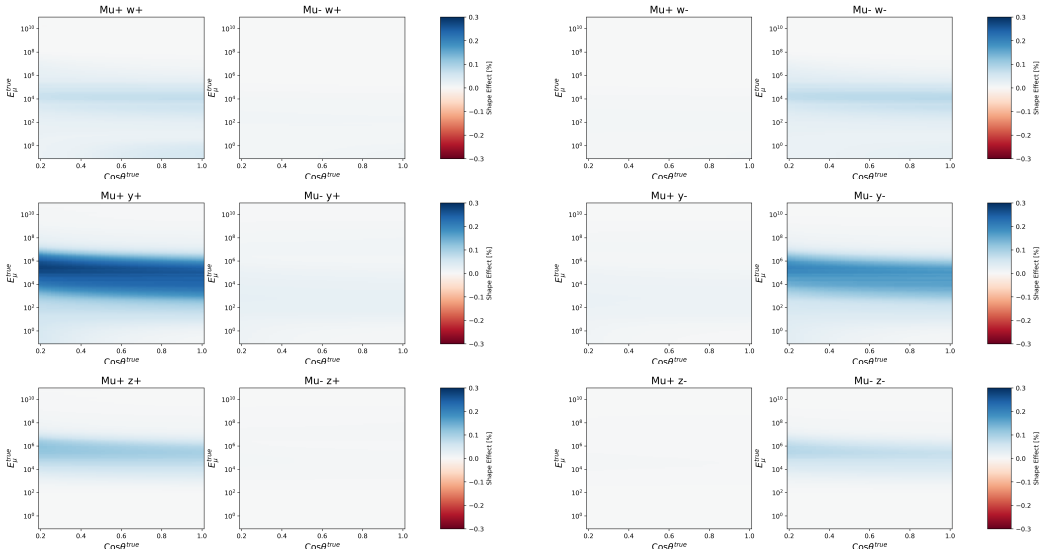

FIGURE 6.2.37: The impacts on muon rates from the Barr gradients effecting kaon-production. From top to bottom: W, Y, and Z. Panels on the left show the impact of perturbing the production rate of $K+$, subdivided into the effects on μ_+ (left) and μ_- (right). The same is shown on the right panels for $K-$.

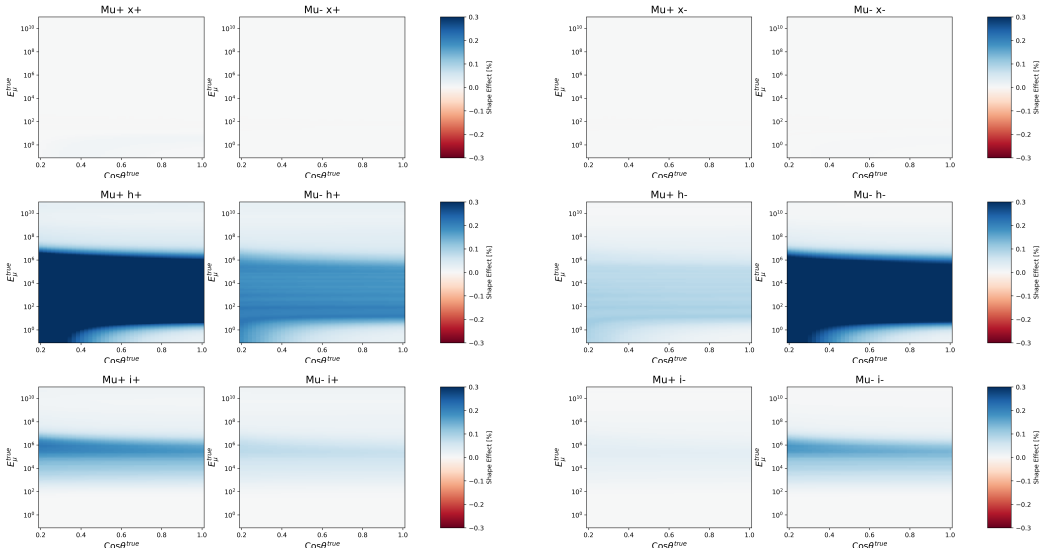

FIGURE 6.2.38: The impacts on muon rates from the Barr gradients effecting kaon-production. From top to bottom: X, H, and I. Panels on the left show the impact of perturbing the production rate of $\pi+$, subdivided into the effects on μ_+ (left) and μ_- (right). The same is shown on the right panels for $\pi-$.

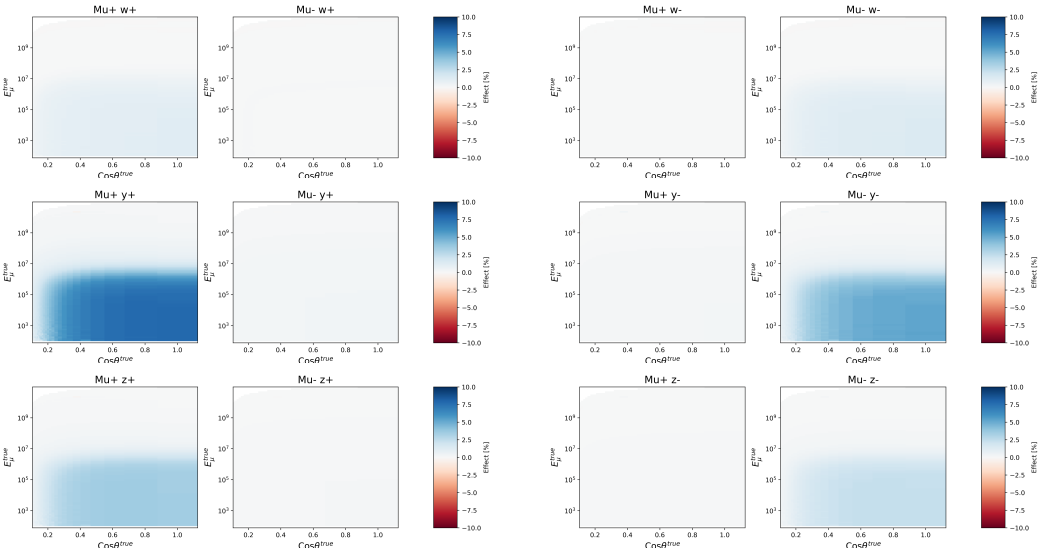

FIGURE 6.2.39: The impacts on underground muon rates from the Barr gradients effecting kaon-production. From top to bottom: W, Y, and Z. Panels on the left show the impact of perturbing the production rate of $K+$, subdivided into the effects on μ_+ (left) and μ_- (right). The same is shown on the right panels for $K-$.

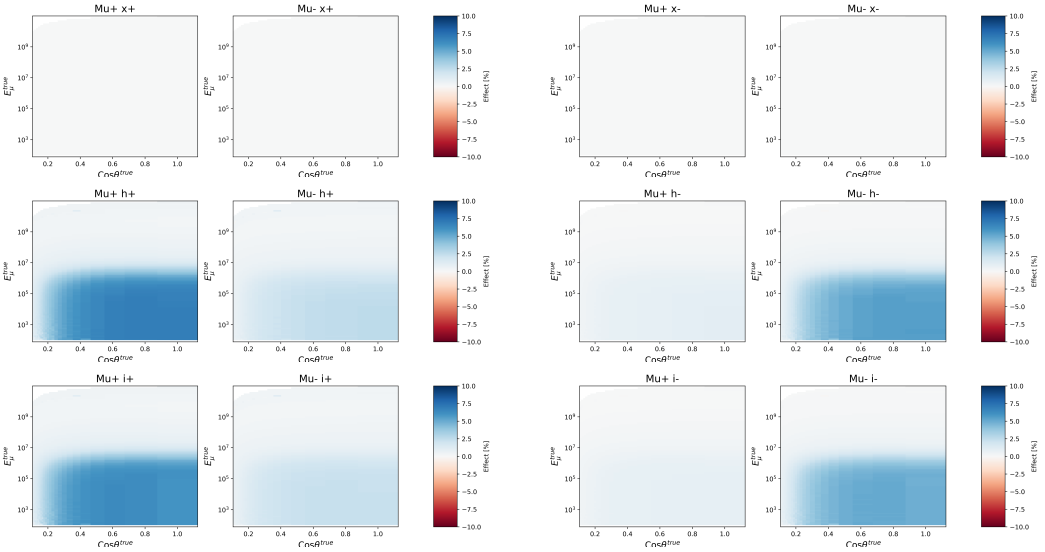

FIGURE 6.2.40: The impacts on underground muon rates from the Barr gradients effecting kaon-production. From top to bottom: X, H, and I. Panels on the left show the impact of perturbing the production rate of $\pi+$, subdivided into the effects on μ_+ (left) and μ_- (right). The same is shown on the right panels for $\pi-$.

Parameter	Minimum	Maximum
$\cos\theta_{reco}$	-1.0	0.0
z_{reco}	n/a	-300
BDT-Track	n/a	0.02
BDT-Cascade	0.2	0.75

TABLE 6.2.5: A series of cuts capable of removing all of the CR muon background.

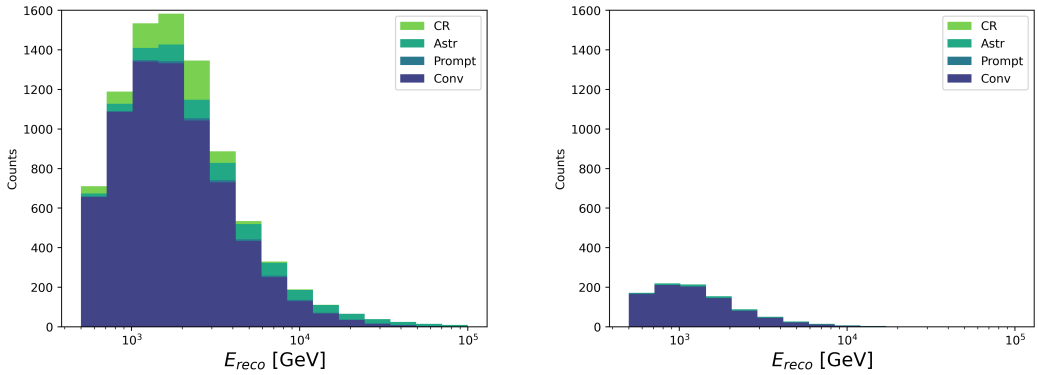

FIGURE 6.2.41: The number of events over the full 10 years of livetime showing the contributions to the total event rate from all even populations. On the left, only a cut on the reconstructed zenith is applied such that $\cos\theta_{reco} < 0$. On the right, the full set of cuts listed in Table 6.2.5 is applied.

events, before (left) and after (right) the extra set of cuts were applied, is shown in Figure 6.2.41. Only 13% of the original neutrino sample passed all cuts.

6.2.11 Normalization

A parameter allowing for the overall normalization of the entire neutrino flux is also allowed to float. It is given a conservative 20% prior driven by a number of effects: livetime O(<1%), ice density O(<1%), volume O(9%) [113], and the neutrino-ice cross-section O(10%) [114]. This normalization does not effect the cosmic ray muon background; it has an independent normalization factor.

Chapter 7

Joint Sterile Analysis

7.1 Overview

This analysis utilizes a binned likelihood-maximization technique comparing some observation, whether it is true data or pseudo-data, against Monte Carlo simulation weighted to the expectation from multiple sterile neutrino hypothesis. Binning is done on reconstructed quantities; bins are linearly spaced in $\cos\theta_{reco}$ and logarithmically spaced in E_{reco}. Sterile neutrino points are chosen uniformly over $|U_{\mu 4}|^2 = \sin^2\theta_{24}$, $|U_{\tau 4}|^2 = \sin^2\theta_{34}\cos^2\theta_{24}$, and Δm^2_{41}. A 19×22 grid in the unitary mixing matrix elements $|U_{\mu 4}|^2$ and $|U_{\tau 4}|^2$, and five discrete mass-squared splittings are explored. These five values are

1. 1.0eV^2 - a commonly chosen reference value used in sterile oscillations studies [115, 116, 51].
2. 3.5eV^2 - a value close to the best-fit point from BEST [20]
3. 5.0eV^2 - a value close to the eight-year IceCube through-going track analysis [22, 23]
4. 7.0eV^2 - a value close to the IceCube 10-year "MEOWS-BDT" 3+1 sterile results.
5. 10.0eV^2 - an intermediate value between those above, and larger mass-squared splitting
6. 100.0eV^2 - a larger mass-squared splitting where fast oscillations will dominate the signal

7.2 Event Selections

Ultimately 7.6 years of tracks and 10 years of cascades were used in this analysis. Two MC samples are used: a track sample generated with approximately 500 years of equivalent livetime and a

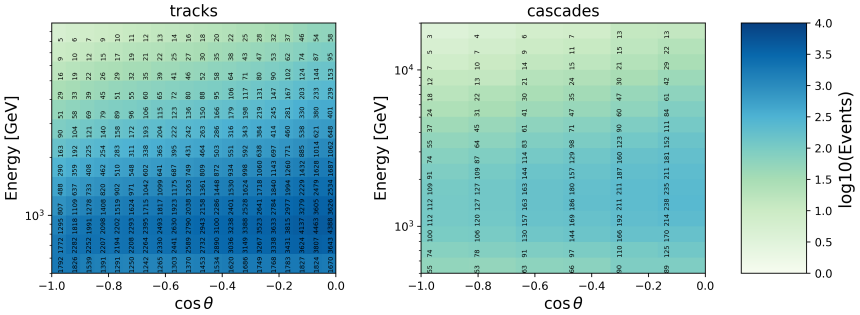

FIGURE 7.2.1: The expected numbers of events in each bin for tracks (left) and cascades (right). Assuming 7.6 years of livetime for tracks and 10 years of livetime for cascades.

cascades sample with approximately 510 years of equivalent lifetime. The central MC expectations are shown in Figure 7.2.1 with tracks on the left and cascades on the right.

7.2.1 Track Event Selection

Since direct neutrino energy reconstruction is impossible for through-going track events, the energy of the muon entering the detector is instead used as a proxy. The track sample of this analysis uses those events with a muon-proxy energy of between 500 GeV and 10 TeV. The event selection is constructed from two sets of cuts, described briefly here, and at length in References [22, 23, 90]. The first of these is the "Golden Filter":

1. Discard events for which fewer than fifteen DOMs are triggered or fewer than six are triggered on direct light.

2. For events with $0 \leq \cos\theta_{\mu}^{reco} \leq 0.2$, discard if the total charge $Q_{tot} < 100$ photoelectrons (PEs) or if the average weighted charge distance < 200 meters/PE.

3. Remove all events with a reconstructed value of $\cos\theta_{\mu}^{reco} \geq 0.2$. This removes down-going track like events that are likely cosmic ray muons.

4. Discard all events with a reconstructed track length less than 200 meters, or a track smoothness < 0.6.

These cuts produce a sample with ν_{μ} purity greater than 99%. An additional "Diamond filter" is also used, selecting events after applying these cuts

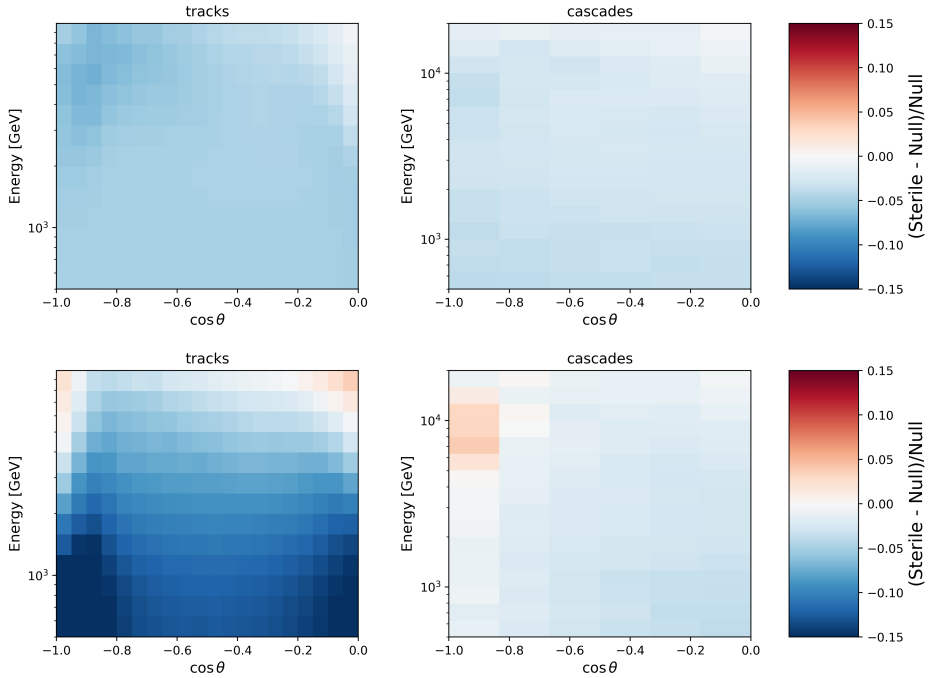

FIGURE 7.2.2: Two signatures of sterile neutrinos in reconstructed space. On the top, the expected disappearance for tracks (left) and cascades (right) for a sterile neutrino model with $\sin^2(2\theta_{24}) = 0.1$ and $\Delta m^2_{41} = 4.5$ eV^2. The same is shown on the bottom but with $\sin^2(2\theta_{34}) = 0.05$.

1. Discard events with fewer than twelve direct light DOM triggers.

2. Discard events with $Q_{tot} \leq 20$ PE outside DeepCore.

3. Discard events with fifteen or fewer DOMs triggered outside DeepCore.

4. Discard events with $\cos\theta_{\mu}^{reco} > 0.05$.

The total track sample is composed of all events which satisfy either the Golden or the Diamond filter.

With these event selections, strong appearance and disappearance signatures are possible. Two possible signatures of sterile neutrino oscillations using these event samples are shown in Figure 7.2.2 in analysis space.

7.2.2 Cascade Event Selection

This final level event filter was developed and published previously for Ref [117]. The likelihood-based reconstruction algorithm monopod is first run on events surviving the level three filter

described in Section 5.3; several quantities are fit and logged including the reconstructed energy, interaction vertex, direction, and a reduced likelihood for the fit (the smaller the reduced log-likelihood is the better). Events for which the reduced algorithm fail, or which have a reduced log-likelihood (rLogL) of greater than 9.1, are discarded. A series of cuts are then applied to reduce the muon contamination:

1. Discard events which are inside the dust layer unless they are high-energy or have rLogl$<$ 7.5.
2. Discard events with a reconstructed vertex with $z > 500$ or $z < -500$.
3. Discard events which are reconstructed as being near the edge, unless they are well-reconstructed with rLogl$<$ 7.6.
4. Discard events near the top or bottom of IceCube unless they are well reconstructed.
5. Discard events with very large, negative, photon delay times. This is common for triggers resulting from uncorrelated bundles of atmospheric cosmic ray muons.

A Boosted Decision Tree classifier is then run on the events which survive these cuts. Only those events which satisfy an energy-dependent cut on the cascade score $s_{cascade}$ are kept. The cut is shown below in Figure 7.2.3 and Equation (7.2.2),

$$s_{\text{cascade}} > 1 - \left(\frac{1}{A + \exp\left[-B(\log E_{reco} - C)\right]} + D \right), \tag{7.2.1}$$

where the constants $A = 1.539$, $B = 5$, $C = 4.1$, and $D = 0.25$.

7.3 Fast Monte Carlo, Event Merging

For the track sample, around twenty billion MC events were simulated. Directly reweighting each of these simulated events for every minimizer step was found to be computationally intractable. To alleviate these issues, a "Fast Monte Carlo" algorithm is used to merge events into meta events, which themselves would be reweighted in fits.

Events are first weighted according to a flux hypothesis, and the contributions to an event's conventional, prompt, and astrophysical weight are all calculated and stored separately. Events

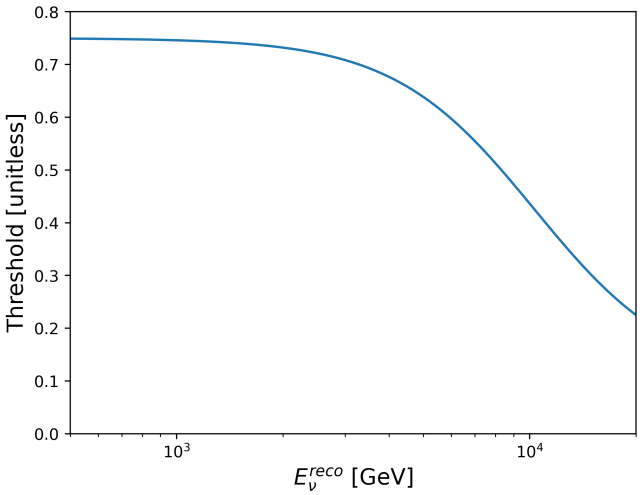

FIGURE 7.2.3: Cascade score $s_{cascade}$ threshold, as a function of energy, below which events are cut.

are then binned, in reconstructed quantities, into a fine grid whose bin widths are a fraction of the normal analysis bin widths; this fraction is defined as the *fastmode scaling*. As an example, a fastmode scaling of 0.5 would use twice as many bins along each axis in analysis space[1], and a scaling of 0.1 would use 10 times as many bins along each axis.

Events within each of these fine bins are then merged into meta-events; the separate flux-weights are added directly, and a weighted-average is done for analysis quantities like energy and zenith. The weighted average is calculated according to Equation (7.3.1) for analysis quantity A in fastmode bin α.

$$A^{\alpha}_{meta} = \frac{\sum_i^n A_{\alpha,i} \left(w^{conv}_{\alpha,i} + w^{prompt}_{\alpha,i} + w^{astro}_{\alpha,i} \right)}{\sum_i^n \left(w^{conv}_{\alpha,i} + w^{prompt}_{\alpha,i} + w^{astro}_{\alpha,i} \right)} \tag{7.3.1}$$

The sum is carried out over all n events in a fastmode bin. These meta-events are then saved with their summed flux-weights and weighted-average analysis quantities. This procedure is carried out for each tested physics hypothesis, although it is only applied to the track sample. A fastmode scaling of 0.1 was used in this analysis and values smaller than 0.25 have been found to produce stable results.

This Fast Monte Carlo procedure was carried out for all tested physics hypotheses.

[1] energy, zenith

7.4 Analysis Test Statistic

The likelihood $\mathcal{L}(\vec{\Theta}, \vec{\eta})$ used in this analysis is defined as the probability of observing a given set of data, or pseudo-data, assuming some physics hypothesis. It is quantified as

$$\mathcal{L}(\vec{\Theta}, \vec{\eta}) = \prod_{i=0}^{\text{bins}} \mathcal{L}_{eff}\left(w_i^{sum}, w_{2,i}^{sum}, k_i\right), \tag{7.4.1}$$

where w_i and $w_{2,i}$ are the sums of the MC weights and MC weights squared, respectively, in bin i; k_i is the observed number of events (or pseudo-events). $\vec{\Theta}$ is the tested physics hypothesis and $\vec{\eta}$ the set of nuisance parameters.

The effective likelihood function $\mathcal{L}_{eff}$, defined in Reference [118], is part of a family of likelihood metrics used to account for MC statistical uncertainty. We use the form where

$$\alpha = \frac{\mu^2}{\sigma^2} + 1 \qquad \text{and} \qquad \beta = \frac{\mu}{\sigma^2}. \tag{7.4.2}$$

In the case where each MC event is just one event, the mean and variance are defined by $\mu = w_i$ and $\sigma^2 = w_{2,i}$, respectively. For the track sample, meta events are used, and $\sigma^2 = w_{2,i}/n$, where n is the number of MC events used to generate that meta-event. The effective likelihood function takes the form of

$$\mathcal{L}_{eff}(\vec{\Theta}|k) = \left(\frac{\mu}{\sigma^2}\right)^{\frac{\mu^2}{\sigma^2}+1} \Gamma\left(k + \frac{\mu^2}{\sigma^2} + 1\right) \left[k!\left(1 + \frac{\mu}{\sigma^2}\right)^{k+\frac{\mu^2}{\sigma^2}+1} \Gamma\left(\frac{\mu^2}{\sigma^2} + 1\right)\right]^{-1}, \tag{7.4.3}$$

where Γ is the gamma function.

The set of nuisance parameters that quantify systematic uncertainties are themselves constrained by some prior. The prior is used to weight the likelihoods which is maximized to form a profile likelihood defined as

$$\mathcal{L}_{\text{profile}}\left(\vec{\theta}\right) = \max_{\vec{\eta}}\left[\mathcal{L}(\vec{\Theta}, \vec{\eta})\Xi(\vec{\eta})\right] \tag{7.4.4}$$

	2DOF	3DOF
68%	2.72	3.51
90%	4.61	6.25
95%	5.99	7.81
99%	9.21	11.34

TABLE 7.4.1: A table listing the test-statistic thresholds assuming Wilk's theorem holds.

where $\Xi(\vec{\eta})$ is the total likelihood penalty for the set of nuisance parameters $\vec{\eta}$. We then construct an analysis test statistic (TS) for producing confidence intervals, which we define as

$$\begin{aligned} TS(\vec{\Theta}) &= -2\left[\log \mathcal{L}_{\text{profile}}(\vec{\Theta}) - \log \mathcal{L}_{\text{profile}}(\vec{\Theta}_{min})\right] \\ &= -2\Delta \log \mathcal{L}_{\text{profile}}(\vec{\Theta}) \\ &= -2\Delta\text{LLH} \end{aligned} \tag{7.4.5}$$

where $\vec{\Theta}_{min}$ is the sterile hypothesis that maximizes the likelihood, and best matches the data (or pseudo-data): the best fit point.

For fit-scans, we assume that this test statistic satisfies Wilk's Theorem [119], and that $\chi^2 = TS$. Threshold values of χ^2 for a given number of degrees of freedom k and a desired confidence level γ are related by

$$\gamma = \frac{1}{2^{k/2}\Gamma(k/2)} \int_0^{\chi^2_{thresh}} dx x^{k/2-1} e^{-x/2}. \tag{7.4.6}$$

This functional form is inverted to solve for the TS threshold for a given confidence level and number of degrees of fredom. A few example thresholds commonly used here are shown in Table 7.4.1 [1].

7.5 Tests

A series of tests were performed to validate the implementation of the nuisance parameters and verify the performance of the fitting framework. Throughout this section, we will refer to two models of the conventional flux: one uses the model from the 8-year sterile neutrino analysis [22, 23]; its set of nuisance parameters are listed in Table 6.2.1. The other model uses the

daemonflux [91] nominal conventional flux model and conventional flux uncertainties ; its set of nuisance parameters are listed in Table 6.2.2. Both were investigated and in the process we found that the 8-year analysis model could yield spurious 3+1 signatures following a mismodeling of the conventional neutrino flux. Since Daemonflux was found to the model less likely to yield spurious signals of sterile neutrinos, it was used as the nominal model for fits to the data.

7.5.1 Previous Results Cross-Check

First we verified we could recover the same sensitivities as from the original eight-year analysis, whose sensitivities are published in References [22] and [23].

New fluxes, gradients, and Fast MC, were generated in logarithmic steps in $\sin^2(2\theta_{24})$ and Δm^2_{41} space using the same techniques as what are used for the joint fits over (Δm^2_{41}, $|U_{\mu 4}|^2$, $|U_{\tau 4}|^2$). Using the new PISA framework, we ran a global-scan of nuisance parameter fits to an Asimov realization: the nominal expectation of the experiment without nuisance parameter or statistical fluctuations. The resulting 90% confidence level sensitivities from the track sample alone are shown in Figure 7.5.1 alongside the sensitivities from the 8-year analysis. From this we conclude that the new fitting implementation in PISA is valid and can be used.

7.5.2 Inject-Recover Systematic Tests

Pseudo-experimental results, or 'realizations,' are generated by perturbing all nuisance parameters according to their priors, simultaneously, and saving the expected event rates without additional statistical variation applied. Fits are then carried out to each of these realizations.

The results are tabulated in two figures where the true injected and recovered values are shown: in Figure 7.5.2 the fits are kept with the priors' centers kept at their original value, and in Figure 7.5.3 the priors are changed to the value of the injected nuisance parameter. In Figure 7.5.2, the flatter the trend is then the more tightly-constrained its prior is compared to the shape effects caused by the nuisance parameter itself; in Figure 7.5.3, the injected values are all recovered exactly. We conclude that the minimization framework successfully recovers the true minimum in fits.

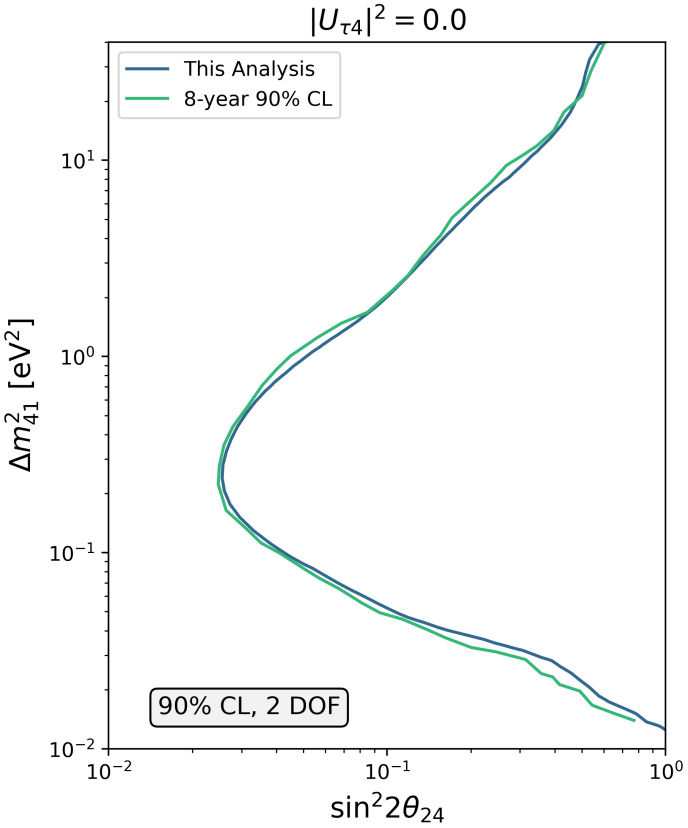

FIGURE 7.5.1: The 90% CL sensitivity contours for two degrees of freedom, using only the track sample, as determined for this analysis (yellow) and the original 8-year tracks sample (green).

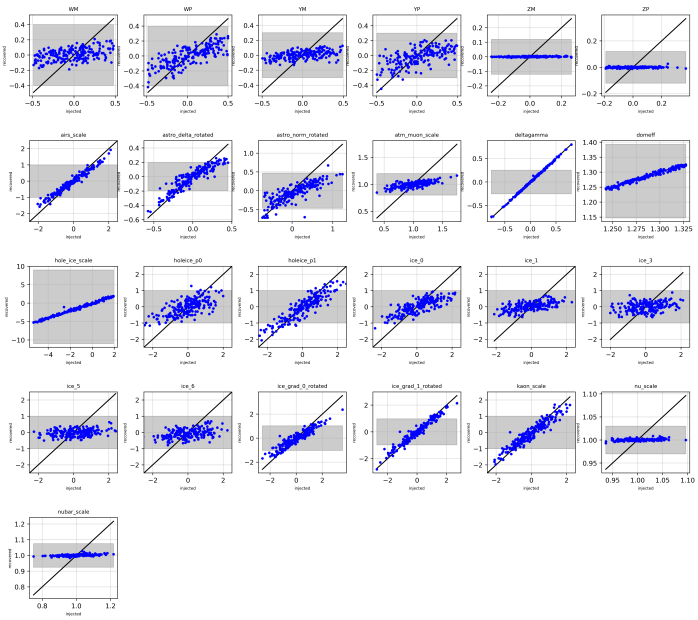

FIGURE 7.5.2: Fit results after injecting various perturbed values for each nuisance parameter and running the fitter. A shaded gray region demonstrates the 1σ prior width on the nuisance parameter's prior.

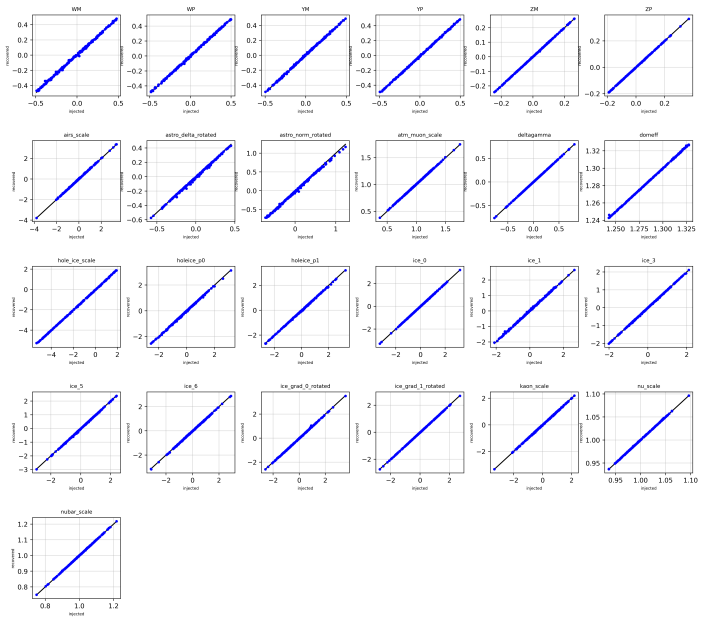

FIGURE 7.5.3: Fit results after injecting various perturbed values for each nuisance parameter and running the fitter. Priors are adjusted in each fit according to the injected values.

7.5.3 Systematic Impact Tests

Another test was done to characterize how strongly each nuisance parameter, or set thereof, effects overall sensitivity. Nuisance parameters were collected into "bundles," and Asimov sensitivity scans [120] were performed while fixing all nuisance parameters of that bundle to their central values. The constraints, compared to the full fits, show the impact of fixing those nuisance parameters. The bundles are

1. Norm(alization): everything is fixed except for the normalization.
2. Astro(physical): astrophysical normalization and the spectral index
3. Conv(entional): Daemonflux [91] parameters, Barr parameters, AIRS scale, and the kaon-nucleon cross-section uncertainty
4. Det(ector): hole ice uncertainty, DOM efficiency, and the bulk-ice uncertainty
5. Muon: the CR muon background[2]

The systematic impact tests were calculated twice for the two conventional flux models: once using the model from the previous 8-year analysis, and once using daemonflux. Both are shown at 90% confidence level and with three degrees of freedom in Figure 7.5.4. For both models we find that the conventional flux uncertainty has the strongest effect on our sensitivity while the detector systematic uncertainties have the second strongest effect.

7.5.4 Signal Inject-Recover

Various points were chosen along the Asimov 90% CL thresholds to test the fitting framework's ability to recover constraints of sterile-neutrino signal-like measurements. Two each were chosen along the contours at 1.0, 4.5, and 10 eV^2; one more was chosen at 100 eV^2. Additionally, three more points were chosen off-grid at various points. Of those three, one was selected as the recovered best-fit point from the 8-year track analysis. Then, we ran a full fit-scan on an Asimov realization generated for each of these simulated signals. Injected values are recovered in all cases

[2]Because of the large, extra, error introduced by the muon background, for this systematic impact test a special realization is generated and fit to where there no muon contribution is added at all.

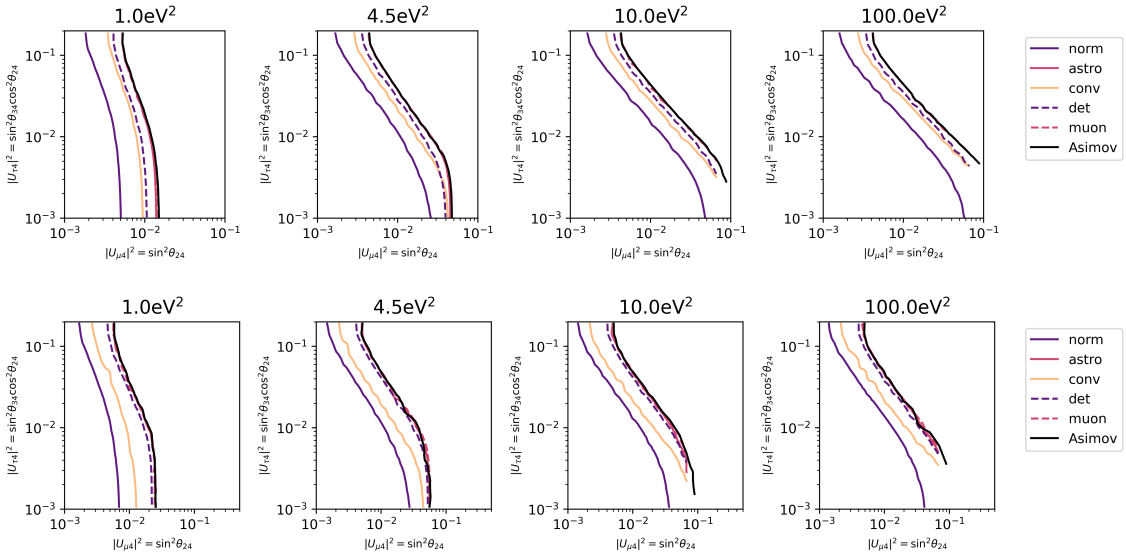

FIGURE 7.5.4: The sensitivity contours for fixing each bundle of nuisance parameters. Contours are shown at 90% CL and 3DOF for various mass-squared splittings; from left to right: 1.0eV^2, 4.5eV^2, 10.0eV^2, and 100.0eV^2. Top: results when using the conventional flux model used in the 8-year analysis, and on bottom: the results when using daemonflux.

where a signal is injected at a grid-point. For the cases where a signal is injected near a grid point, the recovered best fit is sufficiently close, and we find that the minimizer is able to accurately recover an injected 3+1 signal. Exclusion contours for these signal inject-recover tests are shown in Figures 7.5.5 through 7.5.8.

7.6 Sensitivities

7.6.1 Asimov Sensitivity

Two Asimov fit-scans were carried out: once using the conventional flux model from the 8-year analysis and one using daemonflux. The 90% confidence level χ^2 threshold was calculated for three degrees of freedom for each fit scan, and the resulting sensitivity contours are shown in Figure 7.6.1 using daemonflux. Sensitivities for the two different models are shown, overlain, in Figure 7.6.2; here the astrophysical flavor ratio uncertainty was not included in either scan. The change in sensitivity where daemonflux is used as the nominal conventional flux model is due

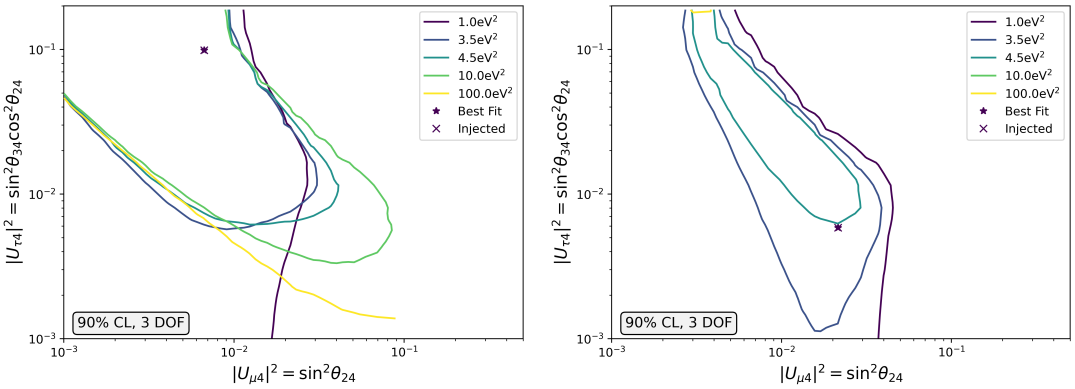

FIGURE 7.5.5: Two signal inject-recover tests.

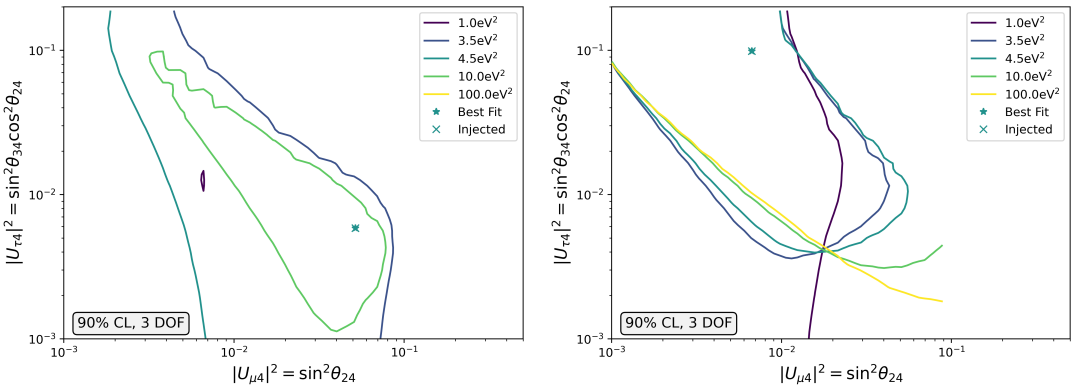

FIGURE 7.5.6: Two signal inject-recover tests.

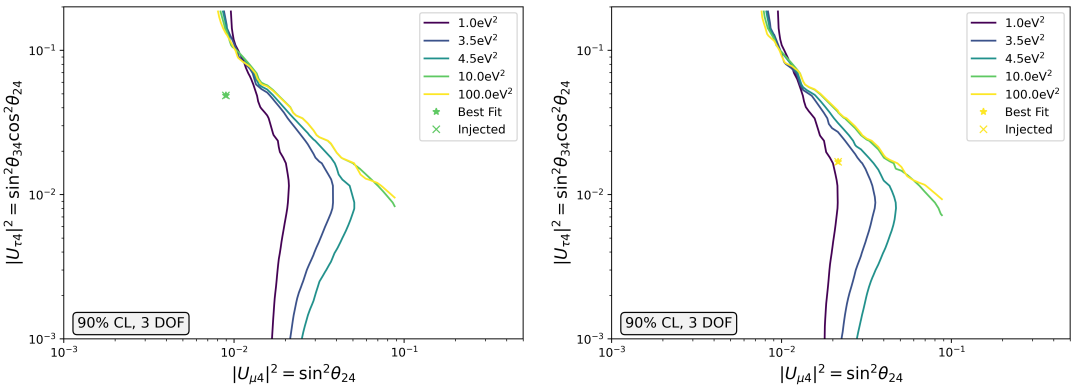

FIGURE 7.5.7: Two signal inject-recover tests.

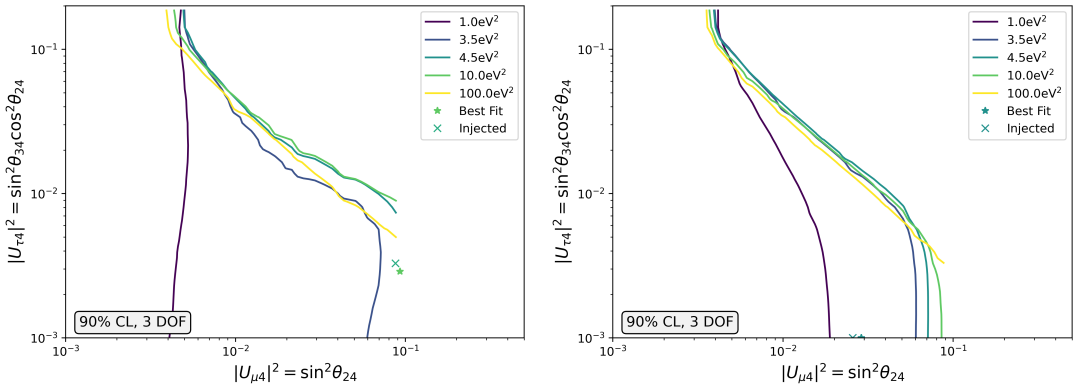

FIGURE 7.5.8: Two signal inject-recover tests.

to the difference in the predicted charge ratio; daemonflux predicts a higher charge ratio and therefore a smaller signature from the resonant $\bar{\nu_\mu}$ disappearance.

These results are plotted compared to the previous phenomenological predictions in Figure 7.6.3. Sensitivities are compared at 90% confidence level and assuming two degrees of freedom $\Delta m^2_{41} = 1.0$ eV^2. The sensitivities calculated for this analysis are similar, although somewhat worse than those predicted earlier in Chapter 4. This is not surprising; here a full treatment of systematic uncertainty is used. We also compare the two degrees of freedom sensitivity at 1.0 eV^2 for this analysis to the results of Super-Kamiokande [116] and DeepCore [115] in Figure 7.6.4. We find that this analysis has strong sensitivity to $|U_{\mu 4}|^2$ when compared to other existing constraints.

7.6.2 Median Sensitivities

We simulated 80 experimental results assuming no new physics by applying Poissonian statistical fluctuations on a nominal event rate. A full fit scan was then carried out for each of these pseudo-experiments, and the exclusion contours were drawn for each. The median location of the contour, the bands containing 68% of the contours, and the bands containing 95% of contours were then calculated for contours at 90% and 95% confidence level. The bands over $|U_{\mu 4}|^2$ are calculated as a function of $|U_\tau 4|^2$ for each explored mass squared splitting. They are then shown in Figure 7.6.5 for contours at 90% CL (top) and 95% CL (bottom). The median sensitivity was observed to converge to the Asimov sensitivity: suggesting Wilks' theorem is valid here.

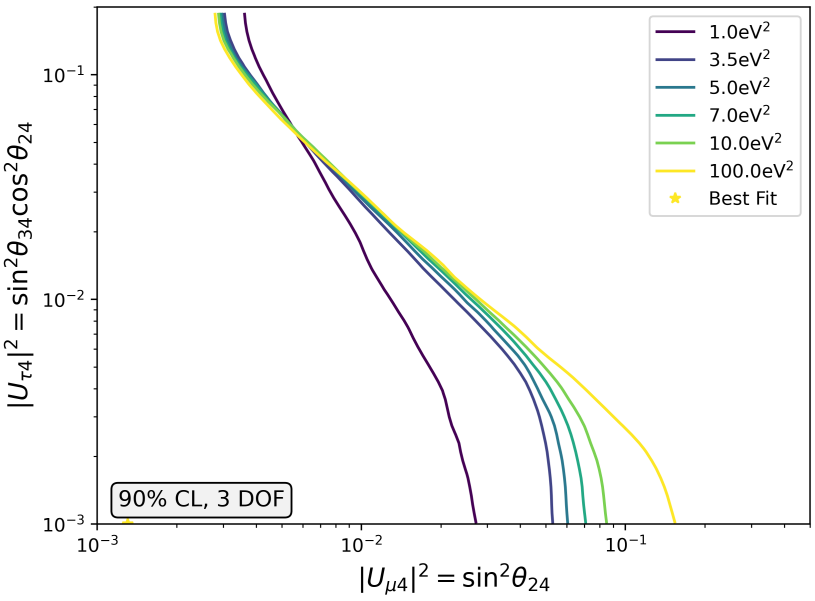

FIGURE 7.6.1: The 90% confidence level sensitivity contours with three degrees of freedom for this analysis; using daemonflux for the conventional flux model

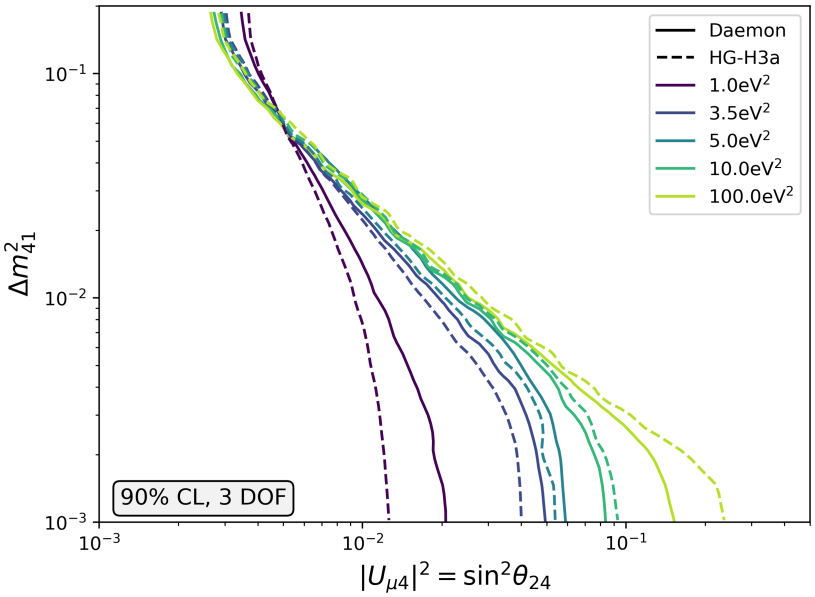

FIGURE 7.6.2: A comparison of the sensitivities calculated for a daemonflux conventional flux model and the conventional flux model used in the 8-year analysis (labeled as *HG-H3a*).

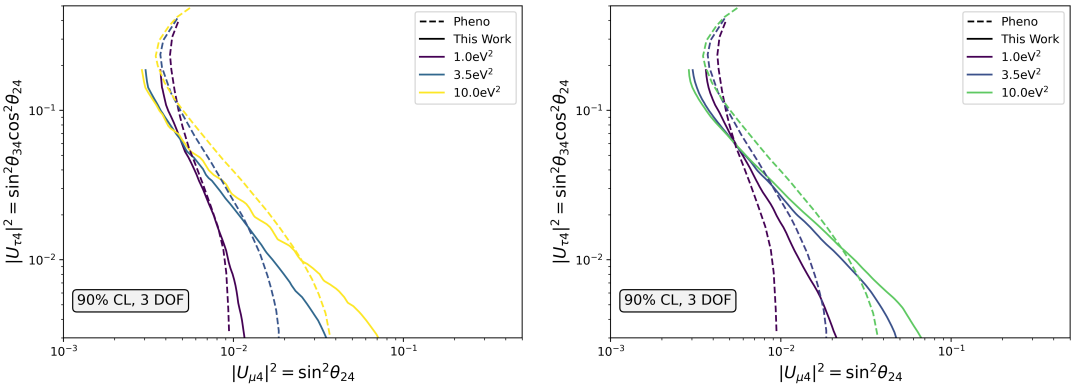

FIGURE 7.6.3: The 90% confidence level sensitivity contours for this analysis compared with previous phenomenological predictions with three degrees of freedom at $\Delta m^2_{41} = 1.0$ eV^2, 3.5 eV^2, and 4.5 eV^2. On the left, using the 8-year analysis conventional flux model, and on the right using daemonflux.

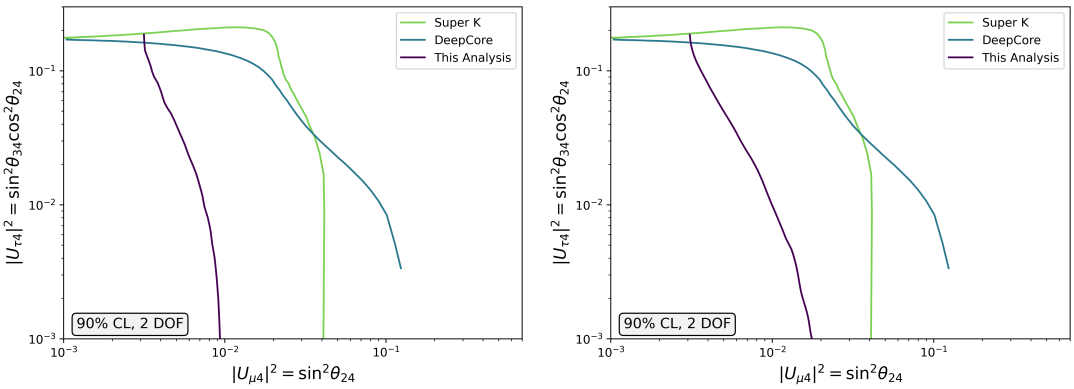

FIGURE 7.6.4: On the left (right) the 90% confidence level sensitivity contours for this analysis with two degrees of freedom at $\Delta m^2_{41} = 1.0$ eV^2 using the same conventional flux model as in the 8-year analysis (daemonflux). Sensitivities from DeepCore [115] and Super-K [116] at 1.0eV^2 are provided for comparison.

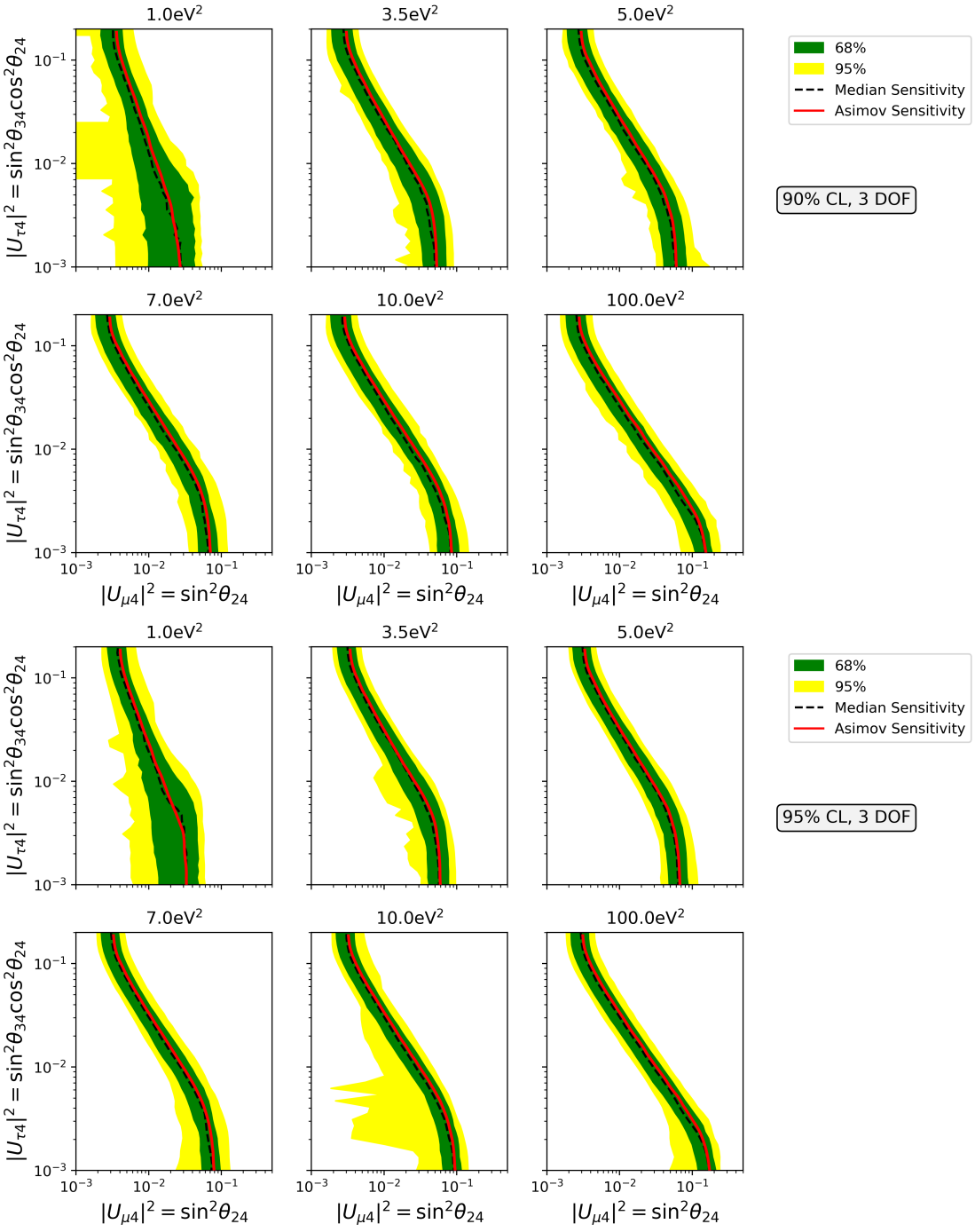

FIGURE 7.6.5: "Brazil Bands" for 90% CL contours (top) and 95% CL contours (bottom).

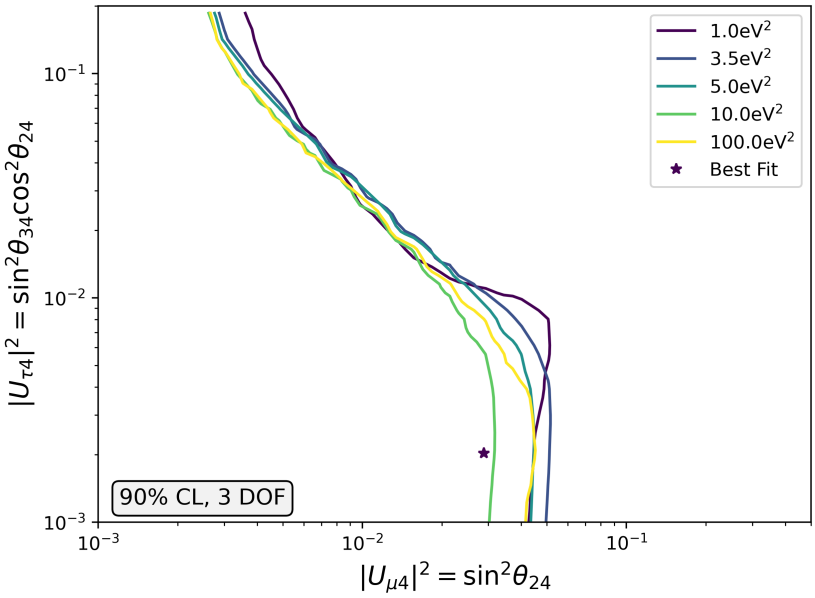

FIGURE 7.7.1: The 90% CL contours for three degrees of freedom. A daemonflux flux is injected and a flux model consistent with the 8-year IceCube sterile search is assumed. The fit prefers the 3+1 sterile neutrino model at a significance of $-2(\mathcal{L}_{best} - \mathcal{L}_{null}) = 4.68$.

7.7 Mismodeling Tests

There is always the possibility that an inaccurate model of some process could mimic the signatures of a 3+1 sterile neutrino model. Several possible sources of such a mismodeling were investigated.

7.7.1 Conventional Neutrino Flux Mismodeling

Newer high-energy IceCube oscillations analyses had begun to adopt the daemonflux [91] cosmic ray and conventional neutrino model at the start of this analysis. To test its relevance we generated a pseudo-experiment where daemonflux is the true neutrino flux with no new physics. Then, fits were run assuming a neutrino flux resulting from a Hillas-Gaisser H3a cosmic ray model [86], Sibyll2.3c interaction model [88], and an AIRS-like atmosphere model [89]. This is the same as the model used in the 8-year IceCube sterile search [22, 23]. The result of a joint-fit are shown in Figure 7.7.1. In this case, a 3+1 sterile model is preferred over the injected (null) physics values with a significance of $-2(\mathcal{L}_{best} - \mathcal{L}_{null}) = 4.68$.

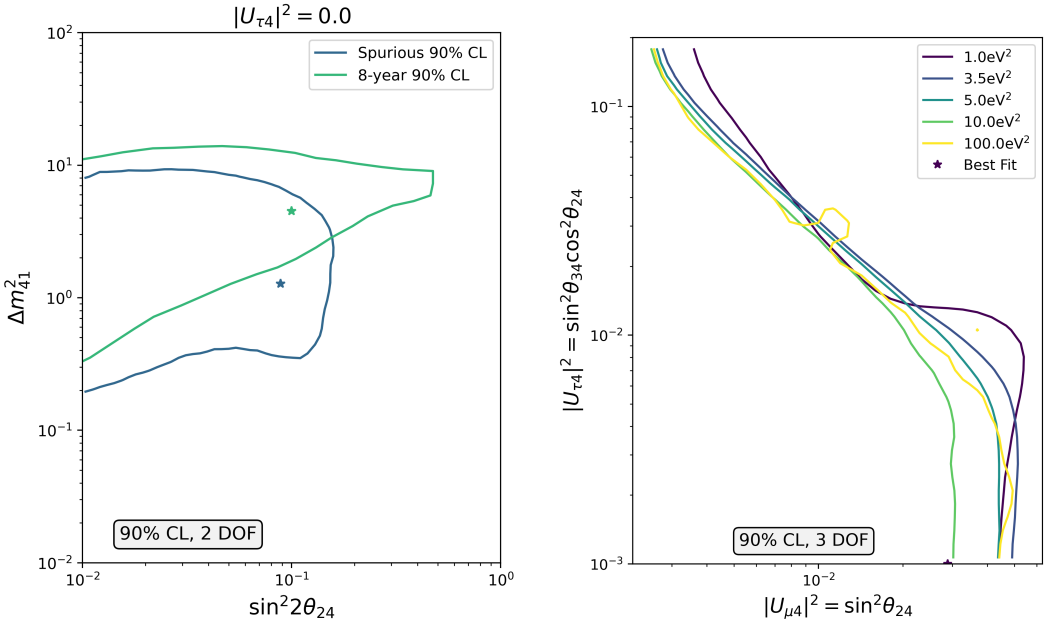

FIGURE 7.7.2: Fit results after injecting daemonflux, but fitting assuming the flux model used in the IceCube 8-year sterile search. (Left) the 90% CL contours for two degrees of freedom, $-2(\mathcal{L}_{best} - \mathcal{L}_{null}) = 5.02$ after fitting over $(\Delta m^2_{41}, \sin^2(2\theta_{24}))$, the results from the 8-year IceCube sterile search are overlain [22, 23]; (right) the 90% CL contours for three degrees of freedom, $-2(\mathcal{L}_{best} - \mathcal{L}_{null}) = 4.7$ after fitting over $(\Delta m^2_{41}, |U_{\mu 4}|^2, |U_{\tau 4}|^2)$

Further, two similar fit-scans were carried out using only tracks. In the first, the fit-scan is carried out fixing $|U_{\tau 4}|^2$ to zero but allowing a more fine scan in Δm^2_{41}; the second is done in a three-degree fit over $(|U_{\mu 4}|^2)$, $(|U_{\tau 4}|^2)$, and Δm^2_{41}. These scans are shown in Figure 7.7.2; in the 2D scan a spurious closed-contour result is recovered at the 90% confidence level. This suggests that if daemonflux is a better description of the truth, then assuming the model used in the 8-year IceCube sterile analysis is likely to yield spurious 3+1 signals given no new physics, or artificially strong signals given sterile neutrinos.

The converse was also investigated; fits were run assuming daemonflux, with its model of conventional flux uncertainty, while the conventional neutrino flux model used in the 8-year IceCube sterile search was injected as a true model. In this case, the best fit was consistent with a three-neutrino hypothesis, as shown in Figure 7.7.3. This suggests that if the model used in the 8-year analysis is a better description of the truth, then assuming daemonflux is not likely to yield spurious signatures of 3+1 sterile neutrinos given no new physics.

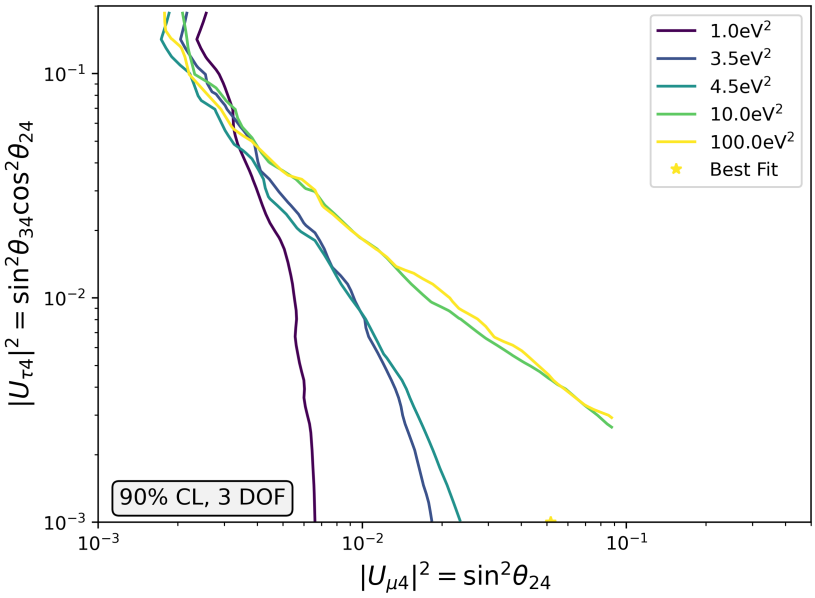

FIGURE 7.7.3: The 90% CL contours for three degrees of freedom. A conventional flux model consistent with the 8-year IceCube sterile search is injected and daemonflux is assumed in fits. $-2(\mathcal{L}_{best} - \mathcal{L}_{null}) = 0.6$.

Two additional checks were run. A neutrino flux prediction was made using the Global Spline Fit [92], the Sibyll2.3c interaction model [88], and the US Standard Atmospheric model [95]. Fit scans were run on a pseudo-experimental result generated from this flux assuming (1) daemonflux and its uncertainties of the cosmic ray flux, and (2) the model used in the 8-year IceCube sterile search. These results are shown in Figure 7.7.4. In both cases, no statistically significant signal is seen; each one is consistent with the injected null model.

In order to minimize the possibility that our choice of conventional neutrino flux model could bias a measurement of sterile neutrino oscillations, or yield a spurious signal, we opted to fully adopt daemonflux as our nominal flux model and as our description of conventional flux uncertainties.

7.7.2 Astrophysical Mismodeling

Recently, the IceCube Neutrino Observatory became the first experiment to observe an excess of astrophysical neutrinos coming from the Milky Way[121]. This extra population of neutrinos is produced from cosmic-ray interactions with the interstellar medium throughout our galaxy:

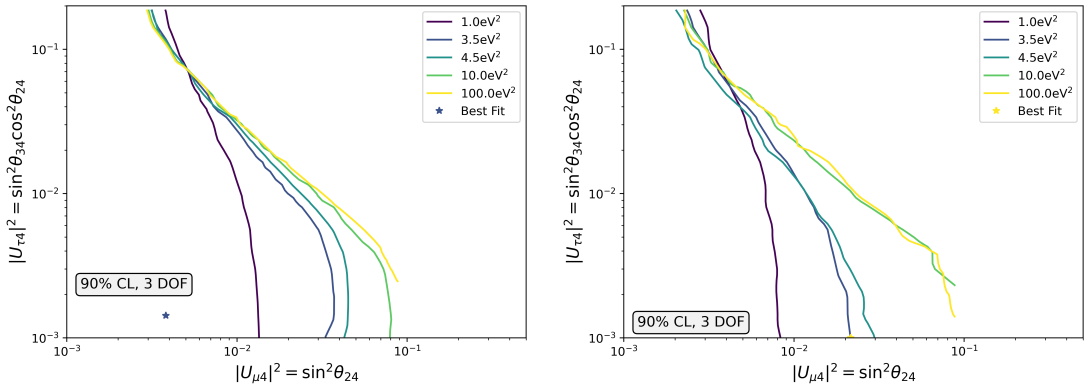

FIGURE 7.7.4: On the left (right), fit results after injecting the new GSF model while assuming the model used in the 8-year IceCube sterile search (daemonflux), $-2(\mathcal{L}_{best} - \mathcal{L}_{null}) = 0.6$ (0.2).

causing the Milky Way to glow with neutrinos. In this, and similar oscillations analyses, the astrophysical neutrino flux has been assumed to be isotropic. A test was carried out where a non-isotropic flux modeling the Milky Way, the KRAγ-50 [122] model, is injected in addition to an isotropic flux but with no new physics signatures. A fit scan is then ran assuming an isotropic flux and the resulting likelihood profile is found. The exclusion contours, with best fit, are shown in Figure 7.7.5. No spurious preference for new physics is seen, and so we conclude that any anisotropic excess in the astrophysical neutrino flux will not bias this analysis' result.

7.7.3 Astrophysical Flavor Mismodeling

Since the chosen prior does not span the full range of astrophysical flavor ratios allowed at 3σ, a flavor-ratio mismodeling test was carried out. A pseudo-experimental result was generated assuming a flavor ratio ($f_e : f_\mu : f_\tau$) of (0.35,0.2,0.45); an allowed value that is not spanned by the astrophysical nuisance parameter. A fit-scan was then carried out injecting the above as the truth, and the resulting 90% CL contours are shown in Figure 7.7.6. The nuisance parameter pulls at the best fit are also shown in Figure 7.7.7. As can be seen, the flavor ratio pulls down to match the injected flavor ratio, and no spurious new physics signature is seen. From this we can conclude that the analysis-level representation of flavor space is sufficiently spanned by this nuisance parameter, and that a true flavor ratio not explicitly accessible will not bias our results.

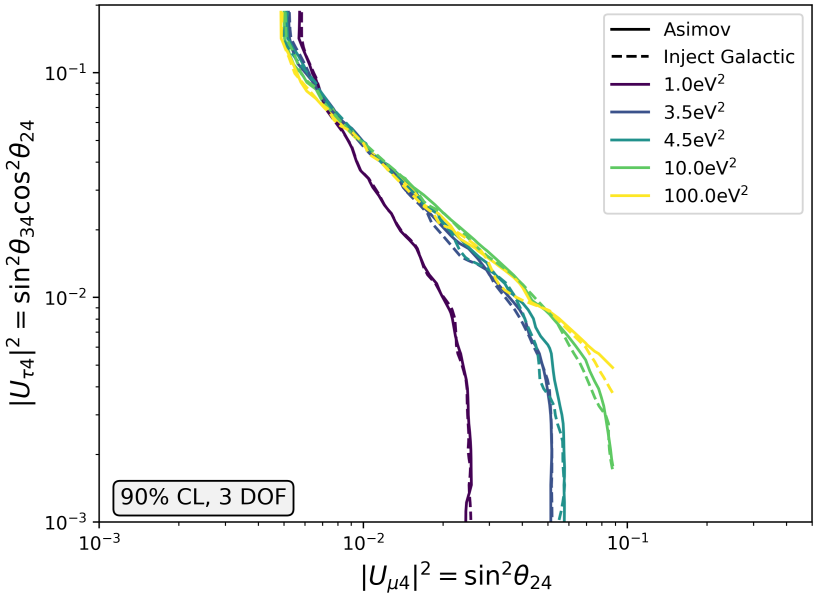

FIGURE 7.7.5: Exclusion contours at 90% CL and for three degrees of freedom for an Asimov realization (solid) and a KRAγ-50 injected neutrino flux (dashed). The contours have considerable overlap and no spurious 3+1 signatures are observed

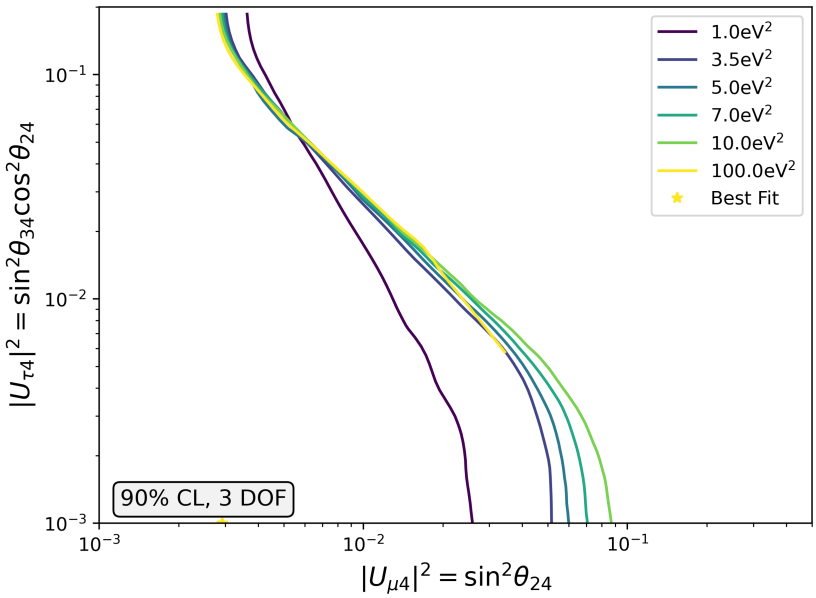

FIGURE 7.7.6: Exclusion contours at 90% CL and for three degrees of freedom while injecting an astrophysical flavor ratio outside the values spanned by the nuisance parameters.

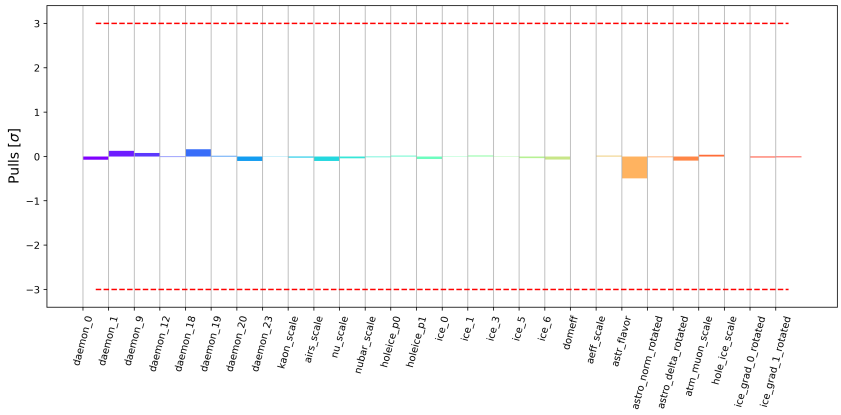

FIGURE 7.7.7: The pulls at the best fit point in the fit-scan shown in Figure 7.7.6.

7.7.4 CR Muon Mismodeling

As discussed earlier in Section 6.2.10, the cosmic ray muon background is considerable for the cascades sub-sample. In addition to those methods in-place to account for its contributions, a few tests were run to check if under-predicting the CR muons could mimic a 3+1 sterile neutrino signature. To this end, fit-scans were run under different situations:

(a) A normal amount of CR muons are injected, but none are assumed, with no MC statistical error

(b) double the expected CR muons are injected, but the normal amount is assumed

(c) double the expected CR muons are injected, but none are assumed and with no additional MC statistical error

The resulting contours are shown in Figures 7.7.8 through 7.7.9 below. No spurious 3+1 sterile signature was seen in any of these tested cases, and so we can conclude that any reasonable cosmic ray muon fluxes beyond our nominal expectation will not bias this analysis significantly.

7.8 Unblinding Procedure

The unblinding procedure used in this analysis is shown in Figure 7.8.1. First, a full 3D fit-scan is applied while fitting to only 5% of the full dataset. No best fit parameters or likelihoods are

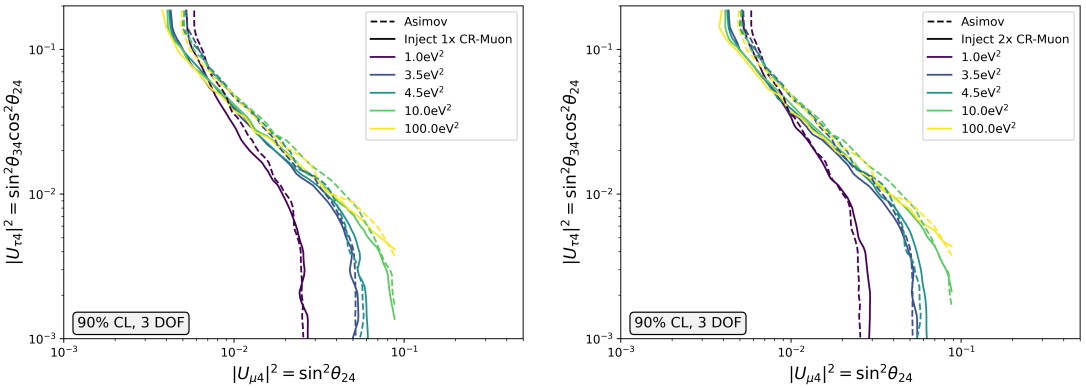

FIGURE 7.7.8: The exclusion contours for situation (a) on the left and (b) on the right with the Asimov sensitivities provided for context

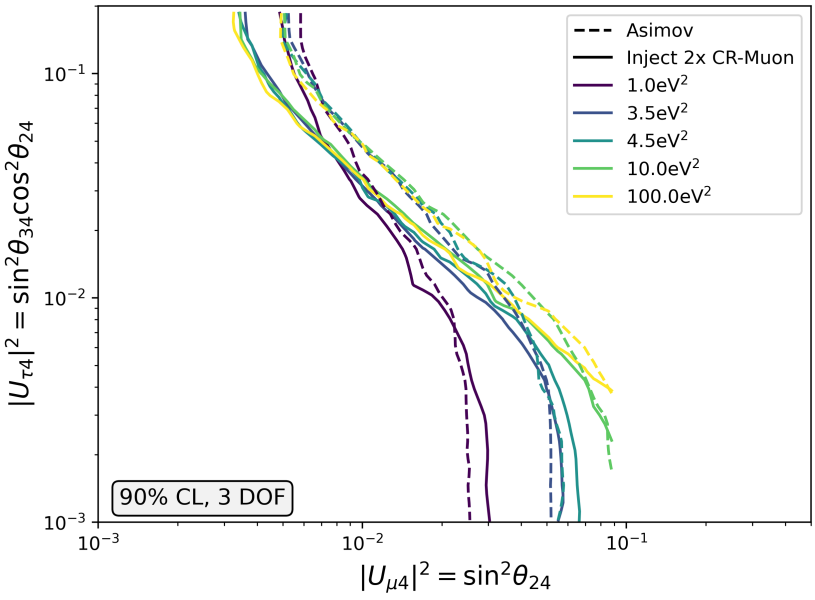

FIGURE 7.7.9: The exclusion contours for situation (c) with the Asimov sensitivities provided for context

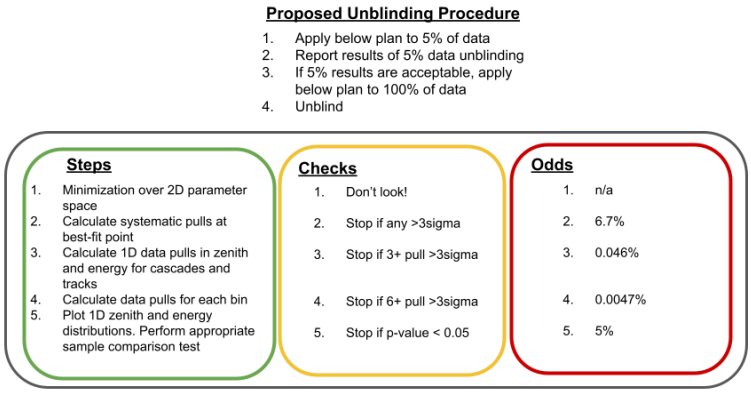

FIGURE 7.8.1: The unblinding procedure used in this analysis and expected probabilities of satisfying the stop condition.

reported. At the best fit point, if any nuisance parameters have a fit value more than 3σ away from their central values, we stop. Then we count the number of bins whose best fit values are more than 3σ away from their expected value; if more than 3 satisfy this condition, we stop.

7.8.1 5% Data Blind Fit Results

First, a fit on 5% of the data was carried out to validate basic functionality and ensure no glaring inconsistencies between data and MC exist. A full fit scan is carried out over the full new-physics phase space, and the best-fit point is found. The nuisance parameter pulls are determined, and shown in Figure 7.8.2; none pulled above 3σ.

Then the 1D pulls were calculated and the 1D distributions calculated; none pulled above 3σ. These are shown in Figure 7.8.3. Finally, the 2D distribution of pulls were calculated and are shown in Figure 7.8.4. Again, nothing pulled above 3σ. P-values were calculated and all found to be within the required bounds. Since all checks passed, we proceeded to blind fits on 100% of the data.

7.8.2 100% Data Blind Fit Results

Before looking at the exclusion contours and "unblinding," we first validate that the fit is sensible. Similar to before, the nuisance parameter pulls were calculated and then the pulls in the 1D

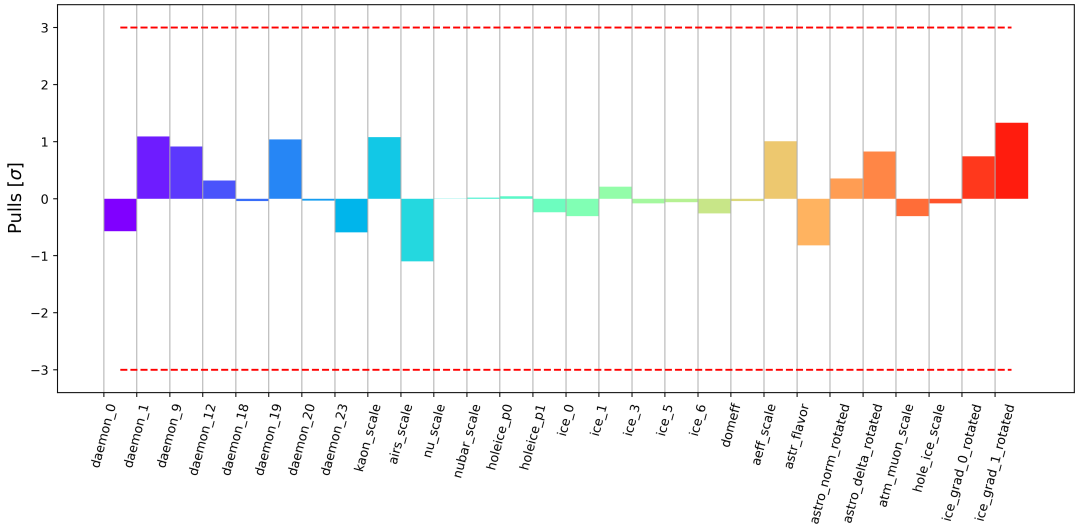

FIGURE 7.8.2: The nuisance parameter pulls at the best fit to 5% of the data.

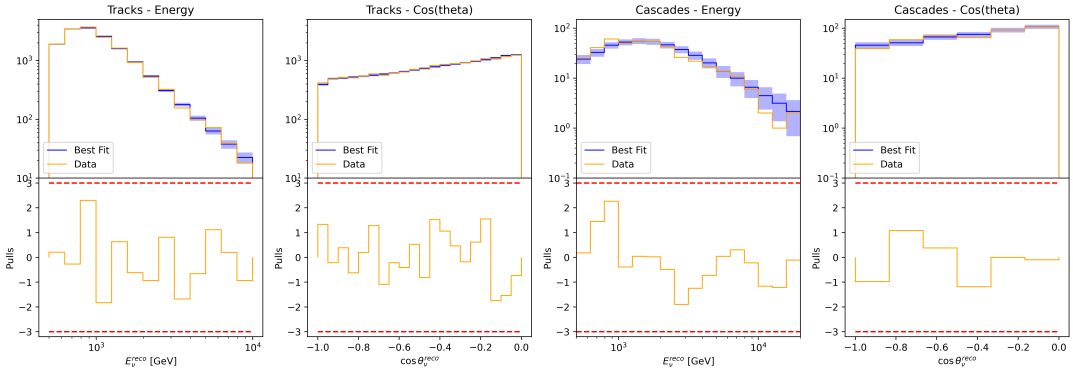

FIGURE 7.8.3: The 1D pulls and distribution of 5% of the data.

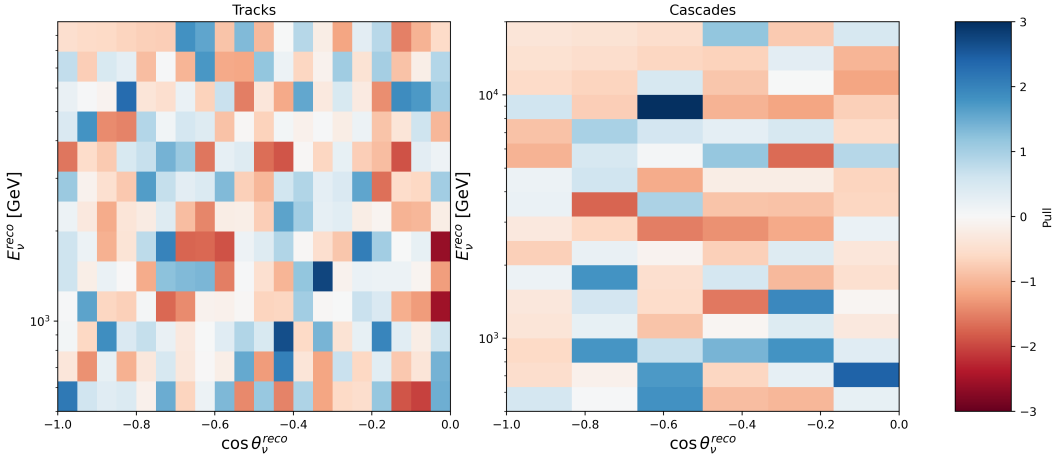

FIGURE 7.8.4: The 2D pulls and distribution of 5% of the data.

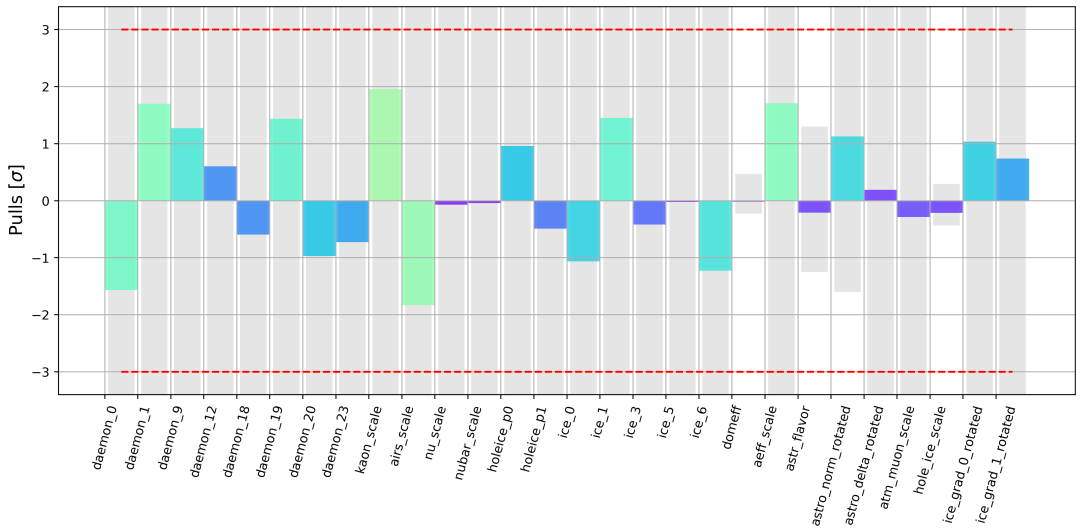

FIGURE 7.8.5: The nuisance parameter pulls at the best fit to 5% of the data.

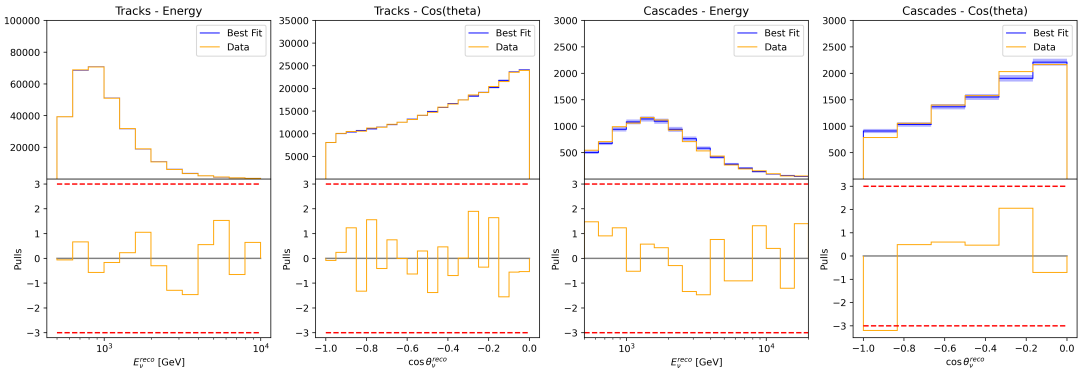

FIGURE 7.8.6: The 1D pulls and distribution of 100% of the data.

distributions. These are shown in Figure 7.8.5 and 7.8.6. For the cascades, one bin pulled at 3σ, and as a consequence the p-value dropped to 0.007: a stop condition.

To investigate this, we suspected an ice-modeling may be a factor. Two ice models were introduced previously in Section 2.2. The track and cascades samples both had relied on the legacy Spice 3.2.1; more recently, however, the improved BFR v2 model had been shown to predict differing photon-DOM counts as a function of $\cos\theta$. This is shown in Figure 7.8.7.

Motivated by these differences, a small sample of 5000 cascades were generated for $\cos\theta \in [-1.0, -0.9]$ and $E_\nu^{true} \in [1\text{TeV}, 2\text{TeV}]$. Using the exact same MC events and energy losses, photon propagation was performed separately using the Spice 3.2.1 and BFR v2 models to generate two

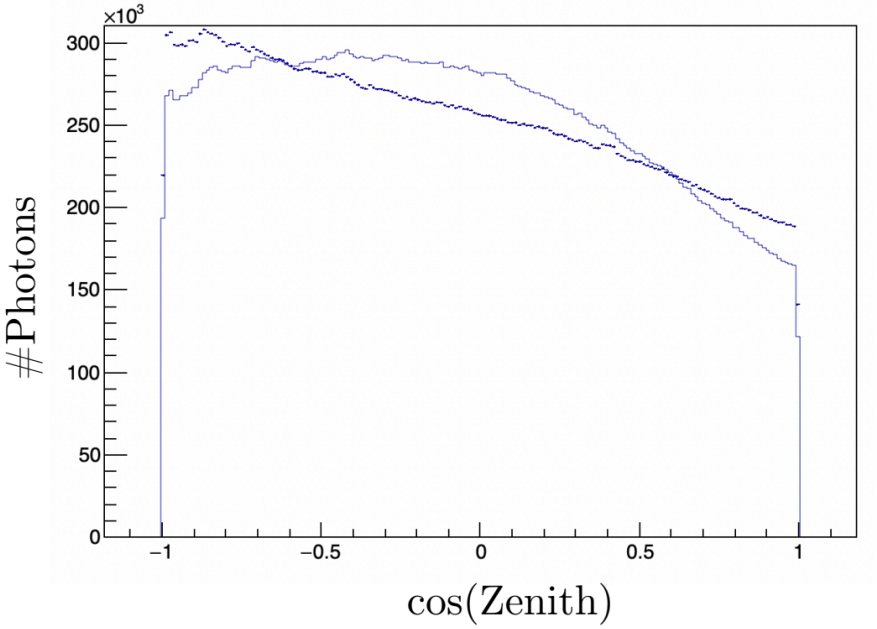

FIGURE 7.8.7: Differences in photon counts for Spice 3.2.1 (dark blue line) and BFR v2 (light blue line).

versions of the sample. The detector simulation, trigger simulation, filter simulation, and even reconstruction was then carried out for each of the two versions. Reconstructed event rates are shown in Figure 7.8.8; a disagreement is observed between the two sample predictions. This disagreement further supported a systematic difference in the predictions between the two ice models.

A separate, low-statistics, MC sample had been prepared internally in IceCube as part of a separate mismodeling test. This sample had been prepared using the BFR v2 ice model, and so we ran this analysis' cascade reconstruction and final level filters on the MC files. BFR v2-generated track MC was similarly already available from a post-unblinding cross-check in a previous analysis. The predicted 1D event rates, as determined for both the BFR v2 and Spice 3.2.1 ice models, are shown in Figure 7.8.9. A similar disagreement was seen between the Spice 3.2.1 and BFR v2 models. As a final test, a realization was generated assuming BFR v2 describes the truth. Then, the Spice 3.2.1 MC was used to perform a fit-scan with the BFR v2-generated realization. The goodness of fit is shown in Figure 7.8.10. By applying the same stop criteria as mentioned earlier, this inject-recover test fails in the same way as the blind fits. Exclusion contours were then prepared for this mismodeling test and are shown in Figure 7.8.11. Here a strong preference

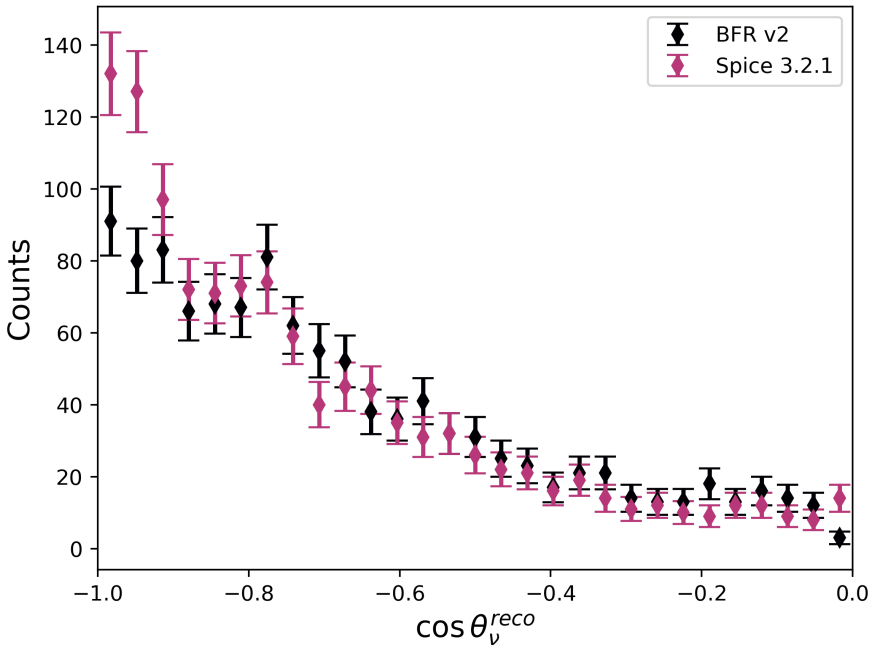

FIGURE 7.8.8: Reconstructed event rates (unweighted) for the BFR v2 and Spice 3.2.1 MC sample versions; error bars are show MC statistical error.

is seen for the injected three-neutrino model.

As the MC predictions begin to deviate at approximately -0.8, shown in Figure 7.8.9, the decision was made to cut the first zenith bin in this analysis, while generating a full high-statistics BFR v2 MC. Our plan is to revise the analysis for publication with the BFR v2 ice model.

7.8.3 Post-Cut 100% Blind Fits

As a sanity-check, two fit-scans were performed prior to re-running the blind fits with 100% of the data: an Asimov scan and a signal inject-recover test. These are shown in Figure 7.8.12. Little change was observed. We then calculated the nuisance parameter pulls, the 1D distribution pulls, and then the 2D distribution pulls; these are shown sequentially in Figures 7.8.13 through 7.8.15. No stop conditions were met.

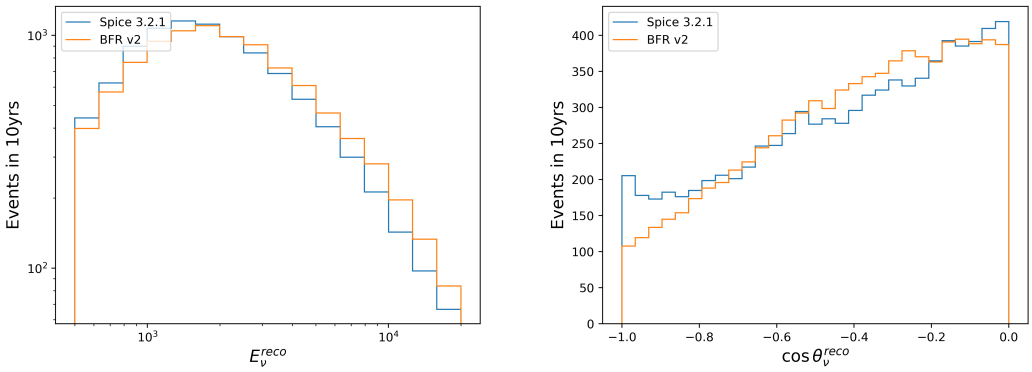

FIGURE 7.8.9: The reconstructed energy (zenith) rates are shown in the left (right) comparing Spice 3.2.1 and BFR v2.

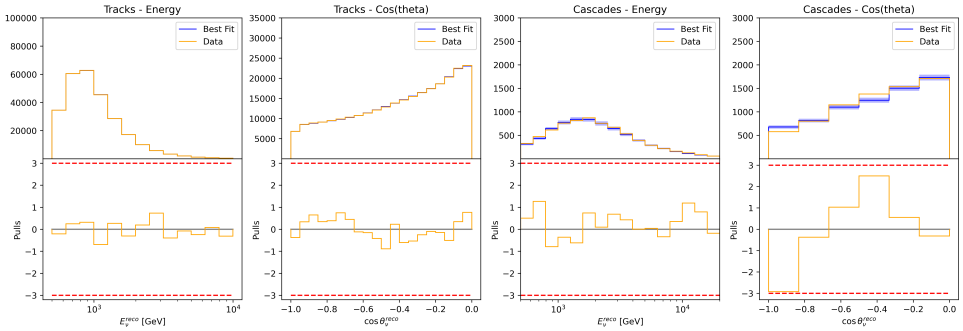

FIGURE 7.8.10: The goodness of fit after injecting a BFR v2-generated realization and fitting with Spice 3.2.1 MC.

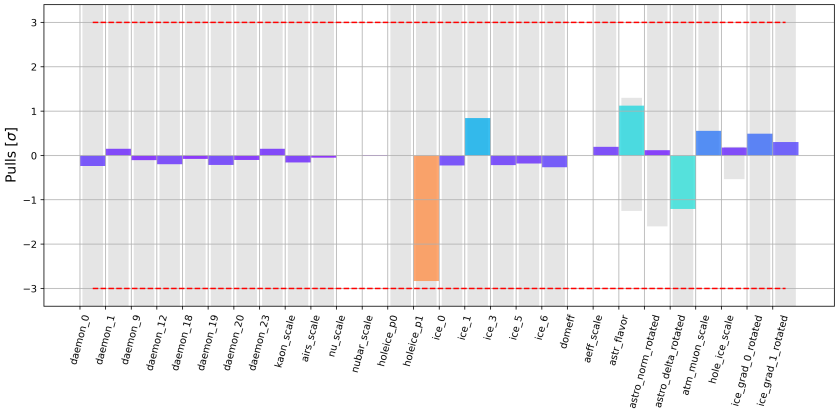

FIGURE 7.8.11: 90% CL exclusion contours with three degrees of freedom after injecting BFR v2 and fitting with Spice 3.2.1.

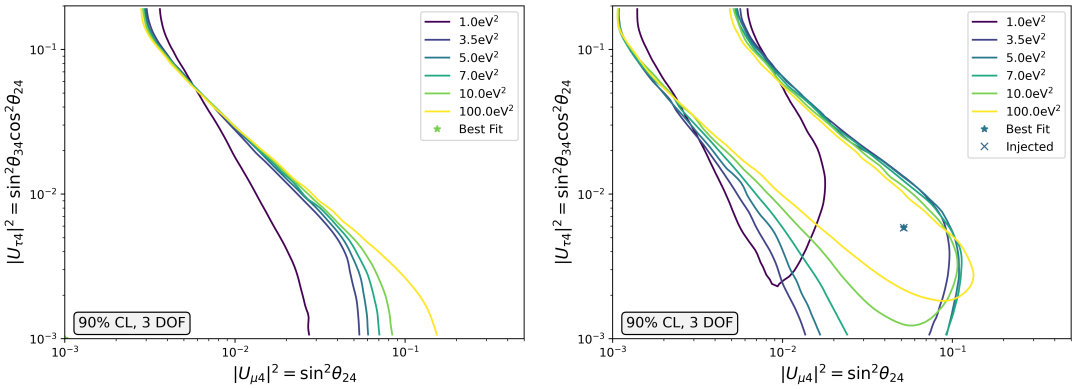

FIGURE 7.8.12: Left: the Asimov sensitivity after cutting the up-going zenith bin in the cascade selection; right: the 90% CL contours after injecting signal and fitting after applying the zenith cut.

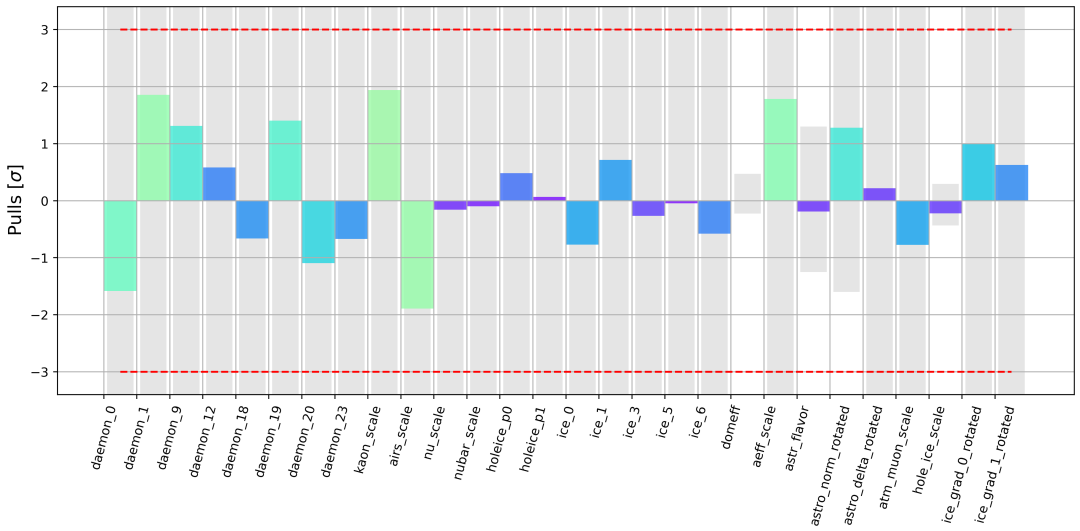

FIGURE 7.8.13: The nuisance parameter pulls at the best fit to 100% of the data after applying the cut.

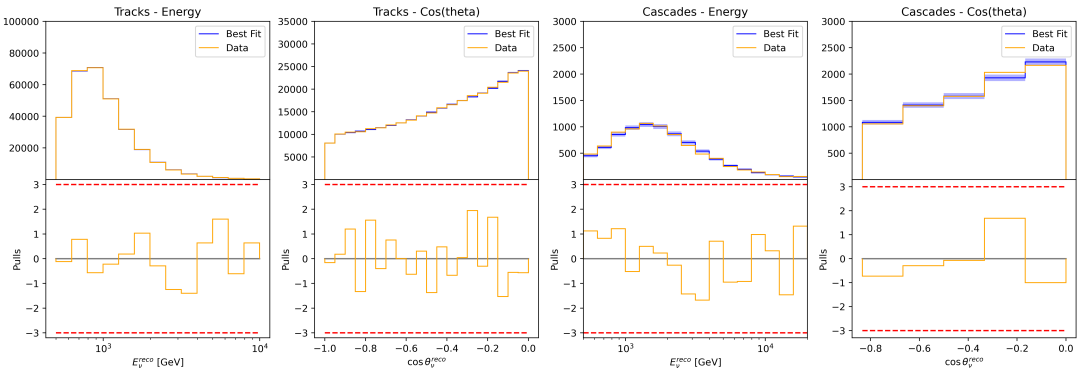

FIGURE 7.8.14: The 1D pulls and distribution of 100% of the data after applying the cut.

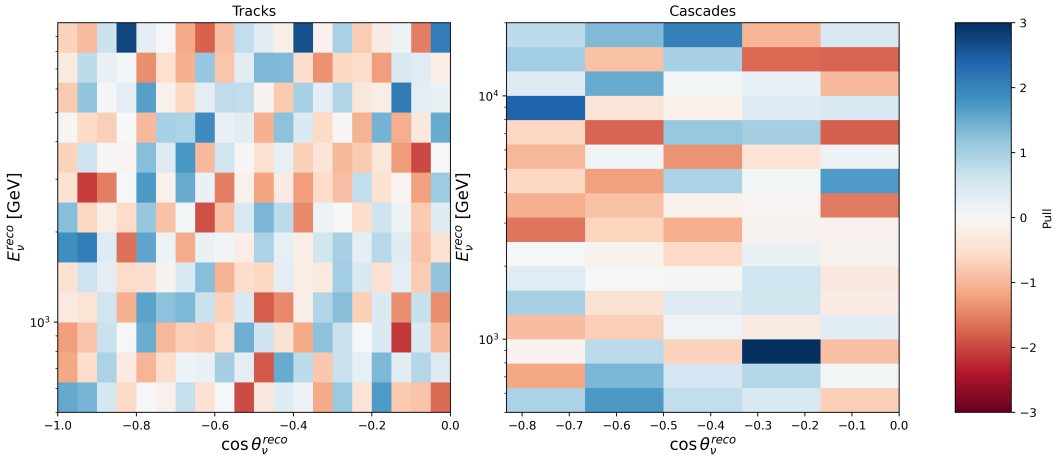

FIGURE 7.8.15: The 2D pulls and distribution of 100% of the data after applying the cut.

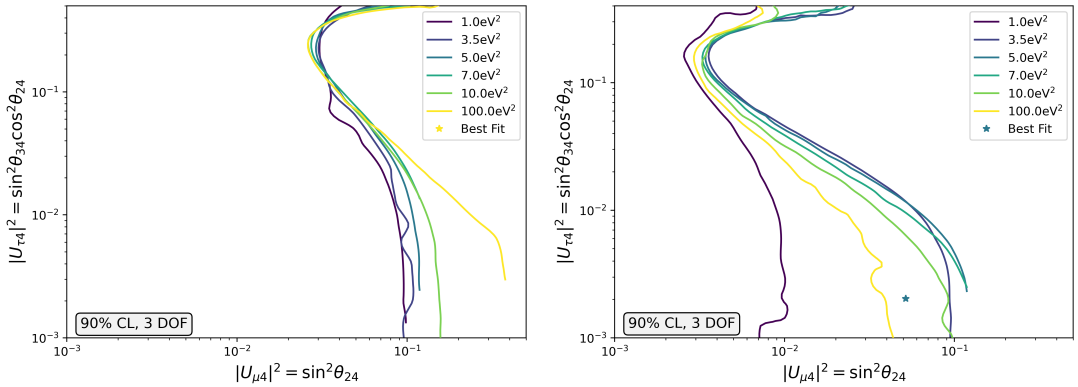

FIGURE 7.9.1: On left (right) the 90% CL exclusion contours with three degrees of freedom from a fit-scan using only the cascade (track) subsample.

7.9 Results

Individually, the track and cascade sub-samples show a difference in their preferred minima: the track sample favors a 3+1 model with $\Delta m^2_{41} = 5.0$ eV^2, $|U_{\mu 4}|^2 = 0.05$, and $|U_{\tau 4}|^2 = 0.002$ at a significance of 1.2σ assuming Wilk's theorem and three degrees of freedom; the cascade sample shows no preference for 3+1 over null. The exclusion contours for each subsample are shown in Figure 7.9.1 for the cascades on the left and tracks on the right. The results of the joint fit are shown in Figure 7.9.2, where the data are seen to show a weak preference for the 3+1 model with $\Delta m^2_{41} = 7$ eV^2, $|U_{\mu 4}|^2 = 0.03$, and $|U_{\tau 4}|^2 = 0.0$ at a significance of 0.26σ. A comparison is included to the median sensitivities in Figure 7.9.3.

Exclusion contours are also shown assuming two degrees of freedom at the 90% confidence level in comparison to results from Super-K and IceCube DeepCore in Figure 7.9.4. The results presented in this analysis are the strongest constraints with three degrees of freedom for $|U_{\mu 4}|^2$ and $|U_{\tau 4}|^2$ to date.

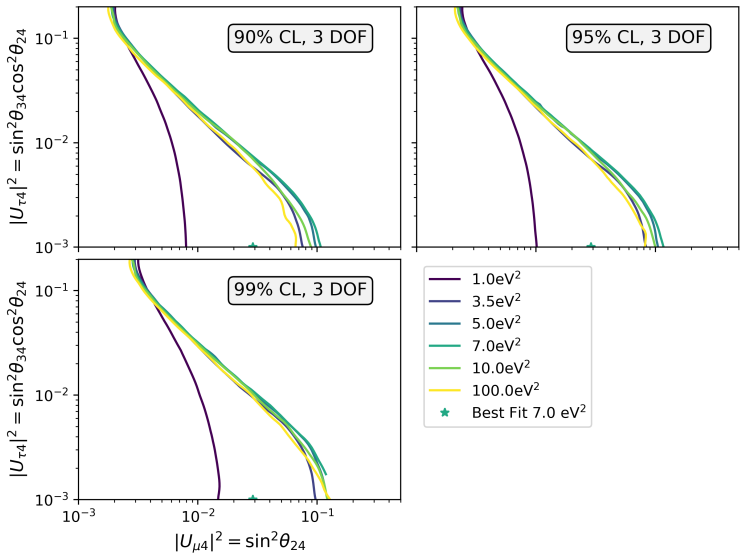

FIGURE 7.9.2: Left to right, top to bottom: the exclusion contours for three degrees of freedom and at a confidence level of 90%, 95%, and 99%. The best fit is at $\Delta m^2_{41} = 7$ eV^2, $|U_{\mu 4}|^2 = 0.03$, and $|U_{\tau 4}|^2 = 0.0$.

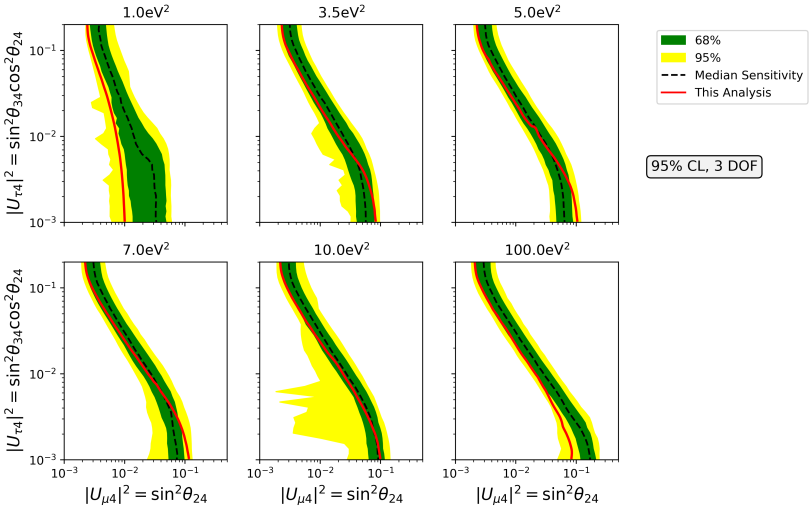

FIGURE 7.9.3: The results of the joint analysis overlain on top of the median sensitivities at the 95% confidence level.

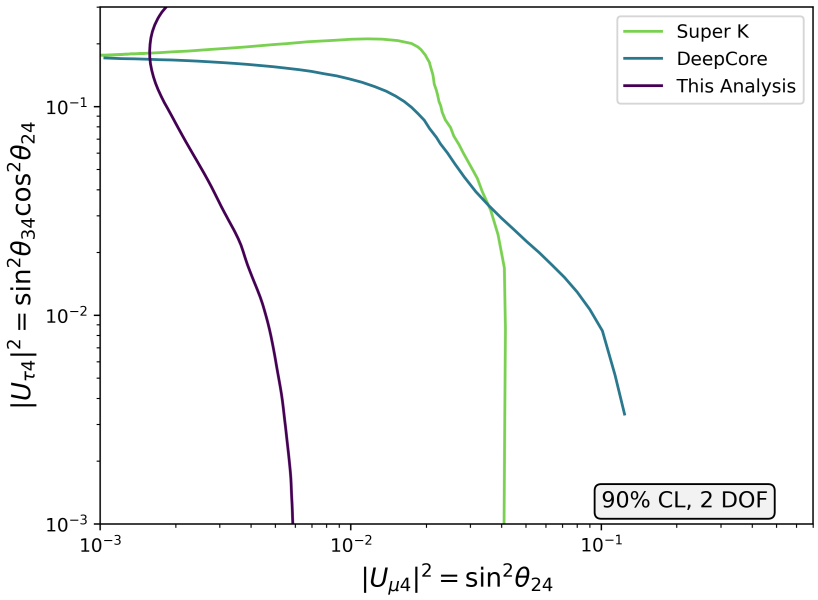

FIGURE 7.9.4: The 90% confidence level results for this analysis with two degrees of freedom at $\Delta m^2_{41} = 1.0$ eV^2. Sensitivities from DeepCore [115] and Super-K [116] at 1.0eV^2 are provided for comparison.

Chapter 8

Discussion & Conclusions

8.1 Discussion

What we have found is that the introduction of the cascades to the track analysis weakens the disappearance signature seen previously. There are also no strong signatures of appearance or disappearance in the cascades channel, and as a consequence further tensions may arise. While future work will implement the newer ice model with birefringence in the nominal expectation for the final results of this analysis, if these discrepancies persist then this would suggest that the track and cascade samples may not be jointly described by a common set of nuisance parameters. And if the lack of strong cascade appearance persists after the ice model updates, then we may find these results to fall into tension with predictions of strong ν_e/ν_τ appearance consistent with the BEST best fit sterile hypothesis.

We have also found weaker constraints compared to previous analyses using the same event selection [22, 23]. One noteable change from previous analyses was a switch from a conventional flux model using Hillas-Gaisser H3a [86], SIBYLL 2.3c [88], and the Barr parametrization [85] to daemonflux [91]. In Section 7.7.1 we had shown that if daemonflux is a better description of the truth, then by using the older model one could expect spurious signatures of sterile neutrino oscillations. Knowing this it is reasonable to expect that the previously observed signatures might weaken in this updated search. This is not to say that no such 3+1 signal-like feature exists in IceCube data, however: more recent results[1] using an updated event selection and reconstruction

[1] as of writing currently under internal paper review

along with daemonflux have found even stronger results for 3+1 sterile neutrinos [123] that are consistent with the best-fit point of this analysis.

8.2 Conclusions

Numerous oscillations persist in neutrino oscillations today: many of which can be solved through additional eV^2-scale oscillations. Such an additional neutrino could not interact weakly in order to be consistent with measurements of Z-boson decay, and so is described as "sterile." Through attempts to test such explanations using sterile neutrinos, several tantalizing signal-like hints have been observed with varying degrees of significance in both $\nu_e/\bar{\nu}_e$ disappearance and ν_μ disappearance; including the 8-year IceCube matter-enhanced sterile neutrino oscillations study in which signal-like hints above the 90% confidence level for the 3+1 light sterile neutrino model were found.

Here, we have presented the first results of a joint track-cascade analysis combining the methods used in previous IceCube analyses along with novel methods developed to needed to handle the additional sources of systematic uncertainty introduced with this new event morphology. We have probed $|U_{\mu 4}|^2$ and $|U_{\tau 4}|^2$ through high-energy events in a search the first time, implemented a new conventional flux model and an updated bulk ice model with an improved system for covariance matrix calculation, and introduced a new starting event sample. Results presented here improve upon world-leading constraints in $U_{\mu 4}$-$U_{\tau 4}$ parameter space, and have opened the door for large-volume Čerenkov neutrino experiments to directly probe the models preferred by experiments like BEST.

Because of challenges in ice modeling, immediate work will focus on the re-simulation of Monte Carlo to update the nominal ice model from Spice 3.2.1 to BFR v2: one which fully accounts for the effects of birefringence in ice. We may then find that the disagreement between the track, cascade, and joint fits persist; this would suggest that the cascade and track samples are not sufficiently described by a common set of nuisance parameters, and further investigation would be of merit. We may instead find a consistent description of sterile neutrinos in both event morphologies: laying the foundations for an even stronger and compelling test of the 3+1 sterile neutrino oscillation model with IceCube.

References

[1] M. Tanabashi et al. Review of Particle Physics. *Phys. Rev. D*, 98:030001, Aug 2018. doi: 10.1103/PhysRevD.98.030001. URL https://link.aps.org/doi/10.1103/PhysRevD.98.030001.

[2] Ivan Esteban, M. C. Gonzalez-Garcia, Alvaro Hernandez-Cabezudo, Michele Maltoni, and Thomas Schwetz. Global analysis of three-flavour neutrino oscillations: synergies and tensions in the determination of θ_{23}, δ_{CP}, and the mass ordering. *Journal of High Energy Physics*, 2019(1), Jan 2019. ISSN 1029-8479. doi: 10.1007/jhep01(2019)106. URL http://dx.doi.org/10.1007/JHEP01(2019)106.

[3] P.F. de Salas, D.V. Forero, C.A. Ternes, M. Tórtola, and J.W.F. Valle. Status of neutrino oscillations 2018: 3σ hint for normal mass ordering and improved cp sensitivity. *Physics Letters B*, 782:633–640, Jul 2018. ISSN 0370-2693. doi: 10.1016/j.physletb.2018.06.019. URL http://dx.doi.org/10.1016/j.physletb.2018.06.019.

[4] F. Capozzi, E. Lisi, A. Marrone, D. Montanino, and A. Palazzo. Neutrino masses and mixings: Status of known and unknown 3ν parameters. *Nuclear Physics B*, 908:218–234, Jul 2016. ISSN 0550-3213. doi: 10.1016/j.nuclphysb.2016.02.016. URL http://dx.doi.org/10.1016/j.nuclphysb.2016.02.016.

[5] S. Schael et al. (ALEPH, DELPHI, L3, OPAL, SLD, LEP Electroweak Working Group, SLD Electroweak Group, SLD Heavy Flavour Group) . Precision Electroweak Measurements on the Z Resonance. *Physics Reports*, 427(5-6):257–454, May 2006. ISSN 0370-1573. doi: 10.1016/j.physrep.2005.12.006. URL http://dx.doi.org/10.1016/j.physrep.2005.12.006.

[6] Lukas Berns. Recent results from T2K, 2021.

[7] AA Aguilar-Arevalo, BC Brown, L Bugel, G Cheng, JM Conrad, RL Cooper, R Dharmapalan, A Diaz, Z Djurcic, DA Finley, et al. Significant excess of electronlike events in the miniboone short-baseline neutrino experiment. *Physical review letters*, 121(22):221801, 2018.

[8] G Mention, M Fechner, Th Lasserre, Th A Mueller, D Lhuillier, M Cribier, and A Letourneau. Reactor antineutrino anomaly. *Physical Review D*, 83(7):073006, 2011.

[9] Anatoly Pavlovich Serebrov et al. First observation of the oscillation effect in the neutrino-4 experiment on the search for the sterile neutrino. *JETP Letters*, 109(4):213–221, 2019.

[10] J. N. Abdurashitov et al. Measurement of the response of a ga solar neutrino experiment to neutrinos from a ^{37}Ar source. *Phys. Rev. C*, 73:045805, Apr 2006. doi: 10.1103/PhysRevC.73.045805. URL https://link.aps.org/doi/10.1103/PhysRevC.73.045805.

[11] Carlo Giunti and Marco Laveder. Statistical significance of the gallium anomaly. *Physical Review C*, 83(6):065504, 2011.

[12] K. N. Abazajian et al. Light Sterile Neutrinos: A White Paper, 2012.

[13] Guo yuan Huang and Shun Zhou. Impact of an ev-mass sterile neutrino on the neutrinoless double-beta decays: A bayesian analysis. *Nuclear Physics B*, 945:114691, 2019. ISSN 0550-3213. doi: https://doi.org/10.1016/j.nuclphysb.2019.114691. URL https://www.sciencedirect.com/science/article/pii/S0550321319301774.

[14] P. Abratenko et al. Search for an anomalous excess of charged-current quasi-elastic ν_e interactions with the microboone experiment using deep-learning-based reconstruction, 2021.

[15] P. Abratenko et al. Search for an excess of electron neutrino interactions in microboone using multiple final state topologies, 2021.

[16] C. A. Argüelles et al. MicroBooNE and the ν_e Interpretation of the MiniBooNE Low-Energy Excess, 2021.

[17] P. B. Denton. Sterile Neutrino Searches with MicroBooNE: Electron Neutrino Disappearance, 2021.

[18] F. Kaether, W. Hampel, G. Heusser, J. Kiko, and T. Kirsten. Reanalysis of the gallex solar neutrino flux and source experiments. *Physics Letters B*, 685(1):47–54, 2010. ISSN 0370-2693. doi: https://doi.org/10.1016/j.physletb.2010.01.030. URL https://www.sciencedirect.com/science/article/pii/S0370269310000729.

[19] M. Laveder. Unbound Neutrino Roadmaps. *Nuclear Physics B - Proceedings Supplements*, 168:344–346, 2007. ISSN 0920-5632. doi: https://doi.org/10.1016/j.nuclphysbps.2007.02.037. URL https://www.sciencedirect.com/science/article/pii/S0920563207001752. Proceedings of the Neutrino Oscillation Workshop.

[20] V. V. Barinov et al. Results from the baksan experiment on sterile transitions (best). *Physical Review Letters*, 128(23), June 2022. ISSN 1079-7114. doi: 10.1103/physrevlett.128.232501. URL http://dx.doi.org/10.1103/PhysRevLett.128.232501.

[21] V. V. Barinov et al. Search for electron-neutrino transitions to sterile states in the best experiment. *Physical Review C*, 105(6), June 2022. ISSN 2469-9993. doi: 10.1103/physrevc.105.065502. URL http://dx.doi.org/10.1103/PhysRevC.105.065502.

[22] M. G. Aartsen et al. eV-Scale Sterile Neutrino Search Using Eight Years of Atmospheric Muon Neutrino Data from the IceCube Neutrino Observatory. *Physical Review Letters*, 125(14), Sep 2020. ISSN 1079-7114. doi: 10.1103/physrevlett.125.141801. URL http://dx.doi.org/10.1103/PhysRevLett.125.141801.

[23] M. G. Aartsen et al. Searching for eV-scale sterile neutrinos with eight years of atmospheric neutrinos at the IceCube Neutrino Telescope. *Physical Review D*, 102(5), Sep 2020. ISSN 2470-0029. doi: 10.1103/physrevd.102.052009. URL http://dx.doi.org/10.1103/PhysRevD.102.052009.

[24] C. Athanassopoulos, L. B. Auerbach, R. L. Burman, D. O. Caldwell, E. D. Church, I. Cohen, J. B. Donahue, A. Fazely, F. J. Federspiel, G. T. Garvey, and et al. Results on $\nu\mu \to \nu e$ neutrino oscillations from the lsnd experiment. *Physical Review Letters*, 81(9):1774–1777, Aug 1998. ISSN 1079-7114. doi: 10.1103/physrevlett.81.1774. URL http://dx.doi.org/10.1103/PhysRevLett.81.1774.

[25] Joachim Kopp et al. Sterile neutrino oscillations: the global picture. *Journal of High Energy Physics*, 2013(5):1–52, 2013.

[26] M. Cirelli, G. Marandella, A. Strumia, and F. Vissani. Probing oscillations into sterile neutrinos with cosmology, astrophysics and experiments. *Nuclear Physics B*, 708(1-3): 215–267, Feb 2005. ISSN 0550-3213. doi: 10.1016/j.nuclphysb.2004.11.056. URL http://dx.doi.org/10.1016/j.nuclphysb.2004.11.056.

[27] S. Gariazzo, C. Giunti, M. Laveder, and Y. F. Li. Updated global 3+1 analysis of short-baseline neutrino oscillations. *Journal of High Energy Physics*, 2017(6), Jun 2017. ISSN 1029-8479. doi: 10.1007/jhep06(2017)135. URL http://dx.doi.org/10.1007/JHEP06(2017)135.

[28] Mona Dentler, Álvaro Hernández-Cabezudo, Joachim Kopp, Michele Maltoni, and Thomas Schwetz. Sterile neutrinos or flux uncertainties? — status of the reactor anti-neutrino anomaly. *Journal of High Energy Physics*, 2017(11), Nov 2017. ISSN 1029-8479. doi: 10.1007/jhep11(2017)099. URL http://dx.doi.org/10.1007/JHEP11(2017)099.

[29] A. Diaz, C.A. Argüelles, G.H. Collin, J.M. Conrad, and M.H. Shaevitz. Where are we with light sterile neutrinos? *Physics Reports*, 884:1–59, Nov 2020. ISSN 0370-1573. doi: 10.1016/j.physrep.2020.08.005. URL http://dx.doi.org/10.1016/j.physrep.2020.08.005.

[30] M. Aker et al. Direct neutrino-mass measurement with sub-electronvolt sensitivity. *Nature Phys.*, 18(2):160–166, 2022. doi: 10.1038/s41567-021-01463-1.

[31] Evgeny K. Akhmedov. Neutrino oscillations in inhomogeneous matter. (In Russian). *Sov. J. Nucl. Phys.*, 47:301–302, 1988.

[32] P.I. Krastev and A.Yu. Smirnov. Parametric effects in neutrino oscillations. *Physics Letters B*, 226(3):341–346, 1989. ISSN 0370-2693. doi: https://doi.org/10.1016/0370-2693(89)91206-9. URL https://www.sciencedirect.com/science/article/pii/0370269389912069.

[33] M. Chizhov, M. Maris, and S. T. Petcov. On the oscillation length resonance in the transitions of solar and atmospheric neutrinos crossing the earth core. 7 1998.

[34] M. V. Chizhov and S. T. Petcov. New Conditions for a Total Neutrino Conversion in a Medium. *Physical Review Letters*, 83(6):1096–1099, Aug 1999. ISSN 1079-7114. doi: 10.1103/physrevlett.83.1096. URL http://dx.doi.org/10.1103/PhysRevLett.83.1096.

[35] E. Kh. Akhmedov and A. Yu. Smirnov. Comment on "New Conditions for a Total Neutrino Conversion in a Medium". *Physical Review Letters*, 85(18):3978–3978, Oct 2000. ISSN 1079-7114. doi: 10.1103/physrevlett.85.3978. URL http://dx.doi.org/10.1103/PhysRevLett.85.3978.

[36] H. Nunokawa et al. Probing the LSND mass scale and four neutrino scenarios with a neutrino telescope. *Physics Letters B*, 562(3-4):279–290, Jun 2003. ISSN 0370-2693. doi: 10.1016/s0370-2693(03)00603-8. URL http://dx.doi.org/10.1016/S0370-2693(03)00603-8.

[37] S. T. Petcov. On the IceCube result on $\bar{n}\bar{u}_\mu \to \bar{n}\bar{u}_s$ oscillations. *International Journal of Modern Physics A*, 32(04):1750018, Feb 2017. ISSN 1793-656X. doi: 10.1142/s0217751x1750018x. URL http://dx.doi.org/10.1142/S0217751X1750018X.

[38] Sandhya Choubey. Signature of sterile species in atmospheric neutrino data at neutrino telescopes. *Journal of High Energy Physics*, 2007(12):014–014, Dec 2007. ISSN 1029-8479. doi: 10.1088/1126-6708/2007/12/014. URL http://dx.doi.org/10.1088/1126-6708/2007/12/014.

[39] V. Barger, Y. Gao, and D. Marfatia. Is there evidence for sterile neutrinos in IceCube data? *Physical Review D*, 85(1), Jan 2012. ISSN 1550-2368. doi: 10.1103/physrevd.85.011302. URL http://dx.doi.org/10.1103/PhysRevD.85.011302.

[40] Arman Esmaili, Francis Halzen, and O.L.G Peres. Constraining sterile neutrinos with AMANDA and IceCube atmospheric neutrino data. *Journal of Cosmology and Astroparticle Physics*, 2012(11):041–041, Nov 2012. ISSN 1475-7516. doi: 10.1088/1475-7516/2012/11/041. URL http://dx.doi.org/10.1088/1475-7516/2012/11/041.

[41] A. Esmaili and A.Y. Smirnov. Restricting the LSND and MiniBooNE sterile neutrinos with the IceCube atmospheric neutrino data. *Journal of High Energy Physics*, 2013(12):1–26, 2013.

[42] Manfred Lindner, Werner Rodejohann, and Xun-Jie Xu. Sterile neutrinos in the light of icecube. *Journal of High Energy Physics*, 2016(1), Jan 2016. ISSN 1029-8479. doi: 10.1007/jhep01(2016)124. URL http://dx.doi.org/10.1007/JHEP01(2016)124.

[43] Sheldon L. Glashow. Resonant Scattering of Antineutrinos. *Phys. Rev.*, 118:316–317, Apr 1960. doi: 10.1103/PhysRev.118.316. URL https://link.aps.org/doi/10.1103/PhysRev.118.316.

[44] Carlos A. Argüelles, Jordi Salvado, and Christopher N. Weaver. nuSQuIDS: A toolbox for neutrino propagation. *Computer Physics Communications*, 277:108346, aug 2022. doi: 10.1016/j.cpc.2022.108346. URL https://doi.org/10.1016%2Fj.cpc.2022.108346.

[45] J. A. Formaggio and G. P. Zeller. From eV to EeV: Neutrino Cross Sections Across Energy Scales. *Rev. Mod. Phys.*, 84:1307–1341, 2012. doi: 10.1103/RevModPhys.84.1307.

[46] Raj Gandhi, Chris Quigg, Mary Hall Reno, and Ina Sarcevic. Ultrahigh-energy neutrino interactions. *Astropart. Phys.*, 5:81–110, 1996. doi: 10.1016/0927-6505(96)00008-4.

[47] Bei Zhou and John F. Beacom. W -boson and trident production in TeV–PeV neutrino observatories. *Phys. Rev. D*, 101(3):036010, 2020. doi: 10.1103/PhysRevD.101.036010.

[48] Bei Zhou and John Beacom. Neutrino-nucleus cross sections for w-boson and trident production. *Physical Review D*, 101, 02 2020. doi: 10.1103/PhysRevD.101.036011.

[49] A. Cooper-Sarkar, P. Mertsch, and S. Sarkar. The high energy neutrino cross-section in the standard model and its uncertainty. *Journal of High Energy Physics*, 2011(8), Aug 2011. ISSN 1029-8479. doi: 10.1007/jhep08(2011)042. URL http://dx.doi.org/10.1007/JHEP08(2011)042.

[50] C. A. Argüelles, J. Salvado, and C. N. Weaver. nuSQuIDS. https://github.com/Arguelles/nuSQuIDS, 2015.

[51] B. R. Smithers, B. J. P. Jones, C. A. Argüelles, J. M. Conrad, and A. Diaz. Cascade appearance signatures of sterile neutrinos at 1–100 tev. *Phys. Rev. D*, 105:052001, Mar

2022. doi: 10.1103/PhysRevD.105.052001. URL https://link.aps.org/doi/10.1103/PhysRevD.105.052001.

[52] R. Abbasi et al. Leptoninjector and leptonweighter: A neutrino event generator and weighter for neutrino observatories. *Computer Physics Communications*, 266:108018, 2021. ISSN 0010-4655. doi: https://doi.org/10.1016/j.cpc.2021.108018. URL https://www.sciencedirect.com/science/article/pii/S0010465521001302.

[53] M.G. Aartsen et al. The IceCube neutrino observatory: instrumentation and online systems. *Journal of Instrumentation*, 12(03):P03012–P03012, mar 2017. doi: 10.1088/1748-0221/12/03/p03012. URL https://doi.org/10.1088/1748-0221/12/03/p03012.

[54] R. Abbasi et al. The IceCube data acquisition system: Signal capture, digitization, and timestamping. *Nuclear Instruments and Methods in Physics Research Section A: Accelerators, Spectrometers, Detectors and Associated Equipment*, 601(3):294–316, 2009. ISSN 0168-9002. doi: https://doi.org/10.1016/j.nima.2009.01.001. URL https://www.sciencedirect.com/science/article/pii/S0168900209000084.

[55] R. Abbasi et al. The design and performance of IceCube DeepCore. *Astroparticle Physics*, 35 (10):615–624, 2012. ISSN 0927-6505. doi: https://doi.org/10.1016/j.astropartphys.2012.01.004. URL https://www.sciencedirect.com/science/article/pii/S0927650512000254.

[56] Raj Gandhi, Chris Quigg, Mary Hall Reno, and Ina Sarcevic. Ultrahigh-energy neutrino interactions. *Astroparticle Physics*, 5(2):81–110, Aug 1996. ISSN 0927-6505. doi: 10.1016/0927-6505(96)00008-4. URL http://dx.doi.org/10.1016/0927-6505(96)00008-4.

[57] M. G. Aartsen et al. Detection of a particle shower at the Glashow resonance with IceCube. *Nature*, 591(7849):220–224, 2021. doi: 10.1038/s41586-021-03256-1. [Erratum: Nature 592, E11 (2021)].

[58] M. G. Aartsen et al. All-sky search for time-integrated neutrino emission from astrophysical sources with 7 yr of icecube data. *The Astrophysical Journal*, 835(2):151, Jan 2017. ISSN 1538-4357. doi: 10.3847/1538-4357/835/2/151. URL http://dx.doi.org/10.3847/1538-4357/835/2/151.

[59] M. G. Aartsen et al. Energy reconstruction methods in the IceCube neutrino telescope. *Journal of Instrumentation*, 9(03):P03009–P03009, Mar 2014. ISSN 1748-0221. doi: 10.1088/1748-0221/9/03/p03009. URL http://dx.doi.org/10.1088/1748-0221/9/03/P03009.

[60] R. Abbasi et al. Measurement of Astrophysical Tau Neutrinos in IceCube's High-Energy Starting Events, 2020.

[61] M. G. Aartsen et al. South pole glacial climate reconstruction from multi-borehole laser particulate stratigraphy. *Journal of Glaciology*, 59(218):1117–1128, 2013. doi: 10.3189/2013JoG13J068.

[62] M. Rongen, R. C. Bay, and S. Blot. Observation of an optical anisotropy in the deep glacial ice at the geographic south pole using a laser dust logger. *The Cryosphere*, 14(8):2537–2543, 2020. doi: 10.5194/tc-14-2537-2020. URL https://tc.copernicus.org/articles/14/2537/2020/.

[63] R. Abbasi et al. In-situ estimation of ice crystal properties at the south pole using led calibration data from the icecube neutrino observatory. *The Cryosphere Discussions*, 2022: 1–48, 2022. doi: 10.5194/tc-2022-174. URL https://tc.copernicus.org/preprints/tc-2022-174/.

[64] R. Abbasi et al. Calibration and characterization of the icecube photomultiplier tube. *Nuclear Instruments and Methods in Physics Research Section A: Accelerators, Spectrometers, Detectors and Associated Equipment*, 618(1):139–152, 2010. ISSN 0168-9002. doi: https://doi.org/10.1016/j.nima.2010.03.102. URL https://www.sciencedirect.com/science/article/pii/S0168900210006662.

[65] Aya Ishihara. The icecube upgrade – design and science goals, 2019.

[66] Lew Classen, Alexander Kappes, and Timo Karg. A multi-pmt optical module for the icecube upgrade, 2019.

[67] R. Abbasi et al. D-egg: a dual pmt optical module for icecube, 2022. URL https://arxiv.org/abs/2212.14526.

[68] M. G. aand others Aartsen. Measurement of atmospheric neutrino oscillations at 6–56 gev with icecube deepcore. *Phys. Rev. Lett.*, 120:071801, Feb 2018. doi: 10.1103/PhysRevLett.120.071801. URL https://link.aps.org/doi/10.1103/PhysRevLett.120.071801.

[69] Z. Li et al. Measurement of the tau neutrino cross section in atmospheric neutrino oscillations with super-kamiokande. *Phys. Rev. D*, 98:052006, Sep 2018. doi: 10.1103/PhysRevD.98.052006. URL https://link.aps.org/doi/10.1103/PhysRevD.98.052006.

[70] N. Agafonova et al. Final results of the opera experiment on ν_τ appearance in the cngs neutrino beam. *Phys. Rev. Lett.*, 120:211801, May 2018. doi: 10.1103/PhysRevLett.120.211801. URL https://link.aps.org/doi/10.1103/PhysRevLett.120.211801.

[71] L.H. Whitehead. Neutrino oscillations with minos and minos+. *Nuclear Physics B*, 908:130–150, 2016. ISSN 0550-3213. doi: https://doi.org/10.1016/j.nuclphysb.2016.03.004. URL https://www.sciencedirect.com/science/article/pii/S0550321316000869. Neutrino Oscillations: Celebrating the Nobel Prize in Physics 2015.

[72] Leila Haegel and. The latest t2k neutrino oscillation results. In *Proceedings of The European Physical Society Conference on High Energy Physics — PoS(EPS-HEP2017)*. Sissa Medialab, oct 2017. doi: 10.22323/1.314.0112. URL https://doi.org/10.22323%2F1.314.0112.

[73] J.H. Koehne, K. Frantzen, M. Schmitz, T. Fuchs, W. Rhode, D. Chirkin, and J. Becker Tjus. PROPOSAL: A tool for propagation of charged leptons. *Comput. Phys. Commun.*, 184:2070–2090, 2013. doi: 10.1016/j.cpc.2013.04.001.

[74] Claudio Kopper. `CLSim`. https://github.com/claudiok/clsim, 2019.

[75] M.G. Aartsen et al. Measurement of south pole ice transparency with the IceCube LED calibration system. *Nuclear Instruments and Methods in Physics Research Section A: Accelerators, Spectrometers, Detectors and Associated Equipment*, 711:73–89, may 2013. doi: 10.1016/j.nima.2013.01.054. URL https://doi.org/10.1016%2Fj.nima.2013.01.054.

[76] M.G. Aartsen et al. Efficient propagation of systematic uncertainties from calibration to analysis with the SnowStorm method in IceCube. *Journal of Cosmology and Astroparticle*

Physics, 2019(10):048–048, Oct 2019. ISSN 1475-7516. doi: 10.1088/1475-7516/2019/10/048. URL http://dx.doi.org/10.1088/1475-7516/2019/10/048.

[77] The IceCube Collaboration. PISA. https://github.com/BenSmithers/pisa, 2023.

[78] Nathan Whitehorn, Jakob van Santen, and Sven Lafebre. Penalized splines for smooth representation of high-dimensional monte carlo datasets. *Computer Physics Communications*, 184(9):2214 – 2220, 2013. ISSN 0010-4655. doi: https://doi.org/10.1016/j.cpc.2013.04.008. URL http://www.sciencedirect.com/science/article/pii/S0010465513001434.

[79] R. Abbasi et al. Low energy event reconstruction in IceCube DeepCore. *The European Physical Journal C*, 82(9), sep 2022. doi: 10.1140/epjc/s10052-022-10721-2. URL https://doi.org/10.1140%2Fepjc%2Fs10052-022-10721-2.

[80] Y. S. Yoon et al. Proton and helium spectra from the cream-iii flight. *The Astrophysical Journal*, 839(1):5, apr 2017. doi: 10.3847/1538-4357/aa68e4. URL https://dx.doi.org/10.3847/1538-4357/aa68e4.

[81] R. Alfaro et al. All-particle cosmic ray energy spectrum measured by the hawc experiment from 10 to 500 tev. *Phys. Rev. D*, 96:122001, Dec 2017. doi: 10.1103/PhysRevD.96.122001. URL https://link.aps.org/doi/10.1103/PhysRevD.96.122001.

[82] M. Iacovacci. Cosmic ray physics with argo-ybj. *Nuclear Physics B - Proceedings Supplements*, 239-240:157–162, 2013. ISSN 0920-5632. doi: https://doi.org/10.1016/j.nuclphysbps.2013.05.025. URL https://www.sciencedirect.com/science/article/pii/S0920563213004027. Proceedings of the 9th workshop on Science with the New Generation of High Energy Gamma-ray Experiments: From high energy gamma sources to cosmic rays, one century after their discovery.

[83] A. V. Karelin et al. The proton and helium cosmic ray spectra from 50 gev to 15 tev. *Astrophysics and Space Sciences Transactions*, 7(2):235–238, 2011. doi: 10.5194/astra-7-235-2011. URL http://www.astrophys-space-sci-trans.net/7/235/2011/.

[84] Paolo Lipari and Silvia Vernetto. The shape of the cosmic ray proton spectrum. *Astroparticle Physics*, 120:102441, 2020. ISSN 0927-6505. doi: https://doi.org/10.1016/

j.astropartphys.2020.102441. URL https://www.sciencedirect.com/science/article/pii/S0927650520300141.

[85] G. D. Barr, S. Robbins, T. K. Gaisser, and T. Stanev. Uncertainties in atmospheric neutrino fluxes. *Phys. Rev. D*, 74:094009, Nov 2006. doi: 10.1103/PhysRevD.74.094009. URL https://link.aps.org/doi/10.1103/PhysRevD.74.094009.

[86] Thomas K. Gaisser. Spectrum of cosmic-ray nucleons, kaon production, and the atmospheric muon charge ratio. *Astroparticle Physics*, 35(12):801–806, 2012. ISSN 0927-6505. doi: https://doi.org/10.1016/j.astropartphys.2012.02.010. URL https://www.sciencedirect.com/science/article/pii/S0927650512000497.

[87] Anatoli Fedynitch et al. Calculation of conventional and prompt lepton fluxes at very high energy, 2015.

[88] Felix Riehn et al. The hadronic interaction model SIBYLL 2.3c and Feynman scaling. *PoS*, ICRC2017:301, 2018. doi: 10.22323/1.301.0301.

[89] Jet Propulsion Laboratory, Version 2, Nov 2014. URL https://www.earthdata.nasa.gov/learn/find-data/near-real-time/airs.

[90] Spencer Axani. Sterile neutrino searches at the icecube neutrino observatory, 2020.

[91] Juan Pablo Yañez and Anatoli Fedynitch. Data-driven muon-calibrated neutrino flux. *Physical Review D*, 107(12), jun 2023. doi: 10.1103/physrevd.107.123037. URL https://doi.org/10.1103%2Fphysrevd.107.123037.

[92] Hans Dembinski, Ralph Engel, Anatoli Fedynitch, Thomas Gaisser, Felix Riehn, and Todor Stanev. Data-driven model of the cosmic-ray flux and mass composition from 10 gev to 10^{11} gev, 2017.

[93] Patrick Heix, Serap Tilav, Christopher Wiebusch, and Marit Zöcklein. Seasonal variation of atmospheric neutrinos in icecube, 2019.

[94] R. Abbasi et al. Observation of seasonal variations of the flux of high-energy atmospheric neutrinos with icecube, 2023.

[95] United States Committee on Extension to the Standard Atmosphere. *U.S. Standard Atmosphere, 1976: Sponsored by the National Oceanic and Atmospheric Administration, National Aeronautics and Space Administration and United States Air Force*. U.S. Government Printing Office, 1976.

[96] R. J. Glauber. Cross sections in deuterium at high energies. *Phys. Rev.*, 100:242–248, Oct 1955. doi: 10.1103/PhysRev.100.242. URL https://link.aps.org/doi/10.1103/PhysRev.100.242.

[97] R.J. Glauber and G. Matthiae. High-energy scattering of protons by nuclei. *Nuclear Physics B*, 21(2):135–157, 1970. ISSN 0550-3213. doi: https://doi.org/10.1016/0550-3213(70)90511-0. URL https://www.sciencedirect.com/science/article/pii/0550321370905110.

[98] V. N. Gribov. A REGGEON DIAGRAM TECHNIQUE. *Sov. Phys. JTEP*, 53:654–672, 1967.

[99] Hans P. Dembinski, Ralf Ulrich, and Tanguy Pierog. Future Proton-Oxygen Beam Collisions at the LHC for Air Shower Physics. *PoS*, ICRC2019:235, 2020. doi: 10.22323/1.358.0235.

[100] R. Abbasi et al. IceCube high-energy starting event sample: Description and flux characterization with 7.5 years of data. *Physical Review D*, 104(2), Jul 2021. ISSN 2470-0029. doi: 10.1103/physrevd.104.022002. URL http://dx.doi.org/10.1103/PhysRevD.104.022002.

[101] Joeran Stettner. Measurement of the diffuse astrophysical muon-neutrino spectrum with ten years of icecube data, 2019.

[102] M. G. Aartsen, M. Ackermann, et al. Characteristics of the diffuse astrophysical electron and tau neutrino flux with six years of IceCube high energy cascade data. *Physical Review Letters*, 125(12), sep 2020. doi: 10.1103/physrevlett.125.121104. URL https://doi.org/10.1103%2Fphysrevlett.125.121104.

[103] Sandip Pakvasa, Werner Rodejohann, and Thomas J Weiler. Flavor ratios of astrophysical neutrinos: implications for precision measurements. *Journal of High Energy Physics*, 2008 (02):005–005, feb 2008. doi: 10.1088/1126-6708/2008/02/005. URL https://doi.org/10.1088%2F1126-6708%2F2008%2F02%2F005.

[104] Carlos A. Argüelles, Kareem Farrag, Teppei Katori, Rishabh Khandelwal, Shivesh Mandalia, and Jordi Salvado. Sterile neutrinos in astrophysical neutrino flavor. *Journal of Cosmology and Astroparticle Physics*, 2020(02):015–015, feb 2020. doi: 10.1088/1475-7516/2020/02/015. URL https://doi.org/10.1088%2F1475-7516%2F2020%2F02%2F015.

[105] Stephen Parke and Mark Ross-Lonergan. Unitarity and the three flavor neutrino mixing matrix. *Physical Review D*, 93(11), jun 2016. doi: 10.1103/physrevd.93.113009. URL https://doi.org/10.1103%2Fphysrevd.93.113009.

[106] M. G. Aartsen et al. A COMBINED MAXIMUM-LIKELIHOOD ANALYSIS OF THE HIGH-ENERGY ASTROPHYSICAL NEUTRINO FLUX MEASURED WITH ICECUBE. *The Astrophysical Journal*, 809(1):98, aug 2015. doi: 10.1088/0004-637x/809/1/98. URL https://doi.org/10.1088%2F0004-637x%2F809%2F1%2F98.

[107] Raj Gandhi, Chris Quigg, Mary Hall Reno, and Ina Sarcevic. Ultrahigh-energy neutrino interactions. *Astroparticle Physics*, 5(2):81 – 110, 1996. ISSN 0927-6505. doi: https://doi.org/10.1016/0927-6505(96)00008-4. URL http://www.sciencedirect.com/science/article/pii/0927650596000084.

[108] Benjamin J.P. Jones. Sterile neutrinos in cold climates. 9 2015. doi: 10.2172/1221354. URL https://www.osti.gov/biblio/1221354.

[109] Carlos Alberto Arguelles Delgado. *New Physics with Atmospheric Neutrinos*. PhD thesis, University of Wisconsin, Madison, January 2015.

[110] Aaron C. Vincent, Carlos A. Argüelles, and Ali Kheirandish. High-energy neutrino attenuation in the Earth and its associated uncertainties. *JCAP*, 1711(11):012, 2017. doi: 10.1088/1475-7516/2017/11/012. [JCAP1711,012(2017)].

[111] Amy Connolly, Robert S. Thorne, and David Waters. Calculation of high energy neutrino-nucleon cross sections and uncertainties using the martin-stirling-thorne-watt parton distribution functions and implications for future experiments. *Phys. Rev. D*, 83:113009, Jun 2011. doi: 10.1103/PhysRevD.83.113009. URL https://link.aps.org/doi/10.1103/PhysRevD.83.113009.

[112] Anatoli Fedynitch, William Woodley, and Marie-Cecile Piro. On the Accuracy of Underground Muon Intensity Calculations. *Astrophys. J.*, 928(1):27, 2022. doi: 10.3847/1538-4357/ac5027.

[113] A Sandrock, R P Kokoulin, and A A Petrukhin. Theoretical uncertainties of muon transport calculations for very large volume neutrino telescopes. *Journal of Physics: Conference Series*, 1690(1):012005, dec 2020. doi: 10.1088/1742-6596/1690/1/012005. URL https://dx.doi.org/10.1088/1742-6596/1690/1/012005.

[114] Alessandro Candido, Alfonso Garcia, Giacomo Magni, Tanjona Rabemananjara, Juan Rojo, and Roy Stegeman. Neutrino structure functions from gev to eev energies, 2023.

[115] M. G. Aartsen et al. Search for sterile neutrino mixing using three years of IceCube DeepCore data. *Physical Review D*, 95(11), Jun 2017. ISSN 2470-0029. doi: 10.1103/physrevd.95.112002. URL http://dx.doi.org/10.1103/PhysRevD.95.112002.

[116] K. Abe et al. Limits on sterile neutrino mixing using atmospheric neutrinos in Super-Kamiokande. *Phys. Rev. D*, 91:052019, Mar 2015. doi: 10.1103/PhysRevD.91.052019. URL https://link.aps.org/doi/10.1103/PhysRevD.91.052019.

[117] H. Niederhausen. *Measurement of the High Energy Astrophysical Neutrino Flux Using Electron and Tau Neutrinos Observed in Four Years of IceCube Data*. PhD thesis, State University of New York at Stony Brook, January 2018.

[118] C. A. Argüelles, A. Schneider, and T. Yuan. A binned likelihood for stochastic models. *Journal of High Energy Physics*, 2019(6), jun 2019. doi: 10.1007/jhep06(2019)030. URL https://doi.org/10.1007%2Fjhep06%282019%29030.

[119] S. S. Wilks. The Large-Sample Distribution of the Likelihood Ratio for Testing Composite Hypotheses. *The Annals of Mathematical Statistics*, 9(1):60 – 62, 1938. doi: 10.1214/aoms/1177732360. URL https://doi.org/10.1214/aoms/1177732360.

[120] Glen Cowan, Kyle Cranmer, Eilam Gross, and Ofer Vitells. Asymptotic formulae for likelihood-based tests of new physics. *The European Physical Journal C*, 71(2), feb

2011. doi: 10.1140/epjc/s10052-011-1554-0. URL https://doi.org/10.1140%2Fepjc%2Fs10052-011-1554-0.

[121] R. Abbasi and other. Observation of high-energy neutrinos from the galactic plane. *Science*, 380(6652):1338–1343, 2023. doi: 10.1126/science.adc9818. URL https://www.science.org/doi/abs/10.1126/science.adc9818.

[122] Daniele Gaggero, Dario Grasso, Antonio Marinelli, Alfredo Urbano, and Mauro Valli. The gamma-ray and neutrino sky: A consistent picture of fermi-lat, milagro, and icecube results. *The Astrophysical Journal Letters*, 815(2):L25, dec 2015. doi: 10.1088/2041-8205/815/2/L25. URL https://dx.doi.org/10.1088/2041-8205/815/2/L25.

[123] Alfonso Garcia-Soto. New Results for eV-scale Sterile Neutrino Searches with IceCube. TeVPA Plenary, 2023.

Appendices

Appendix A

Appendix

A.1 The String 37 Offset

Rumor has it a case of pork chops was air-dropped about 500 meters from the old south pole station long ago in the 1970s. Perhaps its parachute never opened, or perhaps it simply fell silently into the dense and billowing snow. All we can surmise is that despite their determined efforts, the polar residents were unable to find their lost and frozen dinner, and some things that should not have been forgotten were lost. And for three and a half decades the crate passed out of all knowledge.

Until, when chance came, it bubbled up into relevance once more. In the 2008-2009 South Pole season, drilling crews repeatedly hit obstacles as the hot water drill melted its way along a three kilometer deep journey. The solution to these obstacles would draw inspiration from film; taking a pump, an air compressor, and some spare jet fuel, driller Dennis Duling of IceCube fashioned an improvised flame-thrower to burn refuse out of the way of the IceCube hot water drill. But, on one particular pass the drill was pulled back to the surface with what appeared to be part of a frozen pork chop adhered to the side of the drill. Looking into the partially melted column, the team saw what can only be described as *horrifying* and *shown in Figure A.1.1*. Unsure of what they had unearthed, the drill crews elected to move the drill site several meters away into untainted ice. Whatever else rested within that hole will stay there, in the glacier, frozen for eons.

In general, these obstacles are what have lead to IceCube's non-perfect grid. The top-right notch missing in Figure 2.0.1 (right) is due to its proximity to the "old pole" station. Drillers found too much debris in that area which would interfere with drilling, and so the strings that

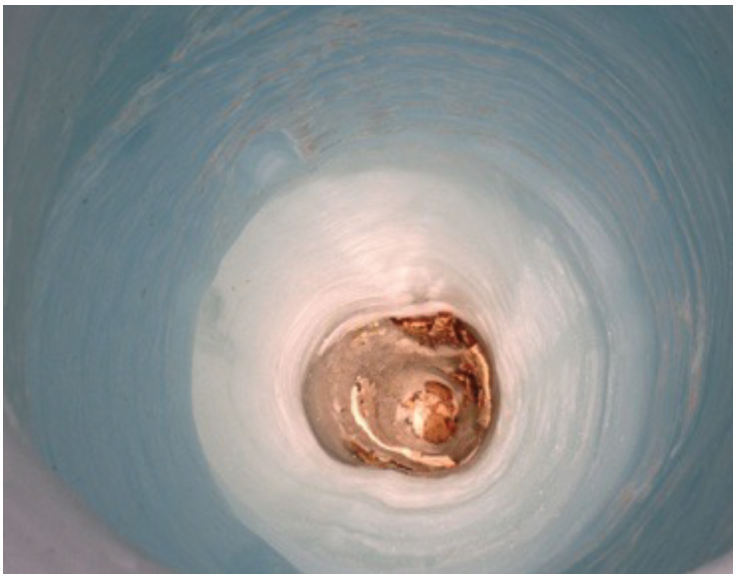

FIGURE A.1.1: Drilling of the hole for string 37 was delayed when the drill operators noticed pork chops were floating to the surface of the hole.

would've been installed there were instead moved into DeepCore. This is why strings 79 and 80 were placed at an odd, internal location. Although now, much of this story may be apocryphal, the story of the pork hole is undeniably true as evidenced by the picture of the pork itself.